AN EXTENDED DOUBLE-GIMBAL SCISSORED-PAIR CONTROL MOMENT GYROSCOPE STEERING CONTROL LAW WITH APPLICATIONS TO ACTIVE DEBRIS REMOVAL AND OCEANOGRAPHIC TARGET TRACKING

by

Cameron P. Creaser

Submitted in partial fulfillment of the requirements
for the degree of Master of Applied Science

at

Dalhousie University
Halifax, Nova Scotia
July 2024

For Mom, Dad, and Aidan. Thanks for always believing in me.

Table of Contents

List of Tables

List of Figures

Abstract

Control Moment Gyroscopes (CMGs) are a unique class of spacecraft momentum exchange actuators which can deliver relatively high control torques on a spacecraft. In this thesis, a Control Momentum Gyroscope design known as the Double-Gimbal Scissored-Pair Control Moment Gyroscope (DGSPCMG) is investigated and applied to a CubeSat placed on three advanced mission case studies in Low-Earth Orbit (LEO). In the first of these case studies, a novel extended DGSPCMG steering control law is introduced which allows the satellite to escape CMG singularities and to perform desaturation of the CMG gimbals while maintaining attitude pointing. In the second case study, the DGSPCMG is applied to enable CubeSat active debris removal missions and a new inertia tensor estimator is presented for tether-assisted inertia estimation of space debris objects. Finally, in the third case study, the DGSPCMG is applied to terrestrial target pointing applications. In addition, this thesis builds a high-fidelity orbital simulation environment for detailed validation of the proposed control laws and an attitude determination system is developed to complement the proposed CMG steering control laws. For the simulation conditions used in this research, the proposed DGSPCMG equipped CubeSat is shown to be highly capable of performing advanced mission objectives in LEO.

List of Abbreviations and Symbols Used

ADCS	Attitude Determination and Control
ADR	Active Debris Removal
BL	Boundary Layer
CCMC	Community Coordinated Modeling Center
CMG	Control Moment Gyroscope
COG	Center of Gravity
COM	Center of Mass
COP	Center of Pressure
COTS	Commercial-off-the-Shelf
DCM	Direction Cosine Matrix
DE432t	Development Ephemeris model 432t
DGCMG	Double-Gimbal Control Moment Gyroscope
DGSPCMG	Double-Gimbal Scissored-Pair Control Moment Gyroscope
ECEF	Earth-Centered Earth-Fixed
ECI	Earth-Centered Inertial
ENZ	East-North-Zenith
ESA	European Space Agency
FOV	Field of View
GAS	Globally Asymptotically Stable
GNC	Guidance, Navigation, and Control
GNSS	Global Navigation Satellite System
ICP	Iterative Closest Points
ICR	In-Cross-Range
IGRF-13	International Geomagnetic Reference Field Generation 13
IMU	Inertial Measurement Unit
JPL	Jet Propulsion Laboratory
KF	Kalman Filter

LEO	Low Earth Orbit
LH	Local Horizon
LiDAR	Light Detection and Ranging
LIF	Luminous Intensity Factor
LORIS	Low-Orbit Reconnaissance Imagery Satellite
MEKF	Multiplicative Extended Kalman Filter
NASA	National Aeronautics and Space Administration
NED	North-East-Down
NEO	NASA Earth Observations (Database)
OD-EKF	Orbit Determination - Extended Kalman Filter
QRIIPIA	Quick-Response Iterative Inertia Properties Identification Algorithm
QUEST	Quaternion Estimation Algorithm
RAAN	Right Angle of the Ascending Node
RW	Reaction Wheel
SCL	Steering Control Law
SGCMG	Single-Gimbal Control Moment Gyroscope
SGP4	Simplified General Perturbations Model 4
SMC	Sliding Mode Control
TCA	Time of Closest Approach
TLE	Two-Line Element
TSE	Two-Stage Estimator
TSR	Tethered Space Robot
UKF	Unscented Kalman Filter
UT	Universal Time
VSDGCMG	Variable-Speed Double-Gimbal Control Moment Gyroscope
VSDGSPCMG	Variable-Speed Double-Gimbal Scissored-Pair Control Moment Gyroscope
WGS84	World Geodetic System 1984

a	Scalar quantity
$\boldsymbol{a}$	Vector quantity
$\mathbf{0}_{n\times m}$	n by m matrix of zeros
$\boldsymbol{I}_{n\times m}$	n by m identity matrix
$\boldsymbol{\mathcal{A}}_1^2$	Direction Cosine Matrix representing a rotation from Frame 1 to Frame 2
$\boldsymbol{\mathcal{F}}_x$	Reference Coordinate Frame X
$(\cdot)^\times$	Skew Symmetric Matrix
$\lvert\cdot\rvert$	Two-norm operation applied on vector
$(\cdot)^T$	Transpose
$\triangleq$	Defined to be equal to
$:=$	Set to be equal to
$\odot$	Hadmard product
$[\boldsymbol{q}\otimes]$	Quaternion product matrix

Acknowledgements

At the heart of this thesis was a supervisor who was equally passionate about space missions as I am. It is with great appreciation that I would like to thank Dr. Robert Bauer for the opportunity to study under his guidance. Dr. Bauer provided endless support for my work and I will be eternally grateful for his devotion to my success. From countless paper reviews to our weekly meetings, Dr. Bauer made continual efforts to make my work a priority. It was a privilege to have had this opportunity.

This thesis is dedicated to my family who has continually backed my academic efforts, listened to me talk about space, and supported me from start to finish. To Mom, I hope you can can rejoice in this accomplishment as much as I can, for you built the foundations which brought me to this point.

Finally, I would like to thank my peers at the Dalhousie Space Systems Laboratory. It has been a pleasure to have worked beside all of you over the past few years pushing LORIS and MANTIS to space. I am extremely proud to have been part of such an intelligent and motivated team.

Chapter 1

Introduction

CubeSats are a specific class of nanosatellites which conform to a geometric standard where the size of the CubeSat is expressed in a number of Units or "U's" defined by 10 cm cubes [2]. Since 1999, the CubeSat platform has grown in popularity with modern CubeSats now performing important scientific and engineering objectives [3]. At the time of writing the subject thesis, developments in miniaturization of satellite payloads and sensors has led to a significant number of CubeSats being launched into Low Earth Orbit (LEO) to carry out primarily science missions [4]. It has been argued that to enable the rapid growth of these advanced CubeSat objectives there will be a rise in demand for highly-agile spacecraft which can rapidly reorient and stabilize their attitude to observe or collect scientific data. This demand could motivate satellite developers to equip their satellites with Control Moment Gyroscopes (CMGs) which tend to have higher torque to power-draw ratios than commonly used reaction wheel (RW) actuators. [5].

While some progress has been made on the miniaturization of CMGs for CubeSat applications in [6][7] and [8], many of these multi-CMG clusters account for a significant portion of the mass and volume ascribed to the CubeSat. Additionally, commercial-off-the-shelf (COTS) control moment gyroscopes are fairly limited, with some designs not conforming to the CubeSat unit standard [6]. It is clear that there is a need to develop orbit-ready CMG designs and control laws which enable the modern day objectives of current highly-agile CubeSat missions.

1.1 The Control Moment Gyroscope

A CMG is typically a fixed momentum device which can be gimballed to change the direction of the stored angular momentum in a spinning flywheel [9]. The gimbal concept is unlike RWs – where the flywheel accelerates or decelerates to change the stored angular momentum about a fixed axis. The most basic CMG is the Single-Gimbal CMG (SGCMG) which grants control about a single axis of a satellite. It follows that for full 3-axis control of the satellite, a minimum of three SGCMGs would be required [9]. Many clusters of SGCMGs have been developed, all which strive to enable 3-axis control while modifying the configuration of the SGCMGs to change the performance characteristics of the cluster.

Two of these SGCMG cluster designs include the Rooftop Array or Pyramid Array CMG [10]. For the case of the Pyramid Array CMG, the cluster produces a desirable feasible angular momentum profile which is spherical [11]. For the case of the Rooftop array, the feasible angular momentum profile is elliptical [10]. The feasible angular momentum profile is a surface in 3d angular momentum space for which the CMG

total angular momentum vector cannot extend beyond this surface. Fig. 1.1 shows the gimbal axes of individual SGCMGs which characterize the Pyramid Array CMGs. It is typical for the gimbal axes to be skewed in this design by 54.74° to achieve a spherical angular momentum profile [7].

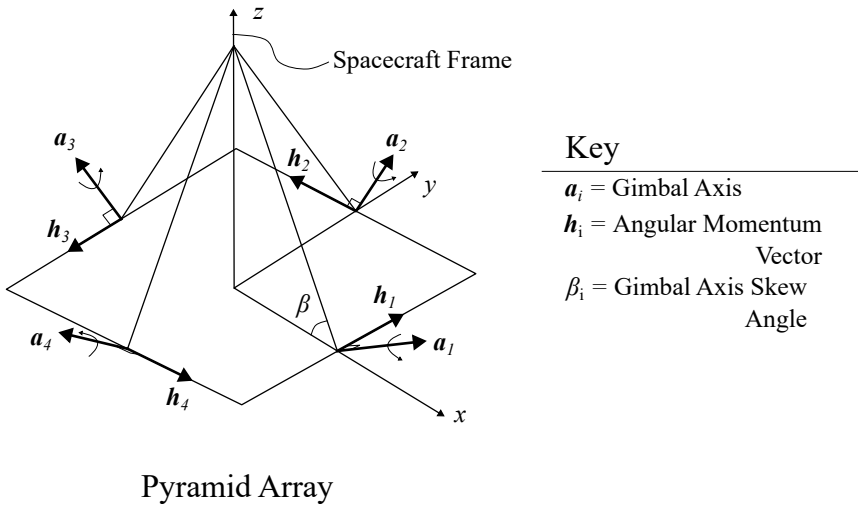

Figure 1.1: Vector Diagram of Pyramid Array CMG Design with 4 SGCMGs Shown.

These CMG designs employ four SGCMGs (each with a single flywheel); however, by adding an additional gimbal to a given flywheel, 3-axis control can be maintained while reducing the number of flywheels. One such example is known as the Variable-Speed Double-Gimbal CMG (VSDGCMG) where a single variable speed flywheel and two gimbal axes can achieve 3-axis control [12][13]. Unlike SGCMGs, Double Gimbal CMGs (DGCMGs) must support some of the torque produced by the CMG in the outer gimbal [9]. Therefore, there is typically a trade-off to be considered with torque generation and the reduction of flywheels. A trade-off associated with VSDGCMGs specifically, is that, although only one flywheel is required, the degree of freedom enabled by the variable speed flywheel is limited to the relatively low torque output of the DC motor driving the wheel. With SGCMG clusters, the requirement for a minimum of three flywheels increases the actuator mass which could complicate their integration into small satellites.

A recent development in CMG designs known as the Double-Gimbal Scissored-Pair CMG (DGSPCMG) presented in [14] has shown promise for use in agile small satellites because it can achieve 3-axis attitude control with only two flywheels and three gimbal axes. The DGSPCMG and its primary components are represented pictorially in Fig. 1.2. A nicety of the subject design is that its internal singularities are only of the hyperbolic type which provides much more flexibility for escape from these singularities. Singularities are a complication of CMGs where for specific scenarios, the CMG loses the ability to produce torque about all axes, making it desirable to avoid these singular states. An added nuance of the DGSPCMG is that the

scissor-pair gimbal acts peripherally like the variable speed aspect of VSDGCMGs in changing the stored angular momentum of the CMG, but the DGSPCMG is not limited to the capabilities of the DC motor driving the flywheel like the VSDGCMG.

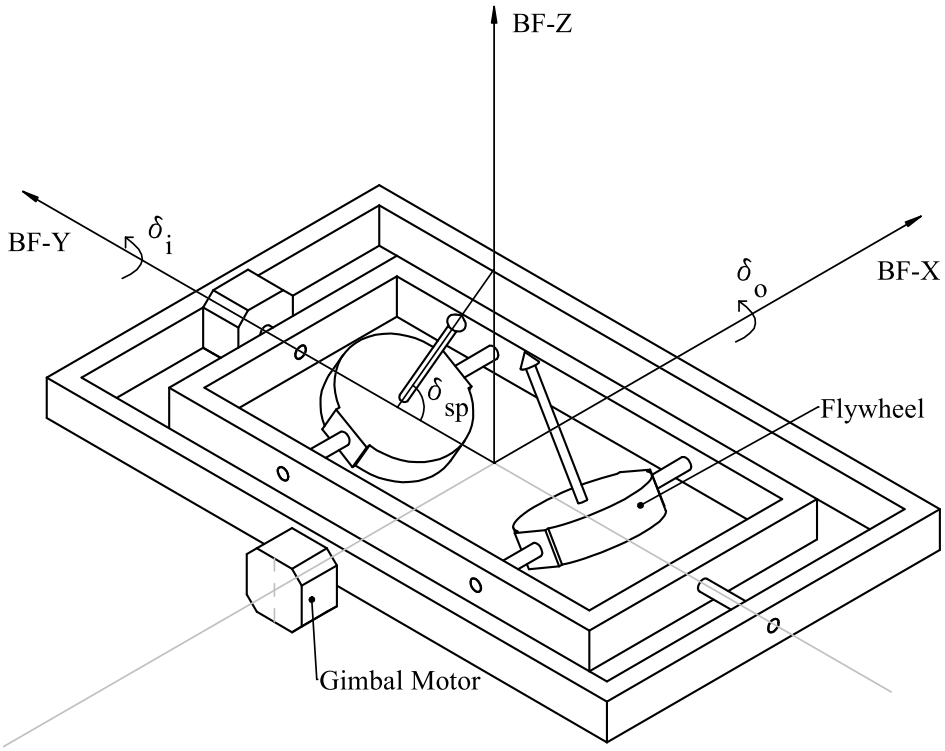

Figure 1.2: Schematic of the DGSPCMG. The symbols $\delta_{sp}, \delta_i, \delta_o$ represent the scissored-pair, inner, and outer gimbal axes, respectively.

While SGCMG clusters and DGCMGs alike have been utilized on current and previous space missions, The DGSPCMG lacks the technical readiness to be applied to real space missions. Despite having a desirable angular momentum profile and relatively manageable singular conditions, more study is required to extend the DGSPCMG to modern advanced agile CubeSat missions. Accordingly, this thesis makes significant steps to extended DGSPCMG gimbal steering control laws (SCLs) and demonstrates the possibility for the use of the DGSPCMG for advanced on-orbit CubeSat missions.

1.2 Case Studies

To introduce the scenarios where the capabilities of the DGSPCMG were analyzed, this section outlines the case studies which were conducted in the subject thesis. The need for technology advancements within these case studies is also addressed.

1.2.1 Earth Observation & Simultaneous Actuator Desaturation

As of March 20th, 2024, there were 9721 active satellites known in orbit [15] with a large portion of these satellites being LEO Earth observation CubeSats [16]. A complication of long-term Earth observation missions is that secular disturbances lead to a buildup of stored angular momentum in momentum exchange actuators like CMGs. Such a buildup eventually necessitates for the actuator to offload excess stored momentum. Without executing momentum dumping, attitude actuators like CMGs will saturate and attitude control will be lost.

Reaction wheel desaturation is a well-studied concept; however, many methods to perform desaturation treat it as a separate operation from nominal pointing [17][18]. More modern methods have been attempting to handle both events simultaneously so that the main objectives of the satellite mission are not disrupted [19]. The desaturation of CMGs is a relatively understudied concept with only a few papers discussing the effect of orbital disturbances on the CMG singularities [20]. The degeneration of a DGSPCMG into a singularity through orbital disturbances is further studied in this thesis and a control methodology is proposed to handle these singularities, actuator saturation effects, and nominal pointing.

1.2.2 Active Debris Removal

According to the European Space Agency (ESA) 2022 space environment report, at the end of 2022 there were 19694 space debris objects in LEO. Already, the chance of collisions among existing space debris is high enough that the number of objects in LEO is expected to increase even without new launches [21]. The effect of having continual growth of space debris objects is known as the "Kessler Syndrome", where the fragmentation of a body from an orbital collision results in a spread of objects which can subsequently cause more collisions [22]. These rapid debris growth projections have lead researchers to develop Active Debris Removal (ADR) missions where agile spacecraft attempt to remove large debris objects from orbit which have a higher probability of causing a collision.

These future ADR missions will require a highly-agile and robust Attitude Determination and Control System (ADCS) to handle capture of large debris objects. CMGs could be a necessary technology to enable this agility; however, for missions where information about the target is lacking, online estimation algorithms will be required to determine the debris' properties on-orbit and subsequently update the CMG control laws. One promising method of debris capture is to attach a long tether cable to the debris object. While the method allows the chaser spacecraft to maintain safe distance from the debris, more work is required to be able to estimate the debris' inertial properties using the tether. The method of estimating space debris inertia with a space tether is advanced in this thesis while applying the DGSPCMG onboard the proposed chaser satellite for attitude control.

1.2.3 Oceanographic Target Tracking

For advanced optical payloads, satellites may be required to slew towards and track a target on Earth by pointing the boresight of an optical sensor at the ground target. While CubeSats have been used extensively in this task for observing terrestrial targets [23][24], it has been argued that CubeSats have been underutilized on oceanographic missions [25]. With future missions like MANTIS (being developed at Dalhousie University) and HYPSO-2 (being developed at the Norwegian University of Science) aiming to perform oceanographic science objectives, there is a need to demonstrate a CubeSat ADCS for oceanographic target tracking. While researchers have demonstrated the advanced capabilities of CMGs for rest-to-rest attitude maneuvers, more work is required to validate the control laws for target tracking campaigns. This research investigates the use of a DGSPCMG-equipped ADCS on an oceanographic target tracking campaign to help address the lack of CubeSat oceanographic missions. The case study was additionally used to further validate the novel extended DGSPCMG control laws developed within the thesis.

1.3 Thesis Overview & Objectives

To support the development of future agile small satellites in LEO, this thesis aims to:

1. Develop a highly-robust and agile steering control law that enables of the use of the DGSPCMG on-orbit. In addition, the steering control law should add the capability to desaturate the CMG momentum without disrupting the spacecraft mission objectives.

2. Propose a new inertia estimation algorithm that determines the inertial parameters of tethered uncooperative space debris on CubeSat ADR missions.

3. Demonstrate precision oceanographic target tracking through simulations of a DGSPCMG-equipped CubeSat with attitude determination algorithms in the loop.

4. Build on the capabilities at Dalhousie University for performing future high-fidelity spaceflight simulations.

In effect, the thesis develops technological improvements for emerging technologies in satellite ADCS but ties all advancements under the use of the DGSPCMG on the discussed mission concepts. By doing so, the advanced capabilities of the DGSPCMG are shown along with the success of the novel control or estimation algorithms proposed within this thesis. Further, the thesis aims to make significant contributions to extending the development of spaceflight simulations at Dalhousie University by building on the work provided in previous theses such as [26]. The present thesis adds, adapts, or modifies many of the orbit and attitude propagation techniques provided in [26] to progress towards having high-fidelity future spaceflight simulations being

performed at Dalhousie University. Efforts made to advance simulation fidelity also act to increase the confidence in the ADCS tested within the simulator.

In pursuit of achieving these objectives, the thesis is organized as follows: Chapter 2 provides a literature review summarizing current commercial and experimental CMG designs. In Chapter 3 the orbit and attitude propagators which drive the simulations are derived. Chapter 3 also includes models for orbital disturbances which impact spacecraft ADCS. Following, in Chapter 4, the algorithms which estimate the spacecraft attitude and orbit are provided in lead up to controlling this attitude in Chapter 5. In relation to attitude control, Chapter 5 presents the DGSPCMG design and its dynamics are derived. A deep discussion is provided for the specific singularities encountered by the DGSPCMG and its momentum envelope. Chapter 5 also develops the novel Extended DGSPCMG steering control law and develops the magnetic torque gimbal compensator. Given that the attitude controller is closely tied to the steering control law, it is also presented in this chapter. Chapter 6 applies the novel Extended DGSPCMG control law on an ADR mission where a novel inertia estimation algorithm is developed. This novel inertia estimator is shown to accurately determine the inertia of tethered debris despite not having an assumption of the tether connection point. Following, in Chapter 7, the third case study of oceanographic target pointing with a CMG is derived and discussed. Target Tracking error metrics are provided in this section to evaluate the proposed ADCS performance on target tracking missions. Finally, Chapter 8 draws conclusions and recommendations based on the research developments made in the thesis.

Chapter 2

Literature Review

With the CubeSat standard gaining popularity and the clear benefits CMGs provide for agile satellites, it would be expected for academic and industrial organizations to pursue the development of micro-sized CMGs. This section investigates the need for further development of CubeSat CMG technology based on a literature study of flown, commercially available, and experimental CMG designs.

2.1 Flown CMG Designs on CubeSat Platforms

Table 2.1 compiles a set of data related to CubeSat-sized CMG designs which were flown on successful space missions. CubeSats which are planned or were canceled were not included in the list. Notably, there has not been a proliferation of CMG-equipped CubeSats with only three publicly-listed mission designs including a CMG. While the CMG used on SCAT++ and SwampSAT acted as the primary attitude actuator, the CMG used on BILSAT was only used as a technology demonstration for 1-axis CMG rotational control.

Table 2.1: Flown CubeSat CMG Units as of 2024

Compilation of Flown CMG Designs & Specifications

Satellite & Ref	**Developer**	**Satellite Size**	**CMG Package Size**	**Cluster Design**	**Steering Law**
SCAT++ [27]	Naval Postgraduate School	2U	0.5U	N/A	N/A
SwampSAT [28]	University of Florida	1U	0.5U	Pyramid	Generally Singularity Robust (GSR)
BILSAT-1 [29]	University of Surrey	$60 \times 60 \times 60$ cm	2U	2-CMG Parallel	Inverse Law

2.2 Commercial and Experimental CMG Designs

Table 2.2 compiles a list of published CMGs where designs provided in literature and available from retail were considered. Highlighted entries in Table 2.2 are CMG designs which are purely experimental and not available as an off the shelf component. The provided list is not a conclusive list of available CMGs, but demonstrates that CubeSat engineering teams are faced with a limited selection of commercial CMGs. In some cases, the available CMG is an SGCMG, which forces the CubeSat developer to further design the cluster and SCL to accommodate the use of the SGCMG. In many cases, a subject matter expert would be required to enable the development of a mission specific CMG cluster and SCL.

Table 2.2: Available CMG Designs as of 2024, Experimental CMG Designs Highlighted

Compilation of Identified CMG Designs & Specifications

Name & Ref	**Manufacturer**	**Volume (mm)**	**Mass (kg)**	**Momentum Storage (Nms)**	**Design Platform**	**Cluster Design**
CMG-10m [30]	Tensor Tech	$100 \times 100 \times 75$	0.29	$10\text{E}-03$	3U	Spherical
Microsat CMG [31]	Honeybee Robotics	$230 \times 125 \times 82$	0.7	$224\text{E}-03$	>6U	Box
Micro-CMG [32]	Veoware Space	$97 \times 97 \times 180$	2.75	0.7	SmallSat	SGCMG
CMG8 [33]	Blue Canyon Technologies	$220 \times 220 \times 300$	10	8	SmallSat	Pallet
CMG Mk.II [34]	University of Surrey	N/A	0.2	0.23	MicroSat	SGCMG
CMG 40s [35]	Airbus	N/A	38	40	Medium	SGCMG
M50 [36]	Honeywell Aerospace	$195 \times 447 \times 714$	28	25	Medium	SGCMG
Baker CMG [7]	Lulea University of Tech	$95.8 \times 95.8 \times 95.8$	0.85	$4.57\text{E}-03$	2U-3U	Pyramid
Gaude CMG [6]	Cranfield University	$100 \times 100 \times 50$	0.25	$0.629\text{E}-03$	2U-3U	Pyramid
Steyn CMG [37]	Stellenbosch University	$47 \times 49.5 \times 94$	0.26	$1.43\text{E}-03$	2U	VSDGSPCMG

Most notably from Table 2.2, only 2 COTS CMGs were identified for the CubeSat design platform. The Microsat CMG is most applicable to CubeSats larger than 6U — a CubeSat bus size which represents only approximately 15% of all launched CubeSats [16]. A complication of the Tensor Tech CMG-10m unit is that this spherical CMG only enables 2-axis control of the spacecraft. A possible reason for the lack of available COTS CMGs is that, as found by Votel and Sinclair (2012), CMGs lack power efficiency when the satellite has principal moments of inertia smaller than 1 kgm^2 [5]. This notion would suggest that CMGs are not viable on a power consumption basis

when the satellite bus is smaller than 6U. Despite this design constraint, the more recent experimental Steyn (2015) Variable-Speed Double-Gimbal Scissored-Pair CMG (VSDGSPCMG) demonstrated a power efficiency which was comparatively greater than similarly-sized reaction wheels systems fitting inside 1U [37]. While power, mass, and volume efficiencies vary for each CMG or RW cluster design, the torque to momentum ratio is consistently higher for CMGs [5].

The findings from considering the available CMG designs indicate that the lack of commercial CMG options would justifiably explain the paucity of CMG usage on flown CubeSat missions. Experimental CMG designs have shown the viability of CMGs for common CubeSat buses in the range of 2U-6U, but these designs are not turnkey solutions, and they would require lengthy development of advanced ADCS and SCLs to support the usage of a CMG. With regards to the DGSPCMG, it is reasonable to expect the design to be similarly power efficient to the Steyn design by nature of the double-gimbal. This power efficiency could be realized all while lacking some of the constraints identified in Section. 1.1 with variable speed CMGs. Like other experimental designs, the DGSPCMG requires further SCL development to be routinely applied on CubeSat missions. This thesis develops these control algorithms and demonstrates their success in high fidelity simulations.

Chapter 3

Attitude and Orbit Propagator

In this chapter the orbit and attitude equations of motion are presented for the focus satellite design. Orbit effects such as disturbance torques and lighting conditions are also established to complete the high-fidelity orbit propagation.

3.1 Mathematical Preliminaries

Prior to developing the attitude and orbit equations of motion which enable the simulations presented in this thesis, some mathematical preliminaries must be addressed. Primarily, an inertial coordinate system is defined to be fixed in position and non-rotating. A non-inertial coordinate system may be rotating or changing in position. For the case of this thesis, many of these coordinate frames are Earth or satellite based and are explained thoroughly in Appendix A. When addressing a coordinate reference frame, vectrix notation is applied from Hughes (2012) [38]. A vectrix, denoted by $\boldsymbol{\mathcal{F}}_x$, represents a set of orthonormal and dextral (right-handed) basis vectors belonging to reference frame "x". Using vectrix notation, it is typical for dot and cross products to be written as:

$$\boldsymbol{a}_x \cdot \boldsymbol{b}_x = \boldsymbol{a}_x^T \boldsymbol{b}_x, \qquad \boldsymbol{a}_x \times \boldsymbol{b}_x = \boldsymbol{a}_x^\times \boldsymbol{b}_x \tag{3.1}$$

Here $\boldsymbol{a}_x = [a_1, a_2, a_3]^T$ is a 3 component column vector expressed in $\boldsymbol{\mathcal{F}}_x$. The operator $()^\times$ represents the skew symmetric matrix which is constructed following:

$$\boldsymbol{a}_x^\times \triangleq \begin{bmatrix} 0 & -a_3 & a_2 \\ a_3 & 0 & -a_1 \\ -a_2 & a_1 & 0 \end{bmatrix} \tag{3.2}$$

To transform a vector from its expression in one reference frame to its equivalent expression in another reference frame, a Direction Cosine Matrix (DCM) is applied via left-hand multiplication. The principal rotation DCMs about the x, y, and z bases vectors of a reference frame are represented by C1, C2, and C3, respectively. A 3-2-1 Euler rotation sequence can therefore be defined by:

$$\boldsymbol{\mathcal{A}}_1^2 = C1(\theta_1)C2(\theta_2)C3(\theta_3) \tag{3.3}$$

where the principal rotation functions "C1(θ)", "C2(θ)", and "C3(θ)" follow the convention provided in the following set of equations:

$$\mathrm{C1}(\theta) = \begin{bmatrix} 1 & 0 & 0 \\ 0 & \cos(\theta) & \sin(\theta) \\ 0 & -\sin(\theta) & \cos(\theta) \end{bmatrix} \tag{3.4}$$

$$\mathrm{C2}(\theta) = \begin{bmatrix} \cos(\theta) & 0 & -\sin(\theta) \\ 0 & 1 & 0 \\ \sin(\theta) & 0 & \cos(\theta) \end{bmatrix} \tag{3.5}$$

$$\mathrm{C3}(\theta) = \begin{bmatrix} \cos(\theta) & \sin(\theta) & 0 \\ -\sin(\theta) & \cos(\theta) & 0 \\ 0 & 0 & 1 \end{bmatrix} \tag{3.6}$$

For the applications within this thesis, $\boldsymbol{\mathcal{A}}_1^2$ represents the subsequent DCM which expresses a vector from $\boldsymbol{\mathcal{F}}_1$ into its expression in $\boldsymbol{\mathcal{F}}_2$. The rotation angles θ_{1-3} about the principal rotation axes are enclosed in the round brackets proceeding C1-3.

3.1.1 Quaternions

Quaternions are another parameterization method to express rotation. In this thesis, quaternions are used to express the spacecraft attitude with respect to the inertial reference frame. A quaternion $\boldsymbol{q}$, is a set of four parameters which posses the unit-norm property $\boldsymbol{q}^T\boldsymbol{q} = 1$ and represent a rotation about the Euler axis $e = [e_1, e_2, e_3]$ through angle θ. A quaternion is then expressed as:

$$\boldsymbol{q} = [\hat{\boldsymbol{q}}, q_4]^T = [q_1, q_2, q_3, q_4]^T = \begin{bmatrix} e_1 \sin(\theta/2) \\ e_2 \sin(\theta/2) \\ e_3 \sin(\theta/2) \\ \cos(\theta/2) \end{bmatrix} \tag{3.7}$$

Note that in Eq. (3.7) the first three elements of the quaternion $\hat{\boldsymbol{q}}$ represent the vector portion, and the fourth component represents the scalar portion following the convention provided in [39]. It is sometimes useful to convert the attitude quaternion to a DCM. The quaternion to DCM conversion is accomplished as follows [40]:

$$\boldsymbol{\mathcal{A}} = \begin{bmatrix} q_4^2 + q_1^2 - q_2^2 - q_3^2 & 2(q_1q_2 + q_3q_4) & 2(q_1q_3 - q_2q_4) \\ 2(q_1q_2 - q_3q_4) & q_4^2 - q_1^2 + q_2^2 - q_3^2 & 2(q_2q_3 + q_1q_4) \\ 2(q_1q_3 + q_2q_4) & 2(q_2q_3 - q_1q_4) & q_4^2 - q_1^2 - q_2^2 + q_3^2 \end{bmatrix} \tag{3.8}$$

Some quaternion operators and identities are additionally defined here following the theory presented in [41] for reference in later sections:

$$\Omega(\boldsymbol{\omega}) = \begin{bmatrix} 0 & \omega_3 & -\omega_2 & \omega_1 \\ -\omega_3 & 0 & \omega_1 & \omega_2 \\ \omega_2 & -\omega_1 & 0 & \omega_3 \\ -\omega_1 & -\omega_2 & -\omega_3 & 0 \end{bmatrix} \tag{3.9}$$

$$\Xi(\boldsymbol{q}) = \begin{bmatrix} q_4 & -q_3 & q_2 \\ q_3 & q_4 & -q_1 \\ -q_2 & -q_1 & q_4 \\ -q_1 & -q_2 & -q_3 \end{bmatrix} \tag{3.10}$$

$$\boldsymbol{q}\otimes = \begin{bmatrix} q_4 & q_3 & -q_2 & q_1 \\ -q_3 & q_4 & q_1 & q_2 \\ q_2 & -q_1 & q_4 & q_2 \\ -q_1 & -q_2 & -q_3 & q_4 \end{bmatrix} \tag{3.11}$$

$$\boldsymbol{q}^{-1} = \frac{1}{|\boldsymbol{q}|^2}[-\boldsymbol{q}_{1:3}\ q_4]^T \tag{3.12}$$

$$\boldsymbol{\mathcal{A}}(\boldsymbol{q}) = (q_4^2 - q_1^2 + q_2^2 + q_3^2)\boldsymbol{I}_{3\times 3} + 2\boldsymbol{q}_{1:3}\boldsymbol{q}_{1:3}^T + 2q_4 \begin{bmatrix} 0 & -q_3 & -q_2 \\ -q_3 & 0 & q_1 \\ q_2 & -q_1 & 0 \end{bmatrix} \tag{3.13}$$

3.2 Perturbed Orbit Dynamics

In this section the translational equations of motion for a satellite orbiting Earth in LEO are presented. The formulations are derived on the basis of ensuring high fidelity and so that unmodeled dynamics exist in the Orbit Determination - Extended Kalman Filter (OD-EKF) presented later in Section. 4.5.

All orbits around Earth are affected by a number of perturbations which change the orbit over time. For the case of LEO, the largest of these perturbations is caused by the oblateness of Earth [42]. The oblateness of Earth causes for the gravitational acceleration experienced by the satellite to vary with position and for the acceleration to not be purely radial. While unperturbed orbital dynamics models such as the Cowell model are sufficient in very short time horizons, a more detailed model is required to account for perturbations which can cause for hundreds of kilometers of change in the orbit [43]. To this end, a zonal harmonic gravity model is presented in this section to address orbital perturbations.

The general equation for the orbital acceleration of the spacecraft in $\boldsymbol{\mathcal{F}}_{ECI}$ is given as:

$$\boldsymbol{a}_{ECI} = \boldsymbol{g}_{ECI} + \frac{\boldsymbol{f}}{m} \tag{3.14}$$

In Eq. (3.14) $\boldsymbol{g}_{ECI}$ is the orbital acceleration around Earth accounting for zonal harmonics, $\boldsymbol{f}$ is the sum of all other perturbing forces on the orbit, and m is the mass of the spacecraft. To yield the $\boldsymbol{g}_{ECI}$ term, the spherical harmonic representation for gravity potential can be considered [44][42][45]:

$$U = \frac{\mu}{r}\sum_{n=0}^{\infty}\left(\frac{R_e}{r}\right)^n \sum_{m=0}^{n} P_{n,m}(\sin\phi)\left[C_{n,m}\cos m\lambda + S_{n,m}\sin m\lambda\right] \tag{3.15}$$

Considering Eq. (3.15), the accuracy and computational load can be seen to greatly depend on the selection of the parameters n and m. The coefficients $C_{n,m}$ and $S_{n,m}$ are the spherical harmonic coefficients specific to a heavenly body and degree n, m. The $P_{n,m}(x)$ functions are the Legendre Polynomials corresponding to degree n, m. Further, μ is the gravitational parameter for Earth, r is the orbital radius, ϕ is the co-latitude defined by $\phi = \frac{\pi}{2} - \delta$, and λ is the celestial longitude. These parameters are derived in detail as part of Appendix A.1.8. To demonstrate the effect of the polynomial degree, n and m can be set to 0 so that Eq. (3.15) reduces to a gravity potential which is constant regardless of ϕ and λ:

$$U_{0,0} = \frac{\mu}{r} \tag{3.16}$$

It is commonplace in the literature to represent the coefficient $C_{n,m}$ as J_n where J_n terms are known as the Jeffery's Constants [44]. When $m = 0$, the harmonic coefficients are known as zonals. When $m \neq 0$ the harmonic coefficients are known as tesserals. For the specific case that $m = n$ the coefficients are known as sectorials. Hereinafter, this thesis only considers a zonal model with $m = 0$ because the contribution of tesserals and sectorials to the gravity potential is substantially smaller than the zonals in short-term time horizons [42]. In addition, it is deemed sufficient to compute a model of order $n = 3$ because the contribution of the J_4 term is three orders of magnitude smaller than the J_2 term [42]. Noting these selected polynomial degrees, the gravity potential from Eq. (3.15) reduces to:

$$U = \frac{\mu}{r}\left[1 - \sum_{n=2}^{\infty}\left(\frac{R_e}{r}\right)^n J_n P_n(\cos\phi)\right] \tag{3.17}$$

The Jeffery's constants used in this work are provided in Table 3.1 up to the J_4 coefficient.

The acceleration due to gravity can be obtained by computing the gradient of the gravitational potential with respect to a spacecraft position vector $\boldsymbol{r}$:

$$\boldsymbol{g} = -\left(\frac{\partial U}{\partial \boldsymbol{r}}\right)^T = -\frac{\partial U}{\partial r}\boldsymbol{i}_r - \frac{\partial U}{r\partial\phi}\boldsymbol{i}_\phi \tag{3.18}$$

or equivalently:

$$\boldsymbol{g} = g_r\boldsymbol{i}_r - g_\phi\boldsymbol{i}_\phi \tag{3.19}$$

Table 3.1: Jeffery's's Constants Obtained from [1]

Jeffery's Zonal Constants for Oblate Earth

Coefficient	**Value**
J_2	0.0010826269
J_3	-0.0000025323
J_4	-0.0000016204

Here, $\boldsymbol{i}_r = [1, 0, 0]^T$ is the radial unit vector and $\boldsymbol{i}_\phi = [0, 0, -1]^T$ is the southward unit vector expressed in $\mathcal{F}_{LH}$. Noting Eq. (3.18), the radial g_r and transverse g_ϕ gravitational acceleration components can be derived by computing the partial differentiation of U with respect to r and ϕ respectively:

$$
\begin{aligned}
g_r = \frac{\partial U}{\partial r} &= \frac{\partial}{\partial r}\left[\frac{\mu}{r} - \frac{\mu}{r}\left(J_2\left(\frac{R_e}{r}\right)^2 P_2(\cos\phi) + J_3\left(\frac{R_e}{r}\right)^3 P_3(\cos\phi)\right)\right] \\
g_r &= \frac{\partial}{\partial r}\left[\frac{\mu}{r} - \frac{\mu R_e^2 J_2}{r^3}P_2(\cos\phi) - \frac{\mu R_e^3 J_3}{r^4}P_3(\cos\phi)\right] \\
g_r &= \left[-\frac{\mu}{r^2} + \frac{3\mu R_e^2 J_2}{r^4}P_2(\cos\phi) + \frac{4\mu R_e^3 J_3}{r^5}P_3(\cos\phi)\right] \\
g_r &= -\frac{\mu}{r^2}\left[1 - 3J_2\left(\frac{R_e}{r}\right)^2 P_2(\cos\phi) - 4J_3\left(\frac{R_e}{r}\right)^3 P_3(\cos\phi)\right]
\end{aligned} \tag{3.20}
$$

Following the same procedure as done for the radial component but with respect to ϕ, the transverse component can be found as:

$$
g_\phi = \frac{3\mu}{r^2}\left(\frac{R_e}{r}\right)^2 \sin\phi\cos\phi\left[J_2 + \frac{1}{2}J_3\left(\frac{R_e}{r}\right)\sec\phi(5\cos^2\phi - 1)\right] \tag{3.21}
$$

For completeness, the Legendre Polynomials are provided here:

$$P_0(x) = 1 \tag{3.22}$$

$$P_1(x) = x \tag{3.23}$$

$$P_2(x) = \frac{1}{2}(3x^2 - 1) \tag{3.24}$$

$$P_3(x) = \frac{1}{2}(5x^3 - 3x) \tag{3.25}$$

By considering Eq. (3.20) and Eq. (3.21) it can be deduced that changes in the acceleration due to gravity occur only for changes in the co-latitude ϕ and orbit radius r. The result is reasonable because the zonal harmonics vary with changes in latitude and are constant for degrees of longitude. Fig. 3.1 normalizes the magnitude

of radial gravity to observe the variation in radial gravity with respect to celestial latitude. The gravitational acceleration vector yielded from Eq. (3.19) is expressed

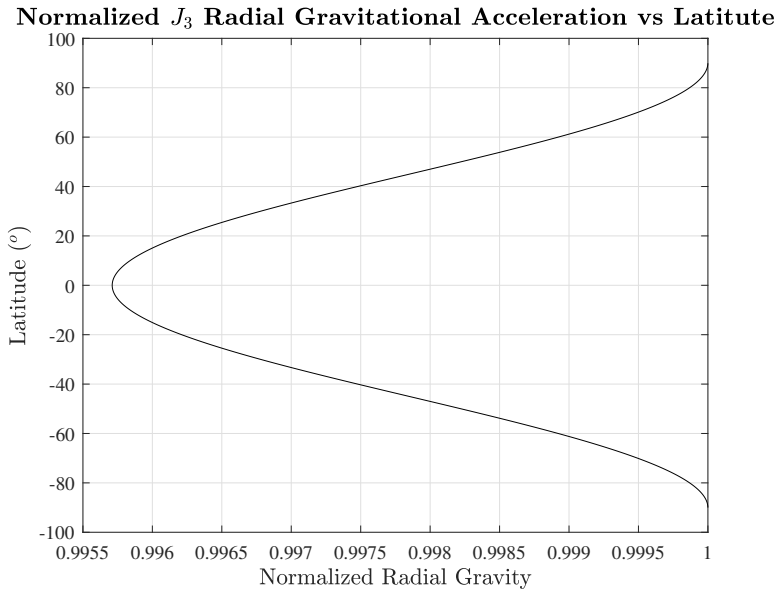

Figure 3.1: Normalized Variation in Radial Gravity with Respect to Latitude

in $\mathcal{F}_{LH}$ and must be expressed in $\mathcal{F}_{ECI}$ for orbit propagation. The transformation to $\mathcal{F}_{ECI}$ is handled by the following equation in the simulator:

$$\boldsymbol{g}_{ECI} = \left(\boldsymbol{\mathcal{A}}_{ECI}^{LH}\right)^{T} \boldsymbol{g} \tag{3.26}$$

In addition, it was found in this work that the direction of $\boldsymbol{g}_{ECI}$ must be corrected dependent on the quadrant of where the satellite position vector lies in the x-y plane of $\mathcal{F}_{ECI}$. The direction can be corrected following:

$$\begin{cases} \boldsymbol{g}_{ECI_1} = -\boldsymbol{g}_{ECI_1}, \text{ if } \boldsymbol{r}_{ECI_1} < 0 \\ \boldsymbol{g}_{ECI_1}, \text{else} \end{cases} \tag{3.27}$$

While the inclusion of J_{2-3} gravity harmonics are significant perturbations for a satellite in LEO, it is shown in [46] and [47] that lunar gravity is the next most significant orbital perturbative force for a satellite with a roughly 400km altitude. It is, therefore, important to include the effects of the Moon as a third body in the orbit dynamics. To accomplish the modeling of this perturbation, lunar ephemeris data was acquired in the simulator for the Julian day at the current simulation time from the MATLAB aerospace block set running the National Aeronautics and Space Administration (NASA) Jet Propulsion Laboratory (JPL) Development Ephemeris model 432t (DE432t). The ephemeris data yields the position of the Moon denoted by $\boldsymbol{r}_l$ in $\mathcal{F}_{ECI}$. The unit direction vector from the satellite COM to the center of the

Moon is:

$$\boldsymbol{u}_s^l = \frac{\boldsymbol{r}_l - \boldsymbol{r}_{ECI}}{|\boldsymbol{r}_l - \boldsymbol{r}_{ECI}|} \tag{3.28}$$

where m_l is the mass of the moon, G is the gravitational constant, and $r_l^s = |\boldsymbol{r}_l - \boldsymbol{r}_{ECI}|$ allows for the gravitational force between the moon and the satellite to be calculated as:

$$f_l = \frac{Gmm_l}{(r_s^l)^2} \tag{3.29}$$

The resulting force vector applied on the satellite expressed in $\mathscr{F}_{ECI}$ is:

$$\boldsymbol{f}_l = f_l \boldsymbol{u}_s^l \tag{3.30}$$

In this work, $\boldsymbol{f} = \boldsymbol{f}_l$ and the effects of other smaller forces are neglected. For long-term simulations in LEO it would be beneficial to include an atmospheric drag force to account for orbit decay.

3.3 Spacecraft Attitude Dynamics

The rotational equations of motion which govern the attitude of the satellite are presented in this section. A rigid-body spacecraft model is considered where the CMG control torques and environmental disturbance torques are all applied about the COM of the satellite. Additionally, the CMG is assumed to be located at the center of mass of the satellite. Per [48], the rigid-body rotational dynamics of a satellite with a CMG become:

$$\boldsymbol{J}\dot{\boldsymbol{\omega}} + \boldsymbol{\omega}^{\times}\boldsymbol{J}\boldsymbol{\omega} = \boldsymbol{u}_{cmg} + \boldsymbol{T}_d \tag{3.31}$$

The symbol $\boldsymbol{J}$ is used to represent the 3×3 spacecraft inertia tensor, $\boldsymbol{\omega}$ represents the spacecraft body-fixed frame rotation rates, $\boldsymbol{u}_{cmg}$ is the CMG produced control torque, and $\boldsymbol{T}_d$ is the sum of all disturbance torques applied to the spacecraft. All torques in Eq. (3.31) are expressed in $\mathscr{F}_{BF}$. The angular momentum vector associated with the spacecraft spin can be calculated as:

$$\boldsymbol{H} = \boldsymbol{J}\boldsymbol{\omega} \tag{3.32}$$

From comparing Eq. (3.31) and Eq. (3.32), one can take the $\boldsymbol{\omega}^{\times}\boldsymbol{J}\boldsymbol{\omega}$ component of Eq. (3.31) to be the gyric torque associated with the spacecraft spin. Knowing these sets of equations allows for the quaternion kinematics equation to be formed which describes the spacecraft attitude as:

$$\begin{bmatrix} \dot{q}_1 \\ \dot{q}_2 \\ \dot{q}_3 \\ \dot{q}_4 \end{bmatrix} = \frac{1}{2} \begin{bmatrix} 0 & \omega_3 & -\omega_2 & \omega_1 \\ -\omega_3 & 0 & \omega_1 & \omega_2 \\ \omega_2 & -\omega_1 & 0 & \omega_3 \\ -\omega_1 & -\omega_2 & -\omega_3 & 0 \end{bmatrix} \begin{bmatrix} q_1 \\ q_2 \\ q_3 \\ q_4 \end{bmatrix} \tag{3.33}$$

The rate quaternion $\dot{\boldsymbol{q}}$ is, therefore, a function of the satellite body rates $\boldsymbol{\omega}$ and the current attitude quaternion $\boldsymbol{q}$. For the case of this thesis, $\boldsymbol{q}$ defines the attitude of $\mathcal{F}_{BF}$ relative to $\mathcal{F}_{ECI}$. Generalized 2U CubeSat geometry is prescribed to model the spacecraft according to the physical parameters provided in Table 3.2

Table 3.2: Spacecraft Physical Parameters

Example Rigid-Body Spacecraft

Model	**Parameter**	**Value**
2U Generalized		
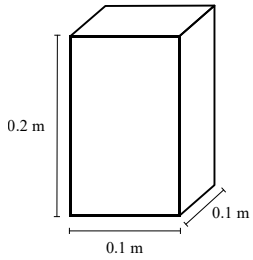	Dimensions	$0.1 \times 0.1 \times 0.2$ m
	Mass	2 kg
	Inertia Tensor	$\begin{bmatrix} 0.00833 & 0 & 0 \\ 0 & 0.00833 & 0 \\ 0 & 0 & 0.00333 \end{bmatrix}$ kgm^2
	Center of Mass	$[0, 0, 0]^T$ m
Tri-Inertial Debris		
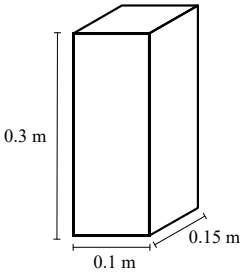	Dimensions	$0.1 \times 0.15 \times 0.3$ m
	Mass	4 kg
	Inertia Tensor	$\begin{bmatrix} 0.0375 & 0 & 0 \\ 0 & 0.0333 & 0 \\ 0 & 0 & 0.0108 \end{bmatrix}$ kgm^2
	Center of Mass	$[0, 0, 0]^T$ m

3.3.1 Torque-Free Motion of a Rigid Body

The torque-free motion of a rigid body is an important point of analysis for the rotational motion of a spacecraft. Particularly for the ADR case study presented later in Chapter 6, the specific rotational motion associated with torque-free tumbling of an axisymmetric or tri-inertial spacecraft has profound implications on the ability to discern inertial properties of a debris object. For this reason, torque-free motion of a rigid body is considered in this section.

There are three cases describing the inertial properties of a rigid body. Firstly, when all the principal moments of inertia (diagonal elements) of $\boldsymbol{J}$ are equal such that $J_{1,1} = J_{2,2} = J_{3,3}$ the body is isoinertial. Secondly, when only two of the principal moments of inertia are equal, the body is described as being inertially axisymmetric. Finally, if all principal moments of inertia are unique such that $J_{1,1} \neq J_{2,2} \neq J_{3,3}$, then

the body is described as being tri-inertial [38]. For both cases of a axisymmetric or tri-inertial body, there exist degenerate spins where precession of the spin axis occurs when observed in the principal axes. A time history of this procession can typically be obtained from the solutions provided in the following subsections assuming the motion is torque free.

Inertially Axisymmetric

The case of $J_t \triangleq J_{1,1} = J_{2,2}$ and $J_a \triangleq J_{3,3}$ is considered in this subsection as it pertains to the selected generalized 2U geometry provided in Table 3.2. Should these equalities be true, the general form of Euler's rotational equation of motion (i.e. the torque-free expression of Eq. (3.31)) may be solved as [38]:

$$\begin{aligned} J_t\dot{\omega}_1 &= (J_t - J_a)\omega_2\omega_3 \\ J_t\dot{\omega}_2 &= (J_a - J_t)\omega_3\omega_1 \\ J_a\dot{\omega}_3 &= 0 \end{aligned} \tag{3.34}$$

A solution to the time history of the spin axis $\boldsymbol{\omega}(t)$ exists by first noting that from Eq. (3.34), $\omega_3 = \omega_{3_0} = \upsilon$ and that the relative spin rate is:

$$\Omega = \left(\frac{J_t - J_a}{J_t}\right)\upsilon \tag{3.35}$$

Provided that the spin about the first principal axis is such that $\upsilon > 0$ then the remaining two solutions are [38]:

$$\begin{aligned} \omega_1(t) &= \omega_{1_0}\cos(\Omega t) + \omega_{2_0}\sin(\Omega t) \\ \omega_2(t) &= \omega_{2_0}\cos(\Omega t) - \omega_{1_0}\sin(\Omega t) \end{aligned} \tag{3.36}$$

At $t = 0$, $\boldsymbol{\omega} = [\omega_{1_0}, \omega_{2_0}, \omega_{3_0}]^T$. For an arbitrarily selected initial spin of $\boldsymbol{\omega} = [0.25, 0.25, 0.25]^T$and inertia properties taken from Table 3.2, the path of the spin axis over time can be observed geometrically in Fig. 3.2 demonstrating that the spin axis is precessing when observed in ω-space.

Tri-Inertial

The less trivial case of a Tri-Inertial body is considered in this section. For the axisymmetric case, the precession path was circular; however, in the tri-inertial case an elliptic precession path can be expected. The case where $J_{1,1} > J_{2,2} > J_{3,3}$ will be evaluated as it pertains to the physical parameters of a tri-inertial space debris presented later in Section. 6.6.2. Drawing on the symbol convention from the previous section, the rotational kinetic energy and angular momentum of the spinning

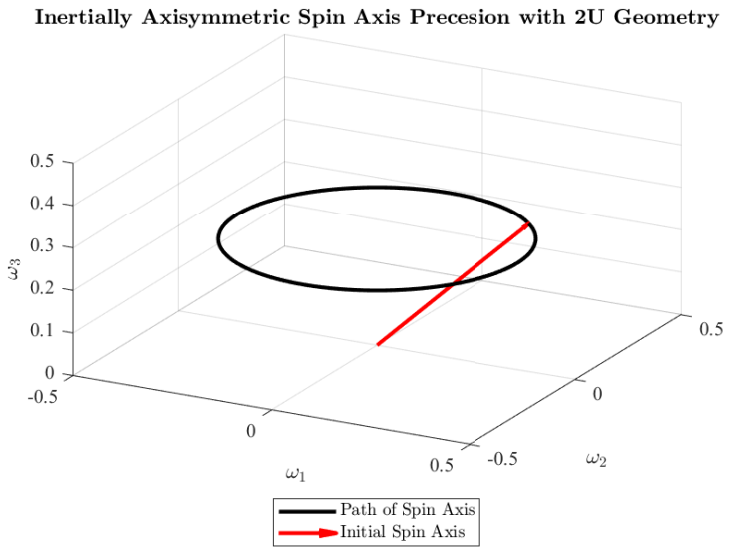

Figure 3.2: Spin Axis Precession for Generalized 2U Geometry

tri-inertial body may be expressed respectively as [38]:

$$2T = J_{1,1}\omega_{1_0}^2 + J_{2,2}\omega_{2_0}^2 + J_{3,3}\omega_{3_0}^2 \tag{3.37}$$

$$h^2 = J_{1,1}^2\omega_{1_0}^2 + J_{2,2}^2\omega_{2_0}^2 + J_{3,3}^2\omega_{3_0}^2 \tag{3.38}$$

A parameter I is also defined which carries the same units as a moment of inertia. I may be calculated as follows:

$$I \triangleq \frac{h^2}{2T} \tag{3.39}$$

It is clear from Eq. (3.39) that I is dependent on initial conditions; however, I is bounded by $J_{1,1} \geq I \geq J_{3,3}$. The case of $J_{2,2} = I$ is a branch point separating the mathematical treatment of $J_{1,1} > I > J_{2,2}$ from $J_{2,2} > I > J_{3,3}$ (referred to as a bifurcation point in [38]). In this research, the general algorithmic process for computing the time history solution of $\boldsymbol{\omega}$ was to assume a constant T so that a family of polhodes could be generated for varying h. A polhode is the path traveled by the vector $\boldsymbol{\omega}$ which is defined by the intersection of the angular energy ellipsoid and angular momentum ellipsoid. The reader is directed to [38] for more detail on these ellipsoids.

The analytical solution to $\boldsymbol{\omega}(t)$ proceeds by finding all three maximum axial spin rates given I and h:

$$\omega_{1_m} = h\sqrt{\frac{I - J_{3,3}}{IJ_{1,1}(J_{1,1} - J_{3,3})}} \tag{3.40}$$

$$\omega_{3_m} = h\sqrt{\frac{J_{1,1} - I}{IJ_{3,3}(J_{1,1} - J_{3,3})}} \tag{3.41}$$

$$\omega_{2_m} = \begin{cases} h\sqrt{\frac{J_{1,1}-I}{IJ_{2,2}(J_{1,1}-J_{2,2})}}, & (J_{1,1} \geq I > J_{2,2}) \\ \frac{h}{J_{2,2}}, & (I = J_{2,2}) \\ h\sqrt{\frac{I-J_{3,3}}{IJ_{2,2}(J_{2,2}-J_{3,3})}}, & (J_{2,2} > I \geq J_{3,3}) \end{cases} \tag{3.42}$$

The resulting analytical solution to $\boldsymbol{\omega}(t)$ is completed by first determining the parameters k and τ using the Jacobian elliptic functions $\mathrm{sn}, \mathrm{cn}, \mathrm{dn}$ in the following sets of equations:[1]

$$(J_{1,1} \geq I > J_{2,2}) \begin{cases} \tau = h\sqrt{\frac{(J_{1,1}-J_{2,2})(I-J_{3,3})}{IJ_{1,1}J_{2,2}J_{3,3}}}(t-t_0) \\ k = \sqrt{\frac{(J_{2,2}-J_{3,3})(J_{1,1}-I)}{(J_{1,1}-J_{2,2})(I-J_{3,3})}} \\ \omega_1 = s_1\omega_{1_m}\mathrm{dn}(\tau,k) \\ \omega_2 = s_2\omega_{2_m}\mathrm{sn}(\tau,k) \\ \omega_3 = s_3\omega_{3_m}\mathrm{cn}(\tau,k) \end{cases} \tag{3.43}$$

$$(J_{2,2} > I \geq J_{3,3}) \begin{cases} \tau = h\sqrt{\frac{(J_{2,2}-J_{3,3})(J_{1,1}-I)}{IJ_{1,1}J_{2,2}J_{3,3}}}(t-t_0) \\ k = \sqrt{\frac{(J_{1,1}-J_{2,2})(I-J_{3,3})}{(J_{2,2}-J_{3,3})(J_{1,1}-I)}} \\ \omega_1 = s_1\omega_{1_m}\mathrm{cn}(\tau,k) \\ \omega_2 = s_2\omega_{2_m}\mathrm{sn}(\tau,k) \\ \omega_3 = s_3\omega_{3_m}\mathrm{dn}(\tau,k) \end{cases} \tag{3.44}$$

$$(I = J_{2,2}) \begin{cases} \tau = \frac{h}{J_{2,2}}\sqrt{\frac{(J_{1,1}-J_{2,2})(J_{2,2}-J_{3,3})}{J_{1,1}J_{3,3}}}(t-t_0) \\ \omega_1 = s_1\omega_{1_m}\mathrm{sech}(\tau) \\ \omega_2 = s_2\omega_{2_m}\tanh(\tau) \\ \omega_3 = s_3\omega_{3_m}\mathrm{sech}(\tau) \end{cases} \tag{3.45}$$

In all listed sets of equations, $s_1s_2s_3 = -1$ where all $s_i = \pm 1$. This specific selection of the s_i parameters leads to 4 variations of sign within each set of equations. Finally, the family of polhodes on the angular energy ellipsoid corresponding to an initial spin of $\boldsymbol{\omega}_0 = [0.25, -0.15, 0.5]^T$ and a tri-inertial body with moments of inertia given in Table 3.2 can be observed in Fig. 3.3. The figure represents the possible precession paths of $\boldsymbol{\omega}$ given varying h but constant T to demonstrate the instability of many of the spins.

The following section develops a host of environmental effects which disturb the satellite from its torque-free rotational motion.

[1]It should be noted that the symbol definition used in this section for k and τ does not hold outside the scope of this section. Further symbol definitions for k and τ are provided in their respective sections.

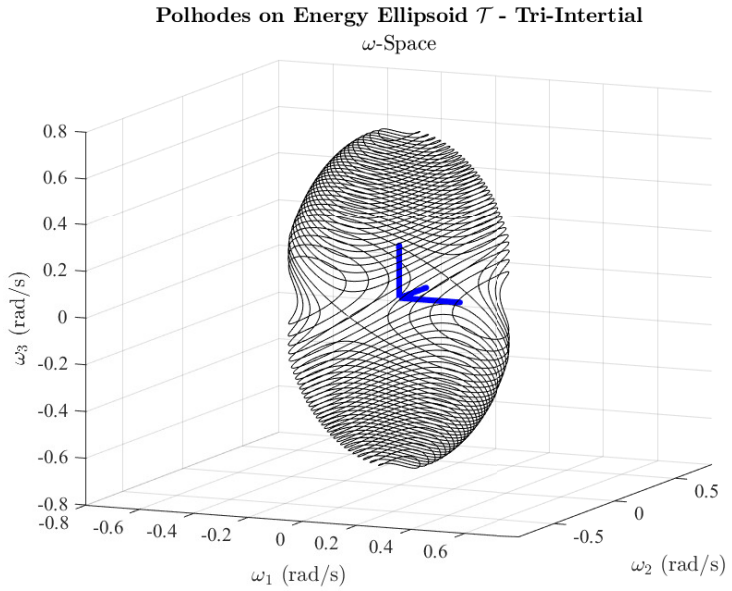

Figure 3.3: Family of Polhodes for $J_{1,1} > J_{2,2} > J_{3,3}$

3.4 Space Environment

To validate the control schemes developed in this thesis it was desired to model a detailed space environment. For small satellites in LEO, there are a number of perturbing torques which can greatly impact the control of the satellite [49]. In this section a detailed space environment model is constructed to accommodate the validation of a CMG-equipped CubeSat ADCS. The work builds off of previous work at Dalhousie University in [26] and [50] by relaxing some worst-case assumptions to improve environment fidelity.

3.4.1 Lighting Conditions

Eclipse

Eclipse occurs when the Earth is positioned between the satellite and the Sun, thereby casting a shadow over the satellite. In this condition, sun-sensors used for attitude determination will not function and solar radiation torques acting on the satellite will be nullified. It is, therefore, necessary to include modeling of eclipse cases within the simulator. There are four eclipse cases which are considered in this thesis, all of which can be viewed pictorially in Fig. 3.4:

1. **Case 1:** The satellite can see the entire Sun (Full Sun).

2. **Case 2:** The satellite can see a fraction of the Sun or is partially illuminated (Partial Eclipse).

3. **Case 3:** The Satellite cannot see the Sun. (Total Eclipse)

4. **Case 4:** The Satellite can see the full circumference of the Sun but Earth is transiting in front and can be fully viewed. (Annular Eclipse)

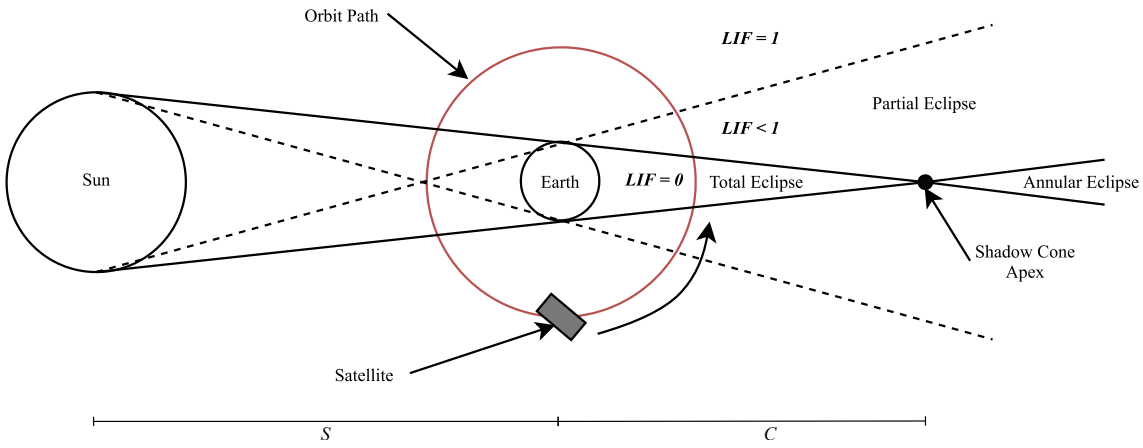

Figure 3.4: Top Down Planar View of Eclipse Cases

By following Fig. 3.4 and adopting the formulations presented in [51], the eclipse cases can be determined for the spacecraft along with the illumination level. First, the shadow cone length C and angular radius ρ_c must be determined. It is convention to let S be the distance from the center of the Earth to the Sun, R_s to be the spherical radius of the photosphere of the Sun (visible surface of the Sun), and, for the formulations in this section, $R_e \triangleq R_p$ represents the radius of the transiting spherical Earth. The definitions lead to:

$$C = \frac{R_p S}{(R_s - R_p)} \tag{3.46}$$

$$\rho_c = \arcsin\left(\frac{R_s - R_p}{S}\right) \tag{3.47}$$

While the length of the shadow cone corresponding to the mean distance to the Sun from Earth is 1.385E6 km with $\rho_c = 0.264°$ [51], Solar ephemeris data was applied at the TLE epoch time to obtain $C = 1.3614\text{E}6$ km with $\rho_c = 0.268°$. The solar ephemeris data obtained from the NASA Horizons systems is provided in Appendix B.

Following the two previously-defined quantities, the vector $\boldsymbol{D}_s$ from the spacecraft COM to the Sun and the vector $\boldsymbol{D}_p$ from the spacecraft COM to the Earth must be calculated. Let $\boldsymbol{S}_i$ be the Earth to Sun vector expressed in $\mathcal{F}_{ECI}$ such that:

$$\boldsymbol{D}_s = \boldsymbol{S}_i - \boldsymbol{r}_{ECI} \tag{3.48}$$

and

$$\boldsymbol{D}_p = -\boldsymbol{r}_{ECI} \tag{3.49}$$

Defining $D_s = |\boldsymbol{D}_s|$, $D_p = |\boldsymbol{D}_p|$ with $\hat{\boldsymbol{D}}_s$,$\hat{\boldsymbol{D}}_p$ being the unit vectors corresponding to $\boldsymbol{D}_s$ and $\boldsymbol{D}_p$, respectively, allows for the calculation of three quantities corresponding to the angular geometry of the Earth transit. The quantity ρ_s represents the angular radius of the Sun, ρ_p represents the angular radius of the Earth, and θ_s is the angular separation between the two celestial bodies. The quantities are calculated by:

$$\rho_s = \arcsin(R_s/D_s) \tag{3.50}$$

$$\rho_p = \arcsin(R_p/D_p) \tag{3.51}$$

$$\theta_s = \arccos\left(\hat{\boldsymbol{D}}_s^T \hat{\boldsymbol{D}}_p\right) \tag{3.52}$$

The corresponding necessary conditions for the various eclipse cases are thereby:

1. **Partial Eclipse:** $D_s > S$ and $(\rho_p + \rho_s) > \theta_s > |\rho_p - \rho_s|$
2. **Total Eclipse:** $S < D_s < (S + C)$ and $(\rho_p - \rho_s) > \theta_s$
3. **Annular Eclipse:** $(S + C) < D_s$ and $(\rho_p - \rho_s) > \theta_s$
4. **Full Sunlight:** else

The luminous intensity of the Sun, I_0 is functionally constant over the surface of the Sun. This means that the luminous intensity experienced by the satellite is proportional to the area of the Sun which is visible to the satellite. The luminous intensity I_0 is provided in Appendix B and the subsequent occluded Sun intensities I can be garnered from:

$$\begin{aligned} I_0 - I = \frac{I_0}{\pi(1-\cos(\rho_s))} \Bigg[& \pi - \cos(\rho_s) \arccos\left(\frac{\cos(\rho_p) - \cos(\rho_s)\cos(\theta_s)}{\sin(\rho_s)\sin(\theta_s)}\right) \\ & - \cos(\rho_s) \arccos\left(\frac{\cos(\rho_s) - \cos(\rho_p)\cos(\theta_s)}{\sin(\rho_p)\sin(\theta_s)}\right) \\ & - \arccos\left(\frac{\cos(\theta_s) - \cos(\rho_s)\cos(\rho_p)}{\sin(\rho_s)\sin(\rho_p)}\right)\Bigg], \text{ Partial Eclipse} \end{aligned} \tag{3.53}$$

$$I_0 - I = I_0\left(\frac{1-\cos(\rho_p)}{1-\cos(\rho_s)}\right), \text{ Annular Eclipse} \tag{3.54}$$

For a satellite in LEO, the satellite should never experience an annular eclipse because D_p is much less than C; however, the formulation is provided here for completeness. In the focus simulations, knowing the exact value of luminous intensity is less important than knowing the fraction of light the satellite is experiencing relative to full Sun illumination. This importance is explained by the fact that the strength of the solar disturbance torque (presented later in this section) can be scaled by the unitless intensity fraction, but cannot be scaled by a luminous intensity quantity which typically has units expressed in J/s. Because of this hierarchy of importance, a normalized luminous intensity factor (LIF) ℓ is calculated in the simulator such

that $\ell = 1$ defines full Sun, $0 < \ell < 1$ defines partial illumination, and $\ell = 0$ is total eclipse. The LIF factor is simply calculated as $\ell = I/I_0$.

It was found in this work that the final arccos term of Eq. (3.53) could become numerically problematic when calculating values of I which are close to 0. To accommodate this numerical issue the following correction was made to force a full eclipse state if I is close to 0:

$$\text{if} \quad \left| \frac{\cos(\theta_s) - \cos(\rho_s)\cos(\rho_p)}{\sin(\rho_s)\sin(\rho_p)} \right| > 1 \Rightarrow I \approx 0 \tag{3.55}$$

Earth Albedo

Albedo refers to the fraction of light which is reflected by a body. This reflected light can sometimes be observed by Sun sensor photodiodes, causing their measurements to be corrupted. The average Bond Albedo (a ratio of reflected sunlight on the range of 0 - 1) is typically accepted to be 0.306 for Earth [52]. The actual albedo, however, experienced by a given observer is highly dependent on aspects including season, latitude/longitude, and cloud coverage. Fig. 3.5 demonstrates this fact by plotting the average observed Earth surface irradiance for a 1 month period from October 2023 - November 2023 from the NASA Earth Observations (NEO) database [53]. Surface albedo, like the map shown in Fig. 3.5, only accounts for a small portion of the overall planetary albedo, with the largest portion coming from light diffusion off the upper atmosphere [54].

Work presented in the literature by Bhanderi (2005) has demonstrated the effects of very high-fidelity albedo models on sun-vector determination [55]. The depth of these models, however, is far outside the scope of the simulations presented in this

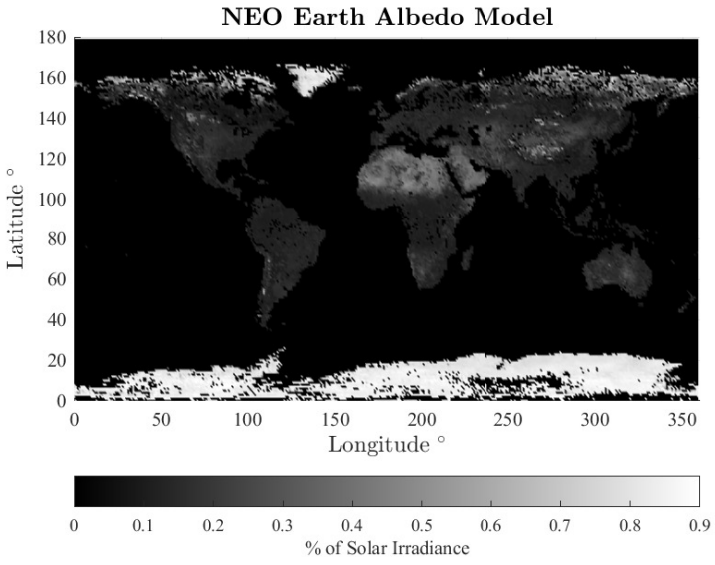

Figure 3.5: Earth Surface Average Irradiance Observation (Oct - Nov 2023)

research. It was, therefore, opted to develop a simplified model largely based on the average observed planetary albedo. Noting the results in [54], the planetary albedo, when averaged over a yearly time span, varies most with respect to latitude. By visual inspection for lack of an available data set, points were selected from the latitude referenced planetary albedo plot in [54] to produce the results shown in Fig. 3.6

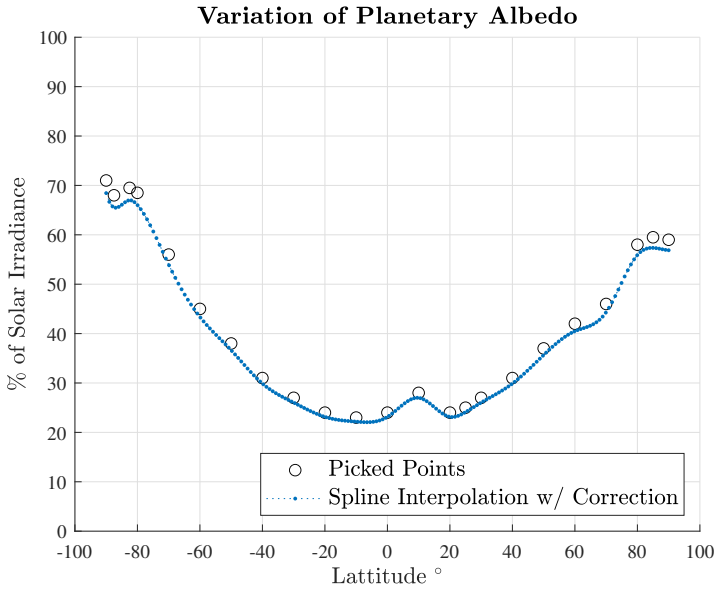

Figure 3.6: Albedo Data Points VS Interpolated Points Representing Planetary Albedo as a Function of Latitude

The data shown by black circles in Fig. 3.6 was subject to a spline interpolation so that the data was smooth and so that there was one data point for each degree of latitude in the model. The data in the latitude reference model was also verified by computing the average model albedo and comparing this average to the accepted planetary albedo of 0.306 [52]. To make this comparison, a weighted average was desired to account for the surface area of Earth for which a corresponding albedo data point has been produced. That is, it was assumed that percent solar irradiance varies only in latitude and not in longitude so that surface area on the unit sphere bounding a latitude of interest may act as weights following Fig. 3.7. The surface area between two bounding latitude parallels may be calculated as [56]:

$$SA_i = 2\pi \left(\sin(\phi_1) - \sin(\phi_2)\right) \tag{3.56}$$

Let ϕ_1 be the upper latitude parallel from the latitude of the albedo data point ϕ_i defined by $\phi_1 = \phi_i + 0.5°$, and ϕ_2 be the lower latitude parallel defined by $\phi_2 = \phi_i - 0.5°$. If the latitude corresponds to a geometric pole (either $90°$ or $-90°$ latitude) the surface area weight is set to 0. The average planetary albedo may then be appropriately

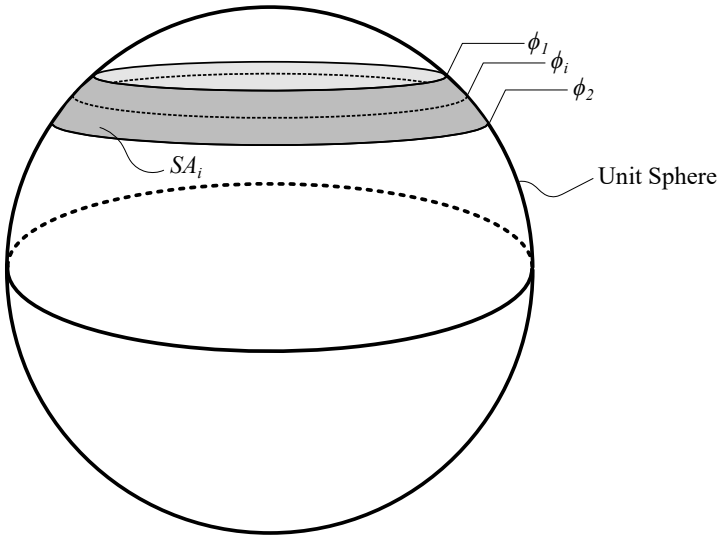

Figure 3.7: Surface Area Used as Weight for Latitude Parallel of Interest in Global Albedo Calculation

calculated as:

$$a = \frac{\sum_i^n SA_i L_{a_i}}{\sum_i^n SA_i} \tag{3.57}$$

In Eq. (3.57) L_{a_i} is the albedo solar irradiance factor for latitude i from the spline interpolation. The result of these formulations resulted in an average planetary albedo of 0.317 – slightly higher than the accepted value. Error in the calculated value was deemed to be a result of minor errors when reading off data points from the latitude referenced plot in [54]. Therefore, a correction factor of 0.964 was applied to all interpolation points so that the average planetary albedo from the model was identical to the accepted value of 0.306. The final planetary albedo model is mapped in Fig. 3.8.

The map in Fig. 3.8 represents the percentage of incoming sunlight which is diffused back into space. To complete the model, it is desired to determine how much of this reflected light is directed towards the spacecraft. To do so, it was assumed that the surface area of the Earth which can be seen by the spacecraft may be considered to a flat plane. This approximation is fairly reasonable for a satellite in LEO but does not hold for satellites in higher altitude orbits. The motivation of this approximation is two-fold. The first reason is to make the albedo model closer to a worst-case example as all incident light will be diffused off a plane with a normal vector pointing directly at the satellite. The second reason is to avoid discretizing the surface of Earth into many planes all with different normal vectors which differently reflect the

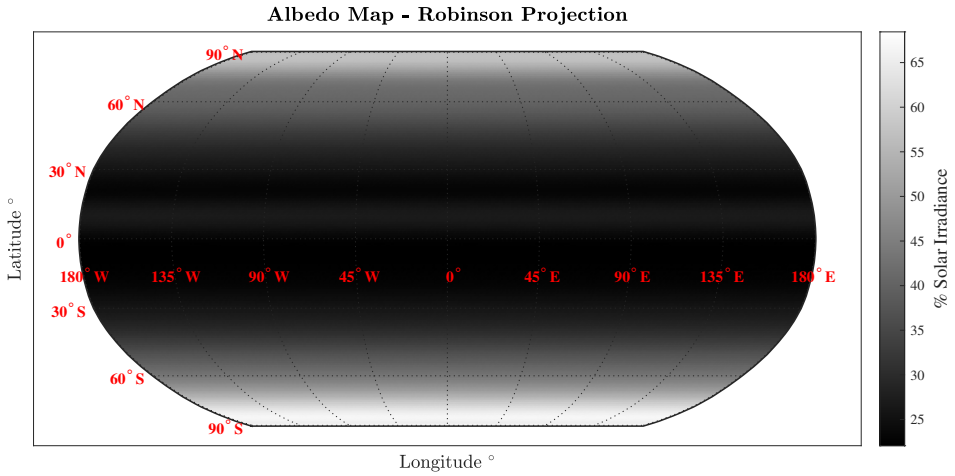

Figure 3.8: Final Albedo Map Applied in Simulator

incoming sunlight. An example of the flat plane under the spacecraft based on the satellite Field of View (FOV) is provided in Fig. 3.9.

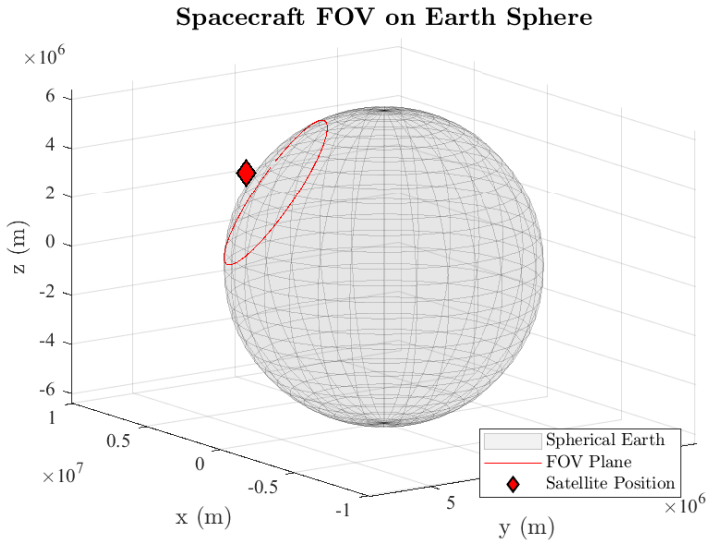

Figure 3.9: FOV Diffusion Plane

For larger FOVs the underlying plane defined by the red circle in Fig. 3.9 is an increasingly poor approximation for the surface of Earth because the curvature of Earth will begin to dominate the actual surface observed by the spacecraft. Provided the locally-flat-Earth approximation is reasonable, an equation for the normalized

intensity of sunlight diffused in the direction of the spacecraft is as follows:

$$L_a^s = L_a(\phi_i)\left(\left(\frac{\boldsymbol{S}_i}{|\boldsymbol{S}_i|}\right)^T\left(\frac{\boldsymbol{r}_{ECI}}{|\boldsymbol{r}_{ECI}|}\right)\right) \tag{3.58}$$

The quantity $L_a(\phi_i)$ is used to represent the lookup table implemented in the thesis' simulator. The function contains all the spline interpolated albedo data points with the correction factor in steps of 1° latitude. For any satellite positions calculated in the simulator that are between these points of latitude, the simulator simply linearly interpolates between the inputted data. By doing so, the simulator always has a determinable solar irradiance factor regardless of the current spacecraft latitude or longitude.

As was previously described, the FOV plane has a normal vector in the direction of the ECI frame satellite position vector. Possessing this direction means that the intensity of the albedo in the direction of the satellite can be found simply by the projection of the incoming sunlight vector onto the direction vector for the spacecraft position when expressed in the ECI frame. It is clear from Eq. (3.58) that the intensity of the albedo diffused towards the satellite is maximized when the angle of incidence between the sunlight direction vector and the FOV plane is 0 rad.

3.4.2 Environmental Disturbance Torques

Aerodynamic Torque

A spacecraft in LEO experiences a small aerodynamic torque when the Center of Pressure (COP) is offset from the spacecraft COM [57]. While it was assumed in [26] and [57] that the atmospheric density at orbital altitudes was constant, it can actually vary greatly over one orbit [58][59]. The atmospheric density is also highly dependent on the solar flux level and geomagnetic activity. At 400km altitude, density variations of around 1600% can occur over the solar cycle, and variations of around 800% can occur during major geomagnetic storms [60]. It is clear that a higher-fidelity aerodynamic torque model must consider variable atmospheric density.

By adapting the foundational work provided in [26], the aerodynamic torque vector can be found by applying:

$$\boldsymbol{T}_a = \frac{1}{2}\rho v_{BF}^2 C_d A_p(\boldsymbol{u}_v^{\times}\boldsymbol{s}_{cp}) \tag{3.59}$$

where ρ is the atmospheric density, v_{BF} is the magnitude of the orbital velocity vector in $\boldsymbol{\mathcal{F}}_{BF}$, C_d is the coefficient of drag, A_p is the area of the spacecraft exposed to the flow perpendicular to $\boldsymbol{u}_v$, the unit direction vector of orbital velocity expressed in $\boldsymbol{\mathcal{F}}_{BF}$, and $\boldsymbol{s}_{cp}$ is the vector from the spacecraft COM to COP expressed in $\boldsymbol{\mathcal{F}}_{BF}$. The variable atmospheric density ρ was obtained in this work from the NRLMSISE-00 model which is considered accurate for orbital altitudes between 0 - 1000 km [61].

The NRLMSISE-00 model as implemented in the simulator takes the following set of inputs to compute the atmospheric density for a given satellite position:

- Geodetic Latitude and Longitude (ϕ_d, λ_d).
- Orbital Altitude h.
- Simulation Year.
- Simulation Day of Year.
- Simulation UT time expressed in seconds.
- F10.7a 3-month average solar flux index.
- F10.7 daily solar flux index for the day prior to the simulation epoch day.
- 7×1 set of ap Magnetic indies.
  - 3-hour ap for simulation epoch time.
  - 3-hour ap for 3 hours prior to simulation epoch time.
  - 3-hour ap for 6 hours prior to simulation epoch time.
  - 3-hour ap for 9 hours prior to simulation epoch time.
  - ap average for 3-hour ap indices 12-33 hours prior to simulation epoch time.
  - ap average for 3-hour ap indices 36-57 hours prior to simulation epoch time.

The F10.7 Solar flux indices were obtained from the Government of Canada space weather database [62]. The Geomagnetic "ap" indices were obtained from the GFZ, Postdam web service [63]. Full datasets obtained from these sources are provided in Appendix B.

Another consideration to be made was in regards to a dynamic calculation of A_p and $\boldsymbol{s}_{cp}$. It was desired in this thesis to dynamically calculate A_p and $\boldsymbol{s}_{cp}$ so that more realistic angular impulses would be observed during a simulation. The method of dynamically calculating the exposed area involves the discretization of the spacecraft geometry into a series of planes – all with a defined unit normal vector and centroid. When the prismatic generalized 2U geometry is applied in the simulation, the result of discretization is 6 planes with normal vectors along the principle axes of $\mathcal{F}_{BF}$. A geometric representation of a single spacecraft plane is provided in Fig. 3.10.

For the case of this section, let the subscript "n" define a particular plane from $n = 1 - 6$. $\boldsymbol{A}_f$ is an $n \times 1$ matrix containing the areas of each plane, $\boldsymbol{C}_f$ is an $n \times 3$ matrix where row n contains the centroid position of plane n expressed in $\mathcal{F}_{BF}$ and $\boldsymbol{N}_f$ is a $n \times 3$ matrix containing the unit normal vectors of each plane. The relationship for the effective projection of a plane into the flow is given by:

$$R_n = \boldsymbol{N}_{f_{n,1:3}}^T \boldsymbol{u}_v \tag{3.60}$$

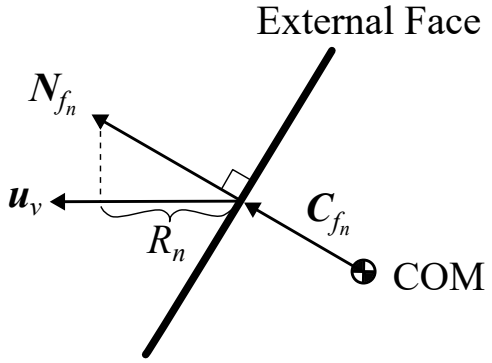

Figure 3.10: External Face Exposed to Flow. Plane Normal Vector and Centroid Location Shown Relative to Spacecraft COM.

where R_n is the nth projection stored in $\boldsymbol{R}$ which is also $n \times 1$. If $R_n < 0$ the plane is on the side of the spacecraft facing away from the flow and its value can be set to 0. Subsequently, the dynamic projected area is found as:

$$A_p = \boldsymbol{A}_f^T \boldsymbol{R} \tag{3.61}$$

The dynamic center of pressure location is less trivial and requires calculation of a weighted average of centroid locations that are weighted based on the effective projected area contribution from each plane. These weights can be found by computing the Hadamard product between the planar areas and effective area projections:

$$\boldsymbol{W} = \boldsymbol{A}_f \odot \boldsymbol{R} \tag{3.62}$$

The centroid locations can then be adjusted based on applied weight by scaling a centroid location by its respective weight:

$$\boldsymbol{C}'_f = W_n \boldsymbol{C}_{f_{n,1:3}} \tag{3.63}$$

Each of the 3 components of $\boldsymbol{s}_{cp}$ were then found in this thesis by computing the weighted average along each column of $\boldsymbol{C}'_f$ as:

$$s_i = \frac{\sum_1^n \boldsymbol{C}'_{f_{1:n,i}}}{\sum_1^n \boldsymbol{W}} \tag{3.64}$$

Residual Magnetic Dipole

The Residual Magnetic Dipole Torque $\boldsymbol{T}_{rmd}$ results from the interaction of the spacecraft magnetic dipole $\boldsymbol{D}$ with Earth's magnetic field vector $\boldsymbol{B}$ at the satellite position [26]. In this work $\boldsymbol{B}$ is first obtained from IGRF-13 expressed in $\mathscr{F}_{NED}$ and then is transformed to its expression in $\mathscr{F}_{BF}$. The IGRF-13 model was applied in this thesis as the model is considered accurate up to 2025 [64]. This accuracy range ensures that,

for a simulation epoch time in early 2023, the simulation is accurate for the typical lifetime of a LEO satellite. Hereinafter, $\boldsymbol{B}$ will represent the Earth's magnetic field expressed in $\mathscr{F}_{BF}$ so that the residual magnetic dipole torque may be computed by:

$$\boldsymbol{T}_{rmd} = \boldsymbol{D}^{\times}\boldsymbol{B} \tag{3.65}$$

Gravity Gradient Torque

The Gravity Gradient Torque represented by $\boldsymbol{T}_{gg}$ results from an imbalance in the force of gravity over the mass of the spacecraft [59]. If the gravitational force were uniform over a body, the Center of Gravity (COG) would be aligned with the COM and, therefore, the gravity gradient torque would be zero. In general, an aligned COG and COM is atypical, and the result is a gravity gradient torque about the spacecraft COM [65] which can be calculated as:

$$\boldsymbol{T}_{gg} = \frac{3\mu}{|\boldsymbol{r}_{ECI}|^3}\boldsymbol{u}_e^{\times}\left(\boldsymbol{J}\cdot\boldsymbol{u}_e\right) \tag{3.66}$$

The symbol $\boldsymbol{u}_e$ is used to denote the nadir-pointing unit direction vector expressed in $\mathscr{F}_{BF}$ which can be calculated following the relationship:

$$\boldsymbol{u}_e = \boldsymbol{\mathcal{A}}_{ECI}^{BF}\left(\frac{-\boldsymbol{r}_{ECI}}{|\boldsymbol{r}_{ECI}|}\right) \tag{3.67}$$

The dot product of the spacecraft inertia tensor with the nadir pointing vector is also defined as:

$$\left(\boldsymbol{J}\cdot\boldsymbol{u}_e\right) = \begin{bmatrix} J_{1,1} & 0 & 0 \\ 0 & J_{2,2} & 0 \\ 0 & 0 & J_{3,3} \end{bmatrix}\cdot\boldsymbol{u}_e = \begin{bmatrix} \begin{bmatrix} J_{1,1} & 0 & 0 \end{bmatrix}^T\cdot\boldsymbol{u}_e \\ \begin{bmatrix} 0 & J_{2,2} & 0 \end{bmatrix}^T\cdot\boldsymbol{u}_e \\ \begin{bmatrix} 0 & 0 & J_{3,3} \end{bmatrix}^T\cdot\boldsymbol{u}_e \end{bmatrix} \tag{3.68}$$

Lorentz Torque

The Lorentz torque $\boldsymbol{T}_l$ is developed when a spacecraft generates an electrostatic charge on its surfaces and the spacecraft is within Earth's magnetic field [66]. This electromagnetic interaction can sometimes be significant enough that researchers have developed methods to vary the location of the charge center in order to stabilize the motion of a satellite [67]. The Lorentz torque is dependent on the electrostatically charged surface traveling with velocity through a magnetic field – the exact case of a spacecraft in LEO. Defining q_l to be the specific charge of the satellite (in coulomb per kilogram - C/kg) , $\boldsymbol{r}_{cc}$ to be the position of the center of charge in $\mathscr{F}_{BF}$, and $\boldsymbol{v}_{BF}$ to be the $\mathscr{F}_{BF}$ orbital velocity vector, leads to the following equation for the Lorentz torque:

$$\boldsymbol{T}_l = \boldsymbol{r}_{cc}^{\times}\left(q_l\boldsymbol{v}_{BF}^{\times}\boldsymbol{B}\right) \tag{3.69}$$

At the time of writing, static surface charging of CubeSats in LEO was a relatively under analyzed problem. Despite the lack of documentation, static discharge severity levels are characterized in NASA-TP-2361 and NASA-HDBK-4002B. Because spacecraft charging is usually a minor issue for satellites in LEO [68], the upper range of the minor discharge severity of 0.5 μC was selected for the magnitude of spacecraft charge from [69]. This selection leads to a specific charge of $q_l = 2.5\text{E}-07$ C/kg after dividing by the spacecraft mass.

Solar Radiation Torque

When a satellite experiences radiation from the Sun which is incident to its external surfaces, a torque can be generated about the spacecraft COM. In this thesis, emphasis is placed on the consideration of the direct solar photon radiation torque $\boldsymbol{T}_{sr}$. Other torques from additional radiative sources are neglected as they are typically at least an order of magnitude smaller than $\boldsymbol{T}_{sr}$ [70]. The solar radiation torque varies most with the spacecraft exposed area to sunlight A_s and the surface reflectance factor q. In this thesis A_s was set to 0.02 m^2 representing the case where the largest exterior face of the satellite is exposed to the Sun. With regards to the value of q, [70] lists a range of 0.4-0.7 for sandblasted aluminum surfaces – a range which is aligned with the selected q value of 0.6 used in [51] and [26] for analysis of CubeSats. In the present work, a value of 0.6 was also established for q by drawing on the aforementioned examples.

The other important factor known as the solar constant F_s has seasonal variations on the order of $\pm 3.5\%$ from nominal and was, therefore, considered a constant value of 1367 W/m^2 in this work [71] as simulation time horizons were well under full seasons. The constant c denoting the speed of light is the final constant value required in the formulations and was set to $3.0\text{E}+08$ m/s in the simulator. The force and momentum arm specific to the solar radiation torque is a result of the cross product of the center of solar pressure vector $\boldsymbol{c}_{sp}$ and the unit direction vector from the satellite to the sun $\boldsymbol{u}_{rb}$ expressed in $\mathscr{F}_{BF}$. The center of solar pressure was assumed to be a worst case location of $\boldsymbol{c}_{sp} = [0, 0, 0.1]^T$m in this work following [26]. The expression which computes the solar radiation torque is:

$$\boldsymbol{T}_{sr} = \ell \frac{F_s}{c} A_s (1+q) \left[\boldsymbol{c}_{sp}^{\times} \boldsymbol{u}_{r_b}\right] \tag{3.70}$$

The satellite to Sun unit vector may be calculated as:

$$\boldsymbol{u}_{r_b} = \boldsymbol{\mathcal{A}}_{ECI}^{BF} \frac{\boldsymbol{S}_i - \boldsymbol{r}_{ECI}}{|\boldsymbol{S}_i - \boldsymbol{r}_{ECI}|} \tag{3.71}$$

Noticeably in Eq. (3.70), the solar radiation torque is scaled by the LIF ℓ. The effect of scaling by ℓ is that the solar radiation torque will be scaled by the intensity of the sunlight which the satellite is currently experiencing. In eclipse, the solar radiation torque becomes zero because $\ell = 0$ in eclipse.

Chapter 4

Attitude & Orbit Determination

Attitude determination algorithms are critical components in the proposed Guidance, Navigation and Control (GNC) system for the DGSPCMG-equipped CubeSat. Functionally, the attitude determination algorithms will estimate the current satellite attitude and orbital states. The estimated state information will be passed, along with the desired states from the orbit propagator, to the spacecraft attitude feedback controller which subsequently commands control inputs to be produced by the CMG.

For all actively-stabilized spacecraft, the development of the ADCS presents a unique challenge of selecting robust algorithms which suit the subject mission. For the present thesis, attitude determination algorithms were selected to build upon the work completed for the LORIS CubeSat in [26]. In consequence, the attitude determination system leverages sun vector and magnetic field readings in the Quaternion Estimation Algorithm (QUEST) to estimate the spacecraft attitude. This estimate is refined by a Multiplicative Extended Kalman Filter (MEKF) prior to being sent to the attitude feedback controller. While in [26] TLEs would have to be propagated as the only available estimate of the spacecraft orbital state, the present work aims to use a Global Navigation Satellite System (GNSS) and Orbit Determination-Extended Kalman Filter to produce a refined estimate of the orbital state. Proceeding sections

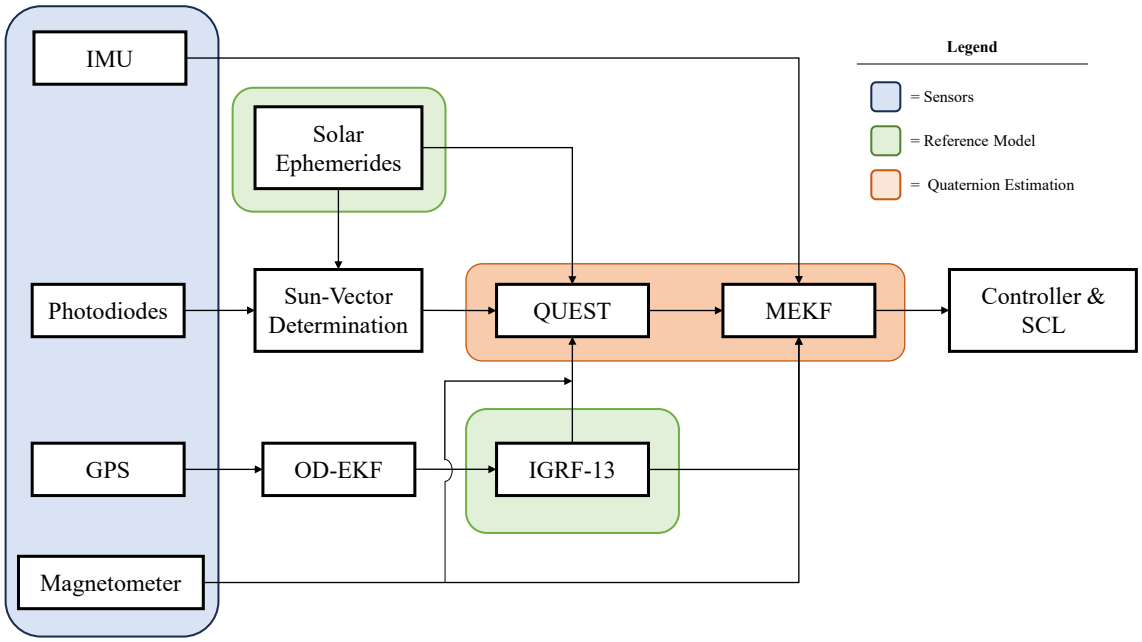

Figure 4.1: ADCS System Architecture for Proposed DGSPCMG CubeSat

within this chapter describe the proposed attitude determination method. The overall ADCS architecture is provided in Fig. 4.1. The attitude sensor models for the system are first provided prior to building the attitude determination algorithms.

4.1 Sensor Models

4.1.1 Inertial Measurement Unit

The Inertial Measurement Unit (IMU) is responsible for measuring the angular rates of the spacecraft. In this thesis the IMU was modeled after the aerospace grade VN-100 IMU from VectorNav. As shown by experimental tests in [26], noise in the IMU measurements will behave close to white noise in the short term, however, in the long term, IMU bias drift will dominate the measurements. Therefore, common IMU models such as that used in [72] add a "random walk" signal to the noisy IMU measurement to account for bias drift.

The measurement noise density for the VN-100 was listed as $ND = 0.0035°/\text{s}/\sqrt{\text{Hz}}$ [73], units that conflict with Simulink blocks which require the noise power as an input. Noise power can be obtained by multiplying the noise variance by the sampling rate dt (selected as 0.25s in this thesis). The proceeding equation can be leveraged to convert the noise density to a noise variance with units specified in radians [74]:

$$\sigma_\eta^2 = \left(ND \frac{\pi}{180} \sqrt{\frac{1}{dt}} \right)^2 \tag{4.1}$$

The desired noise power NP is then calculated as $NP = \sigma_\eta^2 dt$. With regards to the IMU bias drift, the VN-100 datasheet provides a typical in-run IMU bias stability of 5°/hr. The in-run bias represents a typical drift for sensor operation at constant temperature. In both [26] and [72] the random walk signal is produced by integration of a band-limited white noise signal. The same procedure was conducted in the present work, where a bias noise power of $[(5.0\text{E}-06)dt]$ rad^2/s was selected empirically for the bias drift by ensuring that the typical bias drift was less than 5°/hr. Fig. 4.2 displays the resulting bias drift from the noise power selection. The typical 5°/hr limits are shown as dashed lines. A bias exceeding these lines within 3600s would exceed the typical values for the IMU. The full IMU model is provided for completeness as:

$$\boldsymbol{\omega}_m = \boldsymbol{\omega} + \boldsymbol{\eta} + \boldsymbol{b} \tag{4.2}$$

where $\boldsymbol{\eta}$ is the band-limited white measurement noise and $\boldsymbol{b}$ is the bias drift.

4.1.2 Magnetometer

The magnetometer measures Earth's magnetic field vector expressed in $\mathcal{F}_{BF}$. Conveniently the VN-100 IMU is a 10-axis sensor and includes magnetic field measurements as part of its sensed values [73]. With no sensor bias provided by the

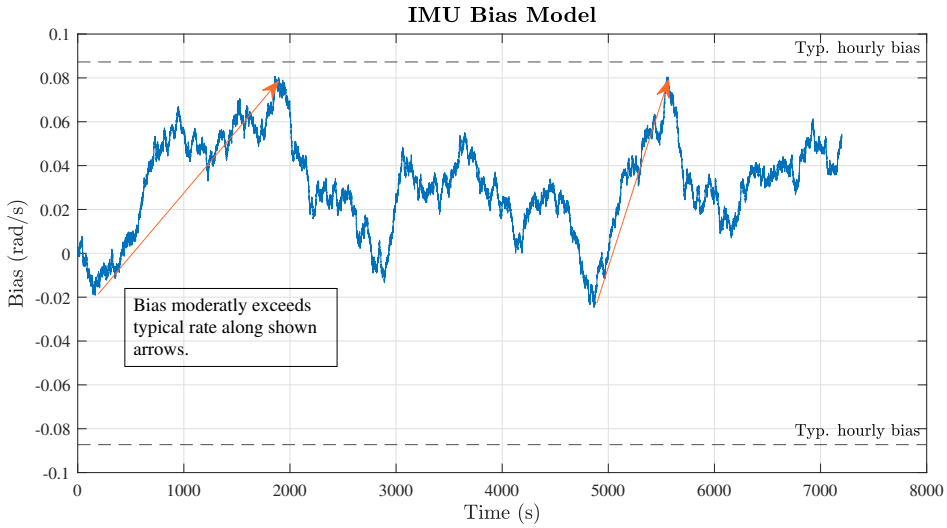

Figure 4.2: Simulated IMU Bias Drift Shown Over Two Hours

VN-100 datasheet, it was assumed that the sensor was only corrupted by band-limited white noise. The noise density was listed for the VN-100 magnetometer as $ND = 140\,\mu\text{Gauss}/\sqrt{\text{Hz}}$. For the subject thesis, the measurements in units of Gauss must be converted to Teslas by noting that 1 Gauss = 10^{-4} T. The noise variance for the magnetometer was calculated in this thesis as:

$$\sigma_\eta^2 = \left(ND(10^{-4})\sqrt{\frac{1}{dt}} \right)^2 \tag{4.3}$$

The resulting magnetometer white noise power was then calculated as $NP = \sigma_\eta^2 dt$. By examining the 3σ bounds in in Fig. 4.3 it can be seen that the simulated noise profile is comparable to the VN-100 specifications.

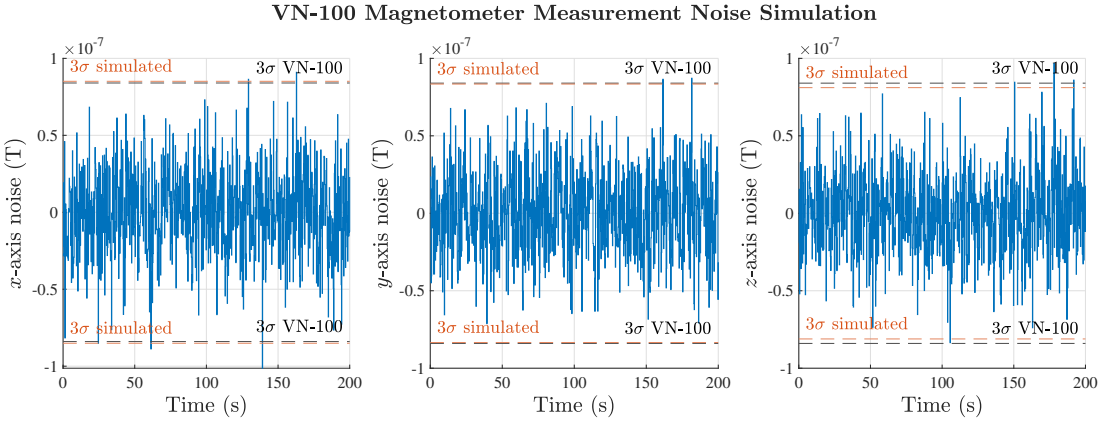

Figure 4.3: Simulated VN-100 Magnetometer Noise With 3σ Comparisons Shown

The magnetometer measurement model is then the sum of the actual $\mathscr{F}_{BF}$ magnetic field vector and the white noise process:

$$\boldsymbol{B}_m = \boldsymbol{B} + \boldsymbol{\eta} \tag{4.4}$$

4.1.3 GNSS Receiver

The GNSS receiver takes navigational messages from GNSS satellites in order to track the position of the spacecraft. While it is typical for velocity measurements to also be made, it was assumed in this work that only the satellite $\mathscr{F}_{ECI}$ position was measured. The GS-2T-Nano GNSS receiver was selected as the modeled GNSS unit for its extremely small form factor. A 6-15 meter typical positional accuracy was listed for the device [75]. For lack of a provided variance or 3σ level, it was assumed in this work that the listed upper range for positional accuracy corresponded to the 3σ level. Fig. 4.4 provides the axial measurement noise profiles for a 200s simulation of the subject GS-2T-Nano receiver.

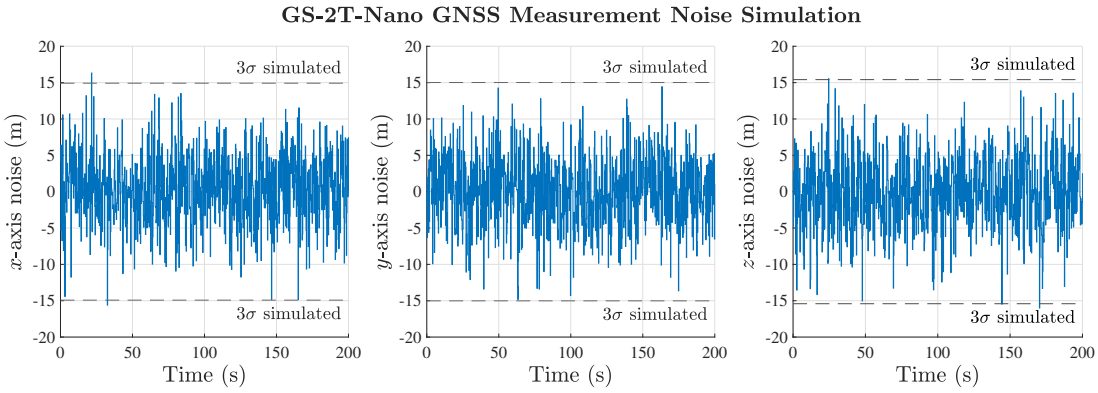

Figure 4.4: Simulated GS-2T-Nano Measurement Noise With 3σ Bounds Shown

The GNSS measurement model can be completed following a similar process to that used for the magnetometer:

$$\boldsymbol{r}_m = \boldsymbol{r}_{ECI} + \boldsymbol{\eta} \tag{4.5}$$

4.1.4 Sun Sensors

The sun sensors modeled in this thesis are analog photodiodes which produce a current based on the intensity of sunlight at the surface of the photodiode [76]. Photodiode sun sensors are advantageous for CubeSats because of having extremely small mass and volume footprints. In this work the coarse photodiodes were modeled after the Advanced Photonix SLCD-61N8 photodiode which has an FOV half angle of 60° [77]. Fine photodiodes were modeled after the VISHAY BPW21R which has a steep drop off in sensitivity for light with an incident angle over 45° [78]. A generalized vector diagram for the light sensitivity of a photodiode based on the incident angle

of the light with the normal vector of the photodiode surface is provided in Fig. 4.5 where all vectors are expressed in $\mathscr{F}_{BF}$. Further addressing Fig. 4.5, the photodiode optical plane normal vector is defined by $\boldsymbol{n}_{ss}$ and the incoming unit direction vector of sunlight is defined by $\boldsymbol{u}_s$. It is clear from Fig. 4.5 that the level of photodiode illumination is dependent on the projection of $\boldsymbol{u}_s$ onto $\boldsymbol{n}_{ss}$.

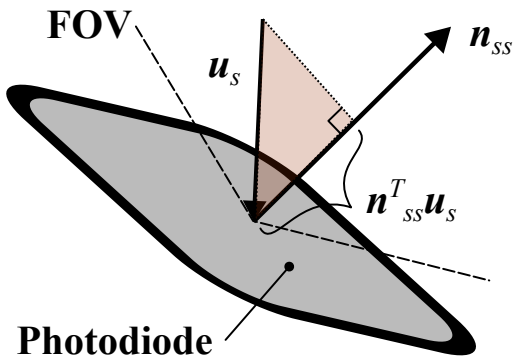

Figure 4.5: Photodiode Vector Diagram for Light Incident to the Photodiode Optical Plane

The current output from a photodiode, was modeled by adapting the work provided in [79], where I_{0_s} is the max current output from the photodiodes and η_{ss} is the band-limited white noise associated with the illumination measurement. I_{0_s} was selected as 50 mA based on the BPW21R forward current listing. In this thesis, the LIF factor ℓ is added to the current output equation from [79] to account for a reduction in photodiode current output when the satellite is partially eclipsed. The resulting equation is formed as:

$$I_p = I_{0_s}\ell\left(\boldsymbol{n}_{ss}^T\boldsymbol{u}_{ss}\right) + \eta_{ss} \tag{4.6}$$

The photodiodes could also be illuminated by albedo. The current output caused by albedo was modeled in the subject thesis as:

$$I_{p_a} = I_{0_s}\ell L_a^s\left(\boldsymbol{n}_{ss}^T(-\boldsymbol{u}_e)\right) \tag{4.7}$$

where $-\boldsymbol{u}_e$ is the negative of the unit nadir direction vector expressed in $\mathscr{F}_{BF}$ defined in Eq. (3.67). If the current output from the sum of albedo illumination and direct sun illumination $(I_p + I_{p_a})$ exceeds I_{0_s} then the current output from the photodiode is saturated to the maximum output of I_{0_s}. The saturation current in the focus work was also set to 50 mA based on the SLCD-61N8 datasheet [77]. Following the work in [26], a sun sensor measurement is also rejected if the output current is not above a threshold $\epsilon_{sc} = 25$ mA to prevent albedo corruption.

The noise profile of a photodiode must be determined experimentally following a procedure like that in [26]. In the absence of lab equipment to perform a noise characterization on the subject photodiodes, the subject thesis specifies band-limited white noise profiles for the sensors empirically. For the case of the SLCD-61N8 coarse

photodiode, a noise variance of $\sigma_\eta^2 = 2.152\text{E} - 04\ \text{mA}^2$ was specified, a value approximately double of that used in [26]. A more refined noise profile was specified for the fine BPW21R with a noise variance of $\sigma_\eta^2 = 3.0\text{E} - 08\ \text{mA}^2$ in order to achieve sub degree determination accuracy. Future ADCS development should responsibly address the characterization of the photodiode noise. Proceeding sections will leverage the previously defined sensor models to determine computationally the attitude of the spacecraft relative to $\mathscr{F}_{ECI}$.

4.2 Sun Vector Determination

Following the work provided in [79], to produce a three-dimensional sun vector estimation, at least three non-parallel and non-coplanar photodiodes are required to be observing the Sun at a given time. To enable three photodiodes to observe the sun simultaneously when not in eclipse, the spacecraft must be equipped with a suite of photodiodes where multiple photodiodes are placed at offset angles on each face of the spacecraft. In the subject work the photodiode placements from [26] are adopted for the coarse sun sensors because the developed placement design enables complete coverage of the body celestial sphere from 18 coarse photodiodes. The fine sun sensors are placed such that the optical plane of the sensors are aligned with the normal vectors of the 6 external spacecraft faces. The proposed photodiode placements are demonstrated in Fig. 4.6. A coverage analysis is provided in Fig. 4.7 where areas in blue represent the projection of a sun sensor FOV cone onto the surface of the celestial sphere corresponding to the satellite. Further, Fig. 4.8 shows the optical plane normal vectors and FOV cones for a cluster of photodiodes placed on the $x+$ face of the spacecraft to demonstrate the non-coplanarity of the photodiodes.

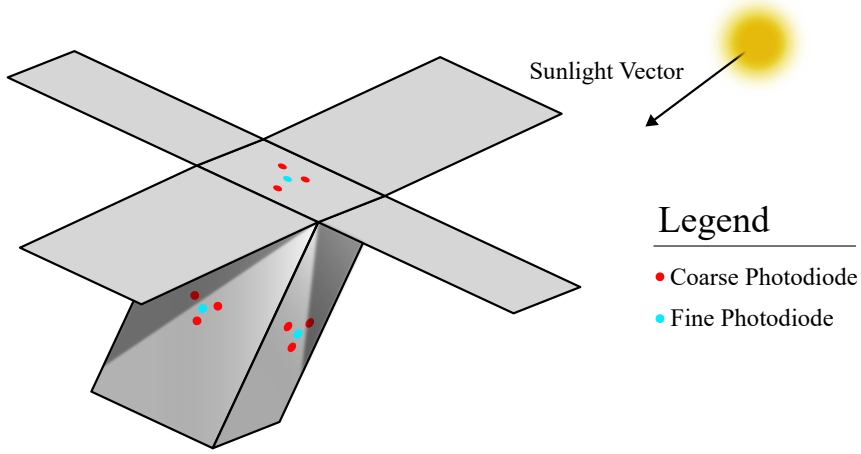

Figure 4.6: Placement of Photodiodes on External Faces of Spacecraft. Photodiodes may be Shadowed by Spacecraft Solar Panels.

While in Fig. 4.6 many photodiodes may be partially illuminated, the sun vector must still be within the FOV of the photodiode for the sensor to output a current.

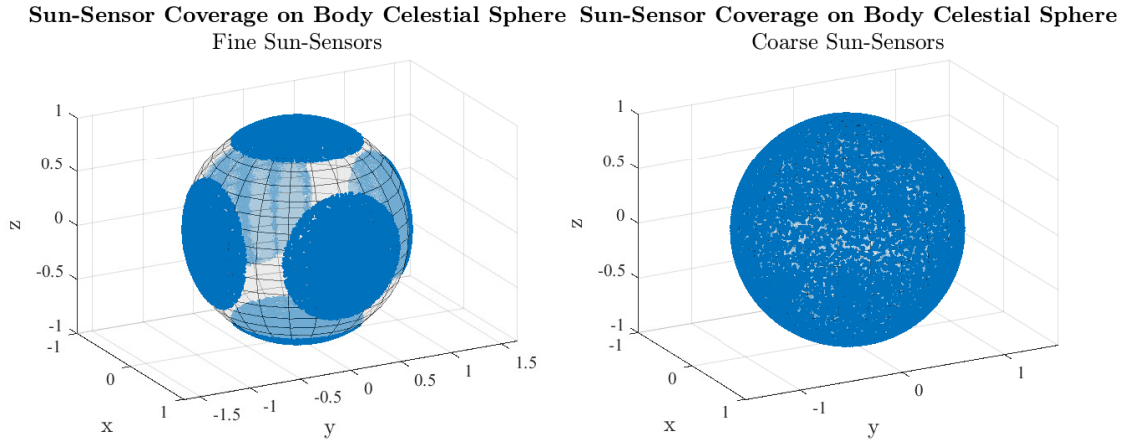

Figure 4.7: Fine Sun Sensor (left) and Coarse Sun Sensor (right) Coverage on Body Celestial Sphere. Areas Outside FOV Projections Represent Exclusion Areas not Viewed by a Sun Sensor.

In addition, the photodiode may also be shaded by a solar panel or appendage which

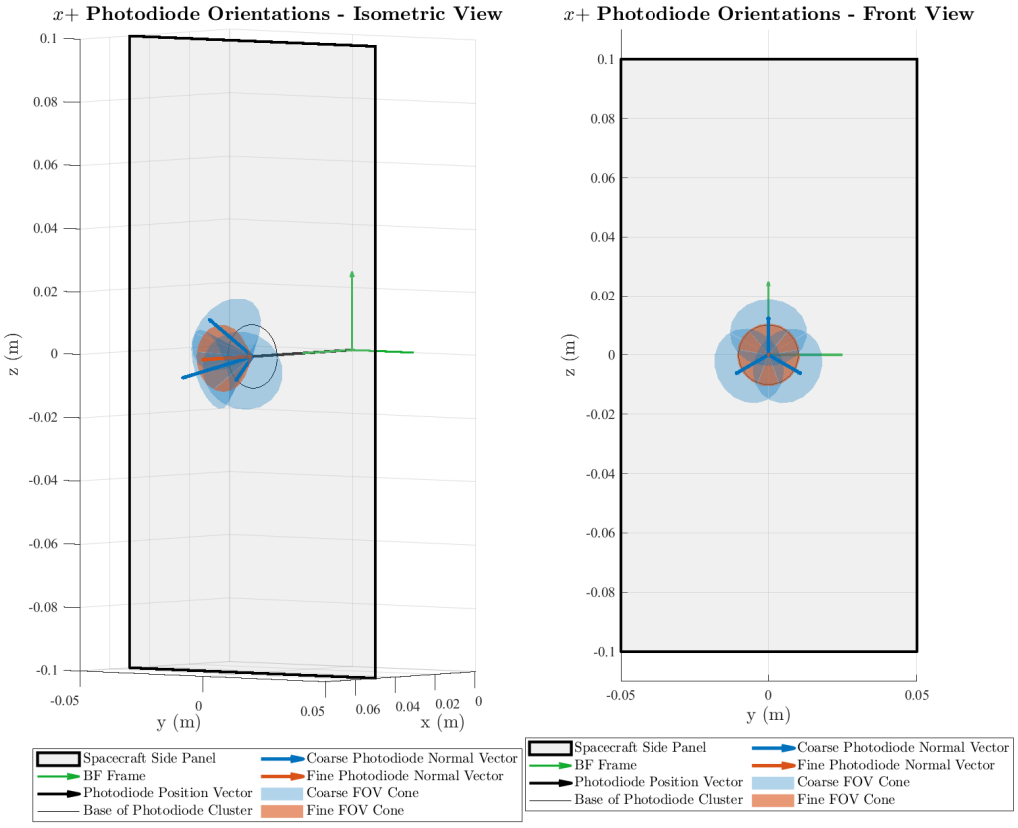

Figure 4.8: Orientation of All Photodiodes on $x+$ Face. Orientations are Repeated Respective to All Six Main External Faces.

would limit it from producing current. A point plane intersection model was used to model shading of the photodiodes.

For a satellite equipped with n number of photodiodes, the work from [79] can be applied to optimally estimate the sun vector in $\mathcal{F}_{BF}$ by using a form of batch least squares. Let $\boldsymbol{H}$ be a $n \times 3$ matrix where the ith row of $\boldsymbol{H}$ corresponds to the optical plane normal vector of photodiode i as:

$$\boldsymbol{H}_{i,1-3} = \boldsymbol{n}_{ss_i}^T = [n_1, n_2, n_3] \tag{4.8}$$

A set of photodiode normal vectors and placement locations are provided in Appendix B. The current output produced by photodiodes observing sunlight is stored in a $n \times 1$ matrix $\boldsymbol{y}$. The matrices $\boldsymbol{H}$ and $\boldsymbol{y}$ should only contain rows with photodiodes which can actually observe the Sun. Action should, therefore, be taken to systematically remove rows from these matrices if $\boldsymbol{n}_{ss}^T \boldsymbol{u}_s$ yields a quantity which is outside the satellite FOV, negative (on the shaded side of the spacecraft) or if the photodiode is shaded by an appendage. The FOV constraint can be modeled by the following logic statement where α represents the FOV half angle of a photodiode:

$$\text{if } \ \boldsymbol{H}_{i,1-3} \boldsymbol{u}_s < \cos(\alpha) \tag{4.9}$$

Provided that at least 3 non-parallel and non-coplanar photodiodes are viewing the Sun, the Sun vector estimation is the solution to the following least-squares problem [79]:

$$\boldsymbol{y} = \boldsymbol{H}\boldsymbol{u}_s + \boldsymbol{\eta} \tag{4.10}$$

Consistent with the measurements models, $\boldsymbol{\eta}$ represents band-limited white noise, which was added in the simulator to a photodiode measurement in Eq. (4.6). The solution to the linear least-squares problem for the Sun vector expressed relative to $\mathcal{F}_{BF}$ is given by:

$$\tilde{\boldsymbol{u}}_s = \left(\boldsymbol{H}^T \boldsymbol{R}^{-1} \boldsymbol{H}\right)^{-1} \boldsymbol{H}^T \boldsymbol{R}^{-1} \boldsymbol{y} \tag{4.11}$$

Here $\boldsymbol{R}$ is a positive definite and diagonal measurement covariance matrix where the noise covariances of individual photodiodes are placed in their respective rows on the diagonal of $\boldsymbol{R}$. The estimate covariance matrix is formed as:

$$\boldsymbol{P}_s = \left(\boldsymbol{H}^T \boldsymbol{R}^{-1} \boldsymbol{H}\right)^{-1} \tag{4.12}$$

In Eq. (4.11) $\tilde{\boldsymbol{u}}_s$ is not constrained to be a normalized unit direction vector. In this work, brute force normalization was employed on $\tilde{\boldsymbol{u}}_s$ because at worst, the effect of performing such an operation induces angular errors on the order of 10^{-1} degrees depending on the photodiode configuration [79]. In addition, the unconstrained estimate *should* yield a unit vector on average, particularly in simulation where sensor calibration is not required. For flight configurations, [79] should be referenced for constrained and calibrated estimation.

Should the estimate be poorly conditioned, it is important to signal to QUEST

and the MEKF downstream that no Sun vector estimate is available. A poorly conditioned estimate can be confirmed in the following equation where the function rcond() computes the reciprocal condition number of the input matrix:

$$\begin{cases} \tilde{\boldsymbol{u}}_s = [0,0,0]^T, \text{if } \text{rcond}(\boldsymbol{H}^T\boldsymbol{H}) < 1.0\text{E}-06 \\ \tilde{\boldsymbol{u}}_s = [0,0,0]^T, \text{if } \ell = 0 \end{cases} \tag{4.13}$$

A Sun vector estimate of $[0,0,0]^T$ signals QUEST and the MEKF that the sun was undeterminable so that the formulations for the satellite state can be changed accordingly. A determinable Sun vector is passed first to QUEST, presented in the following section, as one of the measurement vectors required to estimate the satellite attitude.

4.3 Quaternion Estimation Algorithm (QUEST)

To derive the attitude of a spacecraft it is generally required to obtain a minimum of two vector sets, each set with a vector defined in two different reference frames. The two vector sets criteria is more commonly addressed as Wahba's Problem and seeks to find an optimal solution to an attitude matrix for the spacecraft based on vector measurements [80]. The first useful method for solving Wahba's problem was known as Davenport's q-Method which employs eigenvalue decomposition to allow for fairly robust quaternion estimation from vector measurements [41][81]. A problem for early adoptions of the q-Method was that calculation of the eigenvalue decomposition would lead to the computation time being higher than the sampling rate on rudimentary hardware [81]. It is, for the effect of reducing computation time, that more modern attitude determination systems will employ Shuster's QUEST algorithm [82]. This work employs QUEST for preliminary satellite attitude determination following the formulations provided in [82].

QUEST will make attitude estimations with the $\mathscr{F}_{BF}$ measured magnetic field and Sun vectors along with the $\mathscr{F}_{ECI}$ reference model vectors from IGRF-13 and solar ephemeris data. Hereinafter, for the purposes of the QUEST formulations, a vector set is defined as the combination of the measured and reference vectors defined in their respective $\mathscr{F}_{BF}$ and $\mathscr{F}_{ECI}$ frames. According to [82], QUEST has a unique optimal solution when only two vector sets are provided. Symbol convention for the two vector set case leads to $\boldsymbol{V}_1$ and $\boldsymbol{V}_2$ representing two nonparallel unit reference vectors expressed in $\mathscr{F}_{ECI}$ with two corresponding measured unit vectors defined as $\boldsymbol{B}_1$ and $\boldsymbol{B}_2$ expressed in $\mathscr{F}_{BF}$. For the present work, these vectors are more directly defined as follows:

- $\boldsymbol{V}_1$ = IGRF-13 Magnetic Field Reference Vector
- $\boldsymbol{B}_1 = \boldsymbol{B}_m$ Measured Magnetic Field Vector
- $\boldsymbol{V}_2$ = Solar Ephemeris Sun Direction Vector
- $\boldsymbol{B}_2 = \tilde{\boldsymbol{u}}_s$ Sun Vector Estimation

Noting that a_i is a weighting factor applied to vector sets 1 and 2, respectively, which should be properly selected, the 3×3 attitude profile matrix is formed as:

$$\boldsymbol{B} = \sum_{i=1}^{2} a_i \boldsymbol{B}_i \boldsymbol{V}_i^T \tag{4.14}$$

In this research, the 3×1 matrix $\boldsymbol{Z}$ is defined as the cross product matrix following:

$$\boldsymbol{Z} = \sum_{i=1}^{2} a_i \left(\boldsymbol{B}_i^{\times} \boldsymbol{V}_i \right) \tag{4.15}$$

The symmetric attitude profile matrix can additionally be determined using the following relationship:

$$\boldsymbol{S} = \boldsymbol{B} + \boldsymbol{B}^T \tag{4.16}$$

For implementations of QUEST with more than 2 observations it is typical for the Newton-Raphson method to be implemented to compute the maximum eigenvalue corresponding to the optimal quaternion solution. In the presented case, however, there exists an exact closed-form expression which greatly reduces the required calculations [82]. Following the derivation in [82], the max eigenvalue can be computed as:

$$\lambda_{max} = \sqrt{a_1^2 + 2a_1 a_2 \cos(\theta_V - \theta_B) + a_2^2} \tag{4.17}$$

where:

$$\cos(\theta_V - \theta_B) = (\boldsymbol{V}_1 \cdot \boldsymbol{V}_2)(\boldsymbol{B}_1 \cdot \boldsymbol{B}_2) + |\boldsymbol{V}_1^{\times} \boldsymbol{V}_2||\boldsymbol{B}_1^{\times} \boldsymbol{B}_2| \tag{4.18}$$

Six additional quantities are introduced in Shulster (1981) to compute the optimal quaternion. These quantities are introduced in the following equations where "tr()" is the trace operation on a square matrix, "adj()" is a function which computes adjoint of a matrix, and "det()" computes the determinant of the input matrix.

$$\sigma = \frac{1}{2} \mathrm{tr}(\boldsymbol{S}) \tag{4.19}$$

$$\kappa = \mathrm{tr}(\mathrm{adj}(\boldsymbol{S})) \tag{4.20}$$

$$\Delta = \det(\boldsymbol{S}) \tag{4.21}$$

The remaining quantities are calculated after computation of Eq. (4.19) - Eq. (4.21) as they are dependent on solving the prior equations:

$$\alpha = \lambda_{max}^2 - \sigma^2 + \kappa \tag{4.22}$$

$$\beta = \lambda_{max} - \sigma \tag{4.23}$$

$$\gamma = (\lambda_{max} + \sigma)\alpha - \Delta \tag{4.24}$$

The optimal attitude quaternion $\bar{\boldsymbol{q}}_{opt}$ is obtained from solving the following problem for which $\bar{\boldsymbol{q}}_{opt}$ is obtained as the eigenvector of a 4×4 matrix $\boldsymbol{K}$ corresponding

to the maximum eigenvalue λ_{max}:

$$\boldsymbol{K}\bar{\boldsymbol{q}}_{opt} = \lambda_{max}\bar{\boldsymbol{q}}_{opt} \tag{4.25}$$

For completeness, $\boldsymbol{K}$ may be formed as:

$$\boldsymbol{K} = \left[\begin{array}{c|c} \boldsymbol{S} - \sigma\boldsymbol{I}_{3\times 3} & \boldsymbol{Z} \\ \hline \boldsymbol{Z}^T & \sigma \end{array}\right] \tag{4.26}$$

Since the maximum eigenvalue is already available in a closed-form solution, it is not necessary to compute the eigendecomposition of $\boldsymbol{K}$ for the two vector set case and, therefore, the optimal attitude quaternion calculation proceeds by first computing the parameter $\boldsymbol{X}$ as:

$$\boldsymbol{X} = \left(\alpha\boldsymbol{I}_{3\times 3} + \beta\boldsymbol{S} + \boldsymbol{S}^2\right)\boldsymbol{Z} \tag{4.27}$$

The optimal quaternion estimate is then formed in the following relation as:

$$\bar{\boldsymbol{q}}_{opt} = \frac{1}{\sqrt{\gamma^2 + |\boldsymbol{X}|^2}}\begin{Bmatrix}\boldsymbol{X} \\ \gamma\end{Bmatrix} \tag{4.28}$$

4.3.1 QUEST Covariance Matrix

One of the most important contributions of Shuster's QUEST method was the ability to discern the covariance matrix for the optimal quaternion estimate. The formulations required to compute this matrix are provided in this section because the covariance matrix from QUEST can reasonably be used as an initial measurement covariance estimate later in the MEKF formulations. The formulations begin with the variance of a vector set i defined as:

$$\sigma_i^2 = \sigma_{\boldsymbol{V}_i}^2 + \sigma_{\boldsymbol{B}_i}^2 \tag{4.29}$$

The constant corresponding to the total estimate variance can be calculated for the two vector set solution as:

$$\frac{1}{\sigma_{tot}^2} = \left(\frac{1}{\sigma_1^2} + \frac{1}{\sigma_2^2}\right) \tag{4.30}$$

which leads to the two vector set covariance matrix being computed as:

$$\begin{aligned}\boldsymbol{P}_{QQ} = \frac{1}{4}[\sigma_{tot}^2\boldsymbol{I}_{3\times 3} + |\boldsymbol{B}_1^{\times}\boldsymbol{B}_2|^{-2}[(\sigma_2^2 - \sigma_{tot}^2)\boldsymbol{B}_1\boldsymbol{B}_1^T + (\sigma_1^2 - \sigma_{tot}^2)\boldsymbol{B}_2\boldsymbol{B}_2^T \\ + \sigma_{tot}^2(\boldsymbol{B}_1\cdot\boldsymbol{B}_2)(\boldsymbol{B}_1\boldsymbol{B}_2^T + \boldsymbol{B}_2\boldsymbol{B}_1^T)]]\end{aligned} \tag{4.31}$$

This covariance matrix from Eq. (4.31) is $\mathscr{F}_{BF}$ referenced because of its derivation from $\mathscr{F}_{BF}$ observation vectors. The inertially-referenced covariance matrix may,

therefore, be computed as:

$$\boldsymbol{P}_{qq} = [\bar{\boldsymbol{q}}_{opt}] \begin{bmatrix} \boldsymbol{P}_{QQ} & \boldsymbol{0}_{3\times1} \\ \boldsymbol{0}_{1\times3} & 0 \end{bmatrix} [\bar{\boldsymbol{q}}_{opt}^{T}] \tag{4.32}$$

where $[\bar{\boldsymbol{q}}]$ represents the following quaternion operation:

$$[\bar{\boldsymbol{q}}] = \begin{bmatrix} q_4 & -q_3 & q_2 & q_1 \\ q_3 & q_4 & -q_1 & q_2 \\ -q_2 & q_1 & q_4 & q_3 \\ -q_1 & -q_2 & -q_3 & q_4 \end{bmatrix} \tag{4.33}$$

In the following section the results of quaternion estimation are fed as attitude measurements to a mission mode MEKF for further attitude state estimation.

4.4 Multiplicative Extended Kalman Filter (MEKF)

The MEKF is employed predominantly to filter the IMU measurements and remove IMU bias, but it is also selected as the attitude filter because the multiplicative representation in the MEKF formulations does not violate the unitary constraint placed on all quaternions [83]. In comparison to the quaternion-based Extended Kalman Filter (EKF) with additive formulations presented in [84], the MEKF formulations preserve the unitary constraint. The MEKF is subsequently employed in this work to ensure the validity of the attitude quaternions and filter the IMU sensor.

In this work a "mission mode" MEKF is presented to estimate the key attitude states relating to spacecraft attitude and body rates. The corresponding global attitude state vector is, therefore, defined as $\boldsymbol{x}_k^{true} = [q_1, q_2, q_3, q_4, \omega_x, \omega_y, \omega_z]^T$. Additionally, the proposed MEKF operates in "Dynamic Model Replacement" mode, meaning that accurate IMU data from the VN-100 is used in lieu of a dynamic model. The motivation for these mode selections is twofold, from computational efficiency and determination accuracy standpoints [41]. The foundational concept of these formulations is that, to preserve the unit norm constraint placed on the attitude quaternion, the MEKF will propagate and update a three-component local attitude state error $\boldsymbol{\delta\vartheta}$ and subsequently shift this information to the global attitude state in a reset operation. It follows that the true global quaternion can be found in the subject formulations from a product of the error $\boldsymbol{\delta q}$ and estimate $\hat{\boldsymbol{q}}$ quaternions [41]:

$$\boldsymbol{q}^{true} = \boldsymbol{\delta q}\boldsymbol{\delta\vartheta} \otimes \hat{\boldsymbol{q}} \tag{4.34}$$

The local state, instead of being 7×1 like the global attitude state, is defined instead as a 6×1 vector $\boldsymbol{x}_k = [\boldsymbol{\delta\vartheta}, \boldsymbol{\Delta\zeta}]^T$ where $\boldsymbol{\Delta\zeta}$ is a change in IMU bias. Functionally, the MEKF has three stages which are shown in Table 4.1. The propagation stage moves the previous global state MEKF estimate forward to the present sample time. The update stage updates the local error state vector using sensor measurements and the propagated global state estimate. Finally, in the reset stage, the local

state is shifted to the global state estimate before resetting the local state to zero. To define these stages subscripts are used so that the subscript "$k-1|k-1$" represents a pre propagation value, "$k|k-1$" represents a post propagation value, and "$k|k$" is a post update value.

Noticeably from Table 4.1, there are adjusted formulations for the MEKF in eclipse and in sunlight. Because attitude determination is only possible for the satellite in sunlight, discussion on the MEKF formulations will focus on the sunlight formulations starting on line 24 of Table 4.1.

Propagation

Referring to Table 4.1 line 30, the first effect of dynamic model replacement is observed. The spacecraft body rates are propagated by subtracting the previous IMU bias estimate $\boldsymbol{\zeta}_{k-1|k-1}$ from the raw IMU measured body rate stored in a measurement vector $\boldsymbol{z}_k = [\bar{q}_1, \bar{q}_2, \bar{q}_3, \bar{q}_4, \omega_{m_x}, \omega_{m_y}, \omega_{m_z}]^T$ which contains the QUEST quaternion and IMU measurement. On line 31, the previous quaternion estimate is propagated forward using $\boldsymbol{\omega}_{k|k-1}$ in the quaternion kinematic equation from Eq. (3.33). On line 32 the 6×6 state transition Jacobian matrix $\boldsymbol{F}_k$ is formed by following the provided relationship in [41] and converting it to discrete time. It should be noted that IMU bias is not always an observable state [85][86]. In $\boldsymbol{F}_k$, the IMU bias rows are, therefore, the identity matrix. Finally, the covariance matrix $\boldsymbol{P}_{k|k-1}$ is propagated on line 33 with the noise Jacobian $\boldsymbol{G}_k$ and process noise covariance matrix $\boldsymbol{Q}_k$. While $\boldsymbol{F}_k$ is dependent on $\boldsymbol{\omega}_{k|k-1}$, $\boldsymbol{G}_k$ is a constant matrix which may be calculated as:

$$\boldsymbol{G}_k = \begin{bmatrix} -\boldsymbol{I}_{3\times3}dt & \boldsymbol{0}_{3\times3} \\ \boldsymbol{0}_{3\times3} & \boldsymbol{I}_{3\times3}dt \end{bmatrix} \tag{4.35}$$

The process noise covariance matrix was assembled by empirically scaling a diagonal matrix of IMU noise variances. The symbol σ_v^2 represents the IMU band-limited white noise variance and σ_u^2 represents the variance of the integrated band-limited white noise used to produce the IMU bias. $\boldsymbol{Q}_k$ may, therefore, be assembled as follows:

$$\boldsymbol{Q}_k = 10^{-2} \begin{bmatrix} \sigma_v^2\boldsymbol{I}_{3\times3} & \boldsymbol{0}_{3\times3} \\ \boldsymbol{0}_{3\times3} & \sigma_u^2\boldsymbol{I}_{3\times3} \end{bmatrix} \tag{4.36}$$

Update

The first step of the update stage is to develop the local attitude error parameterization. The local attitude error is parameterized into Rodrigues parameters on lines 36 to 37 for the practicality of the fact that it makes the observation model insensitive to the ambiguity of the sign associated with the QUEST quaternion [41]. The local error vector is shifted into the local measurement vector $\boldsymbol{y}$, along with the $\mathscr{F}_{BF}$ expressed measured magnetic field vector $\boldsymbol{B}_m$ on line 38. Similar to the QUEST algorithm, a set of attitude reference vectors are required in the MEKF. These reference vectors are transformed from their expression in the inertial frame $\mathscr{F}_{ECI}$ to $\mathscr{F}_{BF}$ by applying the

post propagation quaternion $\boldsymbol{q}_{k|k-1}$. The reference vectors are stored in the reference vector $\boldsymbol{h}$ on line 39 and subsequently compared to the local measurement vector by computing the difference between the two vectors on line 40. This difference, also known as the innovation term $\tilde{\boldsymbol{y}}$, is important for the later local state update.

Lines 41 to 45 introduce the measurement matrix $\boldsymbol{H}_k$, the measurement covariance matrix $\boldsymbol{R}_k$, the Kalman Gain matrix $\boldsymbol{K}_k$, and the innovation covariance matrix $\boldsymbol{S}_k$ for the purpose of updating the local state estimate and covariance matrix on lines 44 and 45. Noticeably, an additive update is performed on line 45, an action permissible in the local state but not the global state. Because the local state carries the change in IMU bias denoted by $\boldsymbol{\Delta\zeta}$, the true IMU bias must be calculated as an evolution of the previous IMU bias estimate $\boldsymbol{\zeta}_{k-1|k-1}$. The true IMU bias and associated post update angular rate estimate $\boldsymbol{\omega}_{k|k}$ can be computed using lines 46 and 47.

Reset

The final stage of the MEKF seeks to shift the local attitude error state to a global estimate for the true spacecraft attitude. The reset of the non attitude state (IMU bias) was simply done implicitly on line 46 by adding the change in IMU bias to the previous IMU bias estimate. The quaternion, however, must be reset explicitly. The quaternion reset operation for Rodrigues parameterization of the local attitude error state is provided on line 49. The brute force normalization of the global quaternion attitude estimate is performed on line 50. This operation is theoretically enabled by the use of Rodrigues parameters according to Markley (2014) in [41]. After the reset both $\boldsymbol{\delta\vartheta}_{k|k-1}$ and $\boldsymbol{\Delta\zeta}_{k|k-1}$ are set to $\mathbf{0}_{3\times1}$. This resetting of the local state vector was accomplished in this thesis simply by preformatting the local state vector to be $\boldsymbol{x}_{k|k-1} = \mathbf{0}_{6\times1}$ on line 34 prior to beginning the update stage.

Table 4.1: MEKF Algorithm

Line	Action	Equation
1	Check Eclipse	`if` $\boldsymbol{z}_{k_{1:4}} = [0,0,0,1]^T$
2	**Propagation:**	
3	Propagate $\boldsymbol{\omega}$	$\boldsymbol{\omega}_{k\|k-1} = \boldsymbol{z}_{k_{5:7}} - \boldsymbol{\zeta}_{k-1\|k-1}$
4	Propagate $\boldsymbol{q}$	$\boldsymbol{q}_{k\|k-1} = \frac{1}{2}\Omega(\boldsymbol{\omega}_{k\|k-1})\boldsymbol{q}_{k-1\|k-1}dt + \boldsymbol{q}_{k-1\|k-1}$
5	Compute $\boldsymbol{F}_k$	$\boldsymbol{F}_k = \begin{bmatrix} \boldsymbol{I}_{3\times3} - \boldsymbol{\omega}^{\times}_{k\|k-1}dt & -\boldsymbol{I}_{3\times3}dt \\ \mathbf{0}_{3\times3} & \boldsymbol{I}_{3\times3} \end{bmatrix}$
6	Propagate $\boldsymbol{P}$	$\boldsymbol{P}_{k\|k-1} = \boldsymbol{F}_k\boldsymbol{P}_{k-1\|k-1}\boldsymbol{F}_k^T + \boldsymbol{G}_k\boldsymbol{Q}_k\boldsymbol{G}_k^T$
7	Pre-Format $\boldsymbol{x}_{k\|k-1}$	$\boldsymbol{x}_{k\|k-1} = \mathbf{0}_{6\times1}$
8	**Update:**	
9	Define Measurements	$\boldsymbol{y} = \boldsymbol{B}_m$

Continued on next page

Table 4.1 – continued from previous page

Line	Action	Equation
10	Define References	$\boldsymbol{h} = \boldsymbol{\mathcal{A}}(\boldsymbol{q}_{k\|k-1})\boldsymbol{B}_{IGRF-13}$
11	Innovation	$\tilde{\boldsymbol{y}} = \boldsymbol{y} - \boldsymbol{h}$
12	Eclipse Measurement Covariance	$\boldsymbol{R}_k = 10^5 \boldsymbol{R}_{k_{4:6,4:6}}$
13	Measurement Matrix	$\boldsymbol{H}_k = [(\boldsymbol{\mathcal{A}}(\boldsymbol{q}_{k\|k-1})\boldsymbol{B}_{IGRF-13})^\times \ \boldsymbol{0}_{3\times3}]$
14	Compute Innovation Covariance	$\boldsymbol{S}_k = \boldsymbol{H}_k \boldsymbol{P}_{k\|k-1} \boldsymbol{H}_k^T + \boldsymbol{R}_k$
15	Kalman Gain	$\boldsymbol{K}_k = \boldsymbol{P}_{k\|k-1} \boldsymbol{H}_k^T \boldsymbol{S}_k^{-1}$
16	Refine Covariance	$\boldsymbol{P}_{k\|k} = (\boldsymbol{I}_{6\times6} - \boldsymbol{K}_k \boldsymbol{H}_k)\boldsymbol{P}_{k\|k-1}$
17	Error State Update	$\boldsymbol{x}_{k\|k} = \boldsymbol{x}_{k\|k-1} + \boldsymbol{K}_k \tilde{\boldsymbol{y}}$
18	Update Bias Estimate	$\boldsymbol{\zeta}_{k\|k} = \boldsymbol{\zeta}_{k-1\|k-1} + \boldsymbol{x}_{k\|k_{4:6}}$
19	Update Angular Rate	$\boldsymbol{\omega}_{k\|k} = \boldsymbol{z}_{k_{5:7}} - \boldsymbol{\zeta}_{k\|k}$
20	**Reset:**	
21	Quaternion Reset	$\boldsymbol{q}_{k\|k} = \boldsymbol{q}_{k\|k-1} + \frac{1}{2}\Xi(\boldsymbol{q}_{k\|k-1})\boldsymbol{x}_{k\|k_{1:3}}$
22	Normalize	$\boldsymbol{q}_{k\|k} = \frac{\boldsymbol{q}_{k\|k}}{\|\boldsymbol{q}_{k\|k}\|}$
23	Update Clock	$n_k = n_k + 1$
24	Satellite in Sun	`else`
25	Check Clock	`if` $n_k > 0$
26	Update MEKF Covariance	$\boldsymbol{P}_{k\|k-1} = \boldsymbol{P}_{sun}$
27	Update MEKF Global Attitude State	$\boldsymbol{q}_{k\|k-1} = \boldsymbol{z}_{k_{1:4}}$
28	Reset Clock	$n_k = 0$
29	**Propagation:**	
30	Propagate $\boldsymbol{\omega}$	$\boldsymbol{\omega}_{k\|k-1} = \boldsymbol{z}_{k_{5:7}} - \boldsymbol{\zeta}_{k-1\|k-1}$
31	Propagate $\boldsymbol{q}$	$\boldsymbol{q}_{k\|k-1} = \frac{1}{2}\Omega(\boldsymbol{\omega}_{k\|k-1})\boldsymbol{q}_{k-1\|k-1}dt + \boldsymbol{q}_{k-1\|k-1}$
32	Compute $\boldsymbol{F}_k$	$\boldsymbol{F}_k = \begin{bmatrix} \boldsymbol{I}_{3\times3} - \boldsymbol{\omega}^\times_{k\|k-1}dt & -\boldsymbol{I}_{3\times3}dt \\ \boldsymbol{0}_{3\times3} & \boldsymbol{I}_{3\times3} \end{bmatrix}$
33	Propagate $\boldsymbol{P}$	$\boldsymbol{P}_{k\|k-1} = \boldsymbol{F}_k \boldsymbol{P}_{k-1\|k-1} \boldsymbol{F}_k^T + \boldsymbol{G}_k \boldsymbol{Q}_k \boldsymbol{G}_k^T$
34	Pre-Format $\boldsymbol{x}_{k\|k-1}$	$\boldsymbol{x}_{k\|k-1} = \boldsymbol{0}_{6\times1}$
35	**Update:**	
36	Error Quaternion	$\boldsymbol{\delta q} = \boldsymbol{z}_{k_{1:4}} \otimes \boldsymbol{q}^{-1}_{k\|k-1}$
37	Error Parameterization	$\boldsymbol{\delta\vartheta} = 2\left(\frac{\delta \boldsymbol{q}_{1:3}}{\delta \boldsymbol{q}_4}\right)$
38	Local Measurement Vector	$\boldsymbol{y} = [\boldsymbol{\delta\vartheta} \ \boldsymbol{B}_m]^T$

Continued on next page

Table 4.1 – continued from previous page

Line	Action	Equation
39	Define References	$\boldsymbol{h} = \begin{bmatrix} \mathbf{0}_{3\times1} \\ \boldsymbol{\mathcal{A}}(\boldsymbol{q}_{k\|k-1})\boldsymbol{B}_{IGRF-13} \end{bmatrix}$
40	Innovation	$\tilde{\boldsymbol{y}} = \boldsymbol{y} - \boldsymbol{h}$
41	Measurement Matrix	$\boldsymbol{H}_k = \begin{bmatrix} \boldsymbol{I}_{3\times3} & \mathbf{0}_{3\times3} \\ \boldsymbol{\mathcal{A}}(\boldsymbol{q}_{k\|k-1})\boldsymbol{B}_{IGRF-13})^\times & \mathbf{0}_{3\times3} \end{bmatrix}$
42	Compute Innovation Covariance	$\boldsymbol{S}_k = \boldsymbol{H}_k\boldsymbol{P}_{k\|k-1}\boldsymbol{H}_k^T + \boldsymbol{R}_k$
43	Kalman Gain	$\boldsymbol{K}_k = \boldsymbol{P}_{k\|k-1}\boldsymbol{H}_k^T\boldsymbol{S}_k^{-1}$
44	Refine Covariance	$\boldsymbol{P}_{k\|k} = (\boldsymbol{I}_{6\times6} - \boldsymbol{K}_k\boldsymbol{H}_k)\boldsymbol{P}_{k\|k-1}$
45	Error State Update	$\boldsymbol{x}_{k\|k} = \boldsymbol{x}_{k\|k-1} + \boldsymbol{K}_k\tilde{\boldsymbol{y}}$
46	Update Bias Estimate	$\boldsymbol{\zeta}_{k\|k} = \boldsymbol{\zeta}_{k-1\|k-1} + \boldsymbol{x}_{k\|k_{4:6}}$
47	Update Angular Rate	$\boldsymbol{\omega}_{k\|k} = \boldsymbol{z}_{k_{5:7}} - \boldsymbol{\zeta}_{k\|k}$
48	**Reset:**	
49	Quaternion Reset	$\boldsymbol{q}_{k\|k} = \boldsymbol{q}_{k\|k-1} + \frac{1}{2}\Xi(\boldsymbol{q}_{k\|k-1})\boldsymbol{x}_{k\|k_{1:3}}$
50	Normalize	$\boldsymbol{q}_{k\|k} = \frac{\boldsymbol{q}_{k\|k}}{\|\boldsymbol{q}_{k\|k}\|}$
51	end	

Effect of Eclipse on Attitude Estimation

The formulations outlined in Table 4.1 present a scenario where the MEKF will converge to two different covariance matrices dependent on the eclipse state. In eclipse, there is no attitude measurement available to the MEKF, which leads to a covariance matrix estimate that is different from the covariance matrix produced when attitude measurements are available. To minimize disturbances to the control system when the MEKF switches between estimation modes, it was desired to ensure that the attitude estimate transition from eclipse to Sun remains smooth. Smooth switching was achieved in this research by storing the in-Sun covariance matrix and using it for the first estimate the MEKF makes out of eclipse. In addition, the latest available QUEST quaternion is used as the previously estimated MEKF quaternion to ensure that the MEKF propagation begins near the actual attitude quaternion for every transition from eclipse to Sun. This logic is presented on lines 25 - 28 in Table 4.1. If the spacecraft is in eclipse, the MEKF can still make rough estimates of IMU bias by using modified measurement formulations on lines 9 - 13.

On account of the MEKF collecting a sample count during eclipse, it becomes relatively simple to detect the first in-Sun estimation. As shown on line 25, if the Sun is detected and the sample count n_k is larger than 0 the satellite must be transitioning out of eclipse. The stored covariance matrix and QUEST quaternion can, therefore, be applied to ensure a smooth estimation transition into the Sun estimation mode.

4.5 Orbit Determination - Extended Kalman Filter (OD-EKF)

To this point the formulations presented in preceding sections have assumed that the spacecraft position is known in order to produce the vectors from the reference models such as IGRF-13 or solar ephemerides. For true online implementation, the spacecraft requires a method to determine and propagate its own position relative to Earth. For some time, the industry standard for online spacecraft orbit determination has been to upload TLEs to the spacecraft and have the onboard computer propagate them using the Simplified General Perturbations 4 model (SGP4) [87]. SGP4, however, only provides reasonably accurate orbital predictions for up to 12 hours in advance. Spacecraft autonomy is also limited by SGP4 as reliable up-links are required to update the onboard TLE. [87][88].

The need for spacecraft autonomy has led modern spacecraft to prefer GPS/GNSS sensors to actively measure the spacecraft position [89][88]. In works such as [89][90][91] and [88] orbit determination via GPS is improved by adding a Kalman Filter to refine the GPS measurements. Adopting the methods presented in the literature, enables autonomous fine attitude determination by implementing an Orbit Determination - Extended Kalman Filter (OD-EKF) receiving GPS measurements of satellite position. An additional benefit of this method is the ability to leverage the OD-EKF to estimate spacecraft orbital velocity.

A challenge which is discussed in [89] and [91] is that GPS units draw a significant amount of power. For a CubeSat power bus, it is typical to duty cycle the GPS to reduce the power draw. As a result, the OD-EKF must have continuous-discrete time capabilities. A continuous-discrete time EKF will propagate estimates with a dynamic model in continuous time until a discrete time GPS measurement is available to refine the estimates [91] [92]. Fig. 4.9 describes on a sample by sample basis the synchronization between orbit determination and attitude determination filters. The

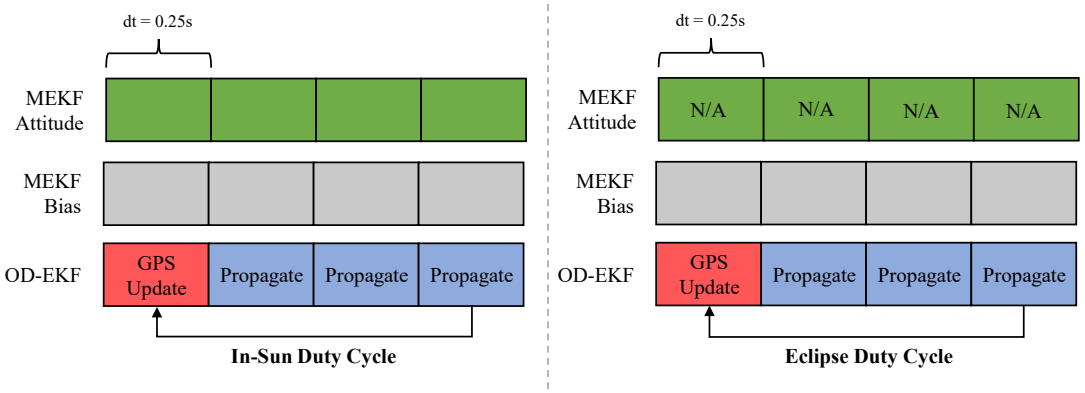

Figure 4.9: ADS Duty Cycles

GPS measurements, it is acceptable to reduce the complexity of the model to save computation resources. To demonstrate the rapid progression of model complexity, we provide the derivation of a Cowell model unperturbed orbit propagation and compare it to that of a J2 perturbed orbit propagation. The Cowell model ECI frame orbital acceleration is provided as:

$$\boldsymbol{a} = -\frac{\mu}{|\boldsymbol{r}|^3}\boldsymbol{r} \tag{4.37}$$

The corresponding partial derivative with respect to r_1 where $\boldsymbol{r} = [r_1, r_2, r_3]^T$ is:

$$\frac{\partial \boldsymbol{a}}{\partial r_1} = -\frac{mu}{|\boldsymbol{r}|^3} + \frac{3\mu}{\boldsymbol{r}^5} r_1^2 \tag{4.38}$$

The partial derivatives of the model are important to consider because nine partial derivatives of the ODE in Eq. (4.37) are required to build the state transition Jacobian for the OD-EKF. That is, if $\dot{\boldsymbol{x}} = f(\boldsymbol{x}(t))$ exists where $f()$ is a nonlinear function, the state transition Jacobian $\boldsymbol{F}_k$ exists as:

$$\boldsymbol{F}_k = \frac{\partial f}{\partial \boldsymbol{x}} \tag{4.39}$$

To make the comparison with the Cowell model, the orbital acceleration in the ECI frame subject to the J2 perturbation can be expressed by following the derivation in [93]. The orbital acceleration with J2 effects included now has three terms instead of one as in Eq. (4.37):

$$a_x = -\frac{\mu r_1}{|\boldsymbol{r}|^3} + \frac{\mu J_2 R_e^2}{2}\left(15\frac{r_1 r_3^2}{|\boldsymbol{r}|^7} - 3\frac{r_1}{|\boldsymbol{r}|^5}\right) \tag{4.40}$$

The derivation of the partial derivative for this acceleration component is provided by Ottemark (2015), however, the expression is already too lengthy to list here [90]. It is, therefore, reasonable to limit the OD-EKF dynamic model to the J2 perturbation. This limitation is further justified by the fact that, with a 25% duty cycle, the OD-EKF will receive sufficiently frequent GPS measurements to ensure that propagation errors over 3 samples are quickly corrected.

The OD-EKF derivation starts by defining the state vector as $\boldsymbol{x}_k = [\boldsymbol{r}_{ECI}\ \boldsymbol{v}_{ECI}]^T$. It follows that the time derivative of the state may be defined as $\dot{\boldsymbol{x}} = [\boldsymbol{v}_{ECI}\ \boldsymbol{a}_{ECI}]^T$. Following Eq. (4.40) the other axial orbital accelerations expressed in the ECI frame are defined as:

$$a_y = -\frac{\mu r_2}{|\boldsymbol{r}|^3} + \frac{\mu J_2 R_e^2}{2}\left(15\frac{r_2 r_3^2}{|\boldsymbol{r}|^7} - 3\frac{r_2}{|\boldsymbol{r}|^5}\right) \tag{4.41}$$

$$a_z = -\frac{\mu r_3}{|\boldsymbol{r}|^3} + \frac{\mu J_2 R_e^2}{2}\left(15\frac{r_3^3}{|\boldsymbol{r}|^7} - 9\frac{r_3}{|\boldsymbol{r}|^5}\right) \tag{4.42}$$

The OD-EKF dynamic model is completed by deriving the differential equation

pertaining to the covariance matrix propagation. In the general EKF equations, the EKF propagates the covariance matrix as:

$$\dot{\boldsymbol{P}}_{k|k-1} = \boldsymbol{F}_k \boldsymbol{P}_{k-1|k-1} \boldsymbol{F}_k^T + \boldsymbol{G}_k^T \boldsymbol{Q}_k \boldsymbol{G}_k \tag{4.43}$$

Noting Eq. (4.39), the state transition Jacobian was derived as:

$$\boldsymbol{F}_k = \begin{bmatrix} \boldsymbol{0}_{3\times3} & \boldsymbol{I}_{3\times3} \\ \boldsymbol{\Phi}_{3\times3} & \boldsymbol{0}_{3\times3} \end{bmatrix} \text{ with, } \boldsymbol{\Phi} = \begin{bmatrix} \frac{\partial a_x}{\partial r_1} & \frac{\partial a_x}{\partial r_2} & \frac{\partial a_x}{\partial r_3} \\ \frac{\partial a_y}{\partial r_1} & \frac{\partial a_y}{\partial r_2} & \frac{\partial a_y}{\partial r_3} \\ \frac{\partial a_z}{\partial r_1} & \frac{\partial a_z}{\partial r_2} & \frac{\partial a_z}{\partial r_3} \end{bmatrix} \tag{4.44}$$

The reader is directed to the work in [90] for the partial derivatives completing the state transition Jacobian as they were implemented in this thesis. Similar to the MEKF, $\boldsymbol{G}_k$ represents the noise Jacobian, $\boldsymbol{Q}_k$ represents the process noise Jacobian, $\boldsymbol{H}_k$ denotes the measurement matrix, and $\boldsymbol{R}_k$ is the measurement noise covariance matrix. In the case of this thesis, the matrices $\boldsymbol{G}_k$, $\boldsymbol{Q}_k$, $\boldsymbol{H}_k$, and $\boldsymbol{R}_k$, were all time independent leading to their assembly in the following set of equations as:

$$\boldsymbol{G}_k = \begin{bmatrix} \boldsymbol{0}_{3\times3} & \boldsymbol{I}_{3\times3} \end{bmatrix} \tag{4.45}$$

$$\boldsymbol{Q}_k = 10^{-3} \boldsymbol{I}_{3\times3} \tag{4.46}$$

$$\boldsymbol{H}_k = \begin{bmatrix} \boldsymbol{I}_{3\times3} & \boldsymbol{0}_{3\times3} \end{bmatrix} \tag{4.47}$$

$$\boldsymbol{R}_k = \sigma_G^2 \boldsymbol{I}_{3\times3} \tag{4.48}$$

$\boldsymbol{Q}_k$ was tuned empirically to place more emphasis on measurements than propagated estimates. $\boldsymbol{R}_k$ was formed using the known measurement variance for the GNSS receiver σ_G^2. The short hand OD-EKF dynamic model is shown in the two following equations where $f(\boldsymbol{r}, t)$ and $f(\boldsymbol{P}_{k-1|k-1}, t)$ represent the nonlinear functions from Eq. (4.40) - Eq. (4.42) and Eq. (4.43) respectively:

$$\dot{\boldsymbol{x}} = f(\boldsymbol{r}, t) = \begin{bmatrix} \boldsymbol{v} \\ a_x \\ a_y \\ a_z \end{bmatrix} \tag{4.49}$$

$$\dot{\boldsymbol{P}}_{k|k-1} = f(\boldsymbol{P}_{k-1|k-1}, t) \tag{4.50}$$

In this paper, the OD-EKF employs RK4 numerical methods to propagate both Eq. (4.49) and (4.50). The RK4 numerical integrator is detailed in depth in [94] and [95]. The update stage equations follow that of the regular EKF as seen in Table 4.2 lines 5 - 11, however, they must be adapted so that the OD-EKF update stage syncs with the GPS and the MEKF. This synchronization was handled by tracking the

number of completed propagation phases n_k and then performing an update phase when a full duty cycle has been completed. The full OD-EKF algorithm is presented in Table 4.2 where the main notable change compared to the general EKF is the conditionality on the update phase shown on Table 4.2 line 6.

Table 4.2: OD-EKF Algorithm

Line	Action	Equation
1	**Propagation:**	
2	Compute $\boldsymbol{F}_k$	$\boldsymbol{F}_k = \begin{bmatrix} \boldsymbol{0}_{3\times3} & \boldsymbol{I}_{3\times3} \\ \boldsymbol{\Phi}_{3\times3} & \boldsymbol{0}_{3\times3} \end{bmatrix}$
3	Propagate State	$\boldsymbol{x}_{k\|k-1} = \texttt{RK4}(f(\boldsymbol{r}, t))$
4	Propagate Covariance	$\boldsymbol{P}_{k\|k-1} = \texttt{RK4}(f(\boldsymbol{P}_{k-1\|k-1}))$
5	**Update:**	
6	GPS Check	`if` $n_k \geq 4$
7	Innovation Error	$\tilde{\boldsymbol{y}} = \boldsymbol{y} - \boldsymbol{H}_k \boldsymbol{x}_{k\|k-1}$
8	Compute Innovation Covariance	$\boldsymbol{S}_k = \boldsymbol{H}_k \boldsymbol{P}_{k\|k-1} \boldsymbol{H}_k^T + \boldsymbol{R}_k$
9	Kalman Gain	$\boldsymbol{K}_k = \boldsymbol{P}_{k\|k-1} \boldsymbol{H}_k^T \boldsymbol{S}_k^{-1}$
10	Update State	$\boldsymbol{x}_k = \boldsymbol{x}_{k\|k-1} + \boldsymbol{K}_k \tilde{\boldsymbol{y}}$
11	Update Covariance	$\boldsymbol{P}_k = (\boldsymbol{I}_{6\times6} - \boldsymbol{K}_k \boldsymbol{H}_k) \boldsymbol{P}_{k\|k-1}$
12	Reset Clock	$n_k = 0$
13	GPS Not Available	`else`
14	Pass Through State	$\boldsymbol{x}_k = \boldsymbol{x}_{k\|k-1}$
15	Pass Through Covariance	$\boldsymbol{P}_k = \boldsymbol{P}_{k\|k-1}$
16	Increment Clock	$n_k = n_k + 1$
17	end	

Chapter 5

DGSPCMG Based Attitude Control

The primary goal of the proposed ADCS is to actively control the spacecraft attitude with the DGSPCMG. Active control of the spacecraft attitude enables the advanced mission concepts discussed in this thesis including ADR and oceanographic target tracking. This chapter discusses the necessary feedback controllers, the novel steering control law for the DGSPCMG, and the system states which govern the utilization of the spacecraft actuators. All of these factors can be observed in Fig. 5.1 where a high-level control architecture for the proposed DGSPCMG-equipped CubeSat is outlined. General CMG-equipped ADCS spacecraft will follow a control flow where the attitude controller is used to determine the desired control torques to be applied to the spacecraft and the steering control law then computes the CMG gimbal rates which produce the desired control torques. The gimbal rate outputs from the steering control law are directly used to actuate the CMG gimbals.

5.1 Feedback Controllers

Sliding Mode - Boundary Layer Controller

Three-axis attitude control can be achieved through a quaternion feedback attitude controller. In this thesis, a Sliding Mode Controller (SMC) was implemented as the attitude controller for its ability to be robust against unmodeled system dynamics or disturbances. The SMC controller was derived based on the work in [96] and [97], but was adapted by adding a boundary layer approximation to remedy the chattering issue which is common for SMC controllers [98]. This section will address the four proposed components of the SMC controller including the sliding surface, reaching law, equivalent control law, and boundary layer approximation. Addressing the sliding surface, let $\boldsymbol{\lambda}$ be a positive definite and diagonal matrix so that the quaternion

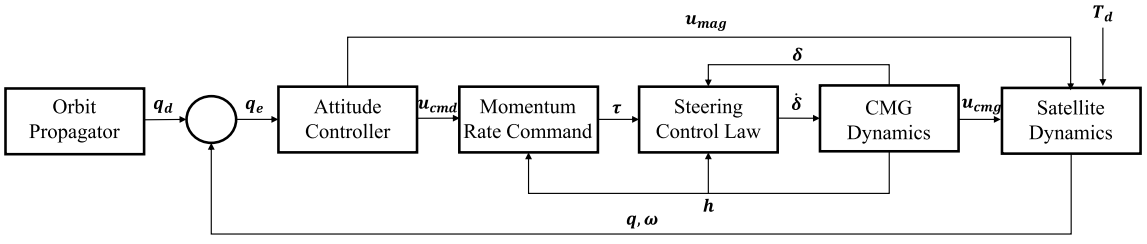

Figure 5.1: High-Level Block Diagram Representing the Control Structure of the DGSPCMG-Equipped CubeSat

feedback sliding surface may be expressed as:

$$\boldsymbol{\sigma} = \boldsymbol{\omega}_e + \boldsymbol{\lambda}\hat{\boldsymbol{q}}_e \text{sign}(q_{e_4}) \tag{5.1}$$

where $\boldsymbol{\omega}_e$ is the body rate error term, $\hat{\boldsymbol{q}}_e$ is the vector portion of the error quaternion, and q_{e_4} is the scalar portion of the error quaternion. The signum function in Eq. (5.1) is represented by "sign()". $\boldsymbol{\lambda}$ was selected as $\boldsymbol{\lambda} = \text{diag}([0.45, 0.45, 0.45]^T)$ in the present thesis by following the parameter specifications in [97]. The error quaternion can be calculated in the following expression knowing the estimated spacecraft attitude from the MEKF $\tilde{\boldsymbol{q}}$ and the desired attitude from the orbit propagator $\boldsymbol{q}_d$:

$$\begin{bmatrix} q_{e_1} \\ q_{e_2} \\ q_{e_3} \\ q_{e_4} \end{bmatrix} = \begin{bmatrix} q_{d_4} & q_{d_3} & -q_{d_2} & -q_{d_1} \\ -q_{d_3} & q_{d_4} & q_{d_1} & -q_{d_2} \\ q_{d_2} & -q_{d_1} & q_{d_4} & -q_{d_3} \\ q_{d_1} & q_{d_2} & q_{d_3} & q_{d_4} \end{bmatrix} \begin{bmatrix} \tilde{q}_1 \\ \tilde{q}_2 \\ \tilde{q}_3 \\ \tilde{q}_4 \end{bmatrix} \tag{5.2}$$

The body rate error term is computed as the difference between the MEKF estimate and the desired value where $\boldsymbol{\omega}_e = \tilde{\boldsymbol{\omega}} - \boldsymbol{\omega}_d$. A reaching law was selected to push the system states towards the sliding surface. Selection of a power-rate reaching law enables relatively fast convergence to the sliding surface while producing low chatter [99]. The present work, therefore, defines the reaching law as:

$$\boldsymbol{u}_n = -k|\boldsymbol{\sigma}|^{\alpha}\text{sign}(\boldsymbol{\sigma}) \tag{5.3}$$

In this reaching law, k and α are both tunable parameters which must be properly selected – where α must be selected within the range of $0 < \alpha < 1$. Selection of α close to 1 leads to slower reaching and an over-damped attitude response. Selection of α close to 0 leads to faster reaching with a higher level of chatter in the control effort. In this thesis a balanced controller was achieved by selecting $\alpha = \frac{3}{7}$. k generally leads to increased control emphasis on pointing error, but should be selected in some regard based on a Lyapunov stability study. The Lyapunov study for the focus controller design is provided in Appendix. C. In the oceanographic target tracking case study, these controller parameters were reevaluated to achieve desirable results for that particular application; however, the parameters provided here represent a balanced and conservative control design based on iterative testing conducted in the present thesis and [100].

The equivalent control signal is engaged once the attitude states reach the sliding surface to ensure that they stay on the sliding surface [97]. The equivalent control signal can be formed as:

$$\boldsymbol{u}_{eq} = \boldsymbol{J}\left(\left(\boldsymbol{J}\boldsymbol{\omega}_e\right)^{\times}\boldsymbol{J}\boldsymbol{\omega}_e - \boldsymbol{\lambda}\text{sign}(q_{e_4})\dot{\hat{\boldsymbol{q}}}_e\right) \tag{5.4}$$

The complete control signal for the SMC design is a sum of the reaching law and the equivalent control law where the subscript "cmd" is used to describe the command

torque signal expressed in $\mathscr{F}_{BF}$:

$$\boldsymbol{u}_{cmd} = \boldsymbol{u}_n + \boldsymbol{u}_{eq} \tag{5.5}$$

Despite some efforts made to reduce chattering to through implementation of an appropriate reaching law, more effort to remedy the SMC chattering issue should be considered to prevent non-continuous control signals being sent to the CMG. It is common for chattering present in the torque command signal to be translated into the CMG gimbal rates rapidly switching between the upper and lower gimbal rate limits [100]. For this reason, the present work modifies all aforementioned control signals in Eqs. 5.1, 5.3 and 5.4 by smoothly approximating listed signum functions with a Boundary Layer (BL) approximation. As shown in [98], introducing the BL solves the chattering issue at the expense of the satellite having a small steady-state pointing error. The BL as implemented in this thesis takes the following form where x represents the input to the approximation and Δ is a tunable parameter to adjust the approximation accuracy (also coupled with steady-state error):

$$\text{sat}(x) = \begin{cases} \text{sign}(x), & \text{if} \quad |x| > \Delta \\ \frac{1}{\Delta}x, & \text{if} \quad |x| <= \Delta \end{cases} \tag{5.6}$$

While the SMC controller can stabilize the satellite from slow spins, it is directly commanding the CMG, which cannot absorb all of the angular momentum associated with large spins like those imparted on the spacecraft during orbital injection. Therefore, the next section introduces a magnetic detumbling strategy to compensate for this rotation regime.

B-dot Magnetic Control

Magnetic detumbling provides a reliable method of damping initial body rates [101]. Unlike control with a CMG, magnetic control is always locally under-actuated because torque produced by the interaction of the magnetorquers with Earth's magnetic field is constrained to lie in a plane orthogonal to the local magnetic field [102]. For this reason, the present thesis only applies magnetic control for damping large spacecraft spins or, as presented later in this chapter, assisting in the CMG escaping from singularities. Adapting the work in [26], a proportional B-dot control law can be formed where $\dot{\boldsymbol{B}}$ represents the rate of change of the magnetic field in $\mathscr{F}_{BF}$:

$$\dot{\boldsymbol{B}} = \boldsymbol{B}^{\times}\boldsymbol{\omega} \tag{5.7}$$

The desired magnetic dipole $\boldsymbol{m}$ to be produced by the magnetic torquers becomes a proportional feedback of the B-dot term:

$$\boldsymbol{m} = -K\dot{\boldsymbol{B}} \tag{5.8}$$

where K is a control gain which must be properly selected for satisfactory performance. In this work, since the governing spacecraft physical parameters are the same

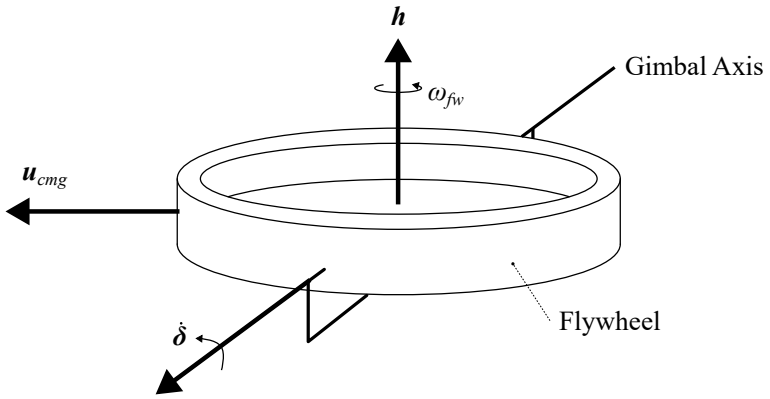

Figure 5.2: Mutual Perpendicularity of Gimbal Rate, Angular Momentum, and Torque Vectors Shown for SGCMG Example

as that used in [26], the K gain was set to 3.0E4 – a value considered ideal for a 2U CubeSat [103]. Additionally, the magnetic dipole $\boldsymbol{m}$ was saturated within the limits of ± 0.2 Am^2 so that the magnetic torquers would not exceed their maximum operating range specified in [26]. The torque applied on the spacecraft is normal to both $\boldsymbol{B}$ and $\boldsymbol{m}$ and can be expressed in $\mathscr{F}_{BF}$ as:

$$\boldsymbol{u}_{mag} = \boldsymbol{m}^{\times}\boldsymbol{B} \tag{5.9}$$

While the formulations for the feedback controllers have been presented in their general form, their implementation in the simulator typically involves the controllers acting on the estimated states or measured states including (from the MEKF) $\tilde{\boldsymbol{q}}$, $\tilde{\boldsymbol{\omega}}$, and (from the magnetometer) $\boldsymbol{B}_m$. With the feedback controllers well defined, the CMG dynamics and gimbal steering algorithms can be developed to produce the control signals discussed in this section.

5.2 DGSPCMG Dynamics

The torque produced by a CMG $\boldsymbol{u}_{cmg}$ is a function of the CMG momentum vector $\boldsymbol{h}$ and the gimbal rate vector $\dot{\boldsymbol{\delta}}$. A cross product relationship exists which states that the CMG torque is always normal to both $\boldsymbol{h}$ and $\dot{\boldsymbol{\delta}}$ as shown in Fig. 5.2. Based on this relationship, a general expression for CMG torque is:

$$\boldsymbol{u}_{cmg} = \dot{\boldsymbol{\delta}}^{\times}\boldsymbol{h} \tag{5.10}$$

In the more specific case of the DGSPCMG, $\boldsymbol{h}$ is a function of the CMG gimbal angles defined by $\boldsymbol{\delta} = [\delta_{sp}, \delta_i, \delta_o]^T$ as shown in Fig. 1.2 where δ_{sp} is the scissor-pair gimbal angle, δ_i is the inner gimbal angle, and δ_o is the outer gimbal angle. For a

CMG onboard a spacecraft, the CMG dynamics are typically expressed as [14][48]:

$$\boldsymbol{h} = \boldsymbol{h}(\boldsymbol{\delta}) \tag{5.11}$$

$$\dot{\boldsymbol{h}} + \boldsymbol{\omega}^{\times}\boldsymbol{h} = -\boldsymbol{u}_{cmg} \tag{5.12}$$

Considering Eq. (5.12), the torque produced by the CMG is a sum of the time rate of change in angular momentum but also a gyric component caused by the rotation of the spacecraft while the CMG posses a non-zero angular momentum. The $\dot{\boldsymbol{h}}$ term is typically computed through a differential equation based on the gimbal angles $\boldsymbol{\delta}$ and the gimbal rates $\dot{\boldsymbol{\delta}}$, given in [48] as:

$$\dot{\boldsymbol{h}} = \boldsymbol{A}(\boldsymbol{\delta})\dot{\boldsymbol{\delta}} \tag{5.13}$$

where:

$$\boldsymbol{A} = \frac{\partial \boldsymbol{h}}{\partial \boldsymbol{\delta}} \tag{5.14}$$

The Jacobian matrix $\boldsymbol{A}$ is a $3 \times n$ matrix which describes the state of the CMG. In many cases, the CMG cluster design may employ $n \neq 3$ gimbals, and the Jacobian matrix would not be square. The DGSPCMG, however, has 3 gimbals which leads to a square Jacobian matrix.

Referring to Fig. 1.2, the scissor-pair gimbal δ_{sp} rotates the two flywheels in equal but opposite directions to modify the magnitude of the DGSPCMG momentum vector. The inner and outer gimbal angles δ_i and δ_o change the direction of the CMG angular momentum vector. Since the flywheels in the DGSPCMG rotate with constant angular velocity, the magnitude of the CMG angular momentum is entirely a function of the scissor-pair angle and the momentum possessed by the flywheels. Thus, the current angular momentum of the CMG can be described by $H = 2H_w \sin\delta_{sp}$, where $H_w = I_{fw}\omega_{fw}$ represents the angular momentum of an individual flywheel. I_{fw} denotes the inertia of the flywheel calculated about its respective spin axis, and ω_{fw} represents the constant angular velocity of the flywheel. Correspondingly, the angular momentum vector based on the inner and outer gimbals and expressed in $\mathscr{F}_{BF}$ is:

$$\boldsymbol{h} = 2H_w \sin\delta_{sp} \begin{bmatrix} \sin(\delta_i) \\ \cos(\delta_i)\sin(\delta_o) \\ \cos(\delta_i)\cos(\delta_o) \end{bmatrix} \tag{5.15}$$

By differentiating Eq. (5.15) as shown by Eq. (5.14), the DGSPCMG Jacobian matrix $\boldsymbol{A}$ is formed where s and c represent sin and cos trigonometric functions:

$$\dot{\boldsymbol{h}} = 2H_w \sin\delta_{sp} \begin{bmatrix} c_{sp}s_i & s_{sp}c_i & 0 \\ c_{sp}c_i s_o & -s_{sp}s_i s_o & s_{sp}c_i c_o \\ c_{sp}c_i c_o & -s_{sp}s_i c_o & -s_{sp}c_i s_o \end{bmatrix} = \boldsymbol{A}\dot{\boldsymbol{\delta}} \tag{5.16}$$

5.2.1 DGSPCMG Singularities

CMGs suffer from a complication known as a singularity where the CMG loses the ability to produce torque about all axes [104][48]. Any CMG cluster design which has less than 6 gimbals will have singular states which complicate its control [105]. Singularities have a number of classifications. Should the total CMG momentum vector from all n CMGs lie on the feasible angular momentum envelope, the singularity is external. If the CMG cluster encounters a singularity and the total momentum vector lies within the feasible angular momentum envelope the singularity is internal [48]. Internal singularities have additional sub classifications into both hyperbolic and elliptic singularities. Typically, hyperbolic singularities are "passable" because the CMG gimbals can be actuated (through a maneuver known as null motion) out of the singularity without producing torque on the spacecraft. For elliptic "impassable" singularities the null motion cannot be applied [48][106]. For a given CMG array of n CMGs, the singularities it experiences will largely be specific to that CMG configuration. Avoiding or escaping from the singular conditions of a CMG has garnered the attention of many researchers as the singularities have both physical and mathematical interpretations which should be considered when designing a CMG gimbal steering control law (SCL) to cope with these singularities.

As briefly discussed, the DGSPCMG design greatly improves the manageability of the singular states by the fact that:

1. The feasible angular momentum surface is spherical.

2. The internal singularities are only of the hyperbolic type.

3. The internal singularities only exist along the δ_o gimbal axis or when $\delta_{sp} = 0$.

Fig. 5.3 provides a visual representation of the DGSPCMG feasible angular momentum surface and internal singularity locations shown inside this surface. A typical convention for the DGSPCMG design is to have the outer gimbal axis aligned with the $\mathcal{F}_{BF}$ x-axis and the inner gimbal axis aligned with the y-axis. Following this convention, it is clear that the internal singularity location is along the x-axis and at the origin.

The internal singularity line shown in Fig. 5.3 arises from the case that if $\delta_{sp} \neq \pm\frac{\pi}{2}$ and $\delta_i = \pm\frac{\pi}{2}$, the angular momentum vector $\boldsymbol{h}$ will lie on the δ_o gimbal axis. In this case any movement of δ_o will not result in a torque. More intuitively, for the internal singularity of $\delta_{sp} = 0$, the DGSPCMG possess no angular momentum and movement of δ_i or δ_o will not result in any torque (null motion). Finally, if $\delta_{sp} = \pm\frac{\pi}{2}$ then the magnitude of Eq. (5.15) is maximized and $\boldsymbol{h}$ will lie on the external singularity surface of Fig. 5.3. The singularities associated with δ_{sp} are further depicted in Fig. 5.4 where it is apparent in the leftmost schematic that the angular momentum vector is 0 and lies at the origin of Fig. 5.3. In the rightmost schematic of Fig. 5.4, $\boldsymbol{h}$ is maximized and would lie on the spherical surface in Fig. 5.3. Fig. 5.5 shows a rendering of the entire DGSPCMG in the aforementioned singularity states where the arrows originating from the flywheels (red) represent the angular momentum vector

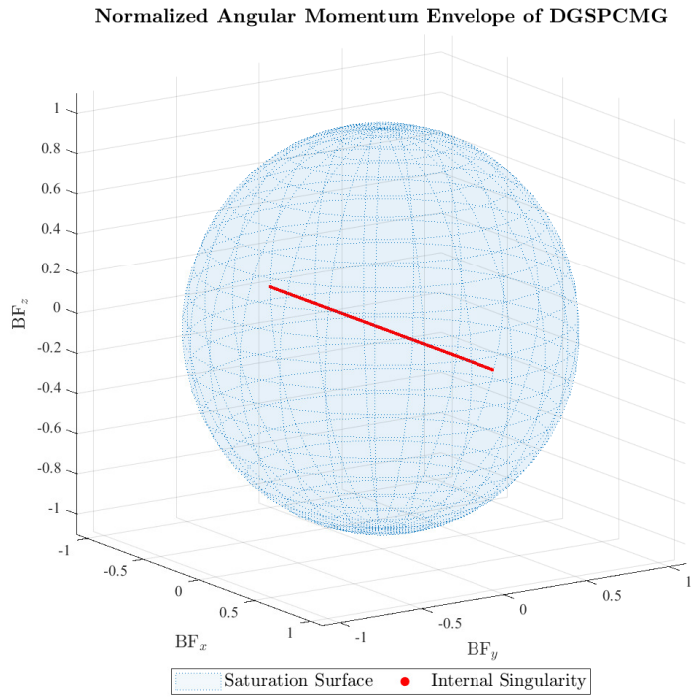

Figure 5.3: DGSPCMG Angular Momentum Envelope with Internal Singularity Case Shown.

of the individual flywheels. The gimbal stepper motors (black) are shown connected to the DGSPCMG chassis in Fig. 5.5.

While the singularities have clear physical interpretations, there are also mathematical interpretations which should be considered. Referring to Eq. (5.16), the DGSPCMG system falls into a singularity if $\text{rank}(\boldsymbol{A}) < 3$. $\text{rank}(\boldsymbol{A}) < 3$ implies that $\det(\boldsymbol{A}) = 0$ and the Jacobian matrix is singular. The analytical solution to the determinant of $\boldsymbol{A}$ is [14]:

$$\det(\boldsymbol{A}) = 2H_w \cos(\delta_{sp}) \sin^2(\delta_{sp}) \cos(\delta_i) = 0 \tag{5.17}$$

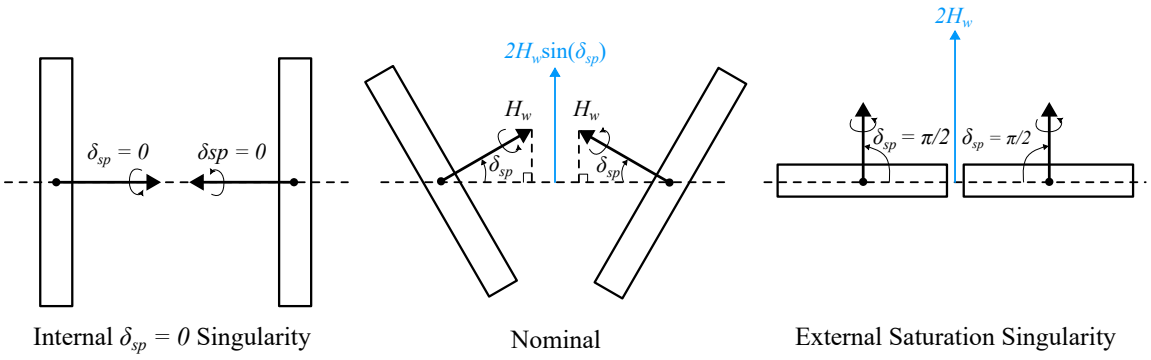

Figure 5.4: Possible DGSPCMG Configurations Based on δ_{sp} Gimbal Angle

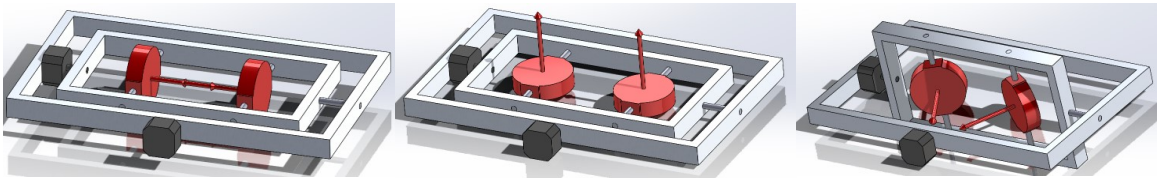

Figure 5.5: Rendering of DGSPCMG Geometry For Discussed Singularity Configurations

A gimbal angle vector $\boldsymbol{\delta}$ that contains any of the aforementioned singularity cases for δ_{sp} or δ_i would satisfy Eq. (5.17) and the DGSPCMG would be experiencing a singularity. δ_o does not appear in Eq. (5.17) which implies that there are no singular conditions related to δ_o. Numerically, if $\boldsymbol{A}$ is singular its inverse does not exist and, as shown in the following sections, it becomes impossible to compute further controlling gimbal rates with the Jacobian matrix. It is, therefore, critically important for the SCL to autonomously avoid these singular conditions to ensure proper function of the ADCS.

5.3 The DGSPCMG Steering Control Law

Recently Kojima *et al.* (2020) presented the DGSPCMG steering control law. The Kojima SCL was shown to be effective at escaping all singular states under ideal conditions. In addition, the SCL does not compute optimization problems to determine the gimbal rates as done in examples such as [107][108][109]. By nature of the DGSPCMG having 3 gimbals, pseudoinverse calculations of the Jacobian matrix are also avoided. By avoiding these two somewhat cumbersome calculations, it becomes more likely that computation of the gimbal rates will not violate the sampling rate as discussed in [110] when computed on basic flight computers. Computational efficiency is particularly valuable when considering that many CubeSats apply low-power computers for their missions [111].

While the Kojima SCL was demonstrated to be effective under ideal conditions, further research was required to avoid singularities effectively when the DGSPCMG was used in the orbital environment. In particular, further development of the SCL was required to identify and handle the case where orbital disturbances push the CMG into a singularity, but the spacecraft is already in the desired attitude. Some authors have proposed hybrid CMG models which supplement the CMG with an additional actuator to compensate for disturbances [20][112]. One such proposal involved supplementing the CMG with RWs [112]; however, such a design is only practical for large satellites. A different method using magnetic torquers and a pyramid array CMG was proposed in [20] where the magnetic torques are applied after each rest-to-rest attitude maneuver to restore the optimal CMG gimbal angles.

It is clear that a desirable DGSPCMG control law should (1) be computationally

efficient, (2) enable singularity escape when subjected to long-term orbital disturbances, and (3) minimally impact the science objectives of the mission when performing singularity escape. To accomplish these tasks, a novel extension of the Kojima DGSPCMG control law was developed in this thesis. The proposed extended control law commands magnetic torques through CMG momentum state feedback to restore the CMG momentum state to a desired state. The extended control law manages the CMG momentum while still maintaining the desired spacecraft attitude to limit impacts on the main mission objectives. In addition, the proposed SCL has the ability to select between gimbal compensation with magnetic torques or only the use of CMG steering to escape from singularities. First, the Kojima control law is presented in the following subsections as the foundation for further work, then the novel extension is developed to enable the use of the DGSPCMG on orbit.

5.3.1 Basic Gimbal Steering

When the CMG is not in a singularity, the basic inverse steering control law may be applied. Addressing Fig. 5.1, the attitude controller torque command signal $\boldsymbol{u}_{cmd}$ is first converted to a momentum rate command $\boldsymbol{\tau}$ by applying the relationship:

$$\boldsymbol{\tau} = -\boldsymbol{u}_{cmd} - \boldsymbol{\omega}^{\times}\boldsymbol{h} \tag{5.18}$$

This momentum rate command becomes the input for the SCL, which for the no singularities case, will compute the basic inverse law to yield the commanded gimbal rates $\dot{\boldsymbol{\delta}}_c$ as:

$$\dot{\boldsymbol{\delta}}_c = \boldsymbol{A}^{-1}\boldsymbol{\tau} \tag{5.19}$$

5.3.2 Internal Singularity Recovery

It was discussed in Section. 5.2.1 that steering the DGSPCMG through null motion can be used to escape from the $\delta_{sp} = 0$ singularity. To steer the CMG through a null motion, a set of gimbal rates $\dot{\boldsymbol{\delta}}$ must be obtained where the angular momentum state of the CMG does not change from being net zero. The net zero constraint implies that the momentum rate command $\boldsymbol{\tau}$ satisfies the following equation and ensures that Eq. (5.13) is valid [14]:

$$\boldsymbol{\tau} = \boldsymbol{A}\boldsymbol{n} = 0 \tag{5.20}$$

The internal singularity related to the case that $\delta_i = \pm\frac{\pi}{2}$ with $|\delta_{sp}| < \frac{\pi}{2}$ must also be considered; however, this singularity is justifiably handled by mechanically limiting the range of δ_i within $\pm\frac{\pi}{2}$ [14]. In the simulator, this mechanical constraint was achieved by saturating the δ_i gimbal to bounds of $\pm\frac{\pi}{2}$. As a result of placing the δ_i constraint, the null motion control law must only be developed for the $\delta_{sp} = 0$ singularity. An effective condition for the execution of the null motion is to execute the null motion if $|\sin\delta_{sp}| < \epsilon_1 (\epsilon_1 \approx 0)$ where ϵ_1 is selected to conform to the resolution of the encoders monitoring the gimbal angles. The null motion is executed by orienting the CMG so that subsequent output torques created by gimballing the scissor-pair are along the Euler axis corresponding to the desired attitude quaternion. That is, if

δ_{sp} is gimballed to move it out of the $\delta_{sp} = 0$ singularity, the torque created slews the satellite towards the desired attitude. The target Euler axis can be extracted from the definition provided in Eq. (3.7) as $\boldsymbol{e}_c = [e_{c_1}, e_{c_2}, e_{c_3}]^T$ provided the desired quaternion $\boldsymbol{q}_d$ is available. The output torque direction of the scissor-pair may, therefore, be related to the target Euler axis by:

$$\boldsymbol{e_c} = -\text{sign}(\dot{\delta}_{sp}) \begin{bmatrix} \sin(\delta_i) \\ \cos(\delta_i)\sin(\delta_o) \\ \cos(\delta_i)\cos(\delta_o) \end{bmatrix} \tag{5.21}$$

In order to direct the scissor-pair output torque direction to be inline with the Euler axis, Eq. (5.21) can be solved with respect to δ_i and δ_o to obtain a set of target null motion gimbal angles $\hat{\delta}_i$ and $\hat{\delta}_o$:

$$\hat{\delta}_i = \sin^{-1}(\text{sign}(e_{c_3})e_{c_1}) \tag{5.22}$$

$$\hat{\delta}_o = \text{atan2}(\text{sign}(e_{c_3})e_{c_2}, \text{sign}(e_{c_3})e_{c_3}) \tag{5.23}$$

A null motion SCL may then be developed which aims to drive the gimbal angles towards the target gimbal angles such that the output torque of the scissor-pair is along the Euler axis as desired. Correspondingly, let k_n represent a null motion control gain which must be properly selected. The resulting gimbal steering control law for the null motion is expressed as [14]:

$$\dot{\boldsymbol{\delta}}_{\boldsymbol{c}} = k_n \begin{bmatrix} 0 \\ \hat{\delta}_i - \delta_i \\ \hat{\delta}_o - \delta_o \end{bmatrix} \tag{5.24}$$

Nominal CMG steering may be resumed when the norm of $\dot{\boldsymbol{\delta}}_{\boldsymbol{c}}$ is near zero, a scenario that indicates that the actual CMG gimbal angles are near the target set of gimbal angles. A tolerance value ϵ_3 can be set so that, if $|\dot{\boldsymbol{\delta}}_{\boldsymbol{c}}| < \epsilon_3$, then a specific SCL known as the partial inverse law may be engaged to ensure that the switch from null motion to basic inverse steering is smooth. The partial inverse steering law commands a gimbal rate to the scissor-pair specifically as:

$$\dot{\delta}_{csp} = \hat{\boldsymbol{A}}_{sp}^T \boldsymbol{\tau} \tag{5.25}$$

where by following [14], $\hat{\boldsymbol{A}}_{sp}$ may be defined as:

$$\hat{\boldsymbol{A}}_{sp} = \frac{1}{2H_w} \begin{bmatrix} \sin(\delta_i) \\ \cos(\delta_i)\sin(\delta_o) \\ \cos(\delta_i)\cos(\delta_o) \end{bmatrix} \tag{5.26}$$

Steering through the partial inverse steering law completes recovery from the $\delta_{sp} = 0$ singularity and ends the null motion.

5.3.3 External Singularity Recovery

In the case of recovering from the $\delta_{sp} = \pm\frac{\pi}{2}$ external singularity, null motion is no longer an option because the CMG possesses a net angular momentum. A point of concern with the $\delta_{sp} = \pm\frac{\pi}{2}$ singularity is that moving the scissor-pair through $\delta_{sp} = \frac{\pi}{2}$ towards $\delta_{sp} = \pi$ has the same effect on the momentum state as moving towards $\delta_{sp} = 0$. Both cases reduce the magnitude of angular momentum stored in the CMG. The latter of the two options, however, is more desirable because it removes the requirement for slip rings in the design of the DGSPCMG. To accommodate this design consideration, a constraint on δ_{sp} is assumed such that $|\delta_{sp}| \leq \frac{\pi}{2}$.

Escape from the $\delta_{sp} = \pm\frac{\pi}{2}$ singularity requires ceasing gimballing of the scissor-pair if δ_{sp} approaches a threshold value of ϵ_2. Should $\cos(\delta_{sp}) < \epsilon_2$ where ϵ_2 is a positive threshold value that satisfies $\epsilon_2 \approx 0$, then scissor-pair gimbal motion is stopped to allow the satellite to inertially slew towards the target attitude. Once the satellite nears the target attitude, the gimbal motion may resume in a manner where the commanded gimbal rate reduces δ_{sp} while slowing body rates and stabilizing the satellite at the target attitude. That is, the saturation singularity recovery SCL involves nominally steering the other two gimbals, while steering the scissor-pair according to the following control law, where k_r is a control gain to be selected properly [14]:

$$\dot{\delta}_{csp} = \begin{cases} 0 & \text{if} \quad \boldsymbol{h} \cdot \boldsymbol{\tau} \geq 0 \\ -k_r \text{sign}(\delta_{sp}) & \text{if} \quad \boldsymbol{h} \cdot \boldsymbol{\tau} < 0 \end{cases} \tag{5.27}$$

This method of singularity escape is effective for rest-to-rest attitude maneuvers in isolated tests; however, in a practical long-term orbital application it does not guarantee singularity recovery [100]. To guarantee escape from the external singularity in orbital applications, it is necessary to develop additional control logic. The following sections introduce the novel extended DGSPCMG control law which robustly escapes the saturation singularity by applying gimbal compensation with magnetic torquers.

5.4 Novel Extended DGSPCMG Steering Control Law for Gimbal Compensation

The Novel Extended DGSPCMG Steering Control Law developed in this section allows for selective CMG steering dependent on when singularity escape through gimbal compensation should be used, or when singularity escape is viable without the use of gimbal compensation. Through this section, both terms of "gimbal compensation" and "momentum management" may be used, with both referring to the case where magnetic torquers produce a torque that allows the CMG gimbals to be actuated without disturbing the attitude of the spacecraft. "Momentum management" may be used more frequently when singularity escape is most easily explained by managing the momentum stored by the CMG. Referring back to Fig. 5.1, this section directly discusses the $\boldsymbol{u}_{mag}$ magnetic torque term which is fed forward from the attitude controller to the satellite dynamics. Within this term is the compensatory torques which allow singularity escape in the DGSPCMG.

To justify the use of compensatory magnetic torques, the relevant scenarios where gimbal compensation could be required on orbit should be considered.

Case 1: Consider an orbital scenario where the spacecraft is tumbling (spinning uncontrolled) such that the CMG scissor-pair enters the external singularity by attempting to absorb the momentum associated with the spin. Fundamentally, to reduce the spin the SCL and attitude controller would, in general, be commanding an increase in the scissor-pair angle, thereby increasing CMG momentum and reducing momentum associated with the spacecraft spin. In an event where the external singularity is reached before completely nulling the body rate, the SCL from Section. 5.3.3 will allow inertial slewing until the target attitude is reached. The inertial slew method, however, is not guaranteed to reach the target attitude in this case because the spacecraft may not be on an attitude trajectory that ensures the scissor-pair may be desaturated from the singularity in finite-time [100]. 3-axis control of the spacecraft would, therefore, be lost.

Case 2: Consider a long term orbital mission where the disturbances presented in Section. 3.4.2 must be rejected by steering the CMG via the basic inverse steering law. In an event where the sum of these disturbances creates an angular impulse which leads to the reduction of δ_{sp} towards $\delta_{sp} = 0$, then the SCL will attempt a null motion. An issue may arise in this event because if the spacecraft is already close to the desired attitude, the execution of a null motion may only moderately increase δ_{sp}. A minor or moderate increase of δ_{sp} may lead to repetitive null motions being executed resulting in a loss of accurate attitude control [100]. Conversely, if the disturbances push the scissor-pair towards the $\delta_{sp} = \pm\frac{\pi}{2}$ singularity then, as discussed in Case 1,

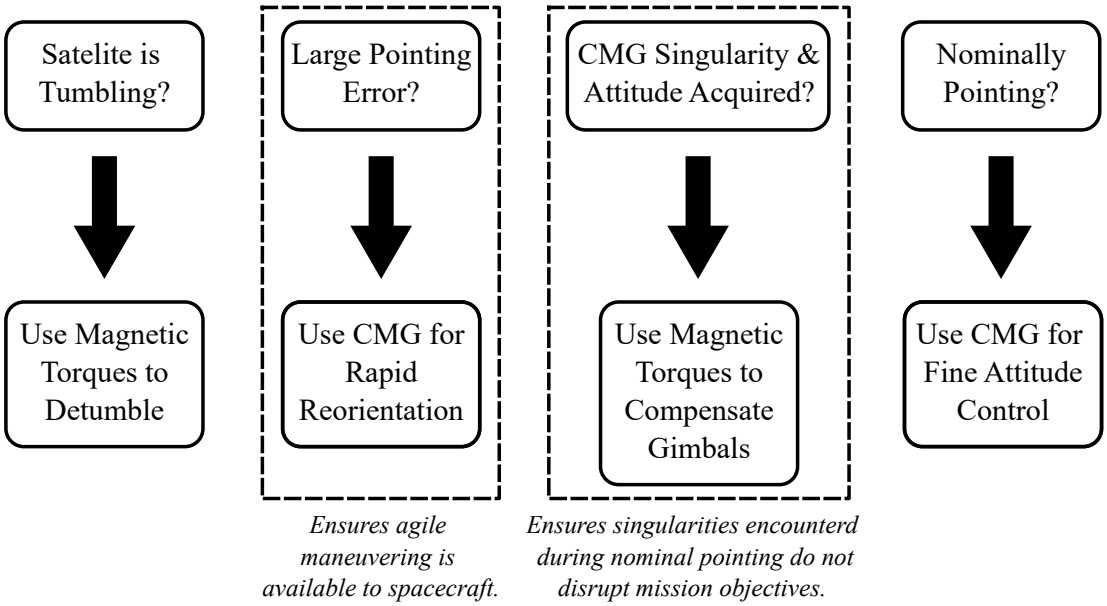

Figure 5.6: High-Level Overview of How the Extended SCL Handles Various Systems States

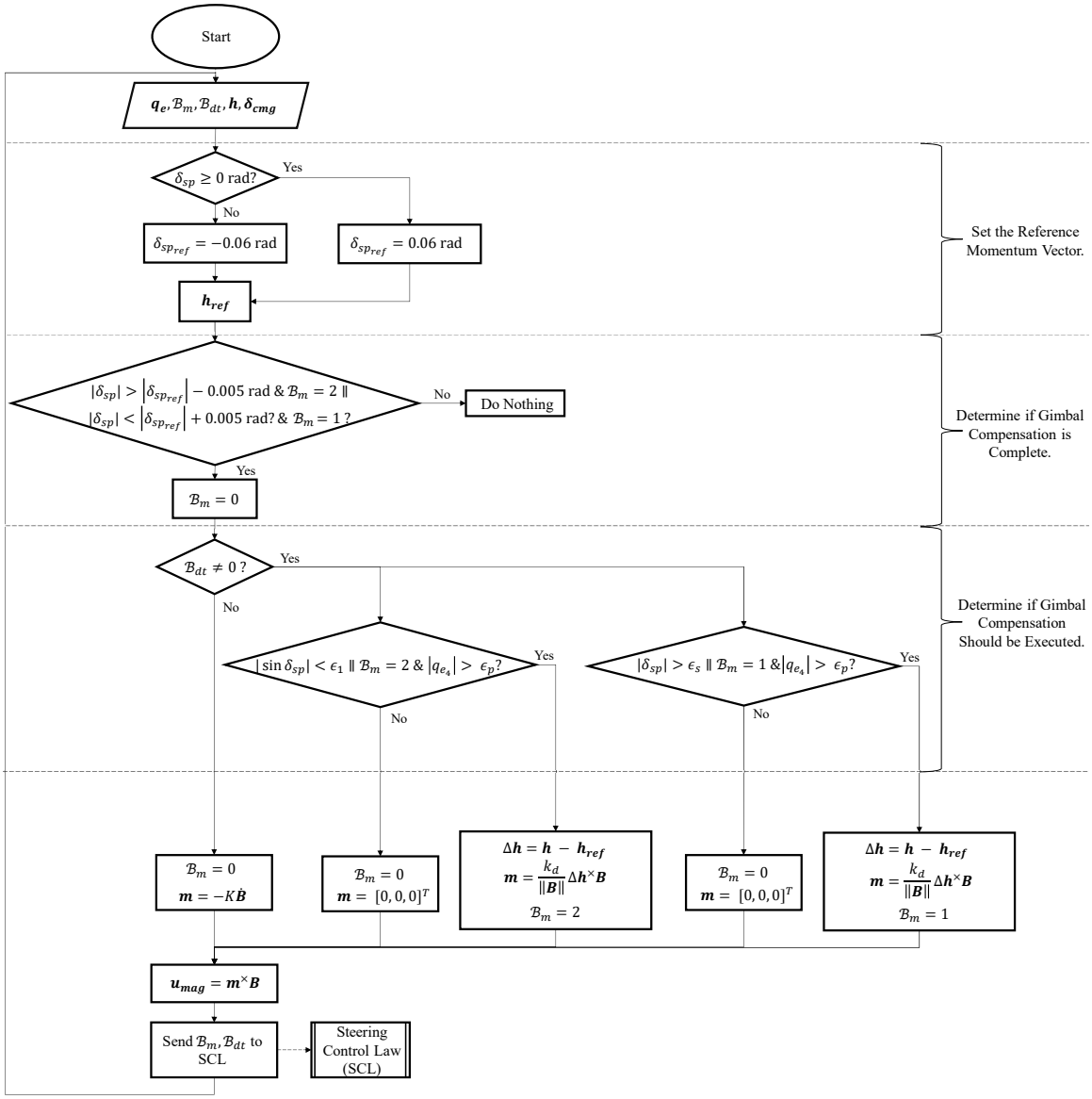

Figure 5.7: Logic Flow Down Chart of Extended DGSPCMG Steering Control Law

gimbal steering will be stopped and only resumed if the satellite is perturbed into an attitude where the reduction of δ_{sp} leads to the acquisition of the desired attitude [100].

In both of the aforementioned cases, attitude control complications related to the CMG being trapped in a singularity can be avoided by managing the DGSPCMG momentum vector with a supplementary actuator. How and when this momentum vector is managed, is dependent on the state of both the satellite and the CMG as shown by the high-level description of the Extended SCL in Fig. 5.6. The details of the Extended DGSPCMG Steering Control Law are presented in Fig. 5.7 to solve the attitude control problems by employing magnetic torquers as the supplementary actuator.

5.4.1 Magnetic Detumbling

As discussed in Case 1, CMG steering should only be switched on after the spacecraft has been successfully detumbled. The control complication related to Case 1 can, therefore, be solved by switching on CMG when the norm of $\boldsymbol{\omega}$ is less than a tolerance threshold ϵ_{dt}. The detumbling control laws which govern the magnetic torquers follow those presented in Section. 5.1 prior to the satellite meeting the tolerance threshold ϵ_{dt} [100].

5.4.2 Momentum Restoration via Momentum Feedback Control

To maintain attitude pointing, the DGSPCMG must hold a net angular momentum corresponding to a scissor-pair angle of $\delta_{sp} \neq 0$. In an ideal scenario without orbital disturbances, the SCL will steer the gimbals in a manner where the net angular momentum is above zero. Practically, however, it is possible for the DGSPCMG to approach $\delta_{sp} = 0$ or $\delta_{sp} = \pm\frac{\pi}{2}$ singularities when exposed to orbital disturbance rejection. The momentum stored by the DGSPCMG can be maintained to a desirable net positive state through an angular momentum feedback loop with magnetic torquers as shown in Fig. 5.1.

Much work has been conducted, particularly on reaction wheel systems, to handle momentum saturation of the actuator. Early studies such as that in [113] handle nominal control separate from desaturation. More modern methods attempt to handle both simultaneously [19]. In the case of highly-agile maneuvering with a DGSPCMG, the ability to manage the stored momentum while maintaining attitude stability is a desirable control characteristic for modern missions.

Attitude control with a momentum feedback controller has been recently discussed in [114]. In the case of [114], the angular momentum feedback controller is used to control the spin axis of a spin stabilized spacecraft. The controller was adapted in this thesis to instead restore the momentum state of the DGSPCMG to desirable values. Fundamentally, the adapted momentum feedback loop will command the magnetic torquers to produce torques that, through the CMG rejecting these torques, cause the CMG momentum vector to align with the desired vector. The momentum feedback loop related to the magnetic field vector is defined by:

$$\boldsymbol{m} = \frac{k_d}{||\boldsymbol{B}||^2}\Delta\boldsymbol{h}^{\times}\boldsymbol{B} \tag{5.28}$$

where k_d is a momentum dumping control gain and $\Delta\boldsymbol{h}$ is the difference between the current and reference momentum vector expressed by:

$$\Delta\boldsymbol{h} = \boldsymbol{h} - \boldsymbol{h_{ref}} \tag{5.29}$$

The $\boldsymbol{h}_{ref}$ vector is, therefore, the desired momentum state of the CMG corresponding to a desired gimbal state which is away from all singularities. The reference

momentum vector can be obtained in the following relationship:

$$\boldsymbol{h_{ref}} = 2I_{fw}\omega_{fw}\sin(\delta_{sp_{ref}}) \begin{bmatrix} \sin(\delta_i) \\ \cos(\delta_i)\sin(\delta_o) \\ \cos(\delta_i)\cos(\delta_o) \end{bmatrix} \tag{5.30}$$

For the DGSPCMG actuator, the magnitude of the stored momentum vector is defined by δ_{sp} with the direction of the vector defined by δ_i and δ_o as shown in Eq. (5.15). If the reference momentum vector $\boldsymbol{h}_{ref}$ is selected to be in a direction defined by the current δ_i and δ_o angles, but with a magnitude defined by $|\delta_{sp_{ref}}|>|\delta_{sp}|$, the CMG momentum state can be increased by pushing the δ_{sp} angle away from the $\delta_{sp} = 0$ singularity. Should $|\delta_{sp_{ref}}|<|\delta_{sp}|$ be chosen instead, the CMG momentum can be decreased such as to push δ_{sp} away from the $\delta_{sp} = \pm\frac{\pi}{2}$ singularity. Steering the DGSPCMG gimbals using the basic inverse steering law from Eq. (5.19) while the momentum feedback controller commands the magnetic torquers to produce compensatory torques, leads to the scissor-pair gimbal moving towards $\delta_{sp_{ref}}$ and thereby the desired reference momentum state $\boldsymbol{h}_{ref}$. A subtlety of the proposed momentum feedback controller combined with the DGSPCMG is that through proper selection of $\boldsymbol{h}_{ref}$ the CMG only needs to gimbal δ_{sp} during momentum management [100]. As a result of the DGSPCMG still possessing net angular momentum during momentum management, the other gimbals consisting of δ_i and δ_o can still be used to maintain the target attitude at the same time.

5.4.3 Gimbal Compensation Logic for the $\delta_{sp} = 0$ Singularity

To avoid the $\delta_{sp} = 0$ singularity a specific set of logic is required to effectively escape the singular case. To prevent pushing the scissor-pair directly through $\delta_{sp} = 0$, $\boldsymbol{h}_{ref}$ should be chosen based on if the scissor-pair angle has approached $\delta_{sp} = 0$ from $\delta_{sp} > 0$ or $\delta_{sp} < 0$. Following Fig. 5.7, the first step of internal singularity escape is to set the reference scissor-pair angle dependent on the gimbal approach direction as shown by the present author's original paper in [100]:

$$\delta_{sp_{ref}} = \begin{cases} \delta_{sp_{ref}} & \text{if} \quad \delta_{sp} > 0 \\ -\delta_{sp_{ref}} & \text{if} \quad \delta_{sp} < 0 \end{cases} \tag{5.31}$$

In terms of selecting between gimbal compensation or null motion, a subsequent set of constraints must be considered. Null motion is most effective for singularity escape when the spacecraft attitude is relatively far from the desired attitude. The predominant reason for this particular efficacy is because null motion can be executed quickly and followed by large control torques being generated by the CMG. In comparison, the speed of momentum restoration is constrained by the proportionally small torques produced by the magnetic torquers and, on top of this constraint, attitude acquisition may still be required after singularity escape [100]. In addition, when the spacecraft is close to the desired attitude, it is desirable to avoid repetitive null motions all with minor increases in δ_{sp} as discussed in Case 2. For these listed reasons,

momentum management should only be executed when the satellite is already at the desired attitude and the scissor-pair is approaching a singularity.

The satellite can be considered to be at the desired attitude when the scalar portion of the error quaternion $q_{e_4} = 1$ based on the unit norm constraint placed on all quaternions. Considering the value of the scalar component of q_{e_4} when the spacecraft is near the desired attitude, a condition for acquired attitude may be defined for the case that q_{e_4} is greater than a positive threshold ϵ_p where $\epsilon_p \approx 1$. To accommodate the quaternion duality issue, where two quaternions can represent the same attitude, the condition for acquired attitude is more generally represented in this thesis as:

$$|q_{e_4}| > \epsilon_p \tag{5.32}$$

In the event that the condition shown in Eq. (5.32) is satisfied and $|\sin \delta_{sp}| < \epsilon_1$ (the previously-defined condition for the $\delta_{sp} = 0$ singularity), then momentum management may be executed following Fig. 5.7. Momentum management should be ended when the δ_{sp} angle is near $\delta_{sp_{ref}}$. Because, the momentum feedback controller is a proportional controller, the scissor-pair angle will asymptotically approach the reference value. To account for the steady state offset, an acceptable δ_{sp} angle must be selected which is larger than the $\delta_{sp_{ref}}$ angle so that momentum management is ended in finite time. The acceptable value may need to be selected through trial and error because of both the gain k_d and saturation limit of the magnetic torquers having meaningful effects on the asymptotic approach of δ_{sp}.

To differentiate between CMG steering methods, flags can be specified which dictate how the CMG will be steered for the various proposed methods. Defining $\mathscr{B}_{dt}$ as the flag signaling completion of the detumble phase, if $\mathscr{B}_{dt} = 0$, then detumbling is in progress and the CMG is inactive. In addition, let $\mathscr{B}_m$ represent the flag signaling the state of the momentum management. Should $\mathscr{B}_m \neq 0$ then the steering law is set to the basic inverse law described in (5.19) and the momentum management maneuver will be active until $|\delta_{sp}| \approx |\delta_{sp_{ref}}|$ [100]. The produced magnetic dipole will be dictated by 5.28 as shown in Fig. 5.7.

5.4.4 Gimbal Compensation Logic for the $\delta_{sp} = \pm\frac{\pi}{2}$ Saturation Singularity

Functionally, a similar logic flow as done for $\delta_{sp} = 0$ was implemented for executing gimbal compensation to escape $\delta_{sp} = \pm\frac{\pi}{2}$. Structurally, the same check is completed for the singularity approach direction as shown in Eq. (5.31) but the condition for execution is modified. If the CMG is allowed to fully saturate to $\delta_{sp} = \pm\frac{\pi}{2}$ before execution of momentum management, then it becomes possible for the CMG to encounter a case where a large attitude reorientation is commanded which would saturate the δ_{sp} angle. In this scenario there may not be any momentum head room (gimbal range from the current δ_{sp} angle to the saturation value) to allow a large attitude reorientation to transpire. Therefore, it is more desirable to execute frequent shorter momentum management maneuvers to keep $\delta_{sp} \approx 0$ than it is to execute fewer larger maneuvers where δ_{sp} is allowed to fully saturate. By this definition, trial and

error was used to select a value $\epsilon_s = 0.4$ rad as the saturation threshold for executing the momentum management maneuver. Therefore, should the condition shown in Eq. (5.32) be met and $|\delta_{sp}| > \epsilon_s$ (the previously-defined condition for the $\delta_{sp} = \pm\frac{\pi}{2}$ external singularity), the momentum management maneuver may be executed. In this scenario we must select a $\delta_{sp_{ref}}$ value which is less than ϵ_s but greater than ϵ_1 such that the CMG is not steered directly into the internal singularity after gimbal compensation. A set of important parameters used to drive the Extended DGSPCMG control law is provided in Table 5.1. Additionally, the actuator limitations related to the maximum CMG gimbal rate $\dot{\delta}_{max}$ and the maximum magnetic torquer dipole moment m_{max} are provided in Table 5.1. These parameters were used to produce the simulations shown throughout this thesis.

Table 5.1: Key Selected Parameters For Extended DGSPCMG Steering Control Law

Extended SCL Parameters

Parameter	**Value and Units**
$\epsilon_1, \epsilon_2, \epsilon_3, \epsilon_s$	0.004, 0.004, 0.04, 0.4 rad
ϵ_p	0.99 (unitless)
ϵ_{dt}	0.1 rad/s
k_n, k_r, k_d	10, 1, 0.02 (1/s)
$\delta_{sp_{ref}}$	0.06 rad
$\dot{\delta}_{max}$	1 rad/s
m_{max}	0.2 Am^2

5.5 Operational Modes

While previous sections have dealt with attitude determination, or how the CMG will be steered for various proposed maneuvers, this section details how the DGSPCMG-equipped ADCS should be operated as a whole at different mission stages. The operational modes for the ADCS seek to ensure that only specific components of the ADCS are operating at specific times. In this thesis, the system state control law which governs how the ADCS operates is more formally referred to as the actuator governor. The complete actuator governor is provided in Fig. 5.8. The symbols $\mathscr{B}_{cmg}$ and $\mathscr{B}_{mag}$ shown in Fig. 5.8 represent the state of the CMG and magnetic torquers respectively. A state equal to 0 (false) indicates that the actuator is not being used or cannot actuate. As previously defined, $\mathscr{B}_{dt}$ is a flag used to indicate the completion of the detumbling phase and $\mathscr{B}_m$ indicates if the Extended DGSPCMG SCL is performing momentum management. For further clarity, the reader is referred to Section. 3.4.1 where ℓ is defined as a parameter for the intensity of sunlight.

The following set of on-orbit cases are addressed by the implementation of the actuator governor:

1. The satellite is tumbling with a rate $|\boldsymbol{\omega}|> 0.05$ rad/s.

   - Use magnetic torquers to detumble.
   - DGSPCMG is inactive to prevent saturation.

2. The satellite is tumbling with a rate $|\boldsymbol{\omega}|< 0.05$ rad/s.

   - Set magnetic torquers to hibernate and wait for momentum management command.
   - DGSPCMG is active and used for fine pointing control.

3. The satellite is entering eclipse or is in eclipse having not completed detumbling.

   - All actuators are inactive.
   - $\mathscr{B}_{dt}$ is reset to zero so that residual high rates are damped by the magnetic torquers on exit from eclipse.

4. The satellite has completed detumbling, is entering or in eclipse but was performing momentum management.

   - All actuators are inactive.
   - $\mathscr{B}_{dt}$ is maintained at 1 so that the satellite prioritizes CMG control upon exit from eclipse.

The final component relating to operational modes is the feedforward torque related to momentum management. Momentum management executed by the Extended SCL is most efficiently performed when the attitude controller commands the opposite torque from that produced by the magnetic torquers. As a result of the local magnetic field being known to reasonable levels of accuracy from the magnetometer, the output torques from the magnetic torquers are also well known. In the case that momentum management is being performed, $\mathscr{B}_m \geq 1$ which indicates that the output torque signal of the attitude controller shall be switched to:

$$\boldsymbol{u}_{cmd} = \boldsymbol{u}_n + \boldsymbol{u}_{eq} + \boldsymbol{u}_{ff} \tag{5.33}$$

where the feed forward term $\boldsymbol{u}_{ff}$ is defined such that $\boldsymbol{u}_{ff} = -\boldsymbol{u}_{mag}$. By implementing this operational change, the downstream DGSPCMG is commanded to output a torque which directly compensates for the momentum management magnetic torque.

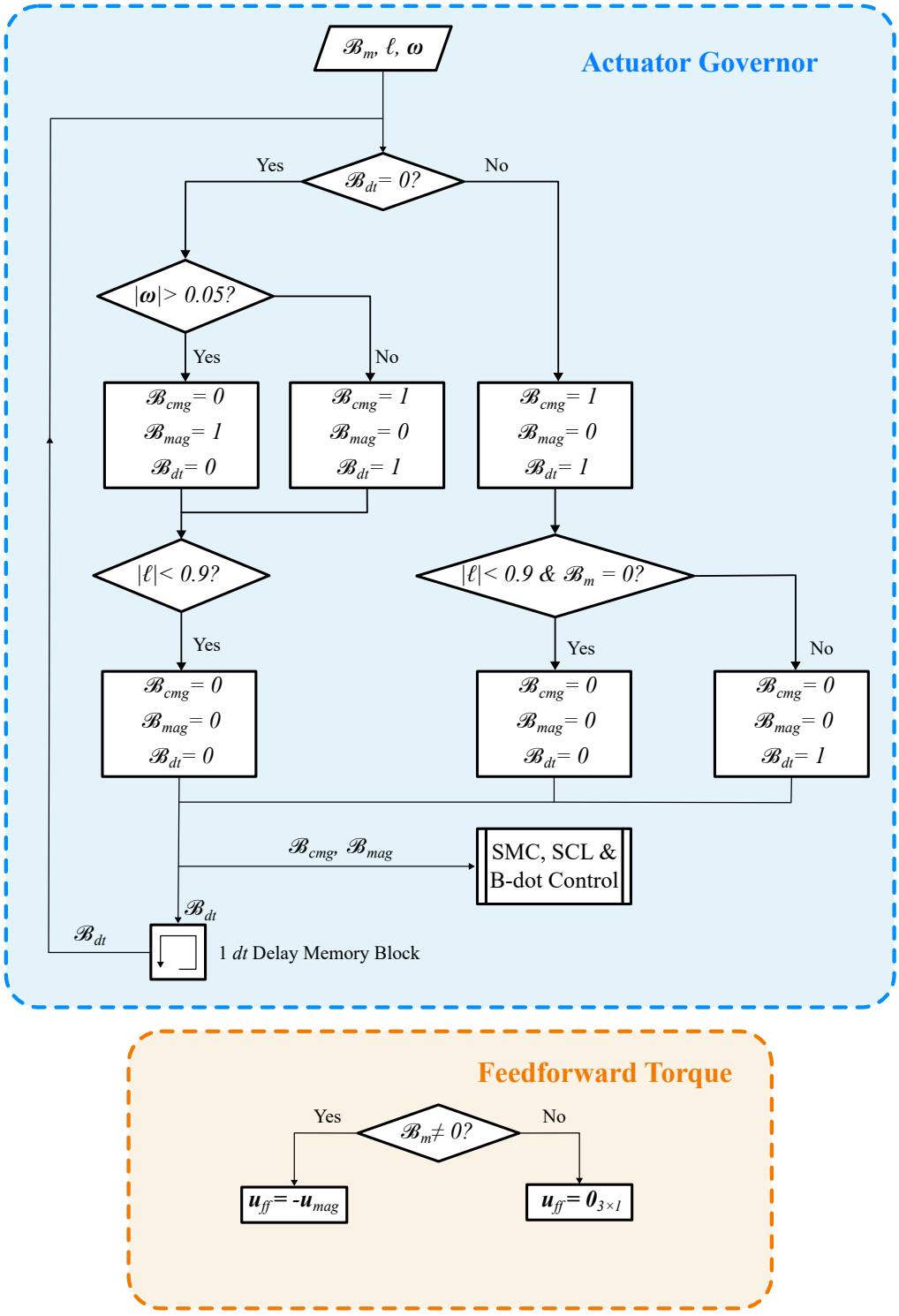

Figure 5.8: Flow Chart for Determining Desired Spacecraft Operational Mode

5.6 DGSPCMG Attitude Control Results

This section presents results used to confirm the intended function of the DGSPCMG Extended Steering Control Law in a nadir pointing Earth observation mission. Three simulation sets are shown. In the first simulation, the spacecraft is provided an initial body rate which requires it to detumble prior to initiating CMG control. The second simulation commands the DGSPCMG to perform a maneuver which causes δ_{sp} to briefly exceed the saturation threshold ϵ_s. The second simulation also demonstrates the ability for the Extended SCL to properly select between gimbal steering and gimbal compensation for singularity escape dependent on the given spacecraft state. The third simulation demonstrates the execution of gimbal compensation to restore the CMG momentum state to a desirable value while still controlling the attitude of the spacecraft.

5.6.1 Simulation 1 - Detumbling

The results in this section were derived from the following list of initial parameters shown in Table 5.2: The spacecraft dynamics during detumbling can best be observed

Table 5.2: Key Initial Conditions for Simulation 1

Simulation 1 Initial Conditions

Description	**Parameter**	**Value and Units**
Initial Spin	$\boldsymbol{\omega}_{t=0}$	$[0.1, -0.2, 0.1]^T$ (rad/s)
Initial Gimbal Positions	$\boldsymbol{\delta}_{t=0}$	$[0.0, 0.0, 0.0]^T$ (rad)
Initial Attitude	$\boldsymbol{q}_{t=0}$	$[0, 0, 0, 1]^T$ (unitless)
Initial Position (ECI)	$\boldsymbol{r}_{t=0}$	$[6.1224\text{E}+06, 2.9266\text{E}+06, -189.3029]^T$ (m)
Initial Velocity (ECI)	$\boldsymbol{v}_{t=0}$	$[-6.3136\text{E}+03, 4.3459\text{E}+03, 0.0000]^T$ (m/s)
Epoch Date	(yyyy-mm-dd)	(2023-01-11)
Epoch Time	t_0	7.1816 (Decimal Hours)
Flywheel Momentum	H_w	0.022 (kgm^2/s)
Obtained TLE:		
1 | 55125U 98067US 23011.29923435 .00058776 00000-0 96732-3 0 9995		
2 | 55125 51.6426 25.5525 0003280 304.5245 55.5434 15.51770375 2070		

by analyzing the results of the MEKF during the detumbling period. The MEKF, during this time, is outputting an estimation of the spacecraft body rates, which are used as the feedback term for the B-dot control law. The MEKF attitude, body rates and bias estimates are provided in Fig. 5.9 - Fig. 5.11. In Fig. 5.9 all true quaternion components q_{1-4} (shown in black) are shown with the QUEST estimated quaternion components $q_{1-4_{QUEST}}$ (shown in gray) and the MEKF estimated quaternion components $q_{1-4_{MEKF}}$ (shown in red) as overlays. Similarly in Fig. 5.10 all true body rate components ω_{1-3} (shown in black) are shown with the IMU measured components $\omega_{1-3_{IMU}}$ (shown in gray) and the MEKF estimated components $\omega_{1-4_{MEKF}}$ (shown in red) as overlays.

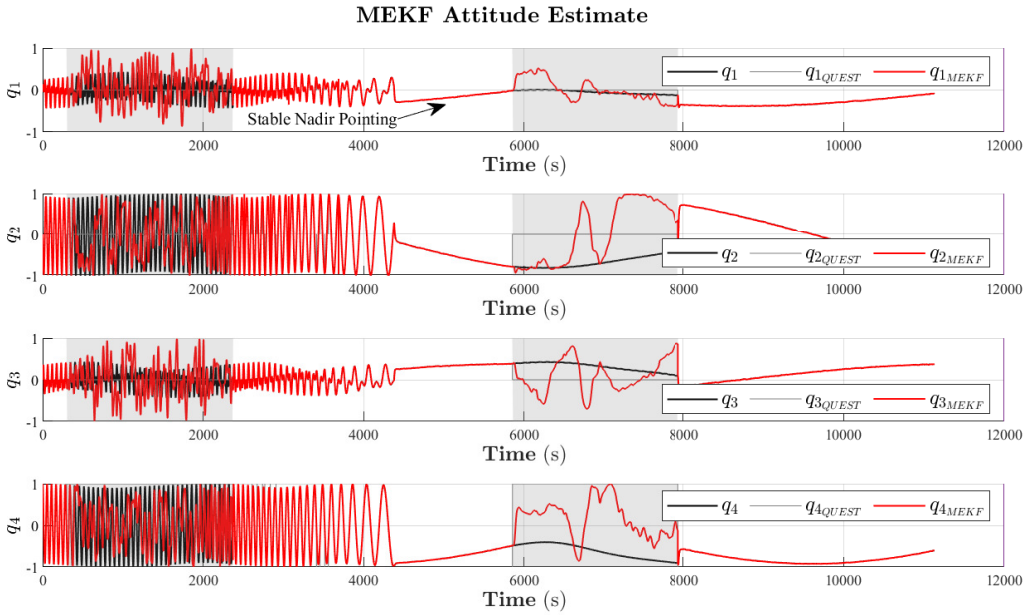

Figure 5.9: MEKF Attitude Estimate During Detumbling Compared to Actual Spacecraft Attitude

The MEKF is shown in Fig. 5.9 - Fig. 5.11 to provide a good estimate of the spacecraft state when not in eclipse (designated by the shaded regions of the plots). Because the covariance matrix from in-sunlight estimation is saved for the exit of inevitable eclipses, it can be observed that the MEKF converges quickly to the actual state on the exit of eclipse. A key detail from the results is best observed in Fig. 5.10. This figure shows that the spacecraft had not yet completed detumbling when entering eclipse at around 300 seconds of simulation time. Because the MEKF can only produce a rough bias estimate in eclipse when lacking the QUEST measurements, detumbling is stopped and only resumed when the spacecraft exits eclipse. It is relatively clear by the gradual reduction in body rates in Fig. 5.10 that the ADCS has properly waited for sunlight before continuing to detumble the spacecraft. The actuation of the magnetic torquers which caused the observed abating body rates is presented in Fig: 5.12.

As shown in Fig. 5.12, the magnetic torquers operate within their nominal dipole

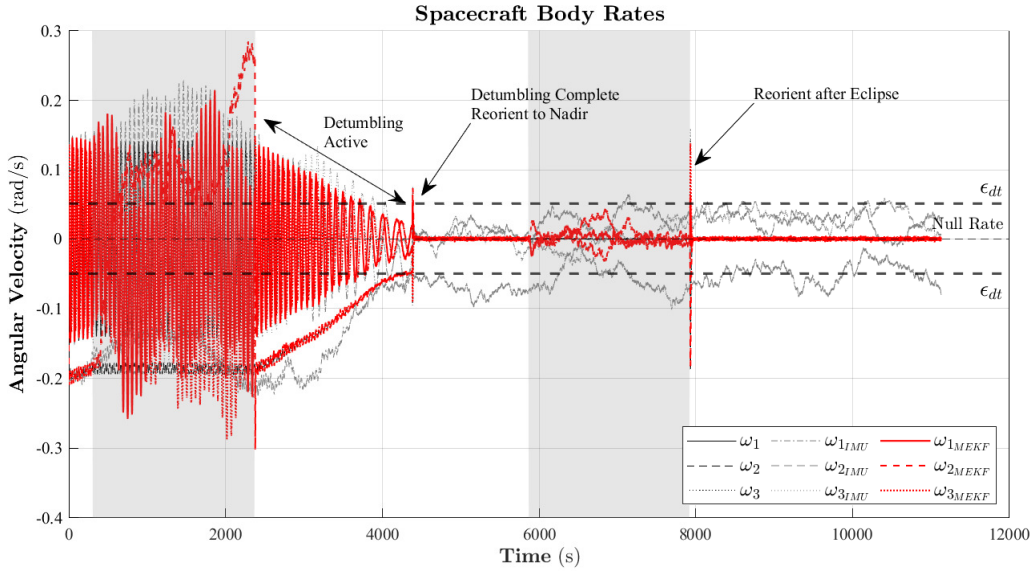

Figure 5.10: MEKF Body Rate Estimate Compared to IMU Measured and Actual Body Rates

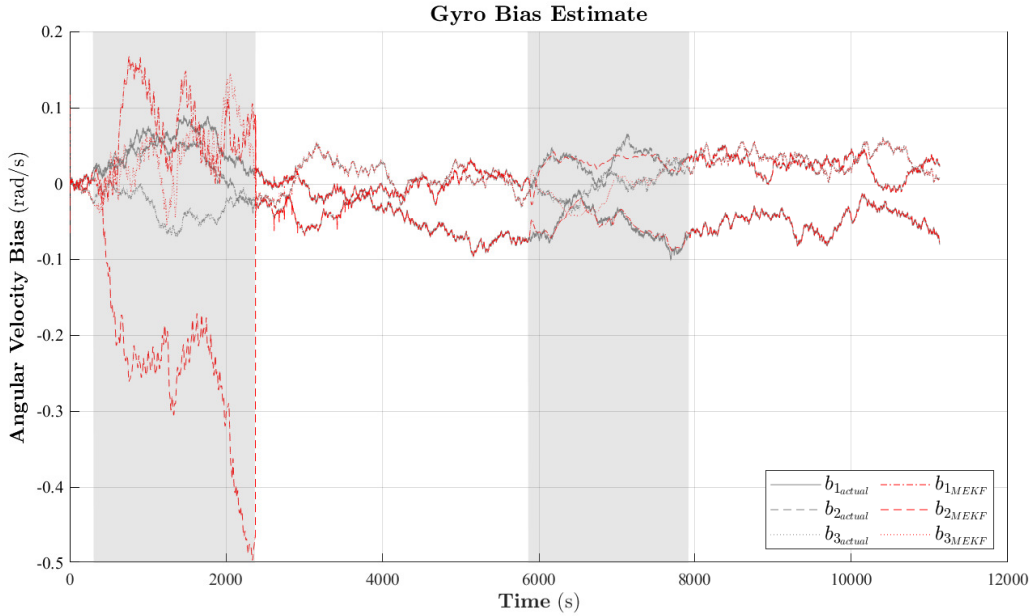

Figure 5.11: MEKF Estimated IMU Bias Compared to Actual IMU Bias

output range of 0.2 Am^2. Only the x-axis and z-axis torquer hit the saturation limit during operation. The magnetic torquers were switched off in favor of using the CMG for fine attitude pointing once the torquers had detumbled the satellite below the detumbling threshold ϵ_{dt}. The spacecraft operational modes which reflect this switch to CMG control are shown in Fig. 5.13.

While all states are set to 0 (false) in eclipse, the actuator governor recognizes

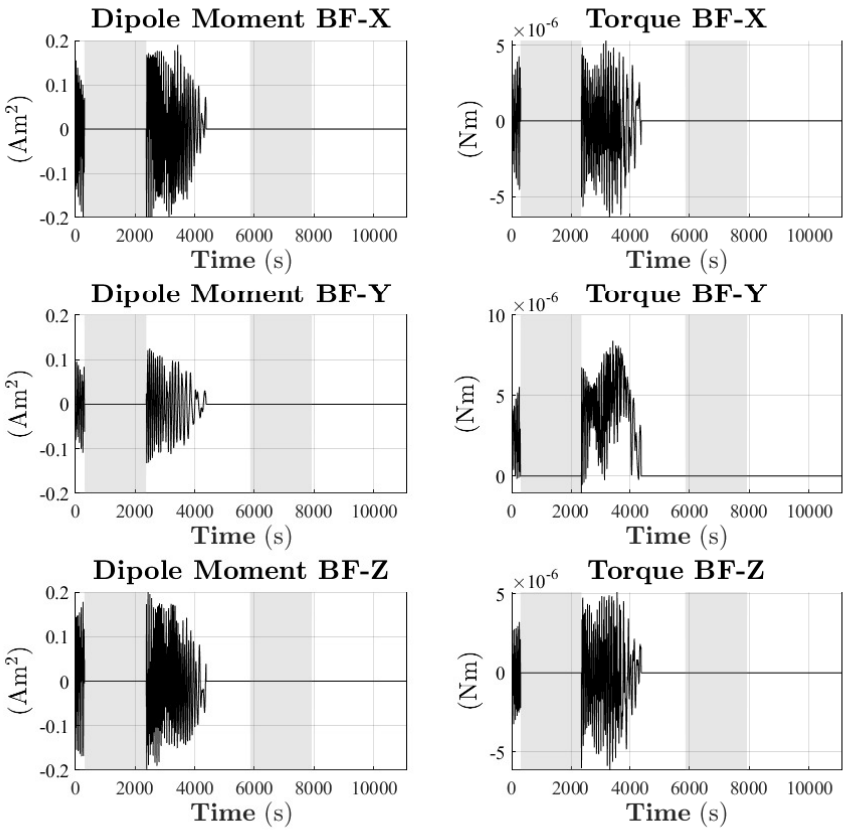

Figure 5.12: Magnetic Torquer Actuation During Detumbling Expressed in $\mathcal{F}_{BF}$

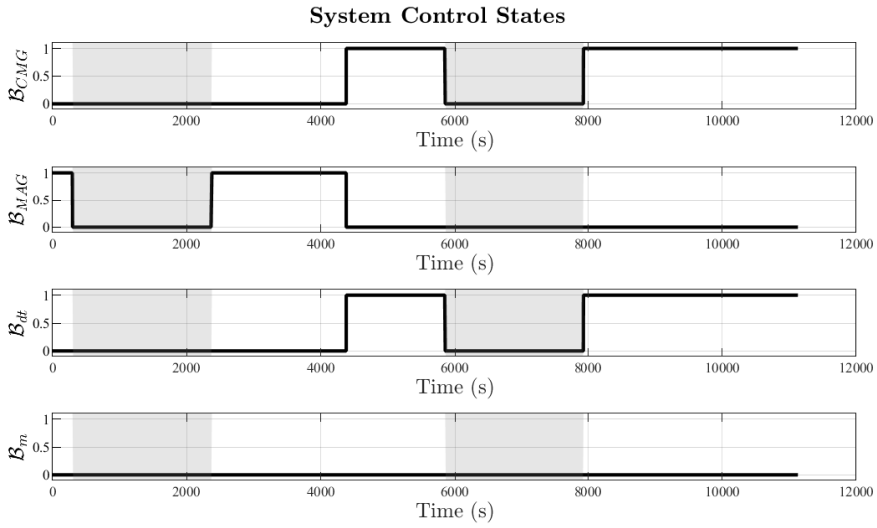

Figure 5.13: Operational Modes Output by Actuator Governor

high body rates on the exit of eclipse and allows the magnetic torquers to complete the detumbling as shown in Fig. 5.13 subplot two. The CMG is briefly switched on

prior to the second eclipse once the magnetic torquers have completed detumbling. This handover is also represented in Fig. 5.9 by the fact that the MEKF is shown to start outputting a stable nadir tracking attitude at around 4500s of simulation time.

Some discussion is necessary to explain how the specific initial condition of $\boldsymbol{\delta}_{t=0} = [0, 0, 0]^T$ was contrived. While it seems counter intuitive to deliberately place the CMG in the $\delta_{sp} = 0$ singularity to start the mission, doing so prevents the CMG from producing unwanted torques during detumbling. Should $\delta_{sp} = 0$ not be selected, the $\boldsymbol{\omega}^{\times}\boldsymbol{h}$ component of Eq. (5.12) demonstrates that the CMG would be producing an uncompensated gyric torque during detumbling by the fact that $\boldsymbol{h}$ would be a non-zero vector. For this reason, it is likely for the DGSPCMG to start an orbital mission with $\delta_{sp} = 0$.

5.6.2 Simulation 2 - Agile Maneuvering

The agile maneuvering results in this section were derived from the following set of initial conditions in Table 5.3. Any initial conditions not listed in this table were identical to the first simulation parameters shown in Table 5.2. The results of this section highlight the ability of the Extended DGSPCMG SCL to effectively select the most ideal singularity escape method based on the satellite state.

Table 5.3: Key Initial Conditions for Simulation 2

Simulation 2 Initial Conditions

Description	**Parameter**	**Value and Units**
Initial Spin	$\boldsymbol{\omega}_{t=0}$	$[0.0, 0.0, 0.0]^T$ (rad/s)
Initial Gimbal Positions	$\boldsymbol{\delta}_{t=0}$	$[0.3, 0.0, 0.0]^T$ (rad)

Highlighted in Fig. 5.14 - Fig. 5.15 is the DGSPCMG gimbal angles and gimbal rates plotted over 5 orbits. In this simulation case the DGSPCMG is initialized so that δ_{sp} is already near the threshold ϵ_s. By doing so, the reorientation maneuvers on exit of eclipse have a higher chance of requiring that the CMG scissor-pair angle exceeds the saturation limit for momentum management during the maneuver.

As shown by Fig. 5.14, the δ_o gimbal has a larger angular travel distance than the other two gimbals because its motion is not limited by any singularities. δ_o is, therefore, free to rotate. On the contrary, δ_i can be observed to rotate inside the provided mechanical limitations of $\pm\frac{\pi}{2}$. Movement outside this range would force the δ_i gimbal through one of the discussed internal singularities. The gimbals follow a relatively smooth trajectory as the MEKF has filtered sensor data to moderate how much noise is present in the system.

Observing the gimbal rates plot in Fig. 5.15 it is apparent that there are 5 peaks in the gimbal rates for each gimbal. These peaks represent the DGSPCMG executing a reorientation maneuver to reacquire nadir pointing after each eclipse. It is fairly clear

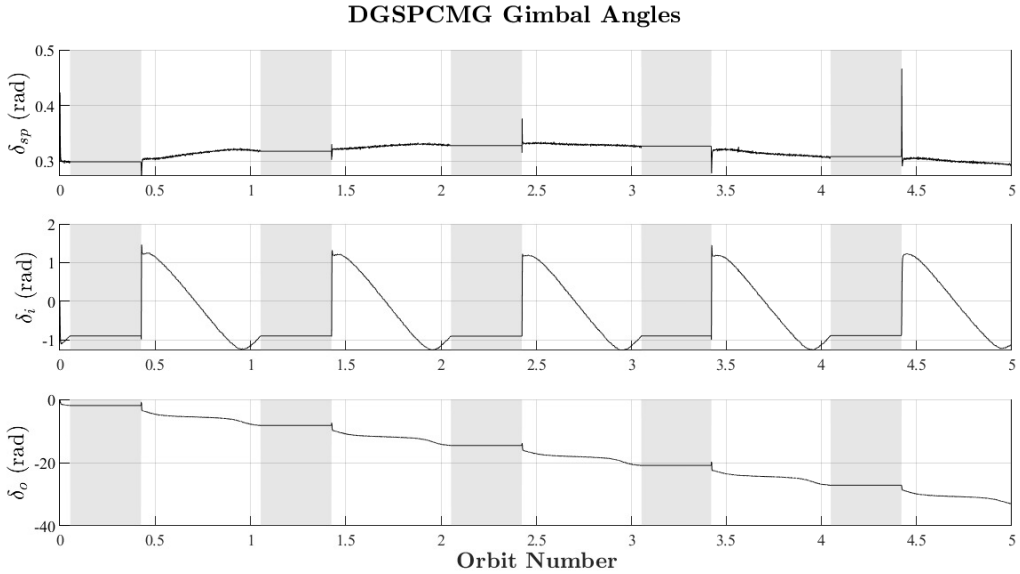

Figure 5.14: DGSPCMG Gimbal Angles For 5 Orbit Simulation

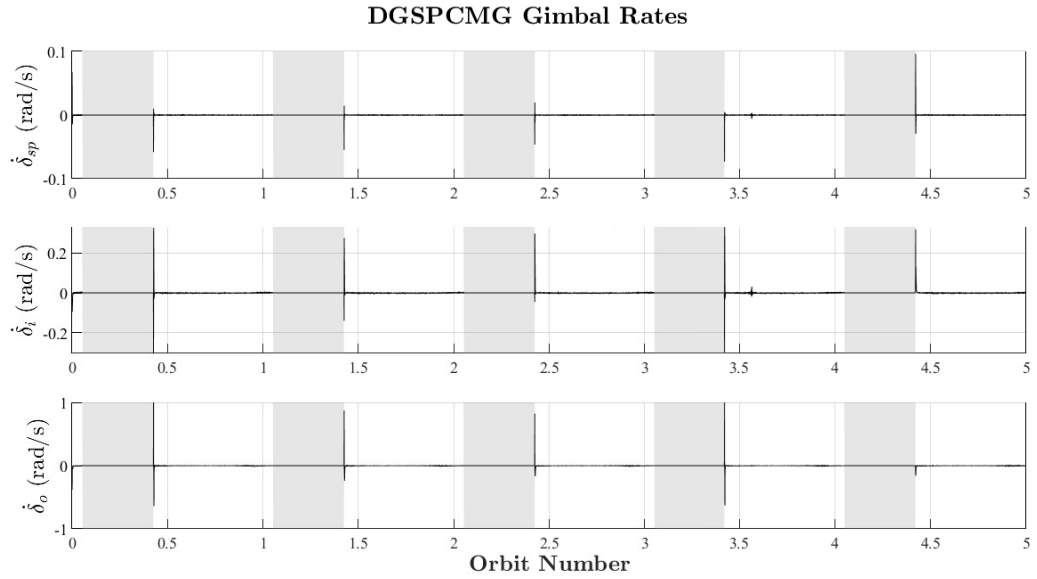

Figure 5.15: DGSPCMG Gimbal Rates For 5 Orbit Simulation

when observing the third subplot of Fig. 5.15 that the outer gimbal is commanded, in general, to perform higher rates than the other two gimbals when performing an agile attitude reorientation maneuver.

Further discussion is required to explain the results of the 5^{th} attitude re-acquisition maneuver. Fig. 5.16 highlights the key points of data. It is clear from Fig. 5.16 that the δ_{sp} angle has exceeded the momentum management saturation threshold of ϵ_s. The Extended DGSPCMG SCL, however, did not command a momentum management maneuver. The lack of action at this moment is an expected and desired result.

Observing the scalar component of the error quaternion in Fig. 5.16, the value is not above the threshold for acquired attitude ϵ_p. For this reason, the Extended DGSPCMG SCL allows for the δ_{sp} angle to exceed ϵ_s — opting to allow for agile maneuvering to correct the attitude error rather than performing gimbal compensation. An added reason that justifies such gimbal steering is that the Extended SCL has the tendency to return the δ_{sp} angle to its pre-maneuver position once the maneuver is completed. Since the pre-maneuver δ_{sp} angle was below ϵ_s, it is reasonable to expect that the angle will return to this nominal operating position if no exorbitantly large disturbances are encountered during the attitude maneuver. By assessing the discussion and results on this gimbal steering methodology, it was concluded that the Extended SCL was properly steering the DGSPCMG for reorientation maneuvers — reserving gimbal compensation for when attitude was already acquired.

To ensure that the DGSPCMG did not enter singularities over the 5 orbit simulation, the singularity measure ($\det(\boldsymbol{A})$) was plotted in Fig. 5.17. While it is clear from Fig. 5.17 that the DGSPCMG did not enter a singularity, it did approach $\det(\boldsymbol{A}) = 0$ at times where δ_i approached its mechanical limitations. The singularity measure was lowest just before the 0.5 orbit mark where δ_{sp} was its closest to 0 rad during the simulation and δ_i was near the mechanical constraint of $\frac{\pi}{2}$.

5.6.3 Simulation 3 - Gimbal Compensation

The results in this section focus on demonstrating that gimbal compensation can effectively assist the DGSPCMG in escaping from singularities while maintaining a desired attitude. The first set of results focuses on the $\delta_{sp} = 0$ singularity escape, while the second set focuses on δ_{sp} desaturation from ϵ_s. Initial conditions leveraged for both escape cases are provided in Table 5.4.

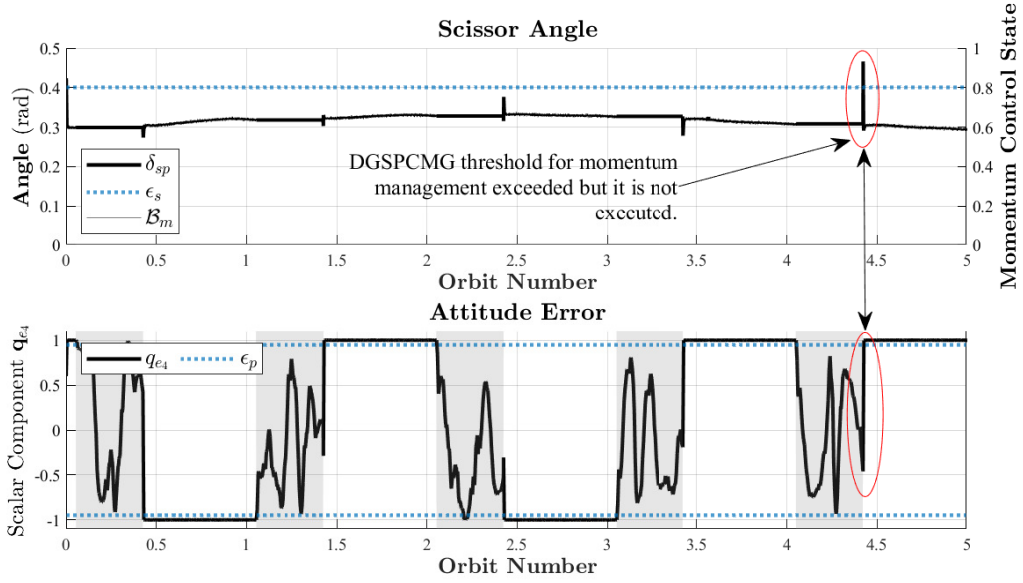

Figure 5.16: Steering of δ_{sp} Corresponding to Value of q_{e_4}

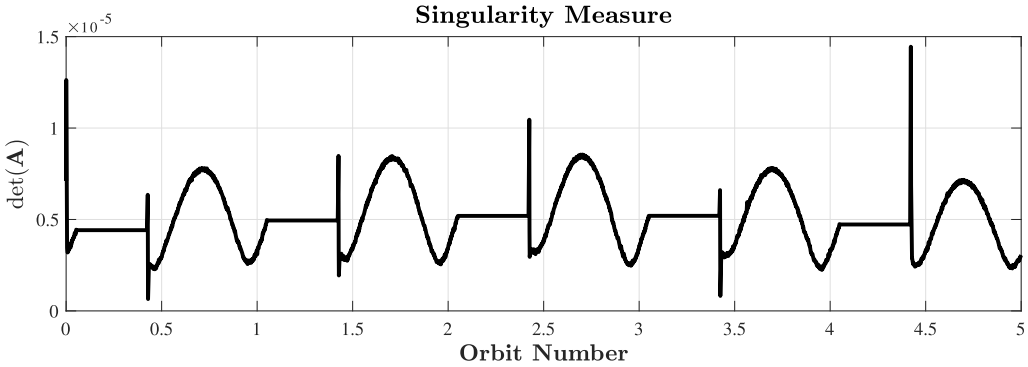

Figure 5.17: Singularity Measure During 5 Orbit Simulation

Table 5.4: Key Initial Conditions for Simulation 3

Simulation 3 Initial Conditions

Description	**Parameter**	**Value and Units**
$\delta_{sp} = 0$ Escape:		
Initial Spin	$\boldsymbol{\omega}_{t=0}$	$[0.0, 0.0, 0.0]^T$ (rad/s)
Initial Gimbal Positions	$\boldsymbol{\delta}_{t=0}$	$[0.0, 0.0, 0.0]^T$ (rad)
δ_{sp} Desaturation:		
Initial Spin	$\boldsymbol{\omega}_{t=0}$	$[0.0, 0.0, 0.0]^T$ (rad/s)
Initial Gimbal Positions	$\boldsymbol{\delta}_{t=0}$	$[0.0, 0.0, 0.0]^T$ (rad)
Stored Flywheel Momentum	H_w	0.005 kgm^2/s
Attitude Determination	N/A	Taken out of the loop
Luminous Intensity Factor	ℓ	1 (constant-unitless)

$\delta_{sp} = 0$ Gimbal Compensation

A common instance of gimbal compensation for the $\delta_{sp} = 0$ singularity is immediately after the first attitude reorientation maneuver where δ_{sp} started the simulation at 0 rad. As discussed in Section 5.6.2, the Extended SCL tends to return δ_{sp} to its pre-maneuver position once the maneuver is completed. In the case the initial position is $\delta_{sp} = 0$, the scissor pair will be returned to $\delta_{sp} = 0$. The difference on the return gimbal trajectory is that this time, the spacecraft is now at the desired attitude and gimbal compensation must be used to increase δ_{sp} to $\delta_{sp_{ref}}$. This gimbal motion is shown by the simulation results provided in Fig. 5.18a - Fig. 5.18e.

Shown in the enlarged plot Fig. 5.18a and Fig. 5.18b, the DGSPCMG first performs a null motion using gimbal steering to escape from $\delta_{sp} = 0$ and carry out

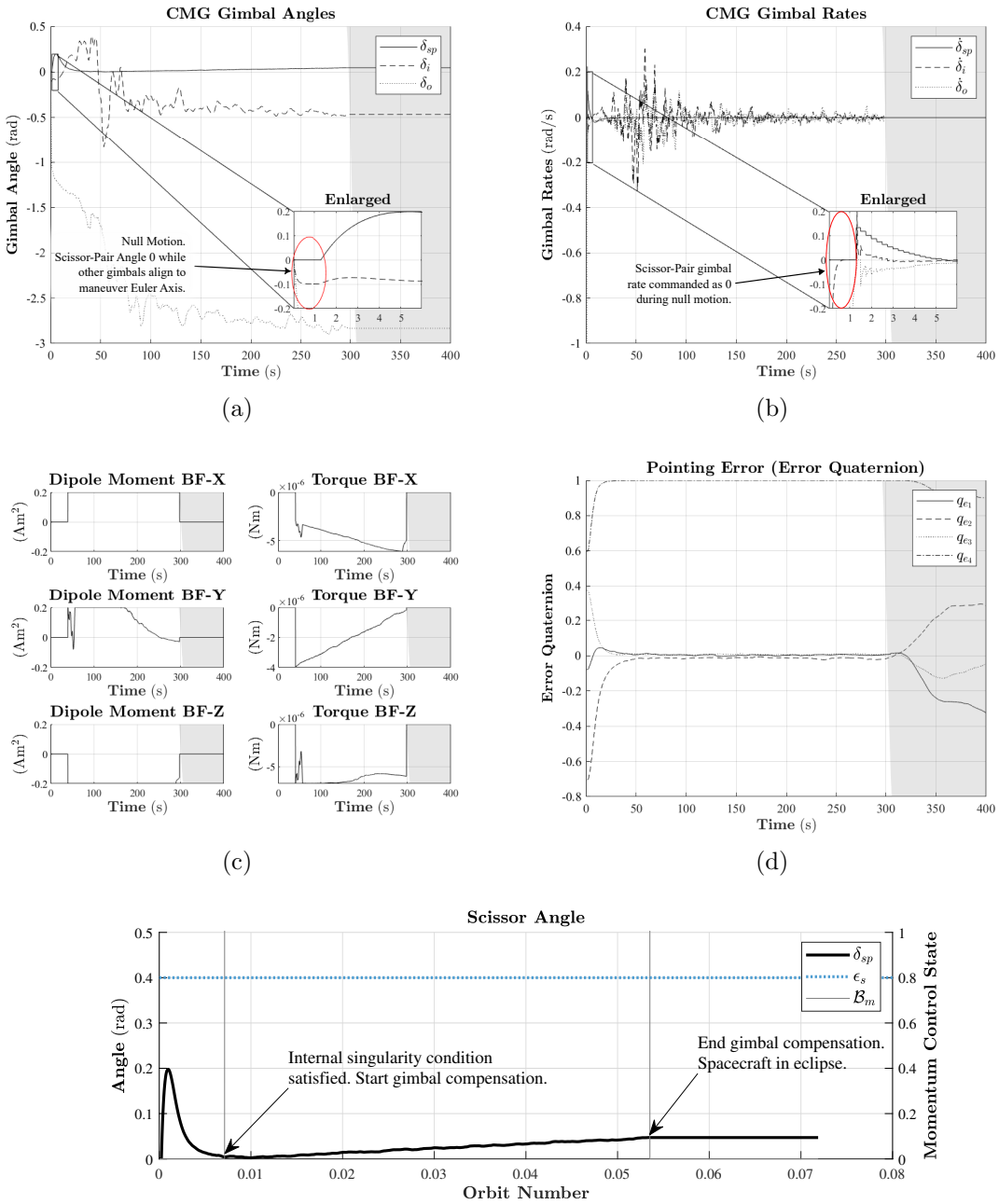

Figure 5.18: Simulation 3 $\delta_{sp} = 0$ Escape After Initial Attitude Acquisition

an agile attitude maneuver. The null motion is known to have been executed by the fact that, as shown in the Enlarged plots, the inner and outer gimbals move for about 1.5 seconds prior to gimballing the scissor pair. This outer and inner gimbal motion produces no torque since the CMG holds no net angular momentum in this position. Observing Fig. 5.18e, the δ_{sp} angle can be seen to be returning to $\delta_{sp} = 0$ after the

maneuver is near complete. This time, as shown by Fig. 5.18d, q_{e_4} is near 1 and gimbal compensation is started. The produced magnetic torquer dipole moments are shown in Fig. 5.18c during gimbal compensation. The δ_{sp} angle can be seen to be increasing in Fig. 5.18e towards $\delta_{sp_{ref}}$ during gimbal compensation.

During the gimbal compensation process, it is demonstrated by Fig. 5.18d that the error quaternion is only mildly perturbed by the execution of gimbal compensation. The results of this figure more conclusively show that the spacecraft is maintaining nadir pointing while directing δ_{sp} towards are desired position. Another noticeable result of the simulations is that, as presented by Fig. 5.18e, the δ_{sp} angle never reaches $\delta_{sp_{ref}} = 0.06$ rad. Gimbal compensation was, therefore, not technically completed. The reason for this lack of completion is because the spacecraft entered eclipse and the actuator governor commanded all actuators to turn off. Completion of gimbal compensation would, therefore, not be expected in this scenario.

δ_{sp} Desaturation Through Gimbal Compensation

Noting the listed values in Table 5.4, the focus simulation in this subsection uses adjusted parameters to more easily force the Extended SCL to execute desaturation of the scissor-pair angle. Primarily, the spacecraft is considered to be always in the Sun over its orbit so that the results will demonstrate an uninterrupted progression of δ_{sp} towards the external singularity. Also, the stored angular momentum in the flywheels has been lowered so that the δ_{sp} angle progresses more quickly to the external singularity. In nominal operations, the larger stored flywheel momentum allows for smaller increases of δ_{sp} to achieve the same net CMG momentum vector. In these results, because ℓ was set to a constant value of 1, the satellite will always be nadir pointing and never lose attitude availability.

Following this set of parameter changes, the scissor-pair angle is plotted with respect to time in Fig. 5.19. As demonstrated by Fig. 5.19, δ_{sp} progresses towards ϵ_s as a result from momentum loading into the CMG by angular impulses experienced over multiple orbits. After the 20^{th} orbit, gimbal compensation is engaged to reset δ_{sp} to $\delta_{sp_{ref}}$. Because the scalar component of the error quaternion q_{e_4} in this hypothetical scenario is always above ϵ_s, the spacecraft and DGSPCMG are always in a state where gimbal compensation is available for singularity escape.

In the focus hypothetical scenario gimbal compensation was active for 3056s – approximately 55% of the simulated orbital period. The gimbal compensation duration represents an ideal scenario because attitude determination was not in the loop. The noise injected into the system by attitude determination could lengthen the gimbal compensation duration. Another factor which could impact the gimbal compensation duration is the flywheel momentum H_w. In this hypothetical case the flywheel momentum was set to 0.005 kgm^2/s, a value only 23% of the nominal simulated value. Larger flywheel momentum can lead to longer gimbal compensations because the magnetic torquers need to offload more stored momentum. When comparing the 55% of orbit spent performing gimbal compensation to the 37.4% of orbit spent in eclipse, there is roughly 7.6% of the orbit remaining for standard gimbal

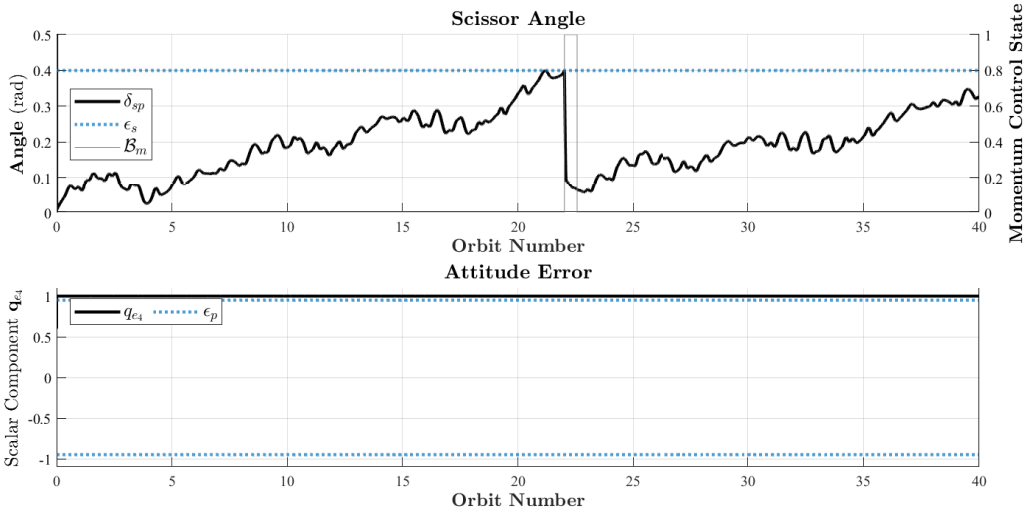

Figure 5.19: Demonstration of $\delta_{sp} > \epsilon_s$ with Acquired Attitude

steering (assuming gimbal compensation is started immediately after eclipse). Since it is unreasonable to expect that gimbal compensation will always be executed by the Extended SCL on the exit of eclipse, the analysis promotes the notion that incomplete gimbal compensations will occur. This result should be expected, as the Extended SCL considers the range of $\epsilon_1 - \epsilon_s$ to be the acceptable nominal operating range for δ_{sp} when attitude has been acquired. An incomplete gimbal compensation leaving δ_{sp} within this range on entry of eclipse will not lead to a re-execution of gimbal compensation on the exit of eclipse.

For the simulation conditions used in this research, the results of this chapter have demonstrated the capabilities of the proposed novel DGSPCMG SCL to robustly achieve 3-axis attitude control of a CubeSat in LEO. The SCL has been shown to execute the most ideal singularity escape method dependent on the state of the satellite and CMG. Subsequent chapters in this thesis will utilize the DGSPCMG SCL to help achieve other advanced mission directives in LEO.

Chapter 6

Inertia Estimation of Uncooperative Tethered Debris in LEO

6.1 Introduction

In the case of defunct spacecraft, spent rocket bodies, or other large debris, it is common for these types of objects to be uncooperative. Uncooperative debris does not send any information about its state to assist in its removal [115]. In addition, it is typical for the inertial parameters of these objects to be unknown or uncertain [116]. To capture uncooperative debris objects, devices including robotic manipulator arms [117], space harpoons [118][119], tethered space robots (TSR)s [120], or tethered nets [119][121][122] have all been studied. In many cases, the tether-based options are preferred because they can be used while maintaining a safe distance from the target debris [123]. With tethered capture methods being favored, significant research effort has been placed on understanding and handling the challenging post-capture dynamics associated with tethered debris.

In research works such as [124][125][126][127], which developed methods to control uncooperative tethered debris, control performance was greatly improved when accurate knowledge of inertial parameters were known for the debris object. Parameters including the debris inertia tensor, debris COM location, and tether attachment point were all generally required in the control formulations. It is, therefore, justifiable to attempt parameter estimation prior to attempting control. Modern inertia estimation methods have generally involved some method of exciting the rotational motion of the debris and monitoring its motion with devices like Light Detection and Ranging (LiDAR) sensors as done in [128][129]. Meng *et al.* (2019) proposed a soft touch probe to excite the rotational motion of the debris and estimate its inertia [130]; however, it is expected that tethers could accomplish the same goal and do so while maintaining distance from the debris.

Other authors have taken a different approach and investigated the relatively understudied concept of estimating inertia properties with a tether. The work proposed by Zhang *et al.* (2015) in [131] can determine 1 principal momentum of inertia and ratios for the other two. More recently, Bourabah *et al.* (2023) employed an Unscented Kalman Filter (UKF) to estimate all three principal moments of inertia [132][133]. To accomplish estimation of all three principal moments of inertia, an assumption is made in [132] that the tether connection point on the debris is known. Efforts to relax assumptions are undertaken in [133]; however, it was shown that it can be troublesome to remove the tether connection point assumption while maintaining a determinable input torque that excites the rotational motion of the debris. Notwithstanding the promising work in the literature, products of inertia have yet to be estimated with a tether and, as a result, a full inertia tensor for the debris has yet to have been formed. The estimator developed in the present work seeks to solve both the tether

connection point assumption and the challenges of estimating the full inertia tensor for the debris.

Towards relaxing the tether connection point assumption and estimating all six inertial parameters, this section develops a two-stage estimator (TSE) consisting of a Kalman Filter and Quick Response Iterative Inertia Properties Identification Algorithm (QRIIPIA) from [134]. By implementing a LiDAR measurement model and by approximating the end point of the tether using tether tension force measurements, the aforementioned goals were achieved for the simulation parameters used within this thesis. Estimation is also demonstrated for the understudied case that a DGSPCMG-equipped chaser CubeSat, having only rudimentary station keeping ability, is used to track the uncooperative debris.

6.2 Tethered System Dynamics

6.2.1 Spacecraft Dynamics

The presented scenario required the development of a separate simulator to propagate the orbital and attitude dynamics of both the chaser and debris satellite. The equations of motion in this ADR simulator were modified to include the tether. Unless the tether is tensioned, the bodies of the chaser and debris act as unique entities following translational dynamics expressed as:

$$\boldsymbol{a}_X = -\frac{\mu}{|\boldsymbol{R}_X|^3}\boldsymbol{R}_X + \frac{\boldsymbol{T}_X}{m_X} + \frac{\boldsymbol{F}_X}{m_X} \tag{6.1}$$

In Eq. (6.1) $\boldsymbol{T}_X$ is the cable tension expressed in $\mathscr{F}_{ECI}$, $\boldsymbol{F}_X$ is the resultant of all forces (other than tension) acting on the body including control thrust, μ is the gravitational parameter of Earth, m_X is the mass of the rigid body, $\boldsymbol{a}_X$ is the translational acceleration of the body, and $\boldsymbol{R}_X$ is the ECI orbital position vector. The subscript X denotes either D or C representing debris or chaser, respectively. For the space debris, it is assumed that $\boldsymbol{F}_D = 0$ because the affect of orbital disturbances is negligible in short time horizons (below 20 minutes in the focus ADR simulations).

The rotational dynamics of either the debris or chaser spacecraft with the tether force included can be expressed as:

$$\dot{\boldsymbol{\omega}}_X = \boldsymbol{J}_X^{-1}\left(\boldsymbol{u}_X + \boldsymbol{r}_{tp,X}^{\times}\boldsymbol{T}_X - \boldsymbol{\omega}_X^{\times}\boldsymbol{J}_X\boldsymbol{\omega}_X\right) \tag{6.2}$$

where $\boldsymbol{J}_X$ is the 3×3 inertia tensor of the rigid body, $\boldsymbol{r}_{tp,X}$ is the position of the tether connection point expressed in $\mathscr{F}_{BF}$ of either the debris or chaser, $\boldsymbol{\omega}_X$ represents the angular velocity of the body, $\boldsymbol{T}_X$ is the tether tension expressed in the BF frame experienced by either the chaser or debris, and $\boldsymbol{u}_X$ is the sum of all torques acting on the body (excluding tether produced torque) expressed in $\mathscr{F}_{BF}$. For the space debris it is assumed that $\boldsymbol{u}_D = 0$.

6.2.2 Tether Dynamics

The dynamics of a flexible tether connected between the chaser and debris at single points was modeled in this thesis by following the derivation provided in [132]. It is shown later that the selection of these points has important implications for estimating the inertia of the debris. For the chaser, the tether connection point must be specifically selected based on the tracking attitude of the chaser. The debris tether connection point is slightly more nuanced, but in general, may be selected arbitrarily.

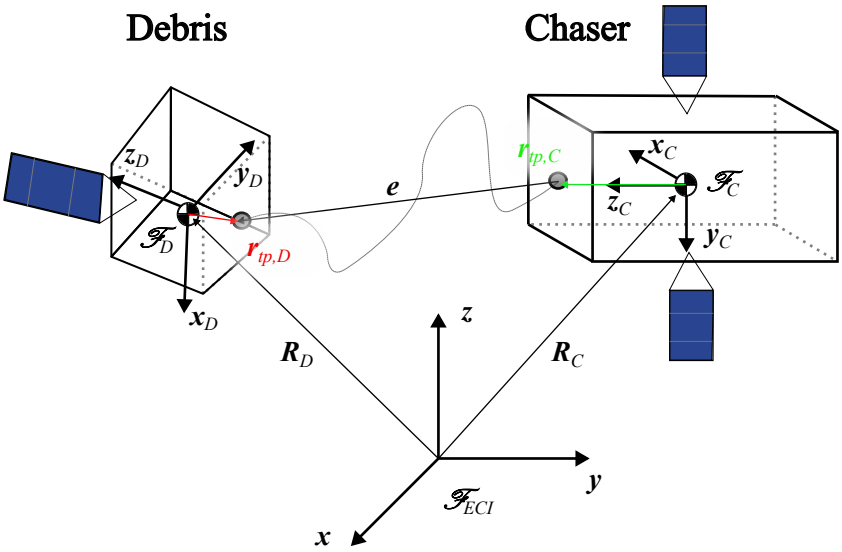

Figure 6.1: Tethered System Schematic

Observing Fig. 6.1, $\mathscr{F}_C$ and $\mathscr{F}_D$ represent the body-fixed frames for the chaser and debris, respectively. Following the figure, an expression which defines the tether vector $\boldsymbol{e}$ as the vector expressed in $\mathscr{F}_{ECI}$ from the chaser tether connection point to the debris tether connection point may be derived. First, the $\mathscr{F}_D$ connection point vector may be expressed in $\mathscr{F}_{ECI}$ by applying the relationship where $\boldsymbol{r}_{tp,X}^{ECI} = \boldsymbol{\mathcal{A}}_{BF}^{ECI}\boldsymbol{r}_{tp,X}$. This transformation relationship is listed generally because the DCM $\boldsymbol{\mathcal{A}}_{BF}^{ECI}$ will be specific to the transformation relating to the debris or chaser. Following Fig. 6.1 the unit direction vector of the tether is obtained by computing:

$$\hat{e} = \frac{\boldsymbol{R}_D + \boldsymbol{r}_{tp,D}^{ECI} - \boldsymbol{R}_C - \boldsymbol{r}_{tp,C}^{ECI}}{|\boldsymbol{R}_D + \boldsymbol{r}_{tp,D}^{ECI} - \boldsymbol{R}_C - \boldsymbol{r}_{tp,C}^{ECI}|} \tag{6.3}$$

The tether was modeled in this work by a single linear spring-damper element and, therefore, the scalar tension developed in the tether follows as:

$$T = k(l - l_0) + c\dot{l} \tag{6.4}$$

Here k is the tensile stiffness of the cable, c is the damping coefficient, l is the current length of the tether , l_0 is the nominal unstretched length of the tether, and $\dot{l}$ is the

rate of change of the tether length. The current length of the tether can be computed as $l = |\boldsymbol{R}_D + \boldsymbol{r}_{tp,D}^{ECI} - \boldsymbol{R}_C - \boldsymbol{r}_{tp,C}^{ECI}|$ by noting the denominator term of Eq. (6.3). The length rate of change $\dot{l}$ is obtained by projecting the relative velocity of the debris tether connection point with respect to the chaser tether connection point along the tether direction vector. The tether length rate of change is, therefore, defined in Eq. (6.5) where $\boldsymbol{v}_D$ and $\boldsymbol{v}_C$ represent the $\mathscr{F}_{ECI}$ expressed orbital velocity vectors of the COM of the debris and chaser, respectively [123]:

$$\dot{l} = \left[\boldsymbol{v}_D + \boldsymbol{\mathcal{A}}_{BF,D}^{ECI}(\boldsymbol{\omega}_D^{\times}\boldsymbol{r}_{tp,D}) - \boldsymbol{v}_C - \boldsymbol{\mathcal{A}}_{BF,C}^{ECI}(\boldsymbol{\omega}_C^{\times}\boldsymbol{r}_{tp,C})\right] \cdot \hat{\boldsymbol{e}} \tag{6.5}$$

Because of the tether being modeled as a cable, it does not support compression. To properly model the cable, the tension in the cable must be set to 0 if the tether is in the unstretched regime. Such an operation can be achieved by implementing the following conditions which compute the tension vector:

$$\boldsymbol{T} = \begin{cases} T\hat{\boldsymbol{e}}, \text{ if } (l > l_0) \wedge (T > 0) \\ \boldsymbol{0}_{3\times 1}, \text{ else} \end{cases} \tag{6.6}$$

To complete the tether model, the tension force experienced by the debris must be equal and opposite to the tether force experienced by the chaser. Since the tether direction vector has been defined to point from the chaser towards the debris, the tension force experienced by the debris may be expressed as:

$$\boldsymbol{T}_D = -\boldsymbol{T}_C \tag{6.7}$$

6.3 Control and Measurement Models

6.3.1 LiDAR Model

In this section a LiDAR model is constructed by simulating relevant measurements which can justifiably be expected to be produced by a LiDAR sensor and point cloud registration algorithm. Point cloud registration is a mathematical problem in 3D computer vision which involves finding the transformation which best aligns two point clouds. Recent works such as [129] or [130] have shown that Point cloud registration algorithms including Iterative Closest Points (ICP) can yield information including debris geometric center, attitude quaternion, and angular rates. Fig. 6.2 displays the reference coordinate frames for a LiDAR sensor on-board the chaser satellite. In this thesis, it was assumed that the LiDAR sensor can see the debris at all times – a simplification which is shown to be reasonable later in Fig. 6.3 where the chaser satellite can be seen to achieve the desired debris tracking attitude well before any inertia estimation is attempted.

Observing Fig. 6.2 two new reference frames have been introduced to describe the model. The first of these reference frames, represented by $\mathscr{F}_{REL}$, is a non-rotating reference frame that is aligned with $\mathscr{F}_{ECI}$ but is fixed to and translates with the

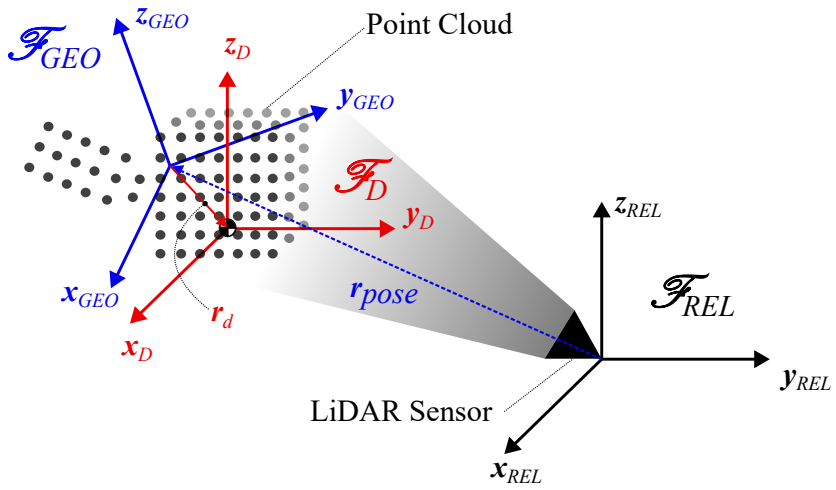

Figure 6.2: Simulated LiDAR Model with Representative Point Cloud for Debris Spacecraft Shown

chaser satellite COM over its orbit. $\mathscr{F}_{REL}$ was used to ease the use of DCMs, but predominantly to simplify pseudo measurement formulations presented later in Section. 6.4.1. $\mathscr{F}_{GEO}$ represents the principle geometric frame which is fixed at the geometric center of the debris point cloud. The vector $\boldsymbol{r}_{pose}$ is expressed in $\mathscr{F}_{REL}$ and locates the position of the geometric center. Fig. 6.2 also shows the vector $\boldsymbol{r}_d$ which is the offset vector between the debris geometric frame and debris body-fixed frame. $\boldsymbol{r}_d$ is expressed conveniently in $\mathscr{F}_D$ [123]. The offset vector is not initially known to the inertia estimator, but can reasonably be assumed to be constant unless the debris is venting mass into space. The LiDAR measurement of $\boldsymbol{r}_{pose}$ was calculated in this work where a white noise process $\boldsymbol{\eta}_r$ was assumed to corrupt the data:

$$\boldsymbol{r}_{pose} = (\boldsymbol{R}_D - \boldsymbol{R}_C) + \boldsymbol{\mathcal{A}}^{ECI}_{BF,D}\boldsymbol{r}_d + \boldsymbol{\eta}_r \tag{6.8}$$

With $\mathscr{F}_{REL}$ sharing alignment with $\mathscr{F}_{ECI}$, the DCM $\boldsymbol{\mathcal{A}}^{ECI}_{BF,D}$ applies to express $\boldsymbol{r}_d$ in $\mathscr{F}_{REL}$. Without loss in generality, Eq. (6.8) is explicitly derived for the case that $\mathscr{F}_{GEO}$ is not rotated relative to the debris BF frame $\mathscr{F}_D$. Should this not be the case, an additional DCM would be required to handle this rotation. Following the convention used earlier in this thesis for measured quantities, let the subscript "m" denote a simulated quantity corrupted by band-limited white noise. The set of measured quantities from the LiDAR sensor model include the debris attitude quaternion $\boldsymbol{q}_{D_m}$, the debris body rates $\boldsymbol{\omega}_{D_m}$, $\dot{\boldsymbol{\omega}}_{D_m}$, and the translational velocity of the debris geometric center $\boldsymbol{v}_{D_m}$. Each measured quantity is affected by a band-limited white noise process defined by $\boldsymbol{\eta}_q$, $\boldsymbol{\eta}_\omega$, $\boldsymbol{\eta}_{\dot{\omega}}$, $\boldsymbol{\eta}_v$, respectively. The set of simulated measurements are, therefore, defined as:

$$\boldsymbol{q}_{D_m} = \boldsymbol{q}_D + \boldsymbol{\eta}_q \tag{6.9}$$

$$\boldsymbol{\omega}_{D_m} = \boldsymbol{\omega}_D + \boldsymbol{\eta}_\omega \tag{6.10}$$

$$\dot{\boldsymbol{\omega}}_{D_m} = \dot{\boldsymbol{\omega}}_D + \boldsymbol{\eta}_{\dot{\omega}} \tag{6.11}$$

Velocity measurements have a more detailed model because the velocity of the debris geometric center, as observed by the chaser in $\mathcal{F}_{REL}$, includes relative velocity and rotation components caused by rotation of the geometric center about the debris COM. Subsequently, the debris geometric center velocity measurement model was derived as follows:

$$\boldsymbol{v}_{D_m} = \boldsymbol{v}_D - \boldsymbol{v}_C + \boldsymbol{\mathcal{A}}_{BF,D}^{ECI} \boldsymbol{r}_d^{\times} \boldsymbol{\omega}_D + \boldsymbol{\eta}_v \tag{6.12}$$

Comparatively to Eq. (6.8), if the debris geometric frame $\mathcal{F}_{GEO}$ is rotated relative to the debris BF frame $\mathcal{F}_D$, an additional direction cosine matrix would be required in Eq. (6.12). In the present thesis, it was assumed that $\mathcal{F}_{GEO}$ and $\mathcal{F}_D$ are offset but not rotated relative to each other, making the additional DCM a 3×3 identity matrix which can, therefore, be omitted from the debris measurement model.

6.3.2 Desired Chaser Attitude

In this section, a desired attitude profile for the chaser satellite is derived which tracks the debris satellite. To ensure the chaser satellite had highly-agile pointing abilities, the DGSPCMG and Extended SCL were applied on-board the chaser. Here, it is worthwhile to discuss in more detail the selection of the tether connection point on the chaser. To minimize attitude perturbations on the chaser control system by tether tension, the chaser can be directed to point at the measured geometric center of the debris. Then, by setting the tether connection point to be along one of the principal inertial axes of the chaser and pointing this axis towards the debris geometric center, disturbances caused by rapid tensioning of the tether can be minimized on the chaser. The selection of this chaser satellite tether connection point is a specific, and critical, design choice to prevent control instability. In the event the tether connection point is not selected carefully or the chaser has not directed the connection point towards the debris, large impulse torques may be imparted on the chaser by nature of the tether tension force vector not being aligned with the chaser tether connection point vector [123].

To compute the desired chaser attitude quaternion a rotation between two vectors must be realized. Observing the vector diagram in Fig. 6.1, the objective of the desired attitude is to point the $z+$ axis of $\mathcal{F}_C$ towards the geometric center of the debris. By definition, this desired attitude is achieved by aligning the $\mathcal{F}_C$ $z+$ basis vector with the pose vector $\boldsymbol{r}_{pose}$. This target tracking attitude problem has been well studied by Wu *et al.* (2018) in [135]. In [135] it was assumed that rotation about the observing basis vector (the vector directed at the target) is desired to be 0 in order to make a 3-axis rotation sequence be fully defined. Adopting the work in [135], the bases vectors of the desired chaser attitude expressed in $\mathcal{F}_{ECI}$ are obtained by starting with the desired $z+$ axis orientation $\boldsymbol{z}_a$ being functionally equivalent to

the unit direction vector of the LiDAR pose vector:

$$\boldsymbol{z}_a = \frac{\boldsymbol{r}_{pose}}{|\boldsymbol{r}_{pose}|} \tag{6.13}$$

The remaining bases vectors of the desired BF frame orientation for the chaser may be computed in Eq. (6.14) noting that $\boldsymbol{y} = [0, 1, 0]^T$ is the y-axis basis vector defining $\boldsymbol{\mathcal{F}}_{ECI}$:

$$\begin{cases} \boldsymbol{x}_a = \boldsymbol{z}_a^{\times}(-\boldsymbol{y})/|\boldsymbol{z}_a^{\times}(-\boldsymbol{y})| \\ \boldsymbol{y}_a = \boldsymbol{z}_a^{\times}\boldsymbol{x}_a \end{cases} \tag{6.14}$$

Using the set of three desired bases vectors allows for a 3-2-1 rotation sequence to be constructed that represents the rotation between $\boldsymbol{\mathcal{F}}_{ECI}$ and the desired chaser BF frame orientation. The following expressions compute the required Euler angles (ϕ, θ, ψ) for the 3-2-1 sequence given that $\boldsymbol{z} = [0, 0, 1]^T$ is the z-axis basis vector of $\boldsymbol{\mathcal{F}}_{ECI}$:

$$\begin{cases} \phi = \arctan\left((\boldsymbol{y}_a \cdot \boldsymbol{z})/(\boldsymbol{z}_a \cdot \boldsymbol{z})\right) \\ \theta = \arcsin\left((-\boldsymbol{x}_a \cdot \boldsymbol{z})\right) \\ \psi = 0 \end{cases} \tag{6.15}$$

The DCM describing the desired orientation of the chaser expressed relative to $\boldsymbol{\mathcal{F}}_{ECI}$ may be computed in Eq. (6.16) where C1$-$3() represent the individual direction cosine matrices for the 3-2-1 sequence following the convention provided in Section. 3.1:

$$\boldsymbol{\mathcal{A}}_{ECI}^{a} = \boldsymbol{C}_1(\phi)\boldsymbol{C}_2(\theta)\boldsymbol{C}_3(\psi) \tag{6.16}$$

The resulting direction cosine matrix may subsequently be converted to a desired attitude quaternion $\boldsymbol{q}_a$ following the derivations provided in [40].

6.3.3 Station Keeping Control Law

In order to tension the tether, the chaser satellite should have the ability to thrust away from the debris. In the case of small chaser satellites, in this case a 2U CubeSat, the satellite may only have rudimentary thrusting capabilities defined by thrust along a single axis. In the present work, it was assumed that the chaser could only provide a thrust force along the z-axis of $\boldsymbol{\mathcal{F}}_C$. To actively control this thrust, a Bang-Bang thruster control scheme was developed in this thesis to give the proposed DGSPCMG-equipped chaser rudimentary station keeping ability. Since the z-axis of $\boldsymbol{\mathcal{F}}_C$ is nominally tracking the geometric center of the debris, the control law developed in this section will only enable thrusting once the chaser has acquired the desired attitude. The discussed Bang-bang controller acts on the station keeping distance error e_s, which is the error in the actual distance between the chaser and debris when compared to the desired distance. e_s was defined in this work as:

$$e_s = \zeta_l - |\boldsymbol{R}_D - \boldsymbol{R}_C| \tag{6.17}$$

$\zeta_l = l_0 + \Delta$ is the selected setpoint distance where Δ is a small offset distance chosen to ensure that under realistic amounts of tether stretch the quantity e_s remains positive. By making this selection of Δ, the chaser will never attempt to thrust towards the debris and will only thrust away from the debris – a desirable characteristic which addresses the rudimentary station keeping constraint. Since the translational control of the satellite is limited to a single axis, the chaser should only fire its thrusters once it has achieved pointing towards the debris. Per [100], attitude acquisition can be confirmed when the scalar component of the error quaternion is above a threshold value ϵ_p which is near one. This threshold for attitude acquisition is identical to the solution implemented in Section. 5.4.3.

Additional considerations must be made to prevent excessively high torques from being developed in the tether. One method of doing so is to limit the allowable relative velocity between the tether and the debris so as to reduce the energy stored in the tether when it is pulled taught. To this end, a relative velocity limit ϵ_v was implemented to stop thrust if the relative velocity of the debris away from the chaser exceeds the limit.

A complication which also effects station keeping in this work is regarding the convergence time of the Kalman Filter (KF) that estimates the debris COM position presented later in Section. 6.4.1 after tension is developed in the tether. When tension is induced in the tether, the motion of the debris changes and the KF is required to converge to this new motion. This convergence is accomplished most effectively by allowing a few discrete-time samples to elapse before creating tension in the cable again. Therefore, a thruster constraint was added based on the number of discrete-time samples which have elapsed since the previous tension event. If the number of elapsed samples is less than a maximum value defined by $n_{k_{max}}$ the station keeping control law will command no thrust. The KF internally counts these samples, resetting the sample count to 0 if it reaches $n_{k_{max}}$ until tension is experienced in the tether again. The resulting station keeping control law is formed in Eq. (6.18) where n_k is the current KF sample count:

$$F = \begin{cases} F = -F_{max}\text{sign}(e_s), \text{ if } (q_{e_4} > \epsilon_p) \wedge (v_{rel} < \epsilon_v) \\ F = 0, \text{ if } n_k \neq 0 \\ F = 0, \text{ else} \end{cases} \tag{6.18}$$

In this control law F_{max} is the thrust produced by the thruster and v_{rel} is the magnitude of the relative velocity of the chaser towards or away from the debris. The vector quantity of relative velocity can be defined as $\boldsymbol{v}_{rel} = \boldsymbol{v}_D - \boldsymbol{v}_C$ so that v_{rel} is positive if the distance between the chaser and debris is increasing. v_{rel} can be computed using the following relationship which is used specifically to preserve the sign (either positive or negative) indicating if the distance between the spacecraft is increasing or decreasing:

$$v_{rel} = (|v_{rel_1}|v_{rel_1} + |v_{rel_2}|v_{rel_2} + |v_{rel_3}|v_{rel_3})/|\boldsymbol{v}_{rel}| \tag{6.19}$$

The thrust force must be projected along $\boldsymbol{z}_C$, where $\boldsymbol{x}_C, \boldsymbol{y}_C, \boldsymbol{z}_C$ are the BF frame bases vectors forming $\boldsymbol{\mathcal{F}}_C$. Then it can be expressed as an equivalent vector in $\boldsymbol{\mathcal{F}}_{ECI}$ to be applied in the transnational equation of motion from Eq. (6.1). Such an operation is conducted because of the previous selection of having the thrust force along the z-axis of $\boldsymbol{\mathcal{F}}_C$. Therefore, the thrust force applied on the chaser in $\boldsymbol{\mathcal{F}}_{ECI}$ can be formed as:

$$\boldsymbol{F} = \boldsymbol{\mathcal{A}}_{BF,C}^{ECI}\left(F\boldsymbol{z}_C\right) \tag{6.20}$$

The attitude acquisition and station keeping tasks are illustrated in Fig. 6.3a - Fig. 6.3f where the spacecraft dynamics are observed in $\boldsymbol{\mathcal{F}}_{REL}$. Green denotes the chaser body and respective BF frame $\boldsymbol{\mathcal{F}}_C$, red denotes the debris body and respective BF frame $\boldsymbol{\mathcal{F}}_D$, the black line represents the tether and the blue line is the path traced by the debris COM over time. All objects are shown to scale. As shown by comparing Fig. 6.3c to Fig. 6.3d, there is no translational motion between the bodies until the chaser acquires a debris pointing attitude. In Fig. 6.3d at 0.4 minutes the debris can be seen to start moving away from the chaser when expressed in $\boldsymbol{\mathcal{F}}_{REL}$. The movement is denoted by the small length of blue line. The translational motion in Fig. 6.3d is caused by the fact that the chaser $z+$ axis is now pointing at the debris (roughly along the tether vector) which means that the chaser has acquired the desired attitude $\boldsymbol{q}_a$ and has begun thrusting away from the debris [123]. In $\boldsymbol{\mathcal{F}}_{REL}$ this motion is observed as the debris moving away from the chaser. Referring to the enlarged window in Fig. 6.3e, there has not been any tension events 1.65 minutes into the simulation because there are no discontinuities in the path of the blue trace which would indicate that the chaser pulled the debris using the tether. In Fig. 6.3f, however, the debris can be seen to remain around 10 meters from the chaser because the nominal length of the tether was set to 10 meters in this simulation. The more jagged and discontinuous blue lines in the enlarged plot of Fig. 6.3f indicate that tension was developed in the tether multiple times.

6.4 Pose Estimation

6.4.1 Center of Mass Estimation

To obtain a determinable input torque that is applied on the debris as a result of tether tension, additional parameters must be estimated prior to estimating inertia. In this work, estimating and tracking the COM location of the debris was considered the "first stage" of the TSE. To achieve estimation of the debris COM location, this section presents a novel pseudo measurement Kalman Filter which estimates some of the relevant translational states of the debris' motion. The derived formulations which estimate these translational components of the debris pose assume that algorithms like ICP have already been implemented to extract rotational components of the debris pose. Rotational pose extraction from visual sensors is a well studied concept which can be seen in works such as [128] and [136].

The translational dynamics of a spacecraft freely flying in space are linear. Such dynamics allows for a new KF to be implemented which can produce the optimal state

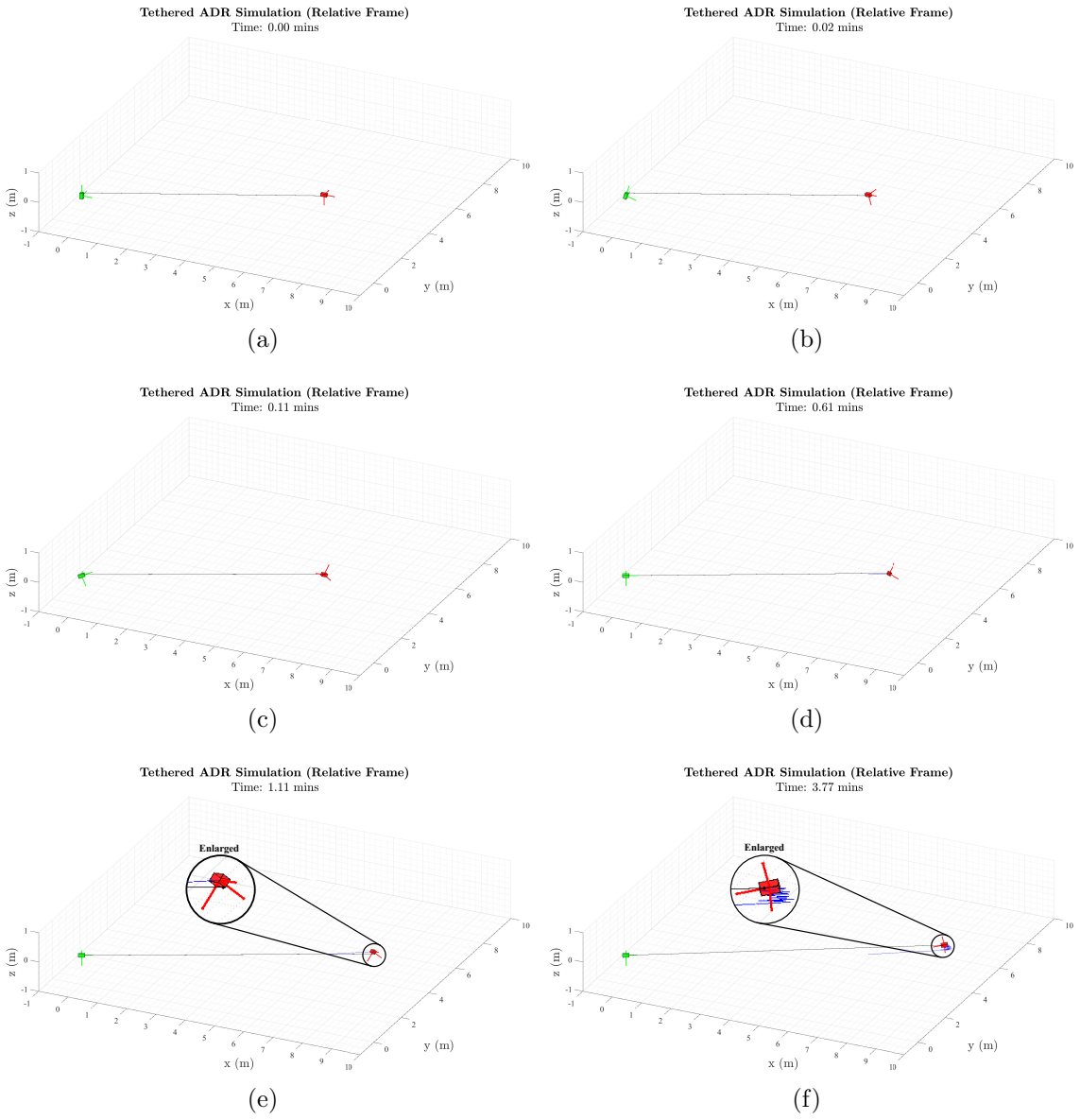

Figure 6.3: Chaser Satellite Attitude and Station Keeping Demonstration

estimate for the translating body. For the case of LiDAR-based translational pose estimation, this section adapts discrete time KF formulations from [137] to improve the KF responsiveness to rapid changes in the rotation and translation of a tethered space debris. Improving the responsiveness of the KF was a critically important research task so that the debris COM location could be estimated accurately despite frequent and brief tension events in the tether. Improved KF responsiveness was achieved by introducing a novel pseudo debris velocity measurements into the KF formulations which are developed in this section. Let dt_e be the sampling time for inertia estimation (selected as 0.05s) so that the KF dynamic model may be formed as:

$$\boldsymbol{x}_k = \begin{Bmatrix} \boldsymbol{v}_{rel,KF} \\ \boldsymbol{r} \\ \boldsymbol{r}_d \end{Bmatrix}_k = \begin{bmatrix} \boldsymbol{I}_{3\times3} & \boldsymbol{0}_{3\times3} & \boldsymbol{0}_{3\times3} \\ dt_e\boldsymbol{I}_{3\times3} & \boldsymbol{I}_{3\times3} & \boldsymbol{0}_{3\times3} \\ \boldsymbol{0}_{3\times3} & \boldsymbol{0}_{3\times3} & \boldsymbol{I}_{3\times3} \end{bmatrix} \begin{Bmatrix} \boldsymbol{v}_{rel,KF} \\ \boldsymbol{r} \\ \boldsymbol{r}_d \end{Bmatrix}_{k-1} = \boldsymbol{F}_k\boldsymbol{x}_{k-1} \tag{6.21}$$

The state vector is 9×1, with the estimated relative velocity vector $\boldsymbol{v}_{rel,KF}$ expressed in $\mathscr{F}_{REL}$, the debris COM position $\boldsymbol{r}$ expressed in $\mathscr{F}_{REL}$, and the COM offset vector from the geometric center $\boldsymbol{r}_d$ expressed in $\mathscr{F}_{BF,D}$ all being 3×1 column matrices. The propagation phase is completed by computing the covariance matrix $\boldsymbol{P}_{k|k-1}$ as:

$$\boldsymbol{P}_{k|k-1} = \boldsymbol{F}_k\boldsymbol{P}_{k-1|k-1}\boldsymbol{F}_k^T + \boldsymbol{Q}_k \tag{6.22}$$

where the process covariance matrix was computed in this thesis as:

$$\boldsymbol{Q}_k = (10\text{E} - 6)\boldsymbol{I}_{9\times9} \tag{6.23}$$

The measurements provided to the KF include the pose vector $\boldsymbol{r}_{pose}$ and a pseudo measurement of debris COM relative velocity by using the KF $\boldsymbol{r}_d$ estimation to remove rotational components from the LiDAR velocity measurement $\boldsymbol{v}_{D_m}$ of Eq. (6.12). It follows that the pseudo velocity measurement may be formulated as:

$$\boldsymbol{v}_{rel_m} = \boldsymbol{v}_{D_m} - \boldsymbol{\mathcal{A}}_{BF,D}^{ECI}\left(\boldsymbol{r}_{d|k-1}^{\times}\boldsymbol{\omega}_{D_m}\right) \tag{6.24}$$

By comparing Eq. (6.24) to Eq. (6.12) it is clear that if the debris spacecraft is not shedding mass, $\boldsymbol{r}_d$ is constant, meaning that the converged $\boldsymbol{r}_{d|k-1}$ estimate value is sufficient to remove rotational components from the relative velocity measurement. Poor initial estimates of $\boldsymbol{r}_{d|k-1}$ could, in theory, cause the KF to diverge by the fact that the relative velocity pseudo measurement would be very poor. To ease these concerns, a convergence study is provided in Section. 6.4.2 to demonstrate KF robustness to poor initial pseudo measurements. To perform the update stage, the measurement vector $\boldsymbol{y}_k = [\boldsymbol{v}_{rel_m}, \boldsymbol{r}_{pose}]^T$ may be formed as a 6×1 vector of relevant debris pose measurements. Applying the measurement matrix $\boldsymbol{H}_k$ leads to the proposed pseudo measurement KF innovation error to be formed as:

$$\tilde{\boldsymbol{y}} = \boldsymbol{y}_k - \boldsymbol{H}_k\boldsymbol{x}_{k|k-1} \tag{6.25}$$

where $\boldsymbol{H}_k$ was derived as follows to accommodate the pseudo measurement:

$$\boldsymbol{H}_k = \begin{bmatrix} \boldsymbol{I}_{3\times3} & \boldsymbol{0}_{3\times3} & \boldsymbol{0}_{3\times3} \\ \boldsymbol{0}_{3\times3} & \boldsymbol{I}_{3\times3} & \boldsymbol{\mathcal{A}}_{BF,D}^{ECI} \end{bmatrix} \tag{6.26}$$

Because $\mathscr{F}_{REL}$ has been defined to be aligned with $\mathscr{F}_{ECI}$ the $\boldsymbol{\mathcal{A}}_{BF,D}^{ECI}$ component of $\boldsymbol{H}_k$ is functionally equivalent to using $\boldsymbol{\mathcal{A}}_{BF,D}^{REL}$ [123]. The measurement covariance matrix $\boldsymbol{R}_k$ was constructed by applying the measurement variances σ_v^2, σ_r^2 for the velocity

and pose quantities, respectively, as follows:

$$\boldsymbol{R}_k = \begin{bmatrix} \sigma_v^2 \boldsymbol{I}_{3\times3} & \boldsymbol{0}_{3\times3} \\ \boldsymbol{0}_{3\times3} & \sigma_r^2 \boldsymbol{I}_{3\times3} \end{bmatrix} \tag{6.27}$$

The remainder of the pseudo measurement KF formulations follow that of the standard KF for the update stage.

6.4.2 Pseudo Measurement Kalman Filter Convergence Study

The convergence of the KF is largely dictated by the spin of the space debris. Not all spins guarantee convergence of the filter. For example, for debris in a flat spin (a spin which is not precessing), the KF will not receive sufficiently rich data to converge to the COM offset vector. The KF converges most efficiently when the spin axis of the debris is precessing. Shown in [137], the original KF formulations receiving only pose vector measurements, converges quickest when the nutation angle of the spin is between 20° - 60°. Spin axis precession is only guaranteed by the spinning body being tri-inertial or inertially asymmetrical. Whilst real debris objects are unlikely to be perfectly isoinertial, it is reasonable to expect some debris objects to experience spin axis precession that is relatively slow. Both these conditions negatively impact the ability of the KF to converge and they should be considered prior to attempting estimation. For the tri-inertial space debris object presented later in Section. 6.6.2, Fig. 6.4 presents an example of a desired degenerate spin where the spin axis experiences are relatively large nutation angle. In such a spin, good estimation performance can be expected.

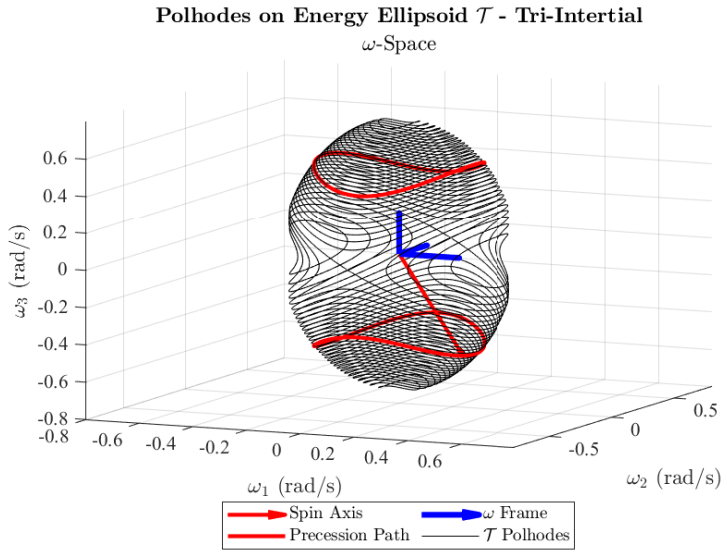

Figure 6.4: Example Degenerate Spin of Tri-Inertial Space Debris Shown as a Polhode on the Energy Ellipsoid

Additional scrutiny should also be placed on the quality of the initial estimate provided to the KF for the COM offset vector $\boldsymbol{r}_d$. For poor initial estimates, the pseudo measurement $\boldsymbol{v}_{rel_m}$ is an increasingly poor representation of the actual debris relative velocity. A convergence study is shown in Fig. 6.5 which displays the amount of time required for the KF velocity estimates to converge when varying levels of error are provided on the initial offset value. The study shows that, even for unreasonable initial estimations where the offset distance is larger than the tether length, the KF is robust to poor initial pseudo measurements.

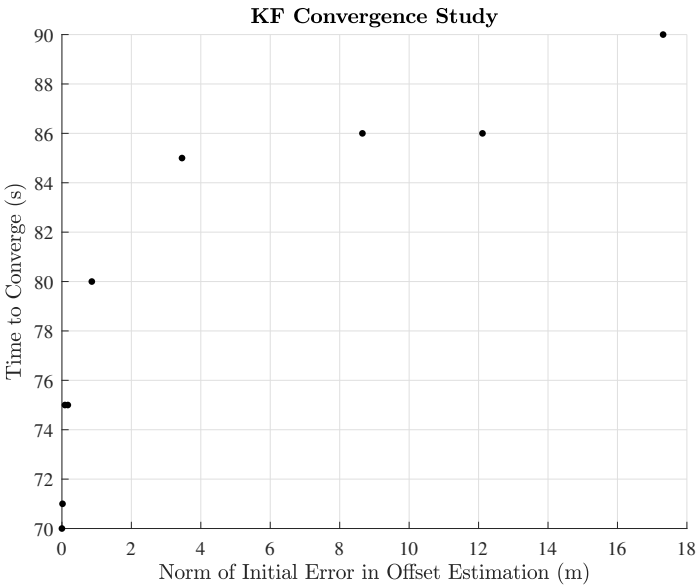

Figure 6.5: Convergence Time of Pseudo Measurement KF with Varying Levels of Error in Initial Offset Estimation

6.5 Inertia Estimation

In this section the Quick-Response Iterative Inertia Properties Identification Algorithm (QRIIPEA) estimator presented in [134] is adapted for estimating the space debris inertia and the dynamics formulations which enable the estimator to be applied on a tethered chaser-debris system are developed. The result of these developments, in combination with the pseudo measurement KF represent the proposed novel Two-Stage Estimator (TSE) which is capable of estimating the complete inertia tensor of tethered space debris. QRIIPEA has previously been shown to be effective for inertia estimation of combined satellite systems because it responds quickly to changes in input or changes in inertia; however, the estimator has yet to be applied to estimating the inertia of space debris using a tether. For the case of the present thesis, QRIIPEA was selected as the secondary filter because it was found in the present author's original work in [123] to allow for relatively fast estimation response to the brief tether tension events. In many cases, these tension events are on the order of

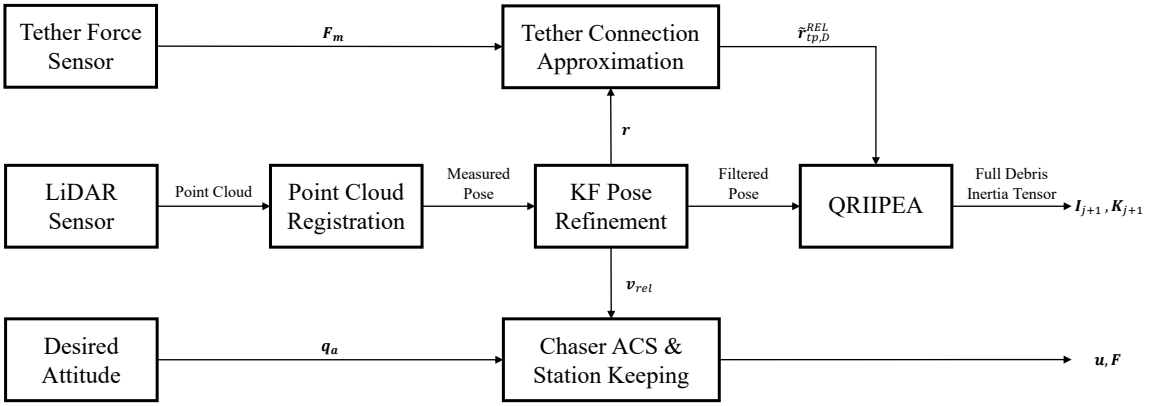

Figure 6.6: Proposed TSE Architecture Showing Interconnection of Filters, Sensors and Control

tens of samples or less. The data flow from sensors to the QRIIPEA algorithm can be seen in Fig. 6.6. Observing Fig. 6.6, the term "Filtered Pose" is used to describe the dataset including $\boldsymbol{q}_{D_m}$, $\boldsymbol{\omega}_{D_m}$ and $\dot{\boldsymbol{\omega}}_{D_m}$.

While the proposed architecture in Fig. 6.6 is capable of complete inertia tensor estimation, it is also capable of removing the debris tether connection point assumption while maintaining a determinable input torque. This feature fulfills the secondary motivation of this work: to relax some of the assumptions required to perform inertia estimation through a tether. The determinable input torque is achieved by (1) the KF estimate of the debris COM in $\mathscr{F}_{REL}$ and by (2) approximating the tether connection point location using tether force measurements. By reasonably estimating or approximating both the aforementioned points, there is sufficient information to determine the torque vector applied to the debris through the tether by the tether being connected offset from the debris' COM. This torque, is fed to QRIIPEA so that all 6 inertial parameters can be estimated for the debris.

The QRIIPEA formulations are provided in Eq. (6.28) by adapting the work presented in [134]. For the present thesis, translational motion components of QRIIPEA were withdrawn to improve calculation efficiency for the subject application. The subscript "$j+1$" represents new estimates or measurements and the "j" terms represent previous estimates or measurements. The forgetting factor ρ must be properly selected within the bounds $0 < \rho < 1$ so that the estimates converge to the actual inertia parameters without being overly sensitive to new measurements. A ρ value close to 0 means that old estimates are quickly suppressed in favor of emphasizing estimation using new estimates. A ρ value near 1 will cause the estimator to value older estimations more highly. Two quantities are estimated including the inertia parameters $\boldsymbol{I}_j$ and a gain matrix $\boldsymbol{K}_j$ through the following iterative relationship:

$$\begin{cases} \boldsymbol{I}_{j+1} = \boldsymbol{I}_j + \boldsymbol{K}_{j+1}\boldsymbol{W}_{j+1}^T(\boldsymbol{T}_{j+1} - \boldsymbol{W}_{j+1}\boldsymbol{I}_j) \\ \boldsymbol{K}_{j+1} = \frac{1}{\rho^2}\left[\boldsymbol{K}_j - \boldsymbol{K}_j\boldsymbol{W}_{j+1}^T(\rho^2\boldsymbol{E}_3 + \boldsymbol{W}_{j+1}\boldsymbol{K}_j\boldsymbol{W}_{j+1}^T)^{-1}\boldsymbol{W}_{j+1}\boldsymbol{K}_j\right] \end{cases} \tag{6.28}$$

In Eq. (6.28) $\boldsymbol{W}_{j+1}$ is the 3×6 output matrix, $\boldsymbol{T}_{j+1}$ represents the 3×1 input torque matrix,$\boldsymbol{E}_3$ is a 3×3 identity matrix, and $\boldsymbol{K}_j$ is a 6×6 gain matrix specific to an estimate of inertia parameters defined by $\boldsymbol{I}_j = [I_{xx}, I_{yy}, I_{zz}, I_{xy}, I_{xz}, I_{yz}]^T$. Representing the identity matrix with $\boldsymbol{E}_3$ was done to avoid confusion here with the inertia parameters matrix. The output matrix is calculated as:

$$\boldsymbol{W}_{j+1} = \boldsymbol{w}_1 + \boldsymbol{w}_2 \tag{6.29}$$

Each $\boldsymbol{w}_n$ component of $\boldsymbol{W}_{j+1}$ is a 3×6 matrix obtained by linearizing the rotational dynamics differential equation shown in Eq. (6.2). $\boldsymbol{w}_{1-2}$ are provided as follows:

$$\boldsymbol{w}_1 = \begin{bmatrix} \dot{\omega}_x & 0 & 0 & \dot{\omega}_y & \dot{\omega}_z & 0 \\ 0 & \dot{\omega}_y & 0 & \dot{\omega}_x & 0 & \dot{\omega}_z \\ 0 & 0 & \dot{\omega}_z & 0 & \dot{\omega}_x & \dot{\omega}_y \end{bmatrix} \tag{6.30}$$

$$\boldsymbol{w}_2 = \begin{bmatrix} 0 & -\omega_y\omega_z & \omega_y\omega_z & -\omega_x\omega_z & \omega_x\omega_y & \omega_y^2 - \omega_z^2 \\ \omega_x\omega_z & 0 & -\omega_x\omega_z & \omega_y\omega_z & \omega_z^2 - \omega_x^2 & -\omega_x\omega_y \\ -\omega_x\omega_y & \omega_x\omega_y & 0 & \omega_x^2 - \omega_y^2 & -\omega_y\omega_z & \omega_x\omega_z \end{bmatrix} \tag{6.31}$$

6.5.1 Input Torque Approximation

The input torque which excites the rotational motion of the debris results from the applied tension developed in the tether being offset from the COM of the debris. The proposed chaser satellite has the ability to measure the tension force vector of the tether by employing a force sensor. In order to develop $\boldsymbol{T}_{j+1}$ as an input to QRIIPEA, the tether connection point on the debris must be approximated by leveraging the tether tension measurement made by the chaser. In practical applications the debris connection point is difficult to know exactly, but it is demonstrated in this work that an approximation of its location is sufficient for inertia estimation.

To determine the tether connection point in $\mathscr{F}_D$, the tether end point must first be located with respect to the $\mathscr{F}_{REL}$ coordinate system. To do so, first let $\boldsymbol{F}_m$ be the 3×1 tether force vector measurement made by the chaser and expressed in $\mathscr{F}_{REL}$ such that the measurement model simulating $\boldsymbol{F}_m$ may be expressed as:

$$\boldsymbol{F}_m = \boldsymbol{T}_C + \boldsymbol{\eta}_T \tag{6.32}$$

where $\boldsymbol{\eta}_T$ is band-limited white noise corrupting the tension measurement. Assuming that the stretched length of the tether is reasonably close to the nominal length, (an assumption which holds for relatively stiff tethers) then the location of the tether endpoint in $\mathscr{F}_{REL}$ may be approximated by computing the unit direction vector of the tether tension measurement and scaling this value by the nominal length of the tether. In an ideal case where no noise is present in the tether tension measurement, the tether tension measurement vector would lie along the true tether vector. As a consequence of these dynamics, the approximate location of the tether connection

point on the debris expressed in $\mathscr{F}_{REL}$ may be described by:

$$\boldsymbol{r}_{tether} = l_0 \frac{\boldsymbol{F}_m}{|\boldsymbol{F}_m|} \tag{6.33}$$

Then by leveraging the KF estimate of the debris COM location $\boldsymbol{r}$ expressed in $\mathscr{F}_{REL}$, the tether-COM offset vector (also expressed in $\mathscr{F}_{REL}$) can be computed following:

$$\tilde{\boldsymbol{r}}_{tc,D}^{REL} = \left(\boldsymbol{\mathcal{A}}_{BF}^{ECI}\boldsymbol{r}_{tp,C} + \boldsymbol{r}_{tether}\right) - \boldsymbol{r} \tag{6.34}$$

In Eq. (6.34), $\boldsymbol{r}_{tp,C}$ is ground truth knowledge of the specifically selected chaser satellite tether connection point and the remaining quantities of Eq. (6.34) are based only on measurements or KF estimates. The assumption that the tether connection point is known in the BF frame of the debris $\mathscr{F}_D$ can, therefore, be removed in the proposed TSE by noting that the tether-COM offset vector in $\mathscr{F}_{REL}$ may be expressed as an equivalent vector in the debris BF frame if the debris' attitude quaternion $\boldsymbol{q}_{D_m}$ is available from point cloud registration. The transformation of the tether-COM offset vector to its expression in $\mathscr{F}_D$ is performed by:

$$\tilde{\boldsymbol{r}}_{tc,D} = \boldsymbol{\mathcal{A}}_{REL}^{BF}\tilde{\boldsymbol{r}}_{tc,D}^{REL} \tag{6.35}$$

In both Eq. (6.34) and Eq. (6.35), the tilde is used to represent that the solution is approximate. In addition to the tether connection point vector, the tether force vector which acts on the debris must also be expressed in $\mathscr{F}_D$ following:

$$\boldsymbol{F}_{D,m} = \boldsymbol{\mathcal{A}}_{REL}^{BF}(-\boldsymbol{F}_m) \tag{6.36}$$

With both the moment arm and force known in $\mathscr{F}_D$, the input-output mapping performed by QRIIPEA can be completed. Therefore, the input torque fed to the QRIIPEA estimator is calculated using the following relationship:

$$\boldsymbol{T}_{j+1} = (\tilde{\boldsymbol{r}}_{tc,D})^{\times}\boldsymbol{F}_{D,m} \tag{6.37}$$

6.5.2 Handling Frequent Tether Slackness

The proposed station keeping control law has been developed to excite the rotational motion of the debris and then allow visual sensors to observe the motion. For the TSE to handle these dynamics an adaptation must be made to the QRIIPEA formulations to prevent the estimator from diverging when no tension is being measured in the tether and the force measurements are dominated by noise. The adaptation involves allowing the estimator to pass through previous estimates of $\boldsymbol{I}_j$ and $\boldsymbol{K}_j$ when no tension is being measured in the tether. Should tension be measured in the cable, then the QRIIPEA formulations can proceed with applying Eq. (6.28) to make new estimates. For the operation to be carried out successfully, the force sensor noise characteristics must be quantified so that a minimum tension threshold ϵ_F can be selected for which the measured tension must be above this threshold for new estimates to be made. The current thesis selected ϵ_F to be above the 99% prediction interval

bound of the band-limited white noise applied in the $\boldsymbol{F}_m$ measurement. If $|\boldsymbol{F}_m| \leq \epsilon_F$ the previous estimates are propagated through as:

$$\begin{cases} \boldsymbol{I}_{j+1} = \boldsymbol{I}_j \\ \boldsymbol{K}_{j+1} = \boldsymbol{K}_j \end{cases} \tag{6.38}$$

Since the estimator operates only when tension is measured in very brief time intervals and is otherwise on stand-by, the effects of environmental external disturbance torques are conveniently minimized. In the case of Scenario 1, presented as part of the ADR case study results, the tension events have a typical duration of 0.3 seconds – a duration which makes it reasonable to neglect environmental disturbance torques in the formulations of the estimator. Moreover, neglecting disturbances is also justified by the fact that the disturbance torques are orders of magnitude smaller than the tether induced torque. With a sample time dt_e of 0.05 seconds, 6 estimations can be produced for a 0.3 second tension event. Also in Scenario 1, the average time spent between tension events was 18.5 seconds. During this time, Eq. (6.38) passes through estimates from the previous tension event, preventing divergence of the TSE and external disturbance torques from affecting the results.

6.6 Active Debris Removal Results

The results presented in this section are used to quantify the performance of the TSE proposed in this chapter. Three simulations are presented with the first simulation demonstrating inertia estimation when the tether connection point is assumed to be known. The following simulation removes this assuming to quantify the inertia estimation quality when the tether connection point assumption is removed. The final simulation updates the DGSPCMG SCL and attitude controller with the estimated debris inertia tensor to demonstrate the post capture attitude control improvement obtained by first estimating debris inertia during an ADR mission.

6.6.1 Simulation 1 - Ideal Conditions & Known Tether Connection Point

The results presented in this section were produced from the set of simulation parameters shown in Table 6.1 governing the two spacecraft, the tether, and the estimators. The debris spacecraft in Simulation 1 was modeled to be an inertially axisymmetric body with overall dimensions of $0.1 \times 0.1 \times 0.3$ (m). These dimensions would classify the debris as a 3U CubeSat which is one U larger than the 2U chaser satellite. The goal of the TSE is to identify the true debris inertia tensor which is defined by products of inertia (off diagonal elements) and principal moments of inertia (diagonal elements) as shown by:

$$\boldsymbol{J}_D = \begin{bmatrix} 0.0333 & 0 & 0 \\ 0 & 0.0333 & 0 \\ 0 & 0 & 0.0067 \end{bmatrix} \text{kgm}^2$$

Table 6.1: Key Initial Conditions for Ideal ADR Simulation

Ideal ADR Simulation Parameters

Description	**Parameter**	**Value and Units**
Debris:		
Mass	m_D	4 (kg)
Initial Spin	$\boldsymbol{\omega}_{D_0}$	$[0.25, -0.15, 0.1]^T$ (rad/s)
Initial Quaternion	$\boldsymbol{q}_{D_0}$	$\frac{\sqrt{2}}{2}[0, 1, 0, 1]^T$ (unitless)
Tether Connection Point	$\boldsymbol{r}_{tp,D}$	$[0.05, 0.05, 0.05]^T$ (m)
Offset Vector	$\boldsymbol{r}_d$	$[0.02, 0.01, -0.02]^T$ (m)
Initial Position	$\boldsymbol{R}_{D_0}$	$[6.12244, 2.92665, -0.00019]^T \cdot 10^3$ (m)
Initial Velocity	$\boldsymbol{v}_D$	$[-2049.4, 4292.6, 6010.1]^T$ (m/s)
Chaser:		
Mass	m_D	2 (kg)
Initial Spin	$\boldsymbol{\omega}_{C_0}$	$[0.00, 0.00, 0.00]^T$ (rad/s)
Initial Quaternion	$\boldsymbol{q}_{C_0}$	$[0, 0, 0, 1]^T$ (unitless)
Tether Connection Point	$\boldsymbol{r}_{tp,C}$	$[0.00, 0.00, 0.10]^T$ (m)
Initial Position	$\boldsymbol{R}_{C_0}$	$[6.12243, 2.92665, -0.00019]^T \cdot 10^3$ (km)
Initial Velocity	$\boldsymbol{v}_C$	$[-2049.4, 4292.6, 6010.1]^T$ (m/s)
Max Thrust	F_{max}	0.5 (N)
Tether:		
Stiffness	k	80 (N/m)
Damping	c	0.5 (Ns/m)
Length	l_0	10 (m)
Control & Estimators:		
KF Parameters	$\boldsymbol{Q}_0$, $\boldsymbol{x}_0$, $\boldsymbol{P}_0$	$\boldsymbol{E}_{9\times9} \cdot 10^{-6}$, $\boldsymbol{0}_{9\times1}$, $\boldsymbol{E}_{9\times9} \cdot 10^{-6}$
QRIIPEA Parameters	$\boldsymbol{I}_0$, $\boldsymbol{K}_0$, ρ	$[0.0015, 0.0015, 0.0015, 0, 0, 0]^T$, $0.1 \cdot \boldsymbol{E}_{6\times6}$, 0.98
Thrust Constraints	ϵ_v, ϵ_p, n_k	0.025 (m/s), 0.9995, 200 (samples)
Station-Keeping Set-point	ζ_l	10.05 (m)
Noise Variances	σ_r^2, σ_v^2, σ_ω^2, $\sigma_{\dot{\omega}}^2$, σ_q^2, σ_T^2	10^{-9}, 10^{-8}, 10^{-8}, 10^{-8}, 10^{-7}, 10^{-8}

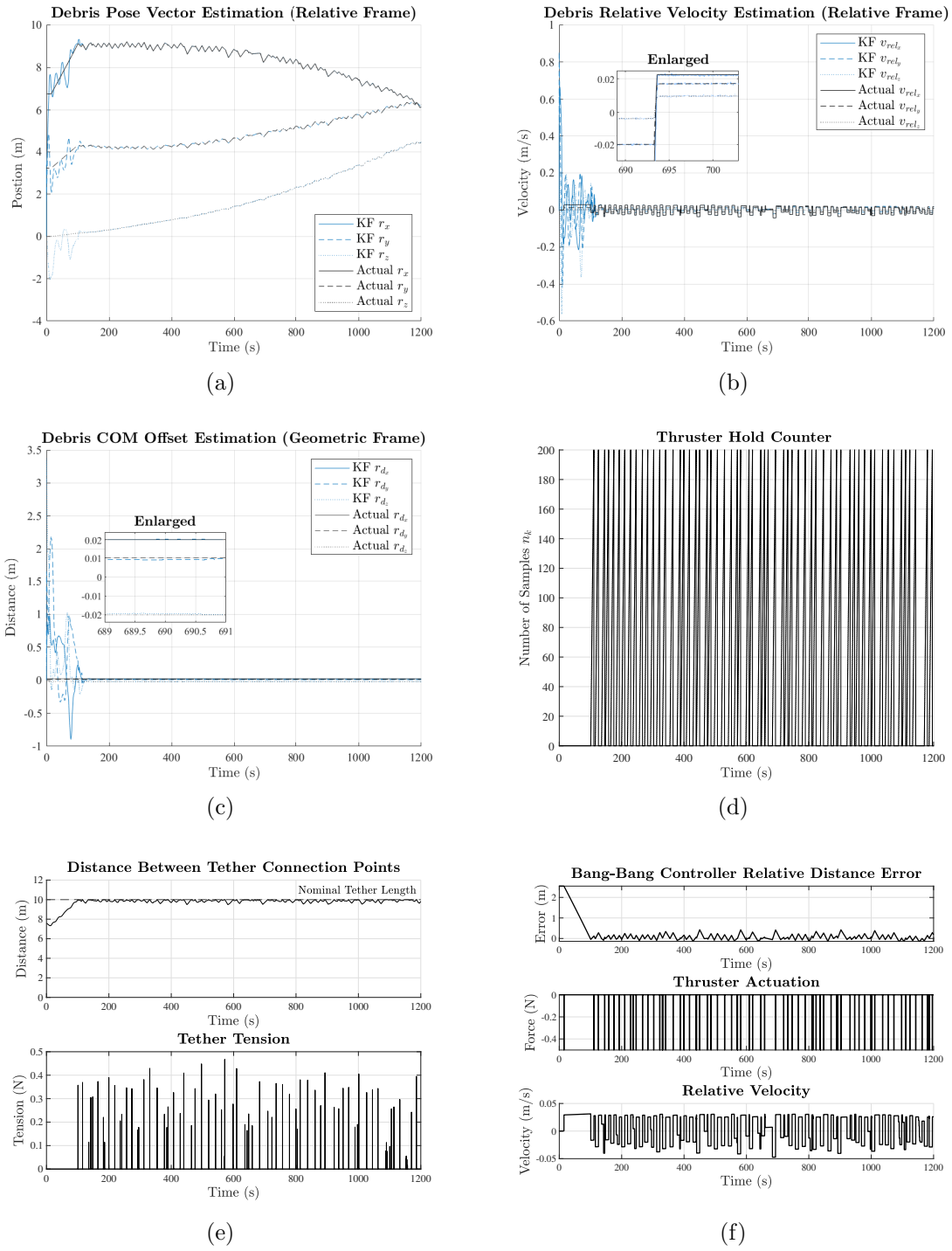

Figure 6.7: Kalman Filter and Tether Results For Inertially Axisymmetric Debris

The first series of results presented in Fig. 6.7a - Fig. 6.7f demonstrates the pseudo measurement KF performance, shows details of the state of the tether, and shows how the thruster was actuated during the simulation. Referring to Fig. 6.7a - Fig. 6.7c

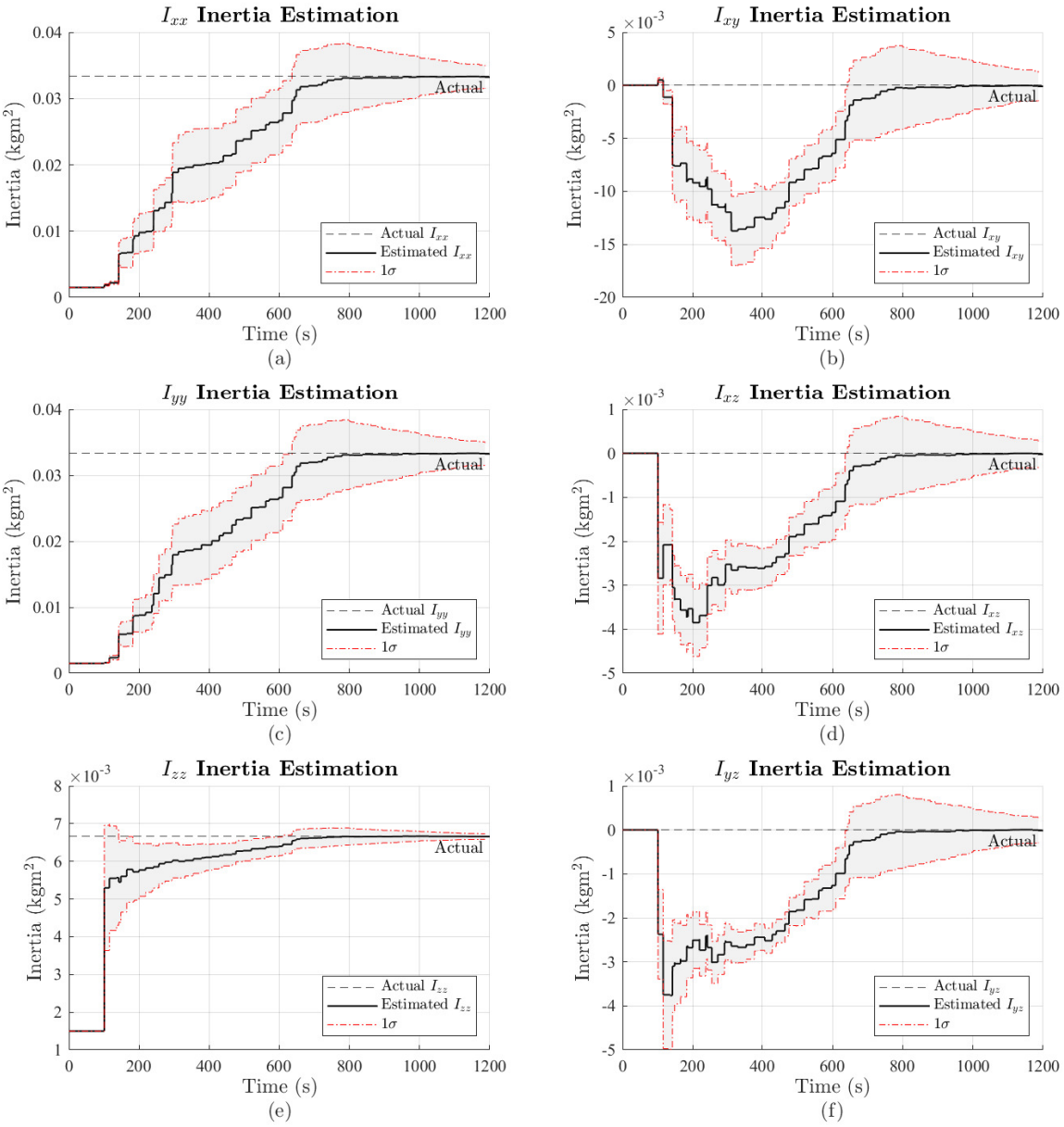

Figure 6.8: Axisymmetric Debris Inertia Estimation

the pseudo measurement KF can be observed to be relatively slowly converging to the actual values of $\boldsymbol{r}$, $\boldsymbol{r}_d$, and $\boldsymbol{v}_{rel,KF}$ while the chaser is backing away from the debris to the station keeping setpoint distance of ζ_l. Around 120s of simulation time, the tether becomes taught and the motion of the debris is perturbed. The KF quickly converges to the true values shortly after this tension event, and remains very responsive to subsequent tension events hereinafter. Having the KF produce an accurate estimation of the debris COM position in Fig. 6.7a is particularly important as this value directly impacts the accuracy of the torque input provided downstream to QRIIPEA. For the simulation conditions used to produce the Simulation 1 results,

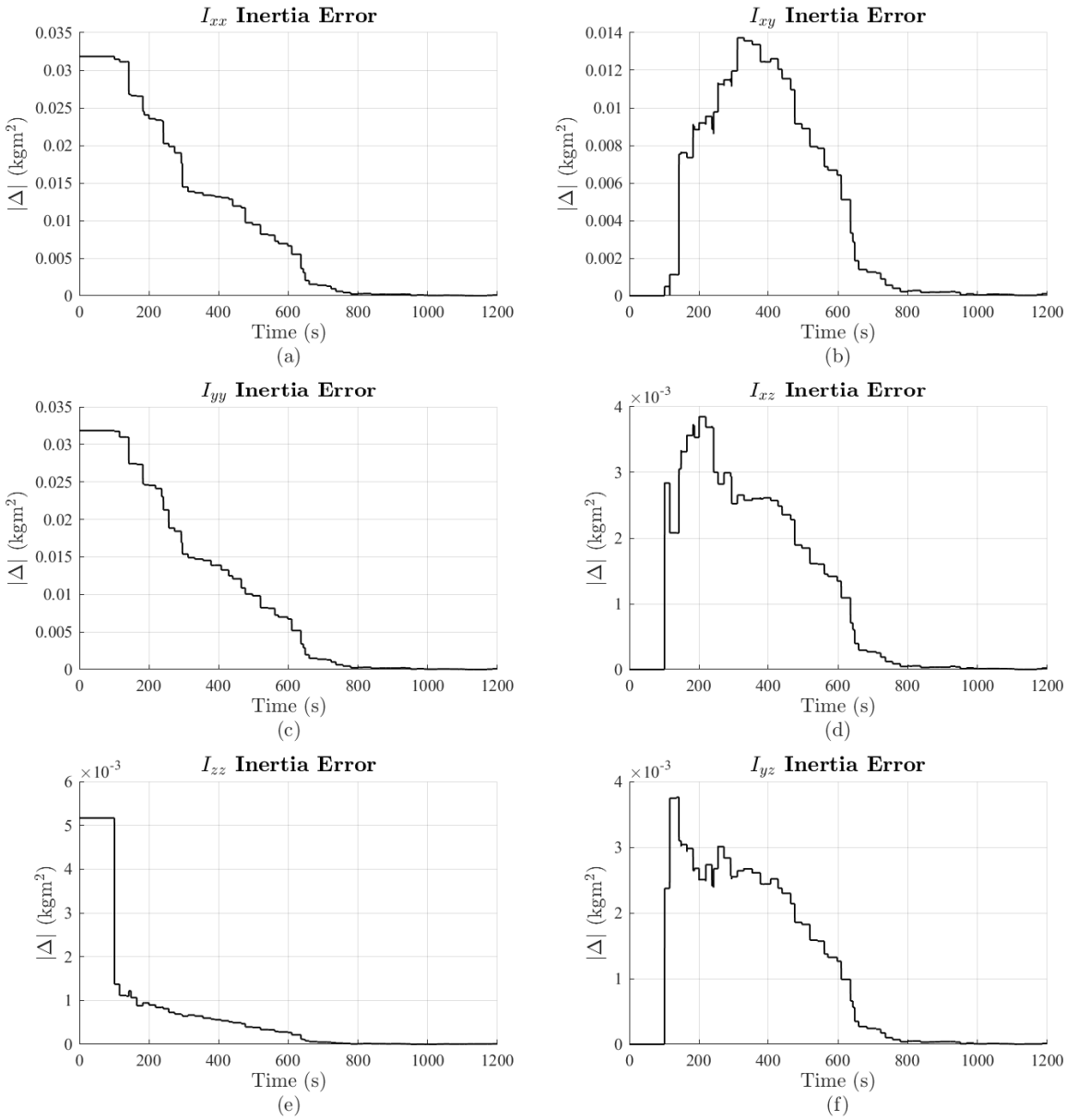

Figure 6.9: Estimation Error

the KF performs well, estimating the COM position $\boldsymbol{r}$ accurately largely because the pseudo velocity measurement has also converged to the true velocity. The KF robustness to the sequence of tension events can be attributed to the proper function of the KF sample thruster constraint shown in Fig. 6.7d. The counter in this simulation can be concluded to be a sufficient constraint to ensure KF convergence after a tension event.

Referring to Fig. 6.7e, the tether can be observed to experience a peak tension of 0.4675 N for the parameters used in this simulation. Also, after the first tension event, the closest distance between both tether connection points was 9.486 m. This

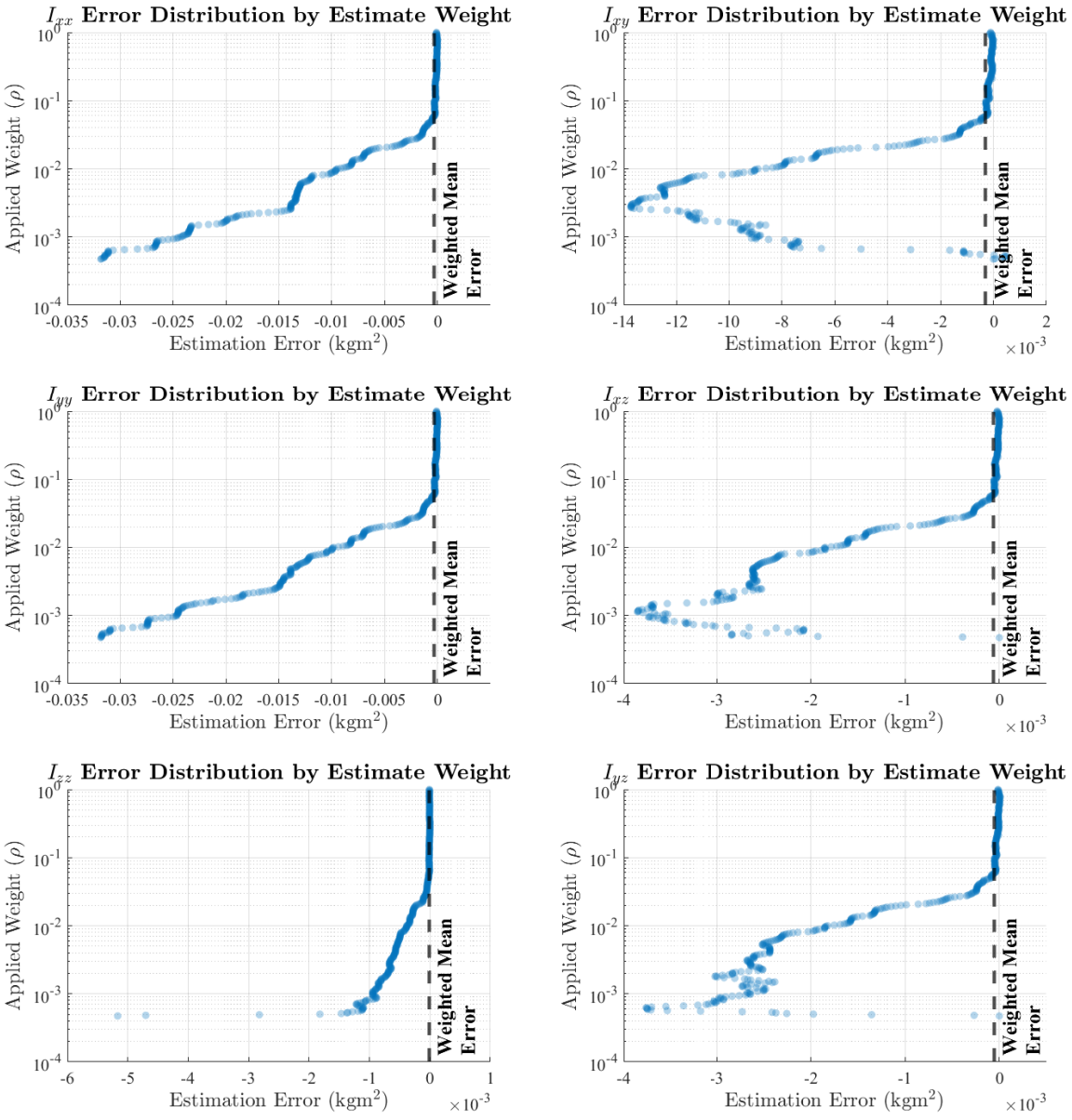

Figure 6.10: Estimation Error Distribution by Estimate Weight with Weighted Average Estimation Error

distance indicates that the thruster actuation, shown in Fig. 6.7f, is adequate to maintain station keeping. The result also suggests that, despite the comparatively larger size of the debris, the chaser and debris are only moderately pulled together by tether tension. Such dynamics are desirable because the chaser is only required to make brief thrusts to correct the station keeping distance as shown by Fig. 6.7f.

The results of the TSE estimating debris inertia with known debris tether connection point are plotted in Fig. 6.8. Having assumed the tether connection point on the debris to be known leads to the proposed TSE producing confident estimates

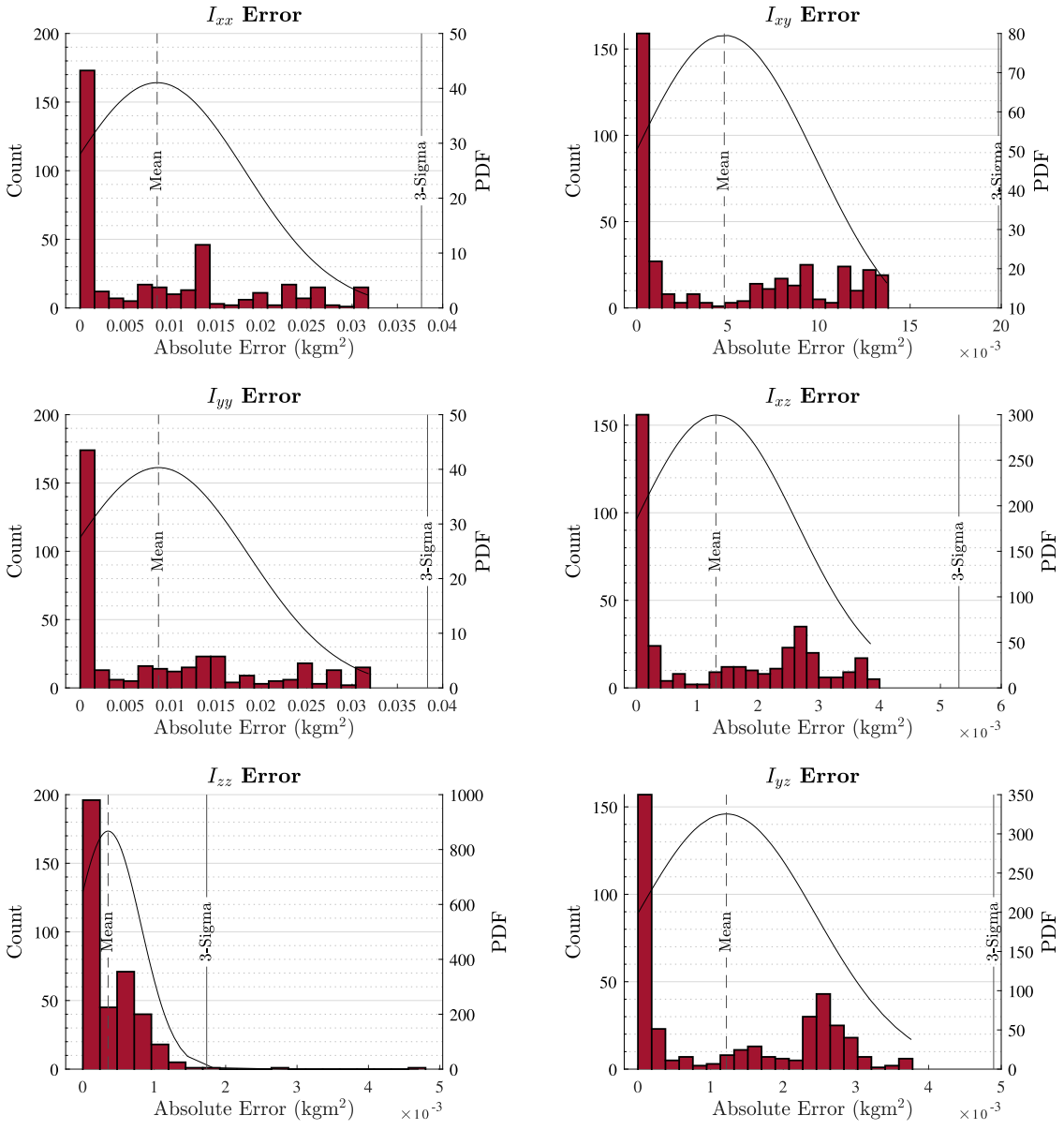

Figure 6.11: Estimation Error Distributions and Mean of Error Distributions Observed Without Considering ρ Factor

for all principal and products of inertia. The TSE is most confident in its estimation of the $\boldsymbol{I}_{zz}$ inertia parameter in Fig. 6.8. This confidence is largely because $\boldsymbol{I}_{zz}$ is the smallest principal moment of inertia, making rotation about this principal axis easily excitable by the tether. Noticeably in Fig. 6.8, the estimates for the products of inertia initially diverge prior to converging back to the true parameters. The reason for this divergence is twofold: the initial selection of the QRIIPEA gain matrix $\boldsymbol{K}_j$ was poor; and the initial estimates provided to QRIIPEA for the principal moments of inertia were far from the true value.

The estimate error progressions over simulation time are provided in Fig. 6.9 to demonstrate the convergence of the estimates. These estimate errors were also plotted as a function of the weight applied to that specific estimate in Fig. 6.10. Referring to Fig. 6.10, it can be observed that QRIIPEA has assigned larger weights to newer, more accurate estimates. The initial estimates which have relatively high errors have been suppressed by QRIIPEA by assigning weights which are orders of magnitude smaller than that applied to the new estimates. The action of estimate weight assignment is performed by the forgetting factor ρ which is repetitively applied for each new estimate, thereby suppressing the effect of older estimates on future estimates. The importance of proper ρ selection can be demonstrated by comparing the results in Fig. 6.10 to the results shown for the equally-weighted error distribution in Fig. 6.11. Referring to Fig. 6.11, the right most axis provides the relative likelihood of an estimate error corresponding to the normally distributed probability density function bell curve in each subplot.

Consider first the principal moment of inertia estimations (I_{xx}, I_{yy}, I_{zz}) which have been estimated to be 0.0332 ± 0.0048, 0.0332 ± 0.0051, $0.0067 \pm 2.094\text{E}-04$ kgm^2, respectively. For these estimates shown with the 3σ confidence level, the average absolute equally-weighted error was 0.0085, 0.0086 and $0.544\text{E}-04$ kgm^2, respectively. The average of estimate errors significantly reduces when accounting for the forgetting factor to $3.305\text{E}-04$, $3.291\text{E}-04$, $1.636\text{E}-05$ kgm^2, respectively, as shown by the dashed lines in Fig. 6.10. The lower average errors are only possible by QRIIPEA having suppressed the poor estimates in favour of more recent accurate estimates.

6.6.2 Simulation 2 - Tri-Inertial Debris & Non Ideal Estimation Conditions

The results presented in this section were produced using parameters largely detailed in Table 6.1. In this simulation the estimator was not provided with knowledge of the tether connection point and, therefore, the tether connection point has to be approximated by the estimator. Parametric changes made for Simulation 2, however, are presented in Table 6.2. The debris spacecraft in Simulation 2 was modeled after an arbitrary tri-inertial body with overall dimensions of $0.2 \times 0.25 \times 0.3$ (m). The goal of the TSE was to identify the true debris inertia tensor which also contains non-zero products of inertia and is defined by:

$$\boldsymbol{J}_D = \begin{bmatrix} 0.1271 & 0 & -0.025 \\ 0 & 0.1083 & 0 \\ -0.025 & 0 & 0.0854 \end{bmatrix} \text{kgm}^2$$

Table 6.2: Key Initial Conditions for Tri-Inertial ADR Simulation

Updated ADR Simulation Parameters From Table 6.1

Description	**Parameter**	**Value and Units**
Debris:		
Mass	m_D	10 (kg)
Tether Connection Point	$\boldsymbol{r}_{tp,D}$	$[0.20, 0.15, 0.00]^T$ (m)

A key parameter which makes inertia estimation more challenging in this simulation is the selection of the debris tether connection point to lie in the x-y plane of the debris body frame. By making this selection, it becomes relatively difficult to excite rotational motion about all axes. In fact, if the tether connection point is selected to be along any one principal inertial axis, it becomes difficult to excite rotational motion about that axis because the tether has not been modeled to carry or transmit a moment about its connection point. The results of this section aim to demonstrate that the proposed TSE can still estimate all principal and products of inertia even when the tether connection point assumption has been removed and when the tether connection point lies in x-y plane of the debris body frame.

The results presented in Fig. 6.12 demonstrate that the principal and products of inertia can still be estimated despite less ideal conditions being provided for estimation. Despite the combination of the tether connection point being approximated using only the tether tension measurements and a relatively poor position for the tether to be attached to the debris, the novel TSE still converges to around the actual inertia parameters as shown in Fig. 6.12. Importantly, as demonstrated by Fig. 6.12d, a non-zero product of inertia is accurately estimated in this simulation. As

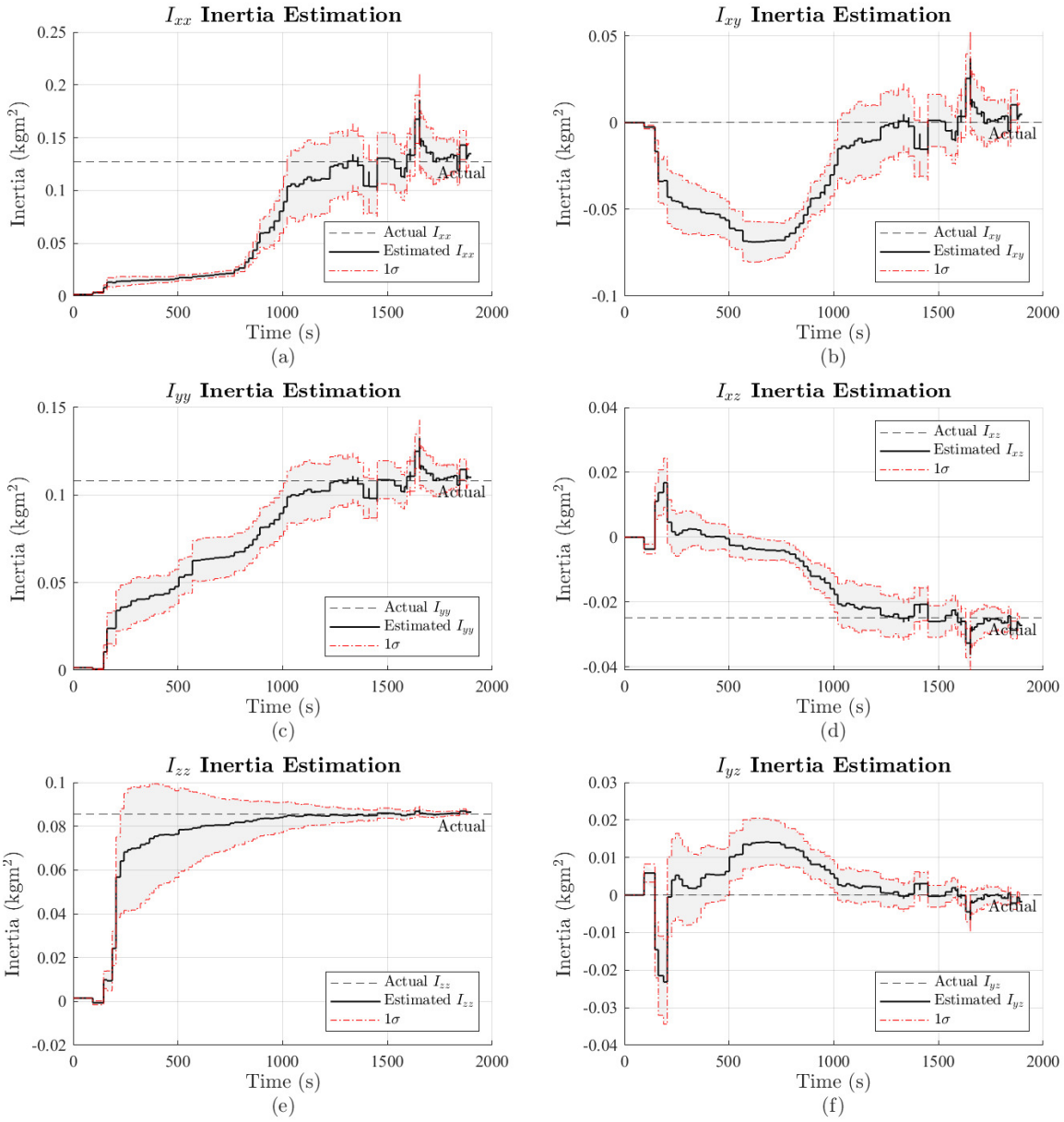

Figure 6.12: Tri-Inertial Debris Inertia Estimation

expected, the I_{zz} parameter converges quickly and accurately when compared to the other inertia parameters because of the tether connection point lying in the x-y plane of the debris body frame.

Further to the inertia estimations, the estimation errors with respect to time are plotted in Fig. 6.13. It is clear in Fig. 6.13, particularly for the the case of the I_{xx} parameter, that the less ideal estimation conditions have negatively impacted the estimator performance. Despite the detriments to the estimations, the selection of ρ near 1 has prevented the TSE from diverging when relatively poor estimations are made. With respect to the principal moments of inertia of I_{xx}, I_{yy}, I_{zz}, the initial

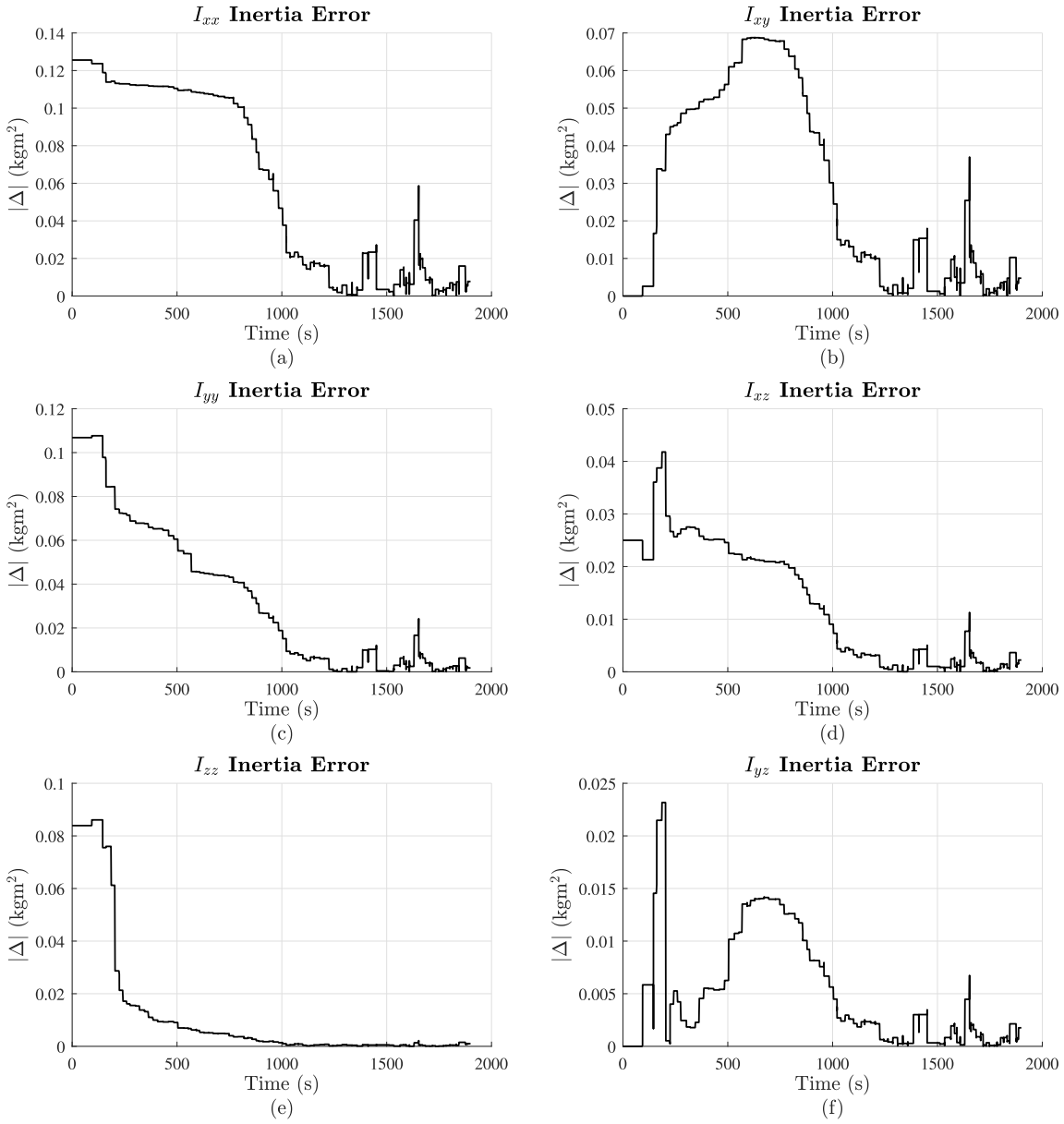

Figure 6.13: Tri-Inertial Debris Estimation Errors

estimation $\boldsymbol{I}_0$ provided to QRIIPEA leads to an initial percent error on estimation of 98.8%, 98.6% and 98.2%, respectively. At the end of the simulation, the final estimation of principal moments of inertia leads to a percent error of 6.09%, 1.63% and 1.18%, respectively. These results indicate that the TSE has made major improvements to the initial estimation despite the poor estimation conditions. With regards to the non-zero product of inertia I_{xz}, this parameter was estimated to a percent error of 8.93%. The confidence in the estimations should also be considered at the simulation end. For the case of I_{xx}, I_{yy}, and I_{zz} the final estimations with the 3σ bound were 0.1349 ± 0.0309, 0.1101 ± 0.0129 and, 0.0864 ± 0.0022 kgm^2, respectively.

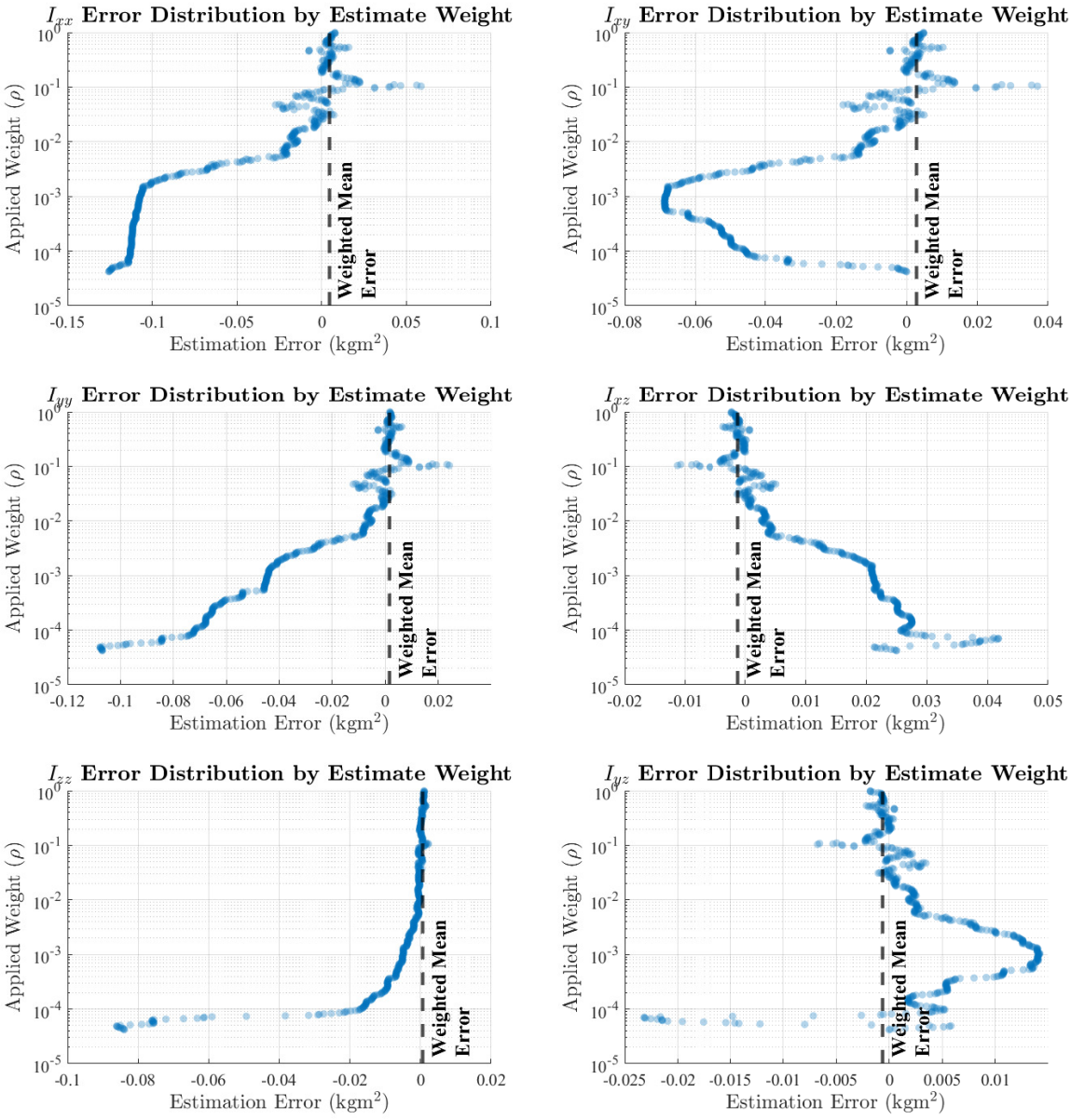

Figure 6.14: Tri-Inertial Debris Estimation Error Distribution by Estimate Weight

The 3σ bound was about an order of magnitude smaller than the estimated quantity, indicating that the TSE is relatively confident in its estimation for the conditions used in this simulation.

The weighted and equally-weighted estimation error distributions are additionally provided in Fig. 6.14 and Fig. 6.15. Observing Fig. 6.14, there are a number relatively large estimation errors having an applied weight of 10^{-1} or greater. This observation is particularly true for both I_{xx} and I_{xy}. A weight of 10^{-1} or larger would have a non-negligible impact on future estimations. The downstream effect of these few poor estimations is that the TSE may need to be operated longer to increase the

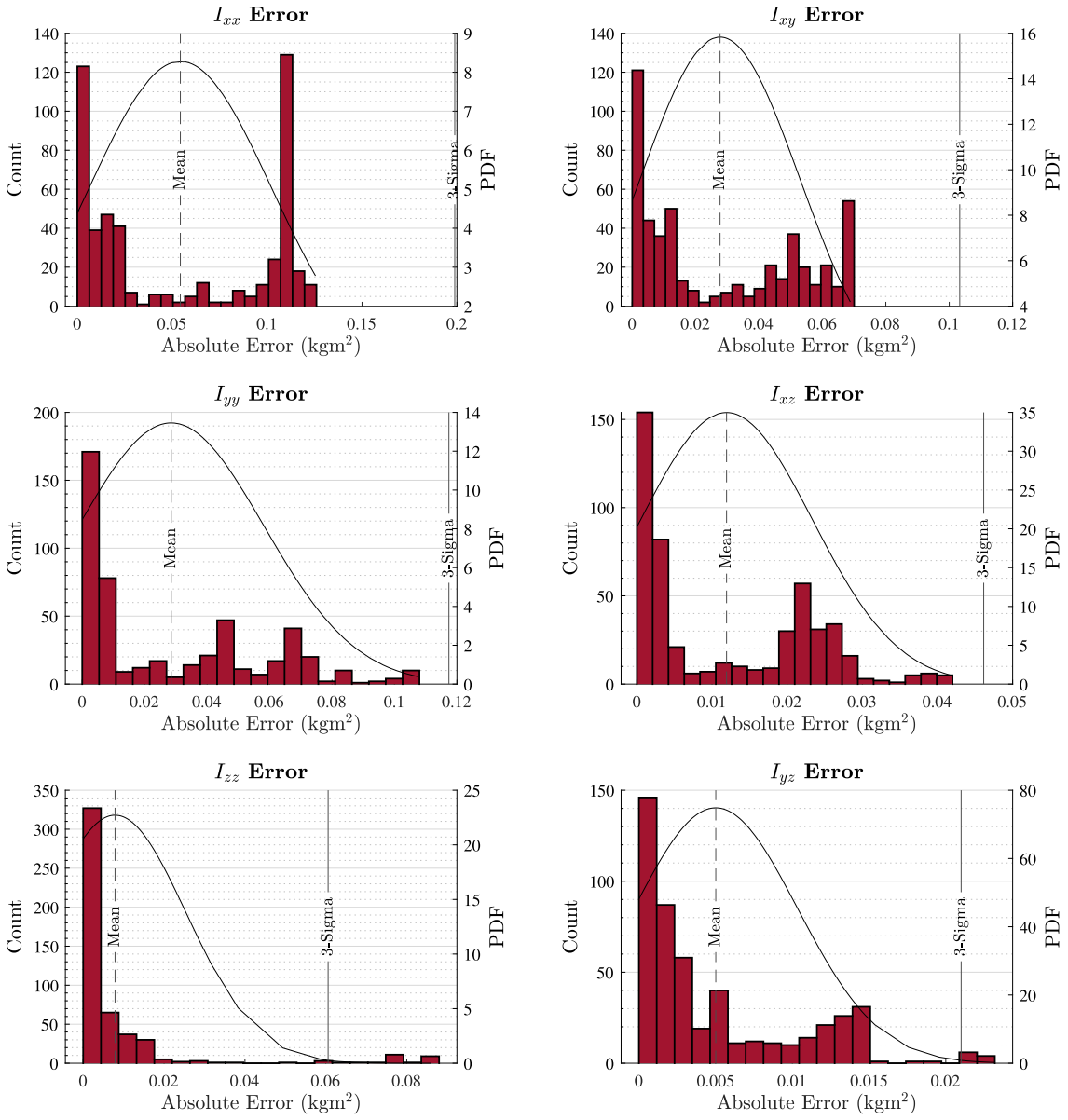

Figure 6.15: Tri-Inertial Debris Estimation Error Distribution and Mean for Equally Weighted Estimations

confidence in its estimations by further suppressing the previous poor estimations. Referring to Fig. 6.15, it can be discerned that, with the exception of the I_{xx} error distribution, the error distributions are quite heavily skewed to a desirable 0 kgm^2. The outlying peak in the I_{xx} distribution can be explained, however, by comparing to the weighted error distribution for I_{xx} in Fig. 6.14. Fig. 6.14 shows a large cluster of estimation errors just larger in magnitude than -0.1 kgm^2 for I_{xx}. These estimations, however, were provided weights on the order of 10^{-4} - 10^{-3} and were computed before the TSE had converged to around the actual values. Such a case

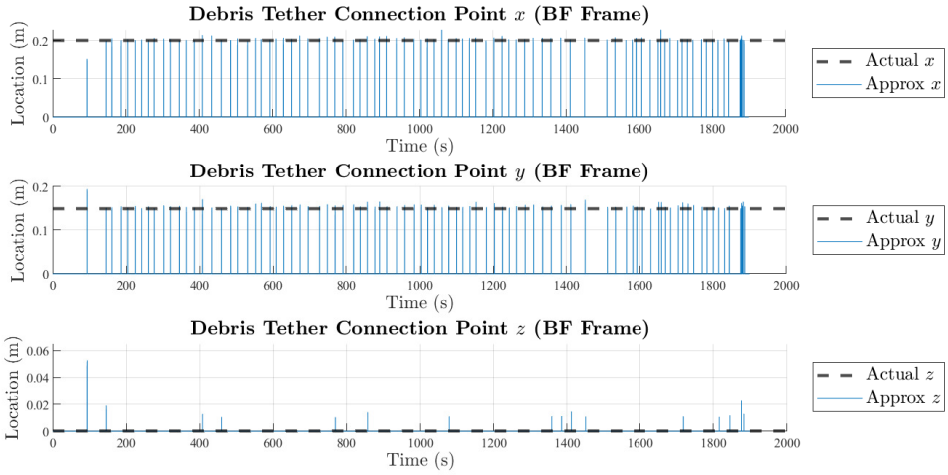

Figure 6.16: Tether Connection Point Approximation

makes these estimates have minimal impacts on the final estimated quantity despite appearing significant in the equally-weighted error plot.

A final consideration regarding the aforementioned results is to verify the accuracy of the tether connection point approximation. Fig. 6.16 compares the actual tether connection point to the approximated tether connection point. Noticeably from Fig. 6.16 is that when no tension is being measured in the cable, there is not sufficient information to approximate the tether location and, therefore, the tether connection point on the debris is only approximated when the tether is under tension and the TSE is estimating the inertia. The z-axis component of the tether connection point approximation expressed in $\mathcal{F}_D$ experiences errors as large as 0.02m after the TSE has converged. The result of these errors would have the largest effect on I_{xx} and I_{yy} estimations. In general, the approximation of the tether connection point is sufficient for inertia estimation subject to the tested simulation parameters.

Comparative Study on Approximated VS Known Tether Connection Point Estimations

It is worthwhile to consider and quantify the expected degradation in estimation performance when the debris' tether connection point is approximated. In this subsection, estimation was performed by the proposed TSE subject to the Simulation 2 scenario for both the case of an approximated tether connection point and an assumed to be known tether connection point. The results of these two simulations are compiled in Table 6.3 for all 6 inertia parameters.

Table 6.3: Comparison of TSE Performance With Known and Approximated Debris Tether Connection Point Subject to Simulation 2 Parameters

Known VS Approximated Debris Connection Point Results

Actual Debris Parameters		**Known Connection Point**			**Approximated Connection Point**		
Parameter	Actual Value (kgm^2)	Estimated Value (kgm^2)	3σ Bound (kgm^2)	Percent Error	Estimated Value (kgm^2)	3σ Bound (kgm^2)	Percent Error
I_{xx}	0.1271	0.1226	0.0069	0.52%	0.1349	0.0309	6.09%
I_{yy}	0.1083	0.1081	0.0030	0.21%	0.1101	0.0129	1.63%
I_{zz}	0.0854	0.0853	$5.63\text{E}-04$	0.04%	0.0686	0.0022	1.18%
I_{xz}	-0.025	0.0249	0.0014	0.55%	-0.0272	0.0020	8.93%
I_{xy}	0.000	$-4.47\text{E}-04$	0.0043	N/A	0.0047	0.0065	N/A
I_{yz}	0.000	$7.62\text{E}-05$	$8.37\text{E}-04$	N/A	-0.0018	0.0013	N/A

The results compiled in Table 6.3 demonstrate that by implementing the tether connection point approximation there is a moderate impact to the estimation quality for inertia parameters already known to be relatively easy to estimate. With the tether connection point on the debris largely along the x-axis, it is shown in Table 6.3 that estimation of components not related to the x-axis only experience a small increase in error by implementing the approximation. The approximation more significantly impacts the parameters known to be difficult to estimate including I_{xx} and I_{xz}. For I_{xx} the percent error on the estimations jumped from 0.52% for the known connection point case to 6.09% for the approximated case. A larger jump in error from 0.55% to 8.93% was experienced in the I_{xz} parameter estimation. The results indicate that for poor tether connection point selections on the debris, the approximation accuracy may need to be improved to maintain the highest quality estimations.

6.6.3 Simulation 3 - Post Estimation Control

This subsection of results analyzes the composite inertia tensor of the chaser-debris system. To compute the inertia tensor of the combined system, it is assumed that the chaser has used the tether to safely reel in the debris and both objects have effectively become fused together into one composite system. Then, the estimated debris inertia tensor can be used to update the DGSPCMG control scheme.

To begin the derivation of the composite inertia tensor the following set of general equations are required to develop the individual principle moments of inertia:

$$\begin{aligned} J_{xx} &= \frac{1}{12} m(z^2 + y^2) \\ J_{yy} &= \frac{1}{12} m(z^2 + x^2) \\ J_{zz} &= \frac{1}{12} m(z^2 + x^2) \end{aligned} \tag{6.39}$$

where the complete inertia tensor $\boldsymbol{J}$ may be developed in the general case using:

$$\boldsymbol{J} = \begin{bmatrix} J_{xx} & -J_{xy} & -J_{xz} \\ -J_{yx} & J_{yy} & -J_{yz} \\ -J_{zx} & -J_{zy} & J_{zz} \end{bmatrix} \tag{6.40}$$

To develop the composite inertia tensor, the orientation of the debris after fusing must be expressed in $\mathcal{F}_C$. Such a detail is important because the chaser control system is derived on knowledge of the $\mathcal{F}_C$ bases vectors and their alignment. Fig. 6.17 shows a hypothetical composite system configuration.

Noting the configuration in Fig. 6.17 it is apparent that the debris is aligned in such a way that the location of the COM in the x-y plane of $\mathcal{F}_C$ does not change. Along the z-axis of $\mathcal{F}_C$, the COM location is highly affected by the addition of the debris and, therefore, it must be recomputed such that the composite inertia tensor may be derived about this new COM location. The new COM location expressed relative to a centroid location selected to be at the base of the debris may be calculated

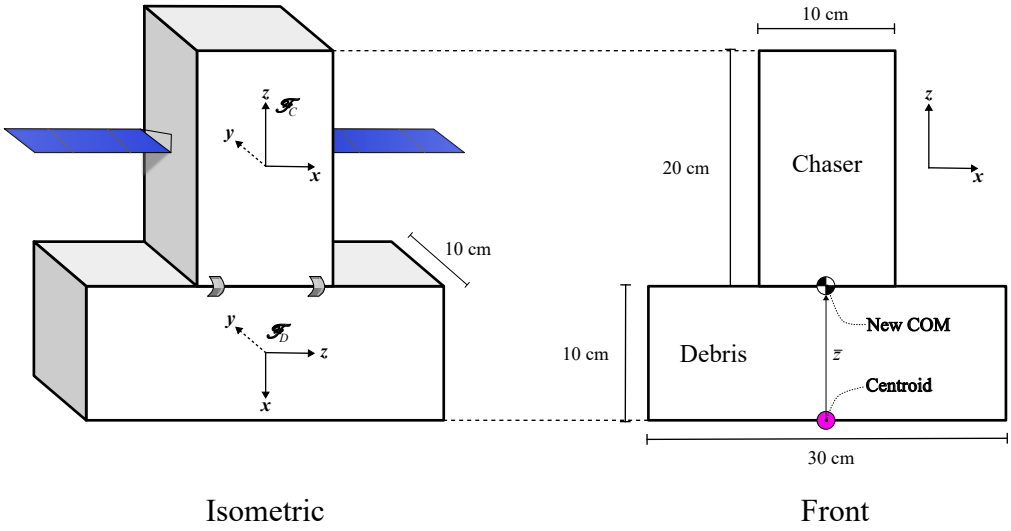

Figure 6.17: Composite Chaser-Debris Rigid Body

using the following relationship where $\bar{z}$ is positive towards the z-axis direction of the chaser:

$$\bar{z} = \frac{\sum_i^n m_i x_i}{\sum_i^n m_i} = \frac{(4)(5) + 2(10+10)}{(4+2)} = 10\text{cm} \tag{6.41}$$

The COM location of the composite system is subsequently located 10 cm from the based of the debris in the positive z direction. The offset vector $\boldsymbol{r}_o$ describing the positional change of the COM with respect to the original chaser and debris COM may be expressed as $\boldsymbol{r}_C = [0, 0, -10]^T$ cm and $\boldsymbol{r}_D = [0, 0, 5]^T$ cm, respectively, for both the chaser and debris. To develop the composite inertia tensor, the inertia tensors of each body must be expressed about a common point, which may be reasonably selected as the new COM location. By applying the parallel axis theorem the inertia tensor of each body may be expressed about the new COM location using the following general equation:

$$\boldsymbol{J} = \boldsymbol{J}_0 + m\left[(\boldsymbol{r}_o \cdot \boldsymbol{r}_o)\boldsymbol{I}_{3\times 3} - \boldsymbol{r}_o \boldsymbol{r}_o^T\right] \tag{6.42}$$

The composite inertia tensor may be computed by summing inertia tensor of each body expressed about the new COM location $\boldsymbol{J}_{COM}^C$ and $\boldsymbol{J}_{COM}^D$, respectively, as:

$$\boldsymbol{J}_{comp} = \boldsymbol{J}_{COM}^C + \boldsymbol{J}_{COM}^D \tag{6.43}$$

An important note should be made regarding the debris inertia tensor. As defined by Fig. 6.17, the BF frame of the debris is not aligned with the chaser BF frame. The principle inertia components of the debris would be expressed differently when following the axes convention provided by the chaser. It is, therefore, necessary to swap the J_{xx} and J_{zz} principle moments of inertia in the debris inertia tensor so that it follows the same convention as that used for the chaser inertia tensor. The

convention of $J_{d_{(1,1)}}$ replaced with $J_{d_{(3,3)}}$ and vice versa, may be expressed as:

$$\boldsymbol{J}_d \left[J_{d_{(1,1)}} \coloneqq J_{d_{(3,3)}} \right] \tag{6.44}$$

$$\boldsymbol{J}_d \left[J_{d_{(3,3)}} \coloneqq J_{d_{(1,1)}} \right] \tag{6.45}$$

The resulting true combined inertia tensor for the inertially-asymmetric debris from Simulation 1 and fused-body convention in Fig. 6.17 was calculated as:

$$\boldsymbol{J}_{comp} = \begin{bmatrix} 0.0450 & 0 & 0 \\ 0 & 0.0717 & 0 \\ 0 & 0 & 0.0367 \end{bmatrix} \text{kgm}^2$$

The resulting inertia tensor derived from the TSE estimated debris inertia was calculated as:

$$\boldsymbol{J}_{comp} = \begin{bmatrix} 0.0449 & 0 & -0.0001 \\ 0 & 0.0727 & 0 \\ -0.0001 & 0 & 0.0364 \end{bmatrix} \text{kgm}^2$$

The following two sets of results compare the control performance over a large attitude reorientation of the DGSPCMG-equipped chaser satellite. The first set in Fig. 6.18 shows control results when the control system does not have knowledge of the debris inertia and Fig. 6.19 shows results when the control system has been updated with knowledge of the estimated debris inertia. There are two key takeaways from the results. The first is that, by comparing Fig. 6.18c to Fig. 6.19c, updating the control scheme with the estimated debris inertia tensor reduces the amount of overshoot in the attitude response. The update also reduces some of the transience seen in Fig. 6.18c. The second takeaway is found by comparing Figs. 6.18d - 6.18f to Figs. 6.19d - 6.19f. In these figures it can be observed that, by updating the controller with the estimated inertia, the DGSPCMG is actuated more efficiently to achieve the attitude reorientation. The effect is most notable by comparing Fig. 6.18d to Fig. 6.19d where the δ_i and δ_o gimbals in the updated case remain closer to their starting position. The gimbal phase plot of Fig. 6.18d for the simulation with uncertain inertia, however, shows the gimbals making large motions with the δ_i gimbal moving towards the singularity position. As a general summary of the comparative results, the DGSPCMG control scheme, when updated with the estimated debris inertia tensor, expends less energy to perform the attitude reorientation maneuver than it would having an uncertain inertia tensor. The results emphasize the importance of the proposed TSE for ADR missions so that the chaser attitude control system can perform the mission objectives most effectively.

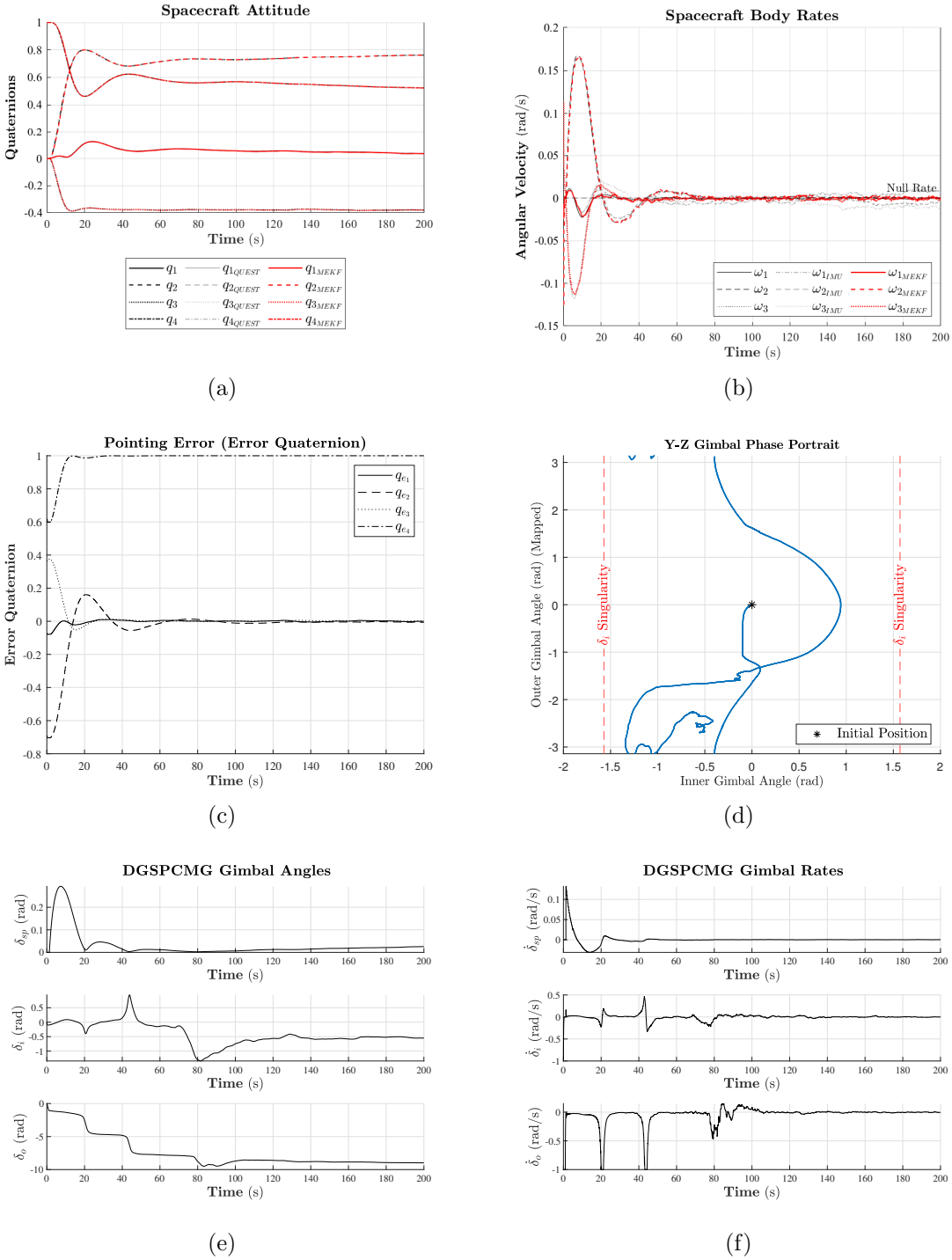

Figure 6.18: Control with Uncertain Inertia Tensor Provided to Attitude Controller

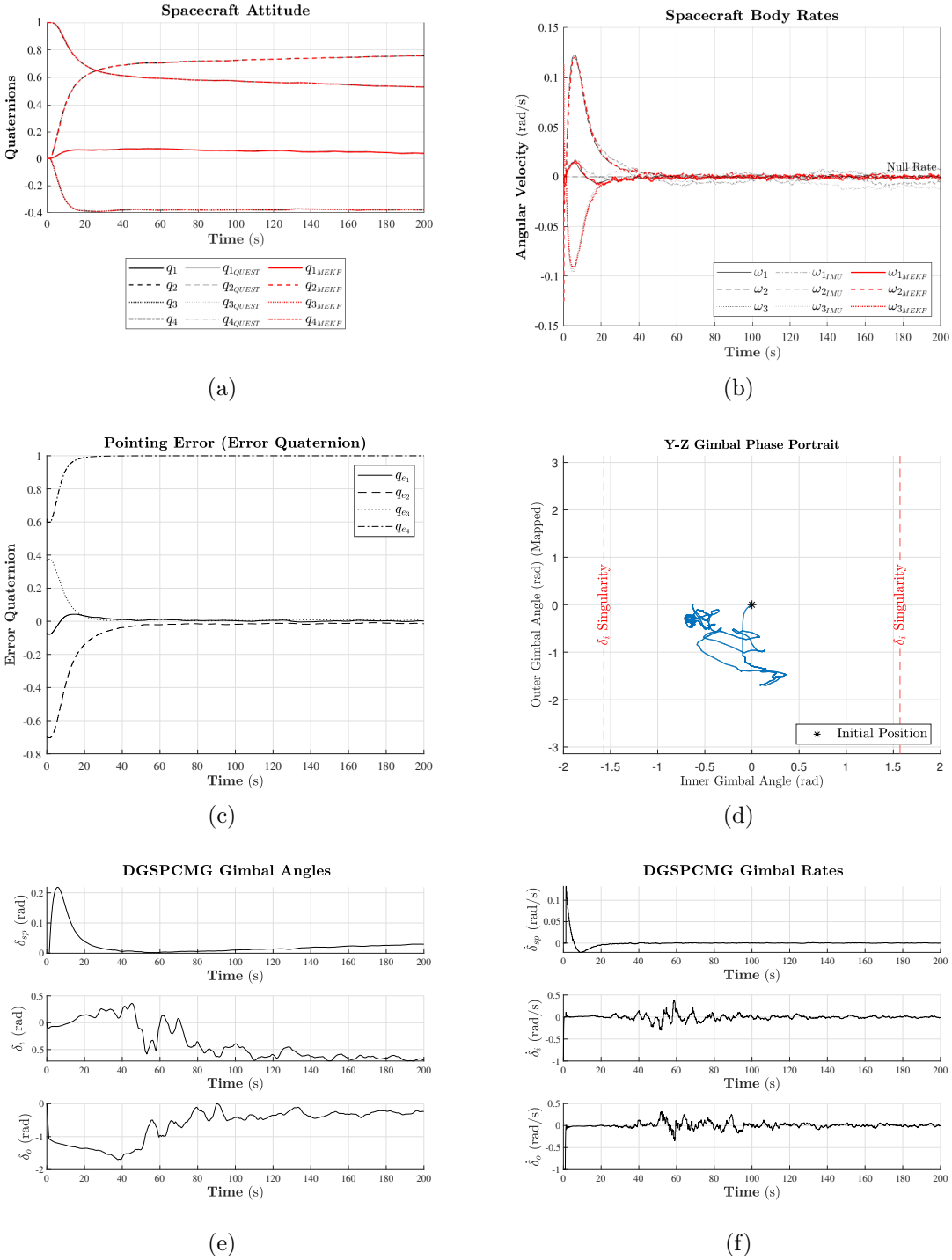

Figure 6.19: Control with Updated Combined Inertia Tensor

Chapter 7

Advancements in Oceanographic Target Tracking with DGSPCMG-Equipped ADCS

7.1 Introduction

The continual development of CubeSats since their introduction in 1999 has drastically extended their ability to perform meaningful scientific objectives [4]. Launches of CubeSats since 2016, like the Planet Labs Dove class of satellites, have demonstrated the merit of CubeSats for performing important Earth observation missions [138]. Even with the advancement of nanosatellites for Earth observation missions, Guerra *et al.* (2016) have argued that CubeSats have made little ingress in the oceanography sector.

Oceanographic satellites are commonly responsible for monitoring changes in the ocean climate, algae bloom or anoxic zone events, major storms, and ever increasing shipping traffic [25]. Some of these oceanographic targets of interest are shown from spacecraft-derived data in Fig. 7.1. While the data compiled in Fig. 7.1 was collected by large satellites, this data could, in theory, be collected by specifically engineered CubeSats that have comparatively small upfront costs compared to mid to large sized satellites. In fact, missions such as MANTIS (being developed at Dalhousie University) or HYPSO-2 (being developed at the Norwegian University of Science and Technology) propose the use of CubeSats for monitoring ocean targets. The goal of both of these missions is to monitor ocean algae blooms.

To enable the success of these aforementioned missions, it is generally required for the CubeSat to have a robust and agile ADCS. A target tracking mission scenario also presents a possible challenge for a DGSPCMG-equipped ADCS because the DGSPCMG will be tasked with autonomously escaping from singularities while actively tracking targets during relatively short orbital passes. The benefits of the proposed Extended DGSPCMG SCL could be fully realized in this mission concept because, as a consequence of its intended design, it prevents singularities of any kind from impacting the intended scientific objectives of the CubeSat. Additionally, literature examples such as [14][107][12][139] have yet to demonstrate agile maneuvering and singularity escape when attitude determination is in the control loop.

The motivation of this section is, therefore, to demonstrate the ability for a complete DGSPCMG-equipped ADCS to perform agile pointing and tracking of sequential oceanographic targets of opportunity. By doing so, the developments and results of the subject case study will also help to address the research gap identified in CubeSat oceanographic capabilities. In this section, target pointing geometry and performance metrics are adopted from [140][23][24] and [58] in order to build a detailed spacecraft target pointing simulation.

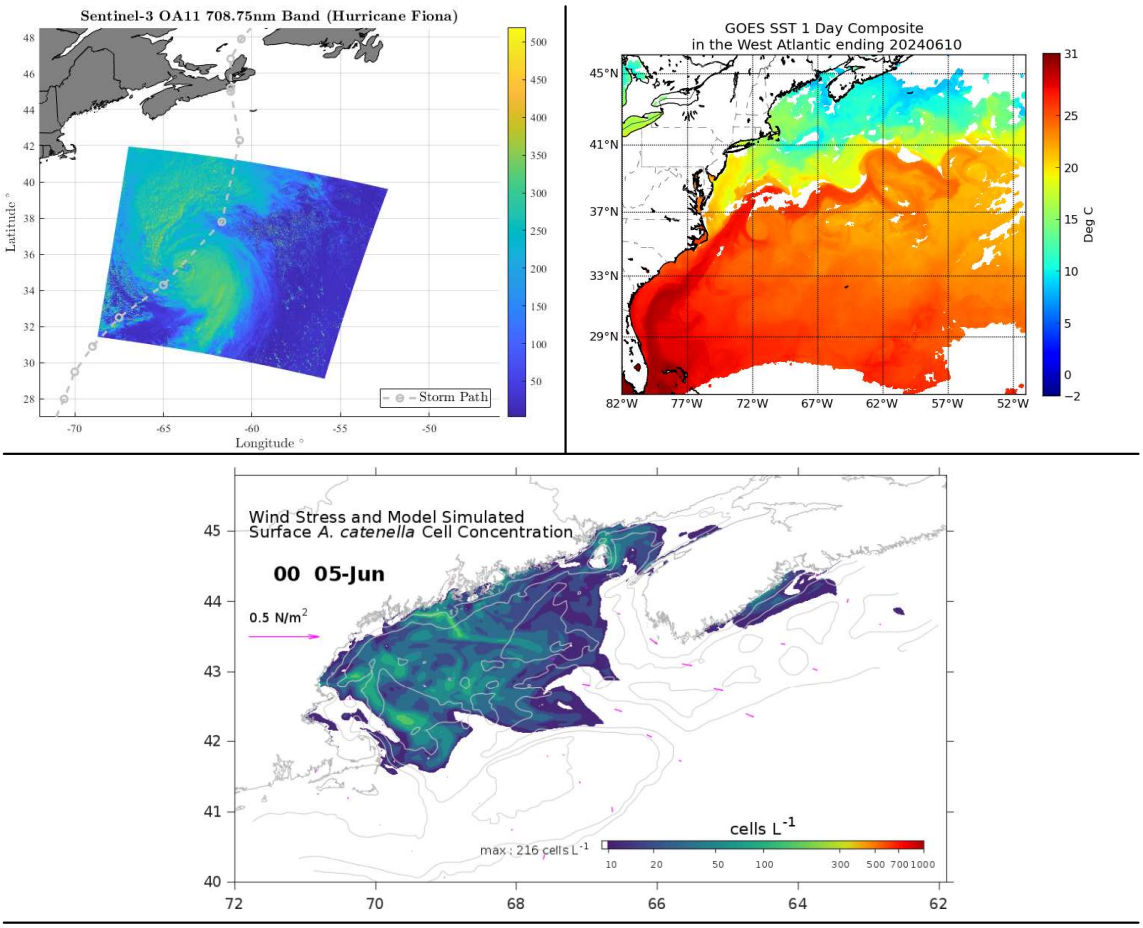

Figure 7.1: Examples of Satellite Derived Oceanographic Data. (left) 2022 Category 3 Hurricane Fiona From Sentinel-2 Data. (right) GOES-16 Sea Surface Temperature on June 10$^{\text{th}}$ 2024. (bottom) Modeled *Alexandrium catenella* (a Group of Marine Plankton) Concentrations in the Gulf of Maine and Nova Scotia Coast on June 5$^{\text{th}}$ 2024. Imagery obtained under public distribution from NOAA National Weather Service & ESA Sentinel Copernicus Service [2024].

7.2 Target Viewing Geometry

Proceeding the definition of the target position and its local reference frame in Appendix A, the viewing angles which dictate how the spacecraft is observing the target may be formulated. These viewing angles are important for quantifying the "value" of a particular observation made by the spacecraft. For example, it is inherently more efficacious to observe a target at the peak elevation angle over the target than it is to observe it at a low elevation angle [141]. The schematic describing the target viewing angles is provided in Fig. 7.2 where the angles are shown in a perspective looking south from the North Pole.

Referring to Fig. 7.2, the Earth angular radius as observed by the satellite is given

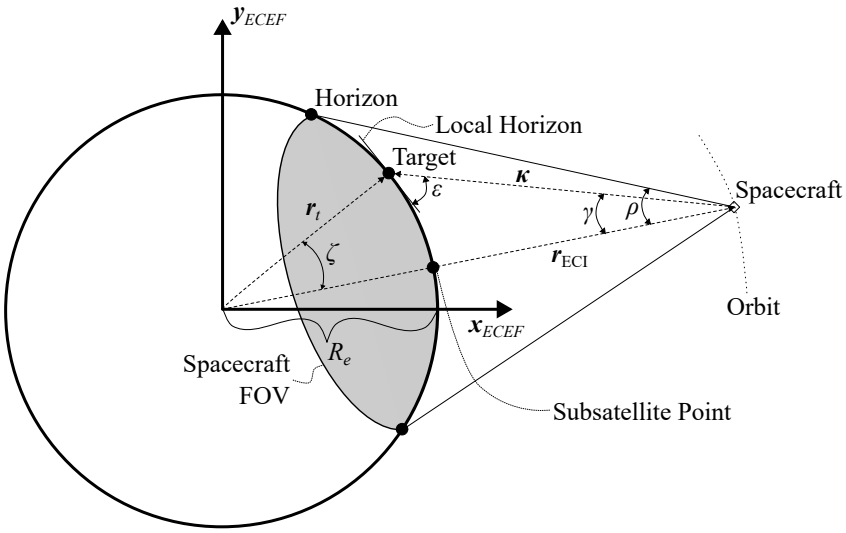

Figure 7.2: Target Viewing Angles Observed from North Pole Looking South.

by:

$$\sin(\rho) = \frac{R_e}{R_e + h} \tag{7.1}$$

where h is the orbital altitude above the surface of Earth. Provided with *a priori* knowledge of the target position vector $\boldsymbol{r}_t$ expressed in $\mathscr{F}_{ECI}$, the Earth central angle can be computed as:

$$\cos(\zeta) = \frac{\boldsymbol{r}_{ECI}^T \boldsymbol{r}_t}{|\boldsymbol{r}_{ECI}||\boldsymbol{r}_t|} \tag{7.2}$$

Continuing with derivations following Fig. 7.2, the nadir angle γ is defined as the angle between the nadir vector $(-\boldsymbol{r}_{ECI})$ and the spacecraft-to-target vector defined by $\boldsymbol{\kappa} = \boldsymbol{r}_t - \boldsymbol{r}_{ECI}$. Following these definitions, γ may be computed as:

$$\tan(\gamma) = \frac{\sin(\rho)\sin(\zeta)}{1 - \sin(\rho)\cos(\zeta)} \tag{7.3}$$

The final angle describing the target observation is the elevation angle, which is the angle between the satellite position and the local horizon of the target. The elevation angle ϵ can be calculated as follows:

$$\epsilon = \frac{\pi}{2} - \zeta - \gamma \tag{7.4}$$

With the angles describing the target pass well defined, the next section develops the desired attitude the spacecraft must follow to observe oceanographic targets.

7.3 Target Tracking Attitude

For satellites carrying optical payloads, it is generally desirable for the spacecraft to observe a target using an attitude that is consistent from one orbit to the next. A method to enable these observations is to apply alignment-constrained desired attitude formulations. In an alignment-constrained attitude, the satellite aligns its observing boresight vector with $\boldsymbol{\kappa}$ and then rotates about the boresight vector to minimize the angle between a secondary $\mathcal{F}_{BF}$ basis vector and a specified constraint vector [23][142][135]. The general procedure for this spacecraft guidance method is to compute an intermediate alignment frame defined by $\mathcal{F}_i$ and then rotate about the aligned basis vector of $\mathcal{F}_i$ to yield the constrained desired attitude reference frame $\mathcal{F}_a$. This procedure is demonstrated pictorially in Fig. 7.3 where the rotation from $\mathcal{F}_{ECI}$ to $\mathcal{F}_i$ is first shown and followed by the final rotation to the desired $\mathcal{F}_a$ constrained target tracking frame. Following the generally accepted convention used previously in this thesis, the optical sensor boresight was selected in this thesis to lie on the $z+$ axis of $\mathcal{F}_{BF}$. Such a selection leads to forming the z-axis basis vector of $\mathcal{F}_i$, expressed in $\mathcal{F}_{ECI}$, as:

$$\boldsymbol{z}_i = \frac{\boldsymbol{\kappa}}{|\boldsymbol{\kappa}|} \tag{7.5}$$

$\boldsymbol{z}_i$ also represents the desired boresight orientation expressed in $\mathcal{F}_{ECI}$. Noting that $\boldsymbol{y} = [0, 1, 0]^T$ is the y-axis basis vector of $\mathcal{F}_{ECI}$, allows for the x-axis basis vector of $\mathcal{F}_i$ expressed in $\mathcal{F}_{ECI}$ to be computed as follows:

$$\boldsymbol{x}_i = \frac{\boldsymbol{z}_i^{\times}(-\boldsymbol{y})}{|\boldsymbol{z}_i^{\times}(-\boldsymbol{y})|} \tag{7.6}$$

The triad represented by $\mathcal{F}_i$ is completed by the y-axis basis vector which is

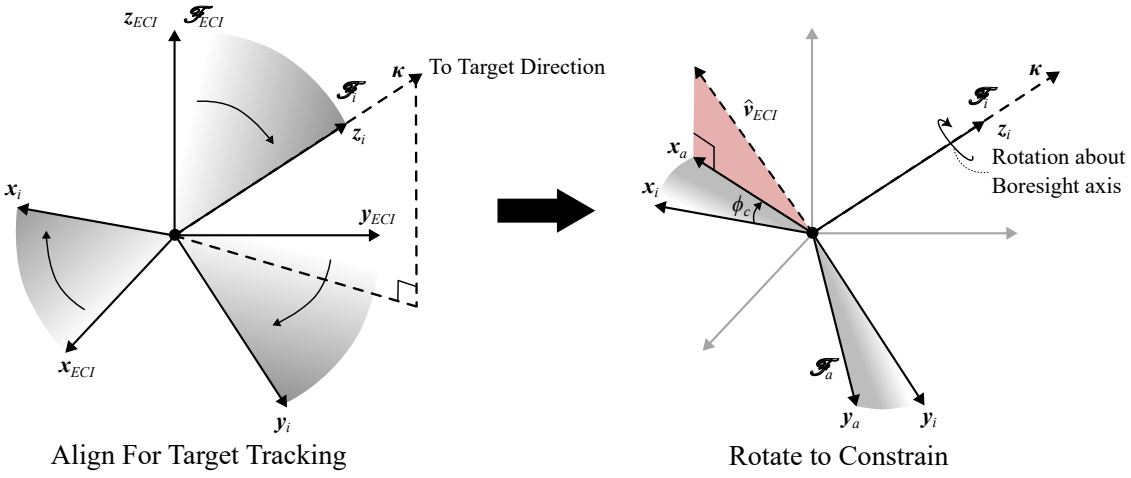

Figure 7.3: Demonstration of Alignment-Constrained Attitude Process

normal to $\boldsymbol{x}_i$ and $\boldsymbol{z}_i$, calculated as follows:

$$\boldsymbol{y}_i = \boldsymbol{z}_i^{\times} \boldsymbol{x}_i \tag{7.7}$$

Allowing the vectors $\boldsymbol{x} = [1, 0, 0]^T$ and $\boldsymbol{z} = [1, 0, 0]^T$ to be the remaining basis vectors of $\mathscr{F}_{ECI}$ when expressed in $\mathscr{F}_{ECI}$, enables a DCM to be formed which transforms a vector from its expression in $\mathscr{F}_{ECI}$ to its expression in $\mathscr{F}_i$. The DCM can be computed as:

$$\boldsymbol{\mathcal{A}}^i_{ECI} = \begin{bmatrix} \boldsymbol{x}_i^T \boldsymbol{x} & \boldsymbol{x}_i^T \boldsymbol{y} & \boldsymbol{x}_i^T \boldsymbol{z} \\ \boldsymbol{y}_i^T \boldsymbol{x} & \boldsymbol{y}_i^T \boldsymbol{y} & \boldsymbol{y}_i^T \boldsymbol{z} \\ \boldsymbol{z}_i^T \boldsymbol{x} & \boldsymbol{z}_i^T \boldsymbol{y} & \boldsymbol{z}_i^T \boldsymbol{z} \end{bmatrix} \tag{7.8}$$

The intermediate target pointing frame is, therefore, fully defined by the described equations in this subsection; however, the desired attitude must still be conveniently constrained by an additional reference direction in the following subsection.

7.3.1 Constrained Attitude

It has been shown in Section. 4.5 that the OD-EKF provides an estimate of the spacecraft orbital velocity vector expressed in $\mathscr{F}_{ECI}$. This estimate is defined here as $\hat{\boldsymbol{v}}_{ECI}$. The estimated velocity vector can be conveniently used as the constraint vector with the secondary alignment vector being the x-axis basis vector of $\mathscr{F}_i$. Because the desired boresight vector $\boldsymbol{z}_i$ is already aligned to $\boldsymbol{\kappa}$, the secondary alignment vector can typically only be rotated such to minimize the angle made with the constraint vector as shown in Fig. 7.3. After this rotation, the attitude is considered to be constrained. The reason for selecting $\hat{\boldsymbol{v}}_{ECI}$ as the constraint vector is so that, when the spacecraft is observing a target from a 90 degree elevation, the aligned-constrained attitude will be identical to the nadir attitude (assuming a spherical Earth). For a 90 degree elevation, the target is directly below the satellite and $\boldsymbol{\kappa}$ will be aligned with $-\boldsymbol{r}_{ECI}$. Because of this alignment, rotation about $\boldsymbol{\kappa}$ can directly align a desired x-axis direction with $\boldsymbol{v}_{ECI}$. By definition in Appendix A, such an attitude is identical to the nadir attitude. Therefore, for all elevation angles other than 90 degrees, the aligned-constrained attitude will be close to the nadir attitude (or as close as possible to it). By being closer to the nadir attitude the spacecraft, which nominally points nadir, needs to expend less energy to achieve a target tracking attitude when approaching the target.

The goal of the constrained attitude is to minimize the angular distance between the constraint vector and the secondary alignment vector by rotating about the desired boresight direction $\boldsymbol{z}_i$ as demonstrated by Fig. 7.3. The rotation which minimizes the angle between $\hat{\boldsymbol{v}}_{ECI}$ and $\boldsymbol{x}_i$ can be found by computing the angle between both vectors when they are projected into the plane normal to $\boldsymbol{z}_i$ (the plane normal to the desired boresight orientation) as demonstrated by Fig. 7.4. These projections are most easily manipulated by expressing both the constraint vector and secondary alignment vector in $\mathscr{F}_{ECI}$ as it is desired to compute an attitude referenced to this inertial coordinate frame. Let $\boldsymbol{c}_B$ represent the projected $\boldsymbol{x}_i$ secondary alignment vector

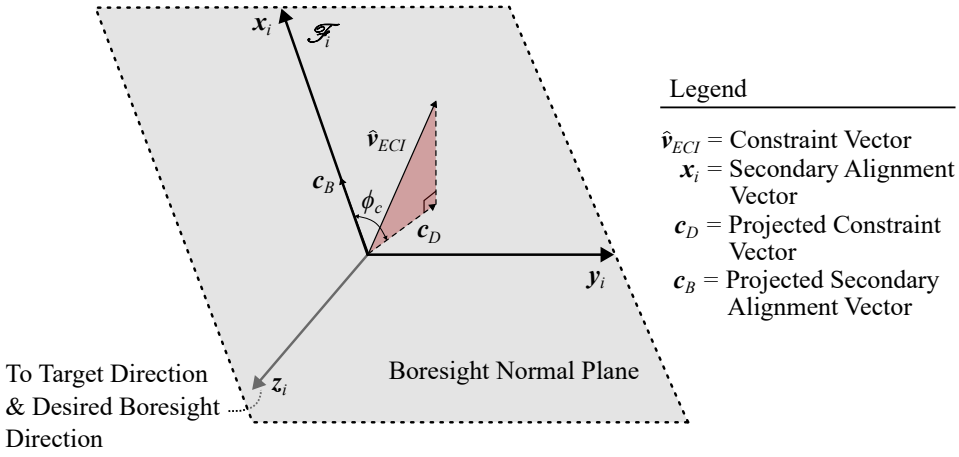

Figure 7.4: Constraint Vector $\boldsymbol{c}_D$ and its Projection Into the Boresight Normal Plane.

and $\boldsymbol{c}_D$ be the projected $\hat{\boldsymbol{v}}_{ECI}$ constraint vector expressed in $\mathscr{F}_{ECI}$. The minimization angle ϕ_c can be computed using the following sequence of equations:

$$\boldsymbol{v}_i = \frac{\hat{\boldsymbol{v}}_{ECI}}{|\hat{\boldsymbol{v}}_{ECI}|} \tag{7.9}$$

$$\boldsymbol{c}_D = \boldsymbol{v}_i - \left(\frac{\boldsymbol{v}_i^T \boldsymbol{p}_D}{\boldsymbol{p}_D^T \boldsymbol{p}_D}\right) \boldsymbol{p}_D \tag{7.10}$$

$$\cos(\phi_c) = \frac{\boldsymbol{c}_B^T \boldsymbol{c}_D}{|\boldsymbol{c}_B||\boldsymbol{c}_D|} \tag{7.11}$$

In the case of the present thesis, $\boldsymbol{p}_D$ is the $\mathscr{F}_i$ projection plane normal vector expressed in $\mathscr{F}_{ECI}$. Based on the selection of the desired boresight vector being functionally equivalent to the z-axis basis vector of $\mathscr{F}_{BF}$ when the spacecraft has achieved the desired attitude, $\boldsymbol{p}_D$ may be calculated as follows:

$$\boldsymbol{p}_D = \left(\boldsymbol{\mathcal{A}}_i^{ECI}\right)^T [0, 0, 1]^T \tag{7.12}$$

Eq. (7.12) is effectively transforming the observing basis vector of $\mathscr{F}_i$ to its expression in $\mathscr{F}_{ECI}$. Following a very similar procedure, the remaining quantity $\boldsymbol{c}_B$ can be computed by expressing the x-axis basis vector of $\mathscr{F}_i$ in $\mathscr{F}_{ECI}$ by using the following relationship:

$$\boldsymbol{c}_B = \left(\boldsymbol{\mathcal{A}}_i^{ECI}\right)^T [1, 0, 0]^T \tag{7.13}$$

Because the secondary alignment vector when expressed in $\mathscr{F}_i$ is the x-axis basis vector, it already lies in the projection plane and, therefore, does not need to go through the same mathematical process as was done in Eq. (7.10).

Using the results of Eq. (7.11) allows the aligned-constrained attitude to be represented by the DCM which performs the transformation from $\mathscr{F}_{ECI}$ to $\mathscr{F}_a$. The

DCM can be computed in the following relationship:

$$\boldsymbol{\mathcal{A}}^{a}_{ECI} = \mathrm{C3}(\phi_c)\boldsymbol{\mathcal{A}}^{i}_{ECI} \tag{7.14}$$

Before being sent to the attitude controller as the target tracking attitude, it is necessary to convert the result from Eq. (7.14) to a desired attitude quaternion $\boldsymbol{q}_d$.

Rotation Direction

A caveat of Eq. (7.11) is that, for the conditions used in this research, it lacked the desired rotation direction about $\boldsymbol{z}_i$. More specifically, Eq. (7.11) yields a positive solution to ϕ_c for all constraint projection vectors $\boldsymbol{c}_D$ which lie in the 1st or 4th quadrant of the projection plane. Fig. 7.5 supports this notion demonstrating that these results may not be desirable.

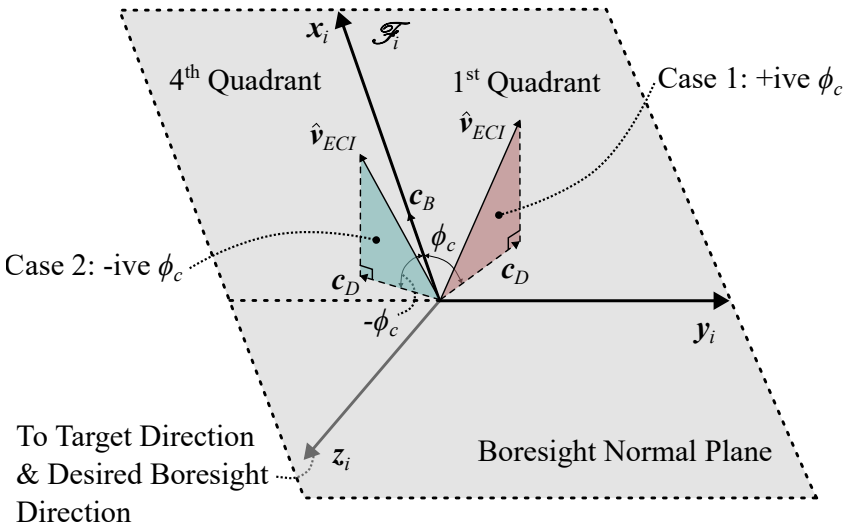

Figure 7.5: Constraint Vector $\boldsymbol{c}_D$ and the Desired ϕ_c Rotation Direction Based on Normal Plane Quadrant

As visualized by Fig. 7.5 and the right-handedness of $\boldsymbol{\mathcal{F}}_i$, it is desired to have a negative ϕ_c minimization angle if the constraint vector projection lies in the 4th quadrant of the projection plane. A negative angle respects the right-handedness of $\boldsymbol{\mathcal{F}}_i$ and, therefore, a rotation about $\boldsymbol{z}_i$ through $-\phi_c$ rotates $\boldsymbol{c}_B$ counter clockwise towards $\boldsymbol{c}_D$. Should $\boldsymbol{c}_D$ lie in the 1st quadrant, a rotation about $\boldsymbol{z}_i$ through ϕ_c is desired and $\boldsymbol{c}_B$ will be rotated clockwise towards $\boldsymbol{c}_D$. The solution to Eq. (7.11) can be modified subject to the following set of conditions:

$$\begin{cases} \phi_c, \text{ if } \boldsymbol{\mathcal{A}}^{i}_{ECI}\boldsymbol{c}_D|_2 \geq 0 \\ -\phi_c, \text{ if } \boldsymbol{\mathcal{A}}^{i}_{ECI}\boldsymbol{c}_D|_2 < 0 \end{cases} \tag{7.15}$$

Most notable from Eq. (7.15) is that $\boldsymbol{c}_D$ is transformed to its expression in $\mathscr{F}_i$ to most easily express the conditions for checking the quadrant within the normal plane. The quadrant of interest corresponding to the desired rotation direction about the boresight axis is then determined by inspecting if the y-component of $\boldsymbol{c}_D$ is above or below zero.

Desired Angular Velocity

The desired angular velocity setpoint is required by the attitude controller for all time over the target tracking maneuver. Following the work in [135] the desired angular velocity of the spacecraft over the target tracking maneuver was computed by applying Eq. (7.16):

$$\boldsymbol{\omega}_d = 2\left(q_4\boldsymbol{I}_{3\times 3} + \hat{\boldsymbol{q}}^{\times}\right)^{-1}\dot{\hat{\boldsymbol{q}}} \tag{7.16}$$

where the components of $\boldsymbol{q}$ and $\dot{\boldsymbol{q}}$ are the simulator propagated actual spacecraft attitude quaternion and rate quaternion. The relationship provided in Eq. (7.16) has the effect of setting the angular velocity error state to be zero during the target tracking campaign when there is no noise present in the angular velocity state. Some studies such as [23] and [24] propagate forward in time the desired attitude and angular velocity states to t_{k+1} with only knowledge of the states at t_k so that a determinable angular velocity setpoint is feasible to compute in online implementation, however, this work was outside the scope of the present thesis. Target tracking performance benefits can likely be achieved by integrating the work from these previous studies into the current thesis' simulator.

7.3.2 Validation of Alignment-Constrained Attitude

To validate the functionality of the proposed attitude, a dot product can be taken between the constraint $\hat{\boldsymbol{v}}_{ECI}$ and the secondary alignment vector $\boldsymbol{x}_i$. Also, an additional dot product can be obtained for both projection vectors $\boldsymbol{c}_D$ and $\boldsymbol{c}_B$, respectively. Two results are expected to be observed. First, if the rotation about the boresight axis through ϕ_c is applied consistently during orbit propagation, the dot product between the projection vectors $\boldsymbol{c}_D$ and $\boldsymbol{c}_B$ should always be unity. In the case of the constraint and secondary alignment vectors $\hat{\boldsymbol{v}}_{ECI}$ and $\boldsymbol{x}_i$, these vectors should only have a dot product of 1 if the satellite reaches an elevation angle of $\epsilon = 90°$. As previously discussed, this particular case allows the $\boldsymbol{x}_i$ vector to align closely with the estimated satellite velocity vector $\hat{\boldsymbol{v}}_{ECI}$. The results of the validation technique are provided in Fig. 7.6 where a satellite target pass was propagated for a target located at 0.65178° S, 24.34995° W.

Observing Fig. 7.6 it is clear that the expected results are obtained. The projection vectors experience a unitary dot product regardless of simulation time indicating that the intermediate frame has been rotated to the desired constrained attitude frame about the boresight axis. Additionally, the constraint vectors themselves experience a dot product of 1 at the 90 degree elevation point as expected. From these results

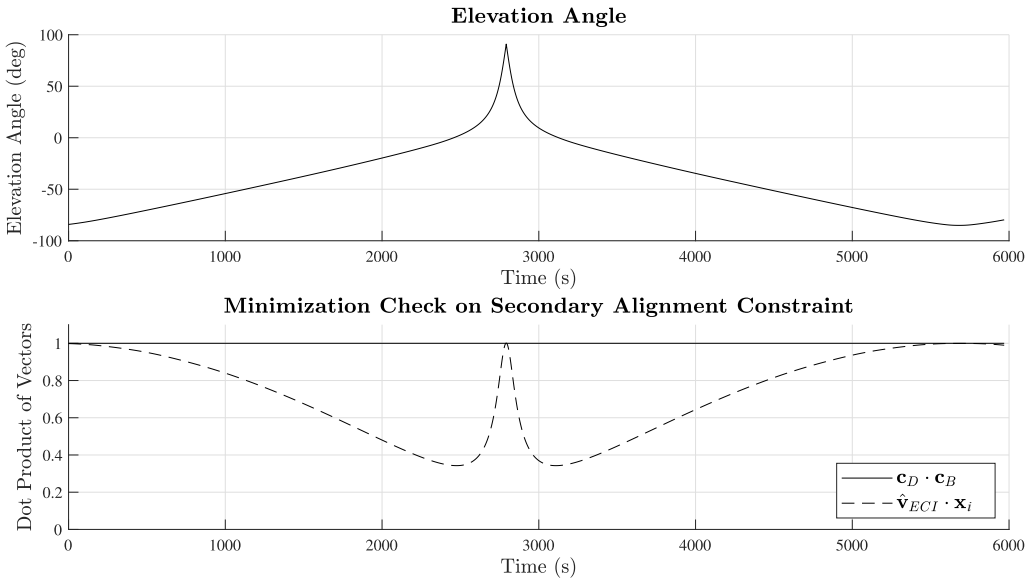

Figure 7.6: Dot Products of Alignment Vectors Used to Validate Constrained Attitude.

the alignment-constrained attitude formulations were considered to be validated.

7.4 Target Tracking Error Metrics

Particularly for optical payloads which may observe ocean targets, it is crucial to quantify errors which express how well the satellite has enabled observation of a target on the surface of Earth. These error metrics can be broken down to pointing errors $\delta\theta$ and mapping errors δs. Mapping errors express the distance between the target location and where the observing boresight maps onto the surface of Earth. Pointing errors are related to angular errors between the desired boresight orientation and the actual boresight orientation. In this thesis, a spherical Earth approximation is applied for computing these error metrics which can induce up to 0.12° of error in the computations [23].

Generally, errors arising from attitude determination and control are lumped into target azimuth errors $\delta\vartheta$[1] and nadir errors $\delta\gamma$. $\delta\vartheta$ describes angular rotation error of the observing boresight about the nadir vector $-\boldsymbol{r}_{ECI}$ and $\delta\gamma$ describes angular error between $\boldsymbol{\kappa}$ and $-\boldsymbol{r}_{ECI}$ [23]. The azimuth angle ϑ is the angle between the subsatellite-target vector $\boldsymbol{r}_{ss}^{t}$ and the spacecraft ground track. This geometry and the subsatellite point are depicted in Fig. 7.7. Instantaneously, the spacecraft velocity vector lies along the ground track which allows the azimuth angle to be calculated as [23]:

$$\cos(\vartheta) = \frac{\boldsymbol{r}_{ss}^{t} \cdot \boldsymbol{v}_{ECI}}{|\boldsymbol{r}_{ss}^{t}||\boldsymbol{v}_{ECI}|} \tag{7.17}$$

[1] $\delta\vartheta$ is not to be confused with $\boldsymbol{\delta\vartheta}$ defined for the MEKF local error parameterization

Azimuthal pointing and mapping errors are a function of the nadir angle γ as shown by:

$$\delta\theta = \delta\vartheta \sin(\gamma) \tag{7.18}$$

$$\delta s = \delta\vartheta |\boldsymbol{\kappa}| \sin(\gamma) \tag{7.19}$$

where the azimuth angle error can be computed by first determining the angle about $-\boldsymbol{r}_{ECI}$ between the actual spacecraft z-axis basis vector $\hat{\boldsymbol{b}}_z$ when expressed in $\boldsymbol{\mathcal{F}}_{NP}$ and the x-axis of $\boldsymbol{\mathcal{F}}_{NP}$ denoted by $\boldsymbol{x}_{NP}$. Let $\hat{\boldsymbol{b}}_{NP_z}$ represent the expression of the vector $\hat{\boldsymbol{b}}_z$ in $\boldsymbol{\mathcal{F}}_{NP}$ and $\boldsymbol{z}_{NP}$ represent the z-axis basis vector of $\boldsymbol{\mathcal{F}}_{NP}$ expressed in $\boldsymbol{\mathcal{F}}_{NP}$ so that the azimuth angle error $\delta\vartheta$ can be computed by the following sequence of equations:

$$\boldsymbol{c}_z = \hat{\boldsymbol{b}}_{NP_z} - \left(\frac{\hat{\boldsymbol{b}}_{NP_z}^T \boldsymbol{z}_{NP}}{\boldsymbol{z}_{NP}^T \boldsymbol{z}_{NP}} \right) \boldsymbol{z}_{NP} \tag{7.20}$$

$$\hat{\boldsymbol{c}}_z = \frac{\boldsymbol{c}_z}{|\boldsymbol{c}_z|} \tag{7.21}$$

$$\vartheta_a = \left| \frac{\cos^{-1}(\hat{\boldsymbol{c}}_z{}^T \boldsymbol{x}_{NP})}{|\hat{\boldsymbol{c}}_z||\boldsymbol{x}_{NP}|} \right| \tag{7.22}$$

$$\delta\vartheta = |\vartheta - \vartheta_a| \tag{7.23}$$

The sequence of equations from Eq. (7.17) - Eq. (7.19) are functionally preforming a projection of the actual spacecraft boresight vector into the x-y plane of $\boldsymbol{\mathcal{F}}_{NP}$ which is defined to have its x-axis in the direction of $\boldsymbol{v}_{ECI}$. The actual azimuth angle of the spacecraft ϑ_a is, therefore, the angle between the aforementioned actual boresight projection vector $\hat{\boldsymbol{c}}_z$ and the x-axis of $\boldsymbol{\mathcal{F}}_{NP}$.

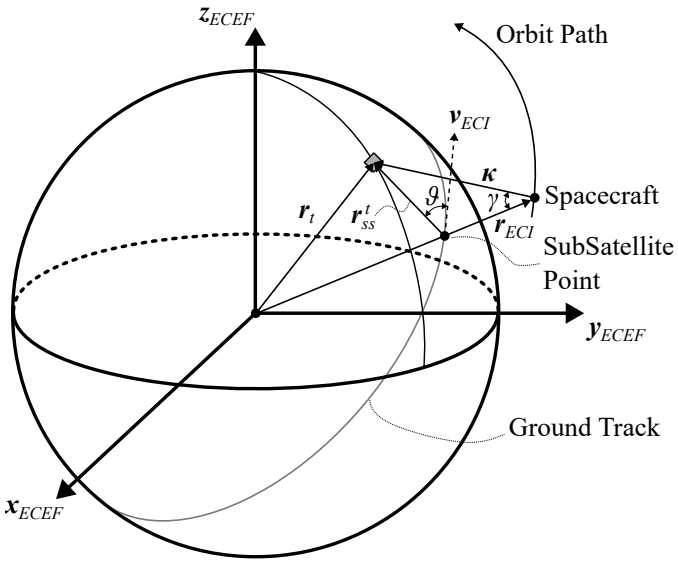

Figure 7.7: Azimuth Geometry and SubSatellite Point Depicted for a Target Located Off the Spacecraft Ground Track.

The nadir angle error is calculated by comparing the actual nadir angle formed by the spacecraft boresight and $-\boldsymbol{r}_{ECI}$ to the desired nadir angle γ. The actual nadir angle γ_a can be obtained through Eq. (7.24) where the actual spacecraft z-axis basis vector expressed in $\mathscr{F}_{ECI}$ is denoted by $\hat{\boldsymbol{b}}_z$ and the unit nadir direction vector expressed in $\mathscr{F}_{ECI}$ is denoted by $\boldsymbol{u}_e^{ECI}$:

$$\cos(\gamma_a) = \frac{\hat{\boldsymbol{b}}_z^T \boldsymbol{u}_e^{ECI}}{|\hat{\boldsymbol{b}}_z||\boldsymbol{u}_e^{ECI}|} \tag{7.24}$$

which leads to the nadir angle error being succinctly calculated as $\delta\gamma = |\gamma - \gamma_a|$.

Nadir mapping errors generally worsen at lower elevation angles ϵ and are related to the distance between the target and the satellite. The nadir errors are calculated as:

$$\delta\theta = \delta\gamma \tag{7.25}$$

$$\delta s = \delta\gamma \frac{|\kappa|}{\sin(\epsilon)} \tag{7.26}$$

Error in the OD-EKF state estimate also leads to a a series of errors worth accounting. The error between the estimated satellite position and true satellite position is calculated as follows:

$$\boldsymbol{\delta r} = \hat{\boldsymbol{r}}_{ECI} - \boldsymbol{r}_{ECI} \tag{7.27}$$

where $\boldsymbol{\delta r} = [\delta r_1, \delta r_2, \delta r_3]^T$. The positional error should be expressed relative to the In-Cross-Range frame $\mathscr{F}_{ICR}$ to derive the in-track, cross-track and radial errors. This reference coordinate frame along with the track directions are detailed in Appendix A. The in-track pointing and mapping errors may be determined from the following equations:

$$\delta\theta = \delta r_1 \sin\left(\arccos\left(\cos(\vartheta)\sin(\gamma)\right)\right) \frac{1}{|\boldsymbol{\kappa}|} \tag{7.28}$$

$$\delta s = \delta r_1 \cos\left(\arcsin\left(\sin(\zeta)\sin(\vartheta)\right)\right) \frac{|\boldsymbol{r}_{targ}|}{|\boldsymbol{\kappa}|} \tag{7.29}$$

The cross-track error metrics are computed following a similar set of equations:

$$\delta\theta = \delta r_2 \sin\left(\arccos\left(\cos(\vartheta)\sin(\gamma)\right)\right) \frac{1}{|\boldsymbol{\kappa}|} \tag{7.30}$$

$$\delta s = \delta r_2 \cos\left(\arcsin\left(\sin(\zeta)\sin(\vartheta)\right)\right) \frac{|\boldsymbol{r}_{targ}|}{|\boldsymbol{\kappa}|} \tag{7.31}$$

Errors along the radial direction of $\mathscr{F}_{ICR}$ can be calculated as follows:

$$\delta\theta = \delta r_3 \sin(\gamma) \frac{1}{|\boldsymbol{\kappa}|} \tag{7.32}$$

$$\delta s = \delta r_3 \frac{\sin(\gamma)}{\sin(\epsilon)} \tag{7.33}$$

While additional sources of error such as sensor mounting errors are likely to exist in a real system, this thesis limited error accounting to the aforementioned sources for lack of a mechanical system to derive other errors.

7.5 Attitude Controller Modifications

Oceanographic target tracking generally requires the spacecraft to follow an attitude trajectory which more rapidly changes when compared to strictly nadir pointing. In addition, pointing accuracy becomes significantly more important to limit the amount of mapping error experienced by the optical payload. To achieve these more stringent pointing requirements, the attitude controller applied in Chapter. 5 and Chapter. 6 was modified in this section to reduce offset errors that were induced by the SMC boundary layer approximation when the spacecraft was roughly pointing along the desired attitude trajectory. The control signal from Section. 5.1 was updated through the addition of an integral component $\boldsymbol{u}_I$ leading to the new control signal to be formed as:

$$\boldsymbol{u}_{cmd} = \boldsymbol{u}_n + \boldsymbol{u}_{eq} + \boldsymbol{u}_{ff} + \boldsymbol{u}_I \tag{7.34}$$

where the integral portion of the control signal may be calculated as:

$$\boldsymbol{u}_I = -\varrho \boldsymbol{K}_I \text{sign}(q_{e_4}) \int \hat{\boldsymbol{q}}_e \tag{7.35}$$

In Eq. (7.35) $\boldsymbol{K}_I = k_I \boldsymbol{J}$ where k_I is the tunable integral gain. ϱ is a scaling function which smoothly merges the integral control signal into the attitude controller. In this work ϱ was calculated as:

$$\varrho = \text{sat}\left(\frac{\epsilon}{\varphi}\right) \tag{7.36}$$

where ϵ is the propagated target pass elevation angle in degrees, and φ is the elevation angle for which at this elevation angle, the complete magnitude of the integral controller is merged into Eq. (7.34). In this work φ was selected as 45°. The saturation function in Eq. (7.36) is used to saturate $\frac{\epsilon}{\varphi}$ on the bounds of 0 - 1. To prevent integral windup, the integral state of Eq. (7.35) was reset to 0 for all ϵ below 0°. The result is a control signal which smoothly merges into the SMC controller while the satellite is performing a target tracking maneuver. For all other time the integral controller does not produce a command signal to avoid undesirable transience being induced into the system when performing large attitude reorientation maneuvers.

7.6 Oceanographic Target Tracking Results

Two sets of simulation results are presented in this section. The first commands the spacecraft to track a single target in a high elevation pass. Results are compared in this section for the same target pass when albedo is considered and not considered in the simulation. The results presented for this comparison are a mixture of attitude

Table 7.1: Key Initial Conditions & Tuned Control Parameters for Target Tracking Simulation 1

Target Tracking Simulation 1 Parameters

Description	**Parameter**	**Value and Units**
Controller Modifications:		
SMC Reaching Law Parameter	α	$\frac{2}{7}$
SMC Control Gain	k	0.0004
SMC Boundary Layer	Δ	0.065
Integral Control Gain	k_I	0.005
Integral Control Merging Value	φ	45°
Initial Conditions:		
Initial Spin	$\boldsymbol{\omega}_{t=0}$	$[0.0, 0.0, 0.0]^T$ (rad/s)
Initial Gimbal Positions	$\boldsymbol{\delta}_{t=0}$	$[0.1, 0.0, 0.0]^T$ (rad)
Geodetic Target Position (lat, long)	(ϕ_d, λ_d)	12.004373° S, 135.016657° E (Arafura Sea near Milingimbi Island)

determination and target tracking performance in order to properly convey the potential effects of albedo on target tracking spacecraft. The second simulation aims to demonstrate the advanced capabilities of the DGSPCMG by commanding the satellite to track two sequential oceanographic targets. Attitude guidance formulations are provided for this simulation to develop a smooth desired attitude trajectory which directs the CMG to maneuver the spacecraft from the first target to the second.

7.6.1 Simulation 1 - Single Oceanographic Target Tracking with a DGSPCMG-Equipped ADCS

The key simulation parameters used to derive the results presented in this section are compiled in Table 7.1. The control parameter modifications in Table 7.1 were selected on the basis of reducing the target tracking nadir angle error metric to be below 1 degree for elevations angles above 45° on a target pass. The 1 degree lumped determination and control tracking error was selected corresponding to the planned pointing requirement for the Dalhousie University MANTIS mission.

The results in Fig. 7.8a - Fig. 7.8c are shown for the Arafura Sea target tracking campaign when albedo affects were considered in the simulation. The Time of Closest Approach (TCA), occurs when the elevation angle reaches its maximum value at 5319s simulation time. At this point, by observing Fig. 7.8a subplot 3, the nadir mapping

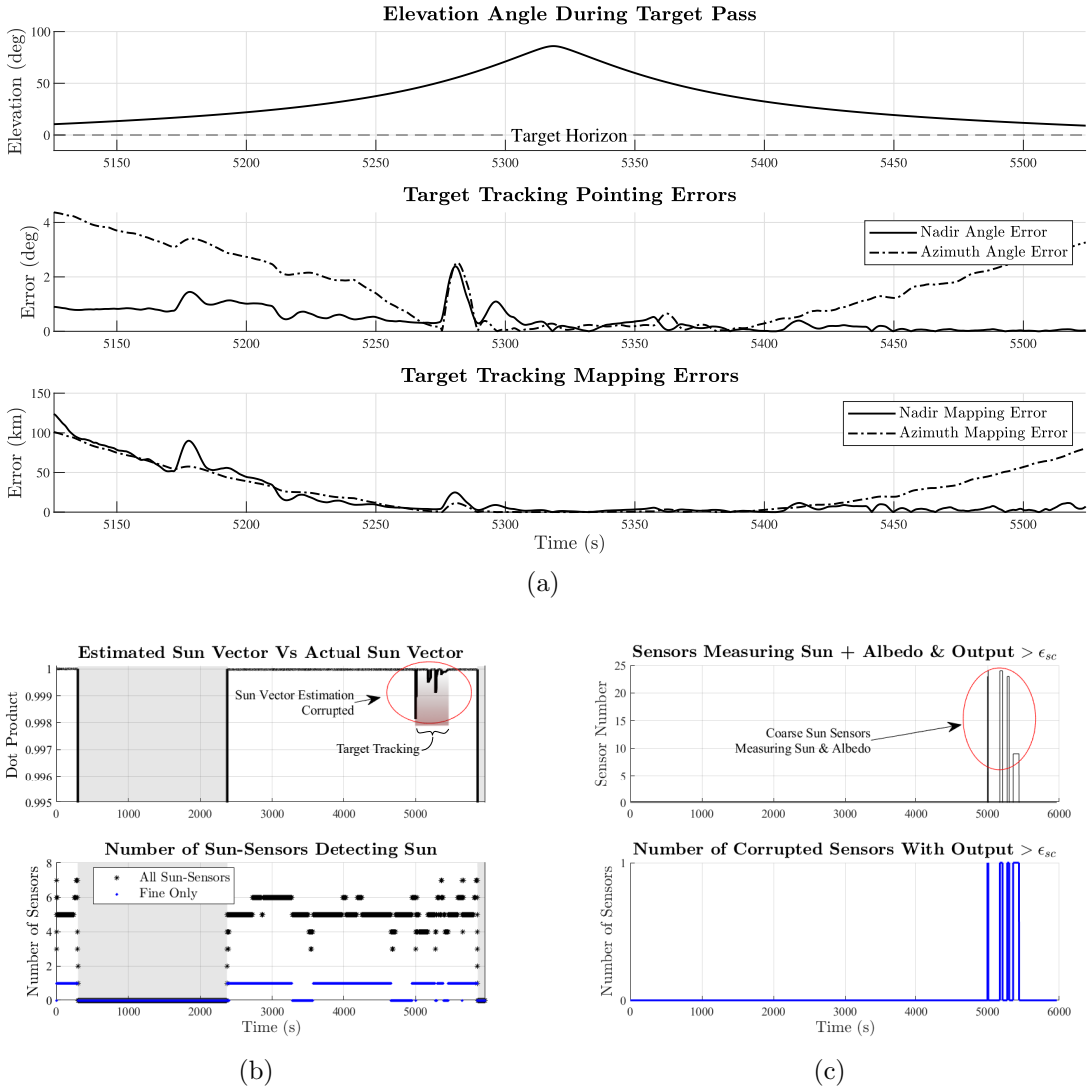

Figure 7.8: Target Tracking Simulation 1 With Albedo Effects Considered. Spacecraft Tracking Static Oceanographic Target in Arafura Sea.

error was a modest 0.4 km. Despite desirable pointing performance at TCA, there are pointing perturbations as large as 2.5° observable in Fig. 7.8a occurring while the satellite is passing the target with an elevation angle over 45°. This pointing perturbation translated to a nadir angle mapping error of 24.86 km. Pointing errors of this magnitude violate the intended sub 1 degree accuracy requirement by roughly 150%. The observed large pointing error was directly related to sun sensor corruption as shown by Fig. 7.8b and Fig. 7.8c. In Fig. 7.8b it is demonstrated that the estimated Sun direction vector was not always parallel to the actual Sun ephemeris direction vector by the fact that the dot product between the two vectors was not always unitary during the target tracking campaign.

The corruption of the estimated sun vector was directly related to a few of the coarse Sun sensors measuring the Sun and albedo at the same time. That is, if a

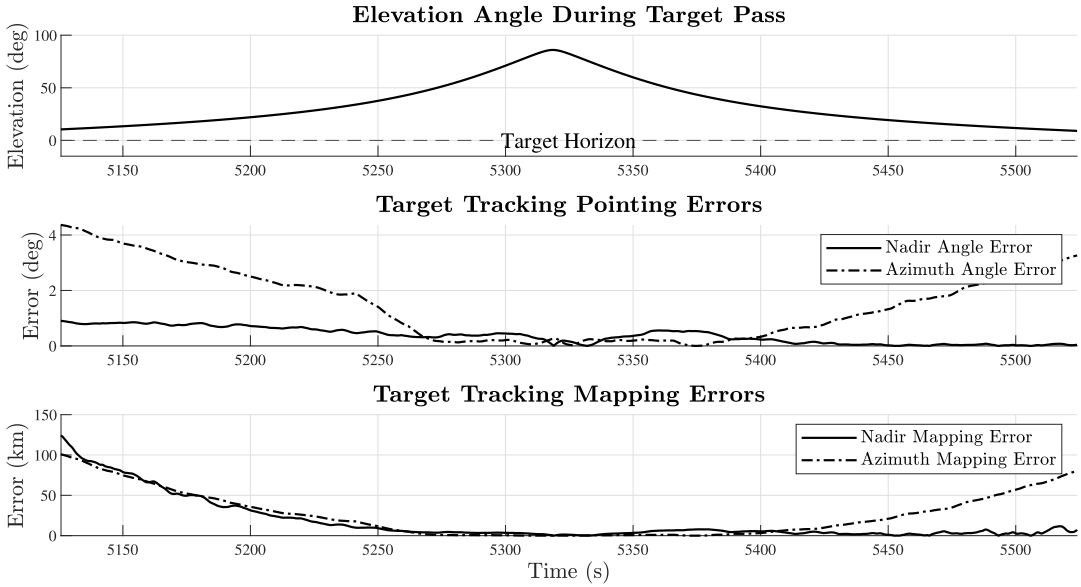

Figure 7.9: Target Tracking Simulation 1 Without Albedo Effects. Spacecraft Tracking Static Oceanographic Target in Arafura Sea.

photodiode output current is to exceed the 25 mA threshold of ϵ_{sc} while measuring both sun and albedo at the same time its measurement will be erroneous. The attitude required for target tracking was shown to be susceptible to albedo corruption in Fig. 7.8b and Fig. 7.8c for the conditions used in this research. Notably by observing Fig. 7.8c, only 1 photodiode was corrupted by albedo at any given simulation time; however, the impacts of this corruption were substantial. The work presented in this thesis emphasizes that future research work should responsibly investigate the estimation of albedo effects to prevent corruption of the proposed ADCS. Work by Cilden-Guler *et al.* (2021) has already made progress in this research field by removing albedo corruption from coarse Sun sensor clusters in [143]. The results presented in this section indicate that a threshold output for preventing albedo corruption may only be viable for strictly nadir pointing missions and may not be sufficient for target tracking missions. While albedo estimation was out of the scope of the present thesis, results presented hereinafter will assume that albedo can be reliably estimated and removed from the sensor outputs.

Results were re-simulated under the assumption that albedo was removed from the Sun sensor measurements. The target tracking error metrics under this assumption are plotted in Fig. 7.9. With albedo effects not considered the the simulation, the proposed ADCS now comfortably tracks the target with nadir angles not exceeding 1 degree when above an elevation angle of 45° over the target. The nadir angle mapping error at TCA for this instance of the simulation was ≈ 0.1 km. A notable observation from Fig. 7.9 is that for elevation angles under 45° the spacecraft experiences a fairly large azimuth error. The predominant reason for this error is that, for these low elevation angles, the merging function ϱ is < 1 and the integral portion of the

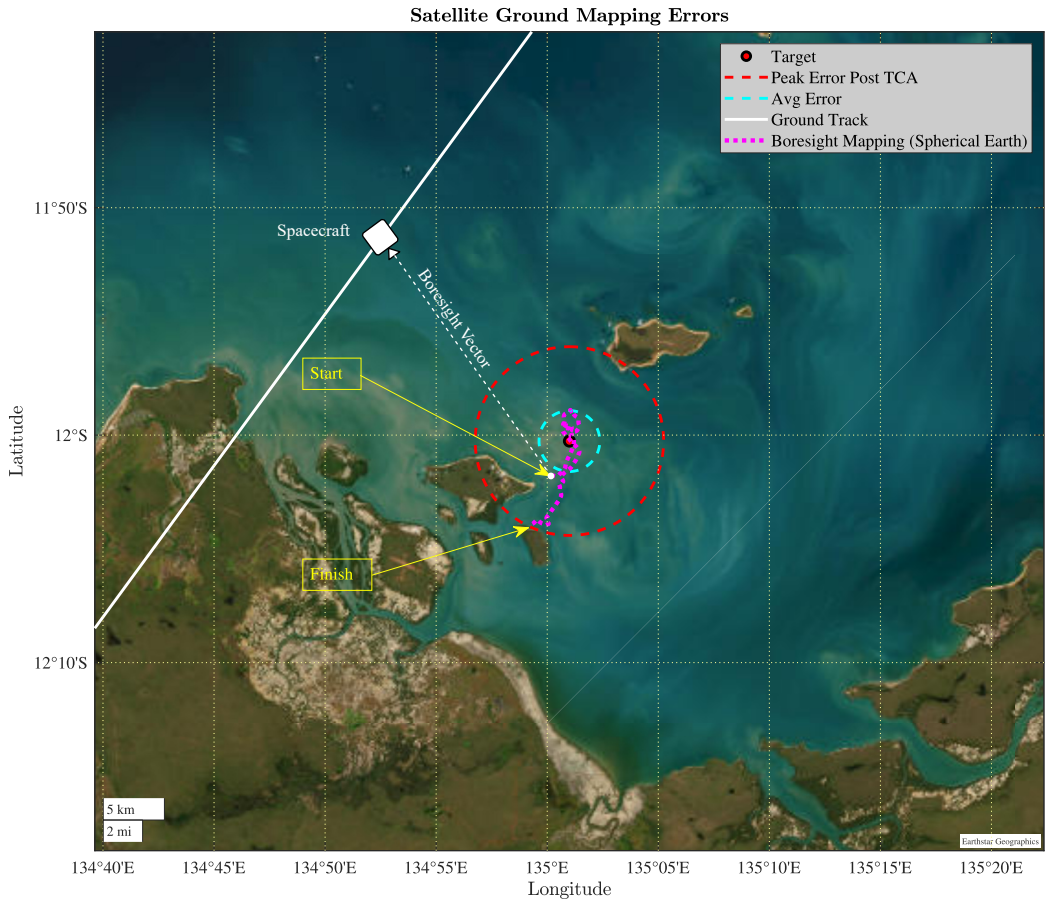

Figure 7.10: Spacecraft Boresight Mapped to the Surface of Earth During Target Tracking.

control signal is, therefore, small compared to the output from the SMC controller. Another intriguing result is that, despite the integral control effect fading out post maneuver, the SMC controller was achieving one of its lowest continuous nadir angle errors over the entire maneuver. In fact, at $\sim 11°$ elevation post TCA the nadir angle error is only $0.02°$. This angular error translates to only 2.5km of mapping error despite the increased distance to the target. It was found that, by performing an earlier reorientation to the target tracking attitude, the pre TCA nadir angle error could be reduced to levels around $0.1°$ with the peak nadir angle error being $0.6°$. It was believed at the time of simulation that performing earlier maneuvers allowed any residual transience from the maneuver to be damped prior to the target tracking campaign leading to improved target tracking accuracy.

The location on the surface of Earth where the spacecraft boresight was mapped during the target tracking maneuver above $45°$ elevation is provided in Fig. 7.10. Circles centered about the target position were provided with radii corresponding to the peak and average nadir angle mapping errors to help visually interperate the spacecraft target tracking accuracy. The spacecraft ground-track is also plotted in Fig. 7.10. The radius of the post TCA peak mapping error circle (red) was 7.7km.

The radius of the average mapping error circle (cyan) specified at the 1σ level was 2.5 ± 2.1 km.

7.6.2 Simulation 2 - Sequential Oceanographic Target Tracking

Simulation 2 presents a new target tracking scenario where the DGSPCMG-equipped ADCS must track two sequential targets and ensure that the spacecraft is observing each target at its respective TCA. All simulation conditions are identical to Simulation 1; however, a second target is added in Indonesia, west of Jendidori, with a location specified by 1.128829° S 135.90° E. To perform sequential target tracking it is necessary to schedule when the spacecraft will observe each target. In this thesis, the target tracking schedule was planned by first propagating the spacecraft orbit and the target positions to obtain the elevation angles with respect to time for each target pass. Then, to allow the satellite to follow a smooth attitude trajectory from 1 target to the next, weights were calculated for each target where, 20 seconds prior to the elevation crossover point from Target 1 to Target 2 the weight for Target 1 was $w_1 = 1$ and $w_2 = 0$ for Target 2. 20 seconds after the elevation crossover point, the weights were set to $w_1 = 0$ and $w_2 = 1$. The elevation crossover point describes the point where the Target 1 pass elevation and Target 2 pass elevation are equal. The propagated target elevations and weights are shown in Fig. 7.11.

With the weights pre-computed, the spacecraft can follow a smooth trajectory between the two targets by finding the weighted average of quaternions which represent the desired tracking attitudes, respectively, for each target. An exact closed form solution exists from Markley (2007) which computes the weighted average between

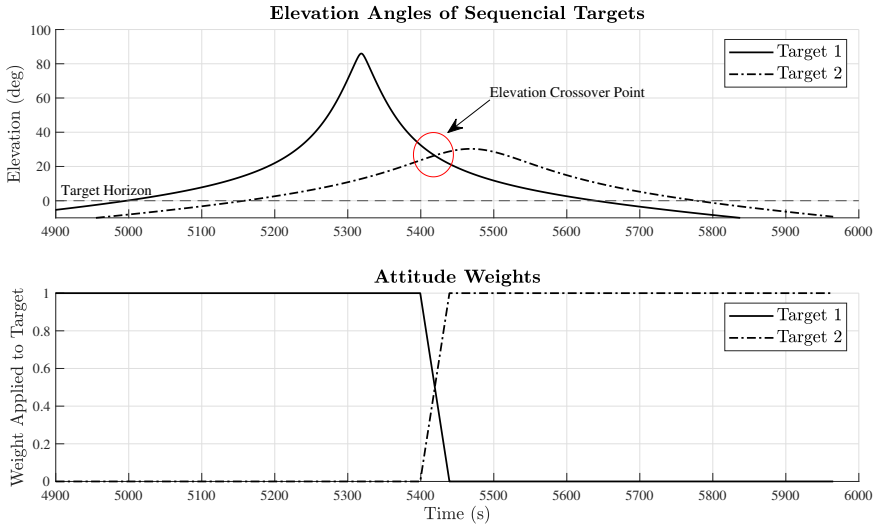

Figure 7.11: Weights Applied to the Observation of Two Sequential Targets. Pre-Propagated Elevation Angles and Weights

two quaternions and is calculated by applying [144]:

$$\boldsymbol{q}_{avg} = \left[\sqrt{\frac{w_1(w_1 - w_2 + z)}{z(w_1 + w_2 + z)}} \boldsymbol{q}_1 + \text{sign}(\boldsymbol{q}_1^T \boldsymbol{q}_2) \sqrt{\frac{w_2(w_2 - w_1 + z)}{z(w_1 + w_2 + z)}} \boldsymbol{q}_2 \right] \tag{7.37}$$

where $z = \sqrt{(w_1 - w_2)^2 + 4w_1 w_2 (\boldsymbol{q}_1^T \boldsymbol{q}_2)^2}$. The average quaternion will direct the satellite boresight in between the two targets at the crossover point because the weights will be equal. More importantly, the average quaternion ensures a smooth desired attitude trajectory from Target 1 to Target 2. The planned maneuver provides the spacecraft with a 28 second period where it will be commanded to track Target 2 prior to reaching the TCA for Target 2.

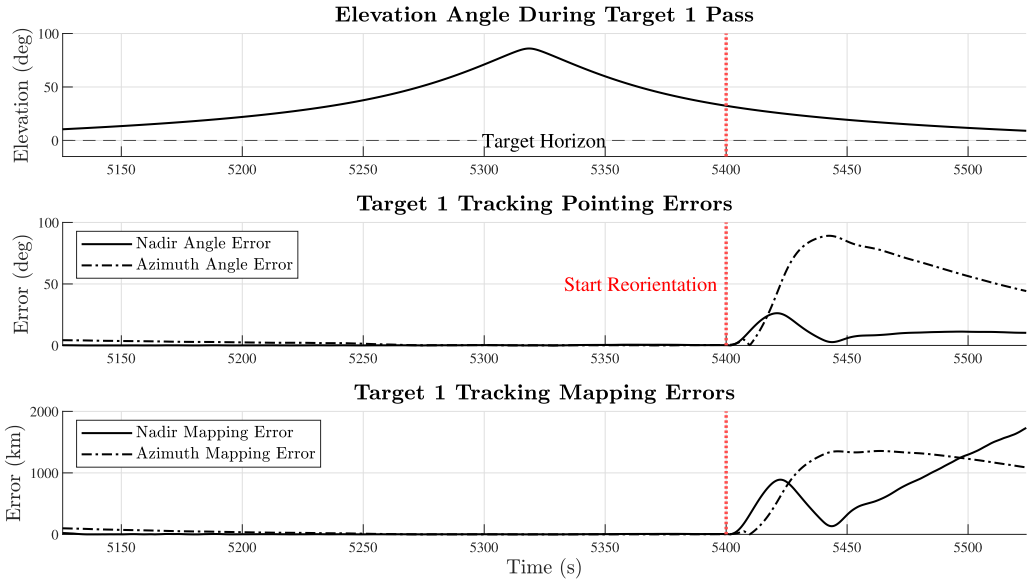

Figure 7.12: Target 1 Tracking Error Metrics in Sequential Target Tracking Mission

The results for the target tracking error metrics are provided in Fig. 7.12 for Target 1 and Fig. 7.13 for Target 2. It is apparent in both Fig. 7.12 and Fig. 7.13 that, during the 40 second target tracking transition maneuver starting at the red dashed line in Fig. 7.12 and ending at the red dashed line in Fig. 7.13, the mapping error is large. A large error should be an expected result as the satellite is being commanded to point its boresight somewhere in between the two targets during this time. The Target 2 tracking campaign tracks a quantitatively worse target pass when compared to the Target 1 pass because the elevation angle peaks at only 30.28° for the Target 2 pass. A low elevation pass indicates that the satellite will be far from the target at TCA and that it will be more difficult to reduce the nadir and azimuth mapping errors. An enlarged plot of Target 2 mapping errors is provided in Fig. 7.14 where the mapping errors are plotted for the tracking duration after the target transition maneuver is completed. The nadir and azimuth mapping errors were 26.1 km and 18.6 km, respectively, at TCA. These errors reduced to the sub 5 km level post TCA,

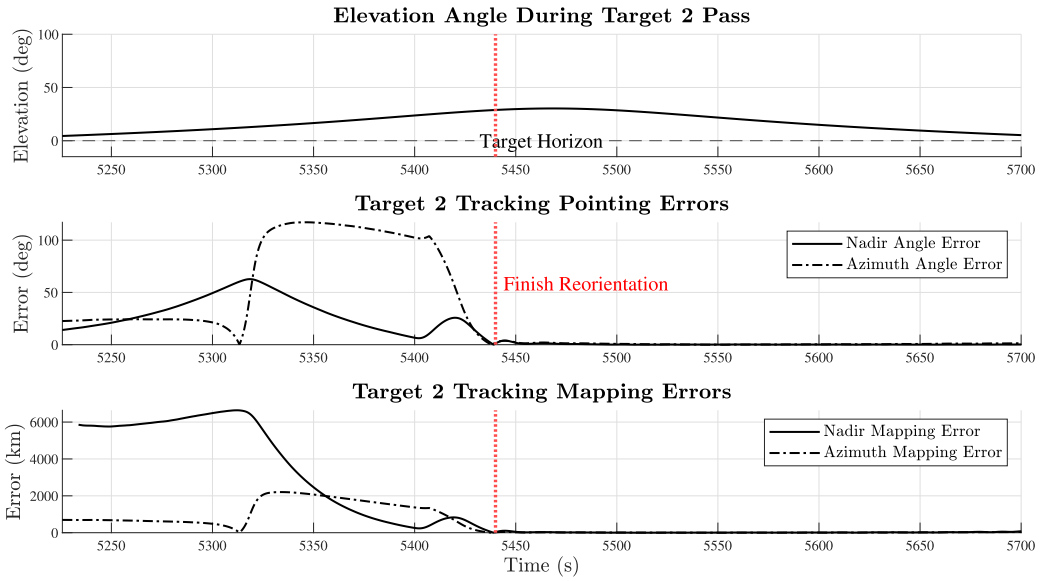

Figure 7.13: Target 2 Tracking Error Metrics in Sequential Target Tracking Mission

despite theory from Eq. (7.26) stating that the errors should increase with lowered elevation angle. Such a result could indicate that there is some undamped transience in the attitude response that improved during the target tracking campaign. As expected, however, the right most trend of the plot in Fig. 7.14 shows increasing mapping error as the spacecraft nears the target local horizon.

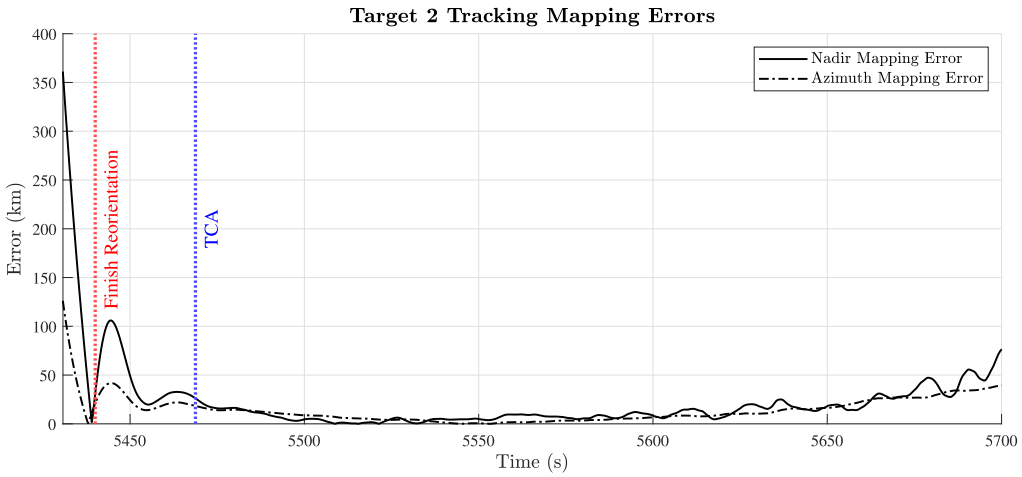

Figure 7.14: Target 2 Mapping Error Post TCA

The target tracking campaign is visualized in Fig. 7.15a - Fig. 7.15f where the spacecraft body frame is shown in orbit relative to Earth. The visualization offers some additional validation of the desired attitude formulations by demonstrating that the spacecraft $z+$ axis is directed towards the targets during the mission as intended.

Noticeably in Fig. 7.15f, while the spacecraft is in the midst of transitioning its attitude from Target 1 to Target 2, the boresight is directed towards the ocean. While expectedly not directed towards a target at this time, it is desirable to observe the boresight directed towards the ocean, as erroneous attitudes directed away from Earth and towards the Sun could damage optical payloads on board the spacecraft. An additional validation can be obtained from Fig. 7.15e where, by close observation, the x-axis basis vector of $\mathcal{F}_{BF}$ is roughly aligned with the x-axis of the nadir pointing frame $\mathcal{F}_{NP}$. The observed vector alignment re-enforces the validations made in Section. 7.3.2 that the alignment-constrained attitude is correctly respecting the $\hat{\boldsymbol{v}}_{ECI}$ constraint vector.

The results presented in Section. 7.6 have leveraged the proposed DGSPCMG-equipped ADCS to enable high-agility target tracking of oceanographic targets. The technology considered in this chapter could be extended to future oceanographic CubeSat missions where agile and precise pointing is desirable. Results presented in this chapter demonstrated that the Extended DGSPCMG SCL successfully performed target tracking objectives and, therefore, avoided complicating singularities while doing so. Pointing and mapping results were somewhat complicated by albedo corruption during off nadir spacecraft attitudes. The observed albedo effects build a motivation for future work to investigate systematically estimating and moderating albedo corruption for target tracking ADCS designs that employ Sun sensors as a primary component of attitude determination.

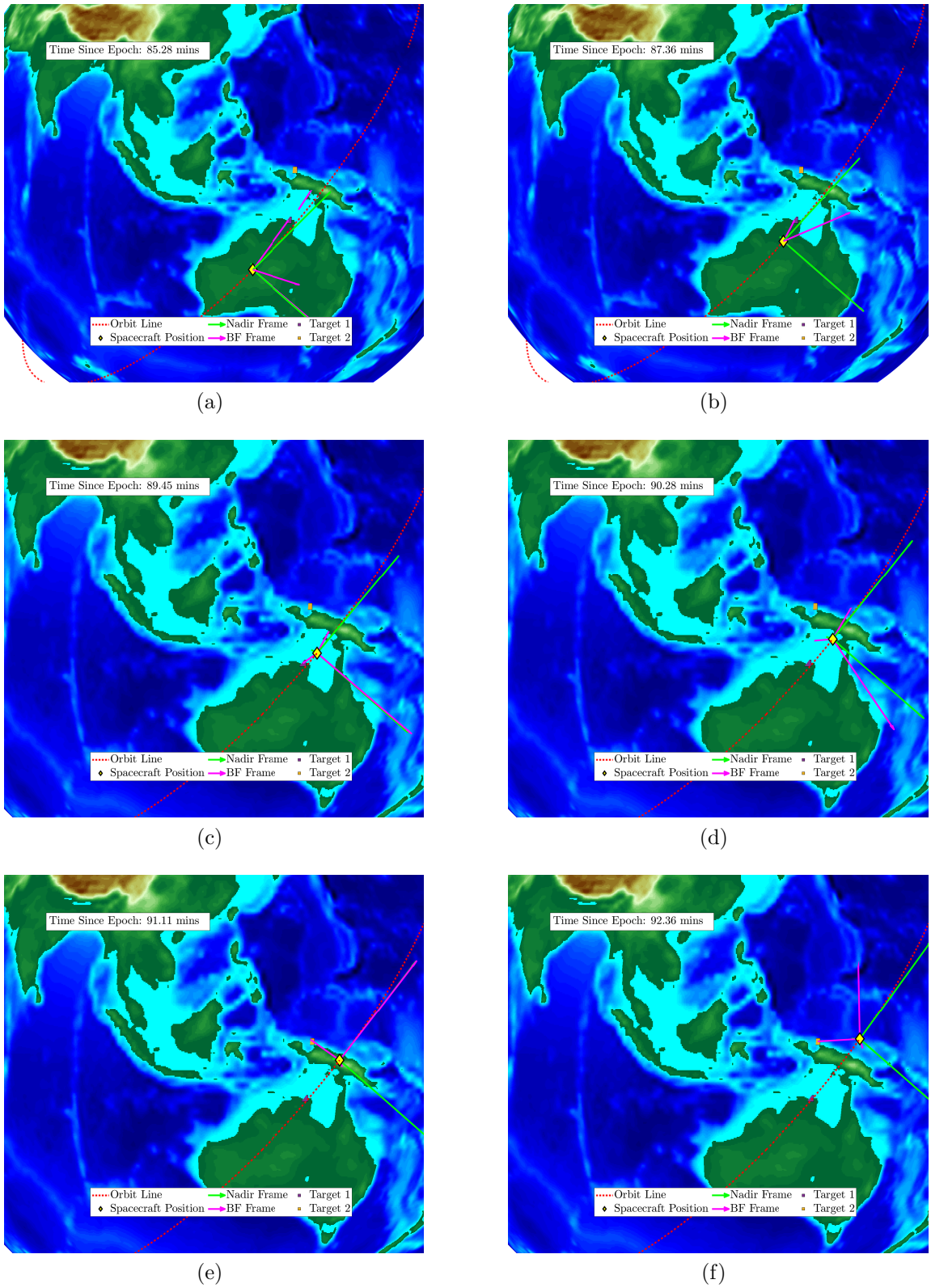

Figure 7.15: Sequential Target Tracking Campaign Visualization for Targets Located in or around the Arafura Sea

Chapter 8

Conclusions and Recommendations

This thesis details the development and verification of a CubeSat attitude control system which leverages the Double-Gimbal Scissor-Pair Control Moment Gyroscope as the primary attitude actuator. Robust on-orbit attitude control was achieved in the focus thesis through the advancement of a novel gimbal steering control law which enables DGSPCMG singularity escape from a variety of complicating singular states identified in the thesis. To quantify the performance of the proposed steering control law, a spacecraft simulator was constructed which models environmental perturbations, realistic attitude sensors, lighting conditions, and spacecraft dynamics. The simulator was extended to multiple case studies in Low-Earth Orbit where the novel steering control law was expected to provide performance benefits because of its ability to provide the spacecraft with agile maneuvering capabilities.

The first of these case studies investigated the use of the proposed SCL for momentum desaturation while maintaining attitude pointing. It was found that the proposed SCL in a nadir pointing mission could maintain pointing while desaturating the DGSPCMG. Additionally, the developments in this case study addressed the understudied case of escaping CMG singularities caused by angular impulses exerted by the environment on the satellite and CMG. The hybrid CMG-magnetorquer configuration was shown, for the simulation conditions used in the research, to enable singularity escape from environmentally induced singularities.

The second case study applied the proposed DGSPCMG SCL on an active debris removal mission where the DGSPCMG-equipped CubeSat was connected to a debris satellite via a flexible tether. With attitude control provided by the DGSPCMG, a novel Two-Stage Estimator was developed which, to the author's best knowledge, is the first published method for estimating all principal and products of inertia for a debris body without assuming the location of the tether connection point on the debris to be known *a priori*. The removal of the tether connection point was achieved by proposing pseudo measurement Kalman Filter formulations which, for the simulation conditions and sensors modeled, accurately estimated the debris center of mass position to be used as a key component of inertia estimation. For the simulation conditions used in this research, under the worst-case scenario, the principal inertia parameters of the debris were estimated to percent errors at or less than 6.1 %.

The final case study demonstrated the use of the DGSPCMG SCL on oceanographic target-tracking missions. The agile maneuvering characteristics made possible by the DGSPCMG were leveraged to perform accurate tracking of sequential oceanographic targets. For target pass elevation angles above 45° the proposed attitude determination and control system achieved an average mapping error of 2.5 ± 2.1 km at the 1σ level for a single target pass. It was found in the results of this section

that Earth albedo effects could have a profound impact on target-tracking accuracy, leading to the recommendation that future ADCS developments investigate the systematic estimation and moderation of albedo effects.

Considering the three evaluated case studies, the contributions of this thesis may be summarized as follows:

1. Development of a robust DGSPCMG steering control law which escapes from singularities expected to be experienced during missions in LEO.

2. A proposed two-stage inertia estimation algorithm which estimates all principal and products of inertia for a tethered debris.

3. Relaxation of the tether connection point assumption typically used for estimation of tethered debris inertia

4. Assessment of expected target tracking error metrics for a DGSPCMG-equipped ADCS.

5. Simulation fidelity additions for future spaceflight simulations performed at Dalhousie University.

Following the advancements made in this thesis, future work should investigate the development of multi-body formulations to model the DGSPCMG. The current thesis has assumed that actuation of the CMG does not affect the spacecraft inertia — a multibody model would relax this assumption allowing for higher fidelity simulations to be studied. Following a similar goal of fidelity improvement, it is recommended that future work consider remodeling the LiDAR sensor used to drive the proposed TSE. Software packages including BlenSor are open source and enable detailed LiDAR sensor simulations. Current algorithms such as Iterative Closest Points could additionally be implemented at this point so that measurements fed to the TSE more closely resemble real-world implementations. A recommendation which further refines the proposed ADCS would be to integrate the GPS models and orbit determination methods presented in [88]. This previous work presents modern orbit determination methods which may enhance the OD-EKF presented in the current thesis. Discussed as part of the target tracking results, the proposed ADCS would also benefit from moderating albedo corruption. One method to avoid albedo corruption may be to implement a star tracker on the spacecraft; however, this sensor still experiences other interfering effects. A detailed study may be required to evaluate methods for avoiding attitude sensor corruption. Notwithstanding potential sensor corruption, the ability to maintain attitude in eclipse by employing a star tracker provides indisputable benefits to the ADCS proposed in this thesis.

Bibliography

[1] "Calculate zonal harmonic representation of planetary gravity - Simulink." [Online]. Available: https://www.mathworks.com/help/aeroblks/zonalharmonicgravitymodel.html

[2] B. M. M. Bomani, "CubeSat Technology Past and Present: Current State-of-the-Art Survey," Glenn Research Center, Cleveland, Ohio, Technical Publication TP-20210000201, Dec. 2021. [Online]. Available: https://ntrs.nasa.gov/api/citations/20210000201/downloads/TP-20210000201.pdf

[3] A. Poghosyan and A. Golkar, "CubeSat evolution: Analyzing CubeSat capabilities for conducting science missions," *Progress in Aerospace Sciences*, vol. 88, pp. 59–83, Jan. 2017. [Online]. Available: https://linkinghub.elsevier.com/retrieve/pii/S0376042116300951

[4] D. Selva and D. Krejci, "A survey and assessment of the capabilities of Cubesats for Earth observation," *Acta Astronautica*, vol. 74, pp. 50–68, May 2012. [Online]. Available: https://linkinghub.elsevier.com/retrieve/pii/S0094576511003742

[5] R. Votel and D. Sinclair, "Comparison of Control Moment Gyros and Reaction Wheels for Small Earth-Observing Satellites," in *Proceedings of the AIAA/USU Conference on Small Satellites*, 2012, p. 7, sSC12-X-1. [Online]. Available: https://digitalcommons.usu.edu/cgi/viewcontent.cgi?article=1080&context=smallsat

[6] A. Gaude and V. Lappas, "Design and Structural Analysis of a Control Moment Gyroscope (CMG) Actuator for CubeSats," *Aerospace*, vol. 7, no. 5, p. 55, May 2020. [Online]. Available: https://www.mdpi.com/2226-4310/7/5/55

[7] N. Baker, "Feasibility and design of miniaturized Control Moment Gyroscope for a 3-axis stabilized Micro Satellite," Master's thesis, Lulea University of Technology, Lulea, Sweden, Oct. 2016. [Online]. Available: https://www.diva-portal.org/smash/get/diva2:1053012/FULLTEXT01.pdf

[8] V. Nagabhushan, "Development of Control Moment Gyroscopes for Attitude Control of Small Satellites," Master's thesis, University of Florida, Gainesville, Florida, 2009. [Online]. Available: https://control.kau.ac.kr/wp-content/uploads/2015/07/DEVELOPMENT-OF-CONTROL-MOMENT-GYROSCOPES-FOR-ATTITUDE-CONTROL-Univ-Florida-Thesis.pdf

[9] A. Siahpush and J. Gleave, "A Brief Survey of Attitude Control Systems for Small Satellites using Momentum Concepts," in *Proceedings of the*

annual conference of Small Satellites. Logan, Utah: Technical Publications Department of Honeywell Satelllite Systems Department, 1988. [Online]. Available: https://digitalcommons.usu.edu/smallsat/1988/all1988/24/

[10] C. K. Moorthy, "A Comparison Study on Control Moment Gyroscope Arrays and Steering Logic," Master's thesis, York University, Toronto Ontario, Dec. 2019. [Online]. Available: https://yorkspace.library.yorku.ca/xmlui/bitstream/handle/10315/37483/KrishnaMoorthy_Chitiiran__2019_Masters.pdf?sequence=2&isAllowed=y

[11] T. F. Sheerin, J. A. Hoffman, and M. D. Carpenter, "Actuator Sizing and Utility Assessment of Control Moment Gyroscopes for an Astronaut EVA Jetpack," in *45th International Conference on Environmental Systems*, Bellevue, Washington, 2015, p. 14. [Online]. Available: http://hdl.handle.net/2346/64524

[12] I. Jikuya, K. Fujii, and K. Yamada, "Attitude maneuver of spacecraft with a variable-speed double-gimbal control moment gyro," *Advances in Space Research*, vol. 58, no. 7, pp. 1303–1317, Oct. 2016. [Online]. Available: https://linkinghub.elsevier.com/retrieve/pii/S0273117716303088

[13] S. Barman and M. Sinha, "Singularity avoidance controller design for spacecraft attitude control using double-gimbal variable-speed control moment gyro," *European Journal of Control*, vol. 70, p. 100782, Mar. 2023. [Online]. Available: https://linkinghub.elsevier.com/retrieve/pii/S0947358023000110

[14] H. Kojima, R. Nakamura, and S. Keshtkar, "Steering control law for double-gimbal scissored-pair CMG," *Advances in Space Research*, vol. 66, no. 4, pp. 771–784, Aug. 2020. [Online]. Available: https://linkinghub.elsevier.com/retrieve/pii/S0273117720303306

[15] T. Kelso, "CelesTrak: SATCAT Boxscore," Mar. 2024. [Online]. Available: https://celestrak.org/satcat/boxscore.php

[16] E. Kulu, "Nanosats Database," Mar. 2024. [Online]. Available: https://www.nanosats.eu/index.html

[17] X.-j. Chen and W. H. Steyn, "Optimal Combined Reaction-Wheel Momentum Management for LEO Earth-Pointing Satellites," in *Smaller than Small: The Next Generation*. Utah, USA: American Institute of Aeronautics and Astronautics, 1998, p. 11. [Online]. Available: https://digitalcommons.usu.edu/smallsat/1998/all1998/50/

[18] S. Tkachev and M. Ovchinnikov, "Use of External Torques for Desaturation of Reaction Wheels," *Journal of Guidance, Control, and Dynamics*, vol. 41, no. 8, Aug. 2018. [Online]. Available: https://arc.aiaa.org/doi/epdf/10.2514/1.G003328

[19] G. Avanzini, E. De Angelis, F. Giulietti, and N. Serrano, "Attitude control of Low Earth Orbit satellites by reaction wheels and magnetic torquers," *Acta Astronautica*, vol. 160, pp. 625–634, Jul. 2019. [Online]. Available: https://linkinghub.elsevier.com/retrieve/pii/S009457651831974X

[20] H. Leeghim and D. Kim, "Singularity-robust control moment gyro allocation strategy for spacecraft attitude control in the presence of disturbances," *Aerospace Science and Technology*, vol. 119, p. 107178, Dec. 2021. [Online]. Available: https://linkinghub.elsevier.com/retrieve/pii/S127096382100688X

[21] J.-C. Liou, "An active debris removal parametric study for LEO environment remediation," *Advances in Space Research*, vol. 47, no. 11, pp. 1865–1876, Jun. 2011. [Online]. Available: https://linkinghub.elsevier.com/retrieve/pii/S0273117711000974

[22] D. J. Kessler and B. G. Cour-Palais, "Collision frequency of artificial satellites: The creation of a debris belt," *Journal of Geophysical Research: Space Physics*, vol. 83, no. A6, pp. 2637–2646, Jun. 1978. [Online]. Available: https://agupubs.onlinelibrary.wiley.com/doi/10.1029/JA083iA06p02637

[23] N. Ibrahim, "Attitude and Orbit Control of Small Satellites for Autonomous Terrestrial Target Tracking," Master's thesis, University of Toronto, Toronto Ontario, 2013. [Online]. Available: https://tspace.library.utoronto.ca/handle/1807/42965

[24] R. Magner, "Extending the Capabilities of Terrestrial Target Tracking Spacecraft.pdf," Master's thesis, University of Toronto, Toronto Ontario, 2018. [Online]. Available: https://tspace.library.utoronto.ca/bitstream/1807/91365/1/Magner_Robert_201811_MAS_thesis.pdf

[25] A. G. Guerra, F. Francisco, J. Villate, F. Aguado Agelet, O. Bertolami, and K. Rajan, "On small satellites for oceanography: A survey," *Acta Astronautica*, vol. 127, pp. 404–423, Oct. 2016. [Online]. Available: https://linkinghub.elsevier.com/retrieve/pii/S0094576515303441

[26] A. Wailand, "Development of a Computer Simulation Tool to Study the Attitude Determination and Control of CubeSats," Master's thesis, Dalhousie University, Halifax, NS, Dec. 2020. [Online]. Available: https://dalspace.library.dal.ca/handle/10222/80095

[27] C. Ortiona, R. D. Jenkins, C. S. Malone, L. T. Dorn, M. P. Schroer, A. Schulenburg, P. M. Oppenheimer, W. M. Crane, D. Sakoda, M. Romano, R. Panholzer, and J. H. Newman, "The Naval Postgraduate School SCAT++ CubeSat Program," in *23rd Annual AIAA/USU Conference on Small Satellites*. Logan, Utah: Utah State University, Aug. 2009. [Online]. Available: https://digitalcommons.usu.edu/smallsat/2009/all2009/80/

[28] J. D. Munoz, V. Nagabhushan, S. Asundi, and N. G. Fitz-Coy, "High fidelity simulation of swampsat attitude determination and control system," *Spaceflight Mechanics*, vol. 140, 2011, publisher: [object Object]. [Online]. Available: http://rgdoi.net/10.13140/RG.2.1.3918.7685

[29] V. Lappas, P. Oosthuizen, P. Madle, L. Cowie, G. Yuksel, and D. Fertin, "MICRO CMGs FOR AGILE SMALL SATELLITES: DESIGN AND IN-ORBIT TESTS," in *6th International ESA Conference on Guidance, Navigation and Control Systems*. Loutraki, Greece: European Space Agency, Oct. 2005. [Online]. Available: https://www.researchgate.net/publication/234224351_Micro_Cmgs_for_Agile_Small_Satellites_Design_and_In-Orbit_Tests

[30] "Tensor Tech," 2024. [Online]. Available: https://tensortech.co/product/category/cmg-series#

[31] E. Mumm, "Honeybee Robotics Spacecraft Mechanisms Corporation." [Online]. Available: https://satcatalog.s3.amazonaws.com/components/3/SatCatalog_-_Honeybee_Robotics_-_MicroSat_CMG_-_Datasheet.pdf?lastmod=20210708011911

[32] "microCMG - Veoware Space," Nov. 2022. [Online]. Available: https://www.veoware.space/microcmg/

[33] "SatCatalog-Blue Canyon Technologies-CMG-8.pdf." [Online]. Available: https://satcatalog.s3.amazonaws.com/components/4/SatCatalog_-_Blue_Canyon_Technologies_-_CMG-8_-_Datasheet.pdf?lastmod=20210708011937

[34] V. J. Lappas, W. Steyn, and C. I. Underwood, "Experimental testing of a CMG cluster for agile microsatellites," in *11th Mediterranean Conference on Control and Automation MED'*. Rhodes, Greece: IEEE, Jun. 2003.

[35] "AVIONICS-CMG40-Datasheet," 2022. [Online]. Available: https://www.airbus.com/sites/g/files/jlcbta136/files/2022-03/AVIONICS-CMG40-60S-v5_2022.pdf

[36] "Honeywell M50 CMG - Datasheet," Sep. 2002. [Online]. Available: https://satcatalog.s3.amazonaws.com/components/6/SatCatalog_-_Honeywell_-_M50_CMG_-_Datasheet.pdf?lastmod=20210708012029

[37] D. Steyn, "Variable Speed Scissored Pair Dual Gimbal Control Moment Gyro for Nano-Satellites," Ph.D. dissertation, Stellenbosch University, Dec. 2015.

[38] P. C. Hughes, *Spacecraft Attitude Dynamics*, ser. Dover Books on Aeronautical Engineering. Mineola, NY: Dover Publications, 2012.

[39] B. Wie, "New Singularity Escape/Avoidance Steering Logic for Control Moment Gyro Systems," in *AIAA Guidance, Navigation, and Control Conference and Exhibit*. Austin, Texas: American Institute of Aeronautics and Astronautics, Aug. 2003. [Online]. Available: https://arc.aiaa.org/doi/10.2514/6.2003-5659

[40] "Quaternion, Direction Cosine Matrix, Euler Angle transformations." [Online]. Available: https://www.vectornav.com/resources/inertial-navigation-primer/math-fundamentals/math-attitudetran

[41] F. L. Markley and J. L. Crassidis, *Fundamentals of Spacecraft Attitude Determination and Control*. New York, NY: Springer New York, 2014. [Online]. Available: http://link.springer.com/10.1007/978-1-4939-0802-8

[42] J. Puttkamer, "Survey and comparative analysis of current geophysical models," National Aeronautics and Space Administration, Washington, D.C, Technical Note TN D-5163, May 1969. [Online]. Available: https://ntrs.nasa.gov/citations/19680007574

[43] S. P. Shuster, "A Survey and Performance Analysis of Orbit Propagators for LEO, GEO, and Highly Elliptical Orbits," Master's thesis, Utah State University, Logan, Utah, 2017. [Online]. Available: https://digitalcommons.usu.edu/etd/6510/

[44] A. Tewari, *Atmospheric and space flight dynamics: modeling and simulation with MATLAB and Simulink*, ser. Modeling and simulation in science, engineering and technology. Boston, Mass: Birkhäuser, 2007.

[45] K. R. Pollock, "An Analysis Of Orbital Propagators for Low Earth Orbit Rendevzous," Post-Doctoral Thesis, Naval Postgraduate School, Monterey, California, Sep. 1994. [Online]. Available: https://calhoun.nps.edu/handle/10945/43012

[46] K. Çagrı, "Mission Analysis of a Double Unit CubeSat BEEAGLESAT," Master's thesis, Istanbul Technical University, Dec. 2014. [Online]. Available: https://www.researchgate.net/publication/281710240_Mission_Analyses_of_a_Double_Unit_CubeSat_BeEagleSat

[47] U. Walter, "Orbit Perturbations," in *Astronautics - The Physics of Space FLight*, 3rd ed. Switzerland: Springer, Cham, Feb. 2019. [Online]. Available: https://link.springer.com/chapter/10.1007/978-3-319-74373-8_12

[48] B. Wie, *Space Vehicle Dynamics and Control*, 1st ed., ser. AIAA Education Series. 1801 Alexander Bell Drive, Reston, VA: American Institude of Aeronautics and Astronautics, 1998.

[49] S. A. Rawashdeh, "Attitude Analysis of Small Satellites Using Model-Based Simulation," *International Journal of Aerospace Engineering*, vol. 2019, pp. 1–11, Apr. 2019. [Online]. Available: https://www.hindawi.com/journals/ijae/2019/3020581/

[50] A. Wailand and R. Bauer, "Development Of An Attitude Determination And Control System For The Loris Cubesat," in *Progress in Canadian Mechanical*

Engineering. Volume 4. University of Prince Edward Island. Robertson Library, Jun. 2021. [Online]. Available: https://library.upei.ca/islandora/object/csme2021:177

[51] J. R. Wertz, "Summary of Orbit Properties and Terminology," in *Spacecraft Attitude Determination and Control*, J. R. Wertz, Ed. Dordrecht: Springer Netherlands, 1978, vol. 73, pp. 36–81, series Title: Astrophysics and Space Science Library. [Online]. Available: http://link.springer.com/10.1007/978-94-009-9907-7_3

[52] "Earth Fact Sheet." [Online]. Available: https://nssdc.gsfc.nasa.gov/planetary/factsheet/earthfact.html

[53] "Albedo (1 month) | NASA," Apr. 2024, publisher: NASA Earth Observations (NEO). [Online]. Available: https://neo.gsfc.nasa.gov/view.php?datasetId=MCD43C3_M_BSA

[54] A. Donohoe and D. S. Battisti, "Atmospheric and Surface Contributions to Planetary Albedo," *Journal of Climate*, vol. 24, no. 16, pp. 4402–4418, Aug. 2011. [Online]. Available: http://journals.ametsoc.org/doi/10.1175/2011JCLI3946.1

[55] D. Bhanderi and T. Bak, "Modeling Earth Albedo for Satellites in Earth Orbit," in *AIAA Guidance, Navigation, and Control Conference and Exhibit*. San Francisco, California: American Institute of Aeronautics and Astronautics, Aug. 2005. [Online]. Available: https://arc.aiaa.org/doi/10.2514/6.2005-6465

[56] DrZ214, "Area of surface between two lines of latitude?" Apr. 2021. [Online]. Available: https://math.stackexchange.com/q/4102850

[57] J. Gießelmann, "Development of an Active Magnetic Attitude Determination and Control System for Picosatellites on highly inclined circular Low Earth Orbits," Master's thesis, RMIT University, Melbourne, Australia, Jun. 2006.

[58] J. R. Werts and W. J. Larson, *Space Mission Analysis and Design*, 3rd ed. Torrance, California: Microcosm, 1999.

[59] M. T. Ferres, "Design and Implimentation of an Attitude Determination and Control System for the AntelSat," Master's thesis, University of the Republic, Monetevideo, Uruguay, Aug. 2015. [Online]. Available: https://www.colibri.udelar.edu.uy/jspui/bitstream/20.500.12008/5214/1/Tas15.pdf

[60] Y. Zheng, "Space Weather in the Thermosphere: Satellite Drag," Greenbelt,MD, 2014. [Online]. Available: https://ccmc.gsfc.nasa.gov/RoR_WWW/SWREDI/2014/SatDrag_YZheng_060514.pdf

[61] S. Kedare and S. Ulrich, "Extending the SPeAD-M86 Model: Incorporating the Effects of F $_{10.7}$ Variations on Atmospheric Density," in *AIAA Modeling and Simulation Technologies Conference*. San Diego, California, USA: American Institute of Aeronautics and Astronautics, Jan. 2016. [Online]. Available: https://arc.aiaa.org/doi/10.2514/6.2016-1188

[62] N. R. C. Government of Canada, "Monthly averages of solar 10.7 cm flux," Mar. 2021. [Online]. Available: https://spaceweather.gc.ca/forecast-prevision/solar-solaire/solarflux/sx-5-mavg-en.php

[63] J. Matzka, O. Bronkalla, K. Tornow, K. Elger, and C. Stolle, "Geomagnetic Kp index," 2021. [Online]. Available: https://dataservices.gfz-potsdam.de/panmetaworks/showshort.php?id=escidoc:5216888

[64] P. Alken, E. Thébault, C. D. Beggan, H. Amit, J. Aubert, J. Baerenzung, T. N. Bondar, W. J. Brown, S. Califf, A. Chambodut, A. Chulliat, G. A. Cox, C. C. Finlay, A. Fournier, N. Gillet, A. Grayver, M. D. Hammer, M. Holschneider, L. Huder, G. Hulot, T. Jager, C. Kloss, M. Korte, W. Kuang, A. Kuvshinov, B. Langlais, J.-M. Léger, V. Lesur, P. W. Livermore, F. J. Lowes, S. Macmillan, W. Magnes, M. Mandea, S. Marsal, J. Matzka, M. C. Metman, T. Minami, A. Morschhauser, J. E. Mound, M. Nair, S. Nakano, N. Olsen, F. J. Pavón-Carrasco, V. G. Petrov, G. Ropp, M. Rother, T. J. Sabaka, S. Sanchez, D. Saturnino, N. R. Schnepf, X. Shen, C. Stolle, A. Tangborn, L. Tøffner-Clausen, H. Toh, J. M. Torta, J. Varner, F. Vervelidou, P. Vigneron, I. Wardinski, J. Wicht, A. Woods, Y. Yang, Z. Zeren, and B. Zhou, "International Geomagnetic Reference Field: the thirteenth generation," *Earth, Planets and Space*, vol. 73, no. 1, p. 49, Dec. 2021. [Online]. Available: https://earth-planets-space.springeropen.com/articles/10.1186/s40623-020-01288-x

[65] A. Siahpush and A. Sexton, "A Study for Semi-Passive Gravity Gradient Stabilization of Small.pdf," in *1st Annual USU Conference on Small Satellites*. Logan, Utah: Utah State University, Oct. 1987, p. 27. [Online]. Available: https://digitalcommons.usu.edu/smallsat/1987/all1987/6/

[66] J. W. Gangestad, G. E. Pollock, and J. M. Longuski, "Lagrange's planetary equations for the motion of electrostatically charged spacecraft," *Celestial Mechanics and Dynamical Astronomy*, vol. 108, no. 2, pp. 125–145, Oct. 2010. [Online]. Available: http://link.springer.com/10.1007/s10569-010-9297-z

[67] A. A. Tikhonov, D. T. Spasic, K. A. Antipov, and M. V. Sablina, "Optimizing the electrodynamical stabilization method for a man-made Earth satellite," *Automation and Remote Control*, vol. 72, no. 9, pp. 1898–1905, Sep. 2011. [Online]. Available: http://link.springer.com/10.1134/S0005117911090116

[68] S. T. Lai, *Fundamentals of Spacecraft Charging*, 1st ed. Princeton, New Jersey: Princton University Press, Nov. 2011. [Online]. Available: https://assets.press.princeton.edu/chapters/s9500.pdf

[69] R. R. Roe, "MITIGATING IN-SPACE CHARGING EFFECTS—A GUIDELINE," Jun. 2022. [Online]. Available: https://standards.nasa.gov/sites/default/files/standards/NASA/B/0/2022-06-07-NASA-HDBK-4002B-Approved.pdf

[70] R. Bohling, F. Carroll, J. Clark, D. Debra, B. Dobrotin, R. Fischell, A. Fleig, D. Fosth, J. Gatlin, H. Perkel, R. Roberson, A. Sabroff, E. Scott, C. Spenny, and B. Tinling, "Spacecraft Radiation Torques," National Aeronautics and Space Administration, Washington, D.C, Technical Report NASA SP-8027, Oct. 1969. [Online]. Available: https://ntrs.nasa.gov/citations/19710014836

[71] "Earth Orbit Environmental Heating," National Aeronautics and Space Administration, Goddard Space Flight Center, Lesson Learned Lesson No. 683, Feb. 1999. [Online]. Available: https://llis.nasa.gov/lesson/693

[72] Y. Yang, "Quaternion-Based LQR Spacecraft Control Design Is a Robust Pole Assignment Design," *Journal of Aerospace Engineering*, vol. 27, no. 1, pp. 168–176, Jan. 2014. [Online]. Available: https://ascelibrary.org/doi/10.1061/%28ASCE%29AS.1943-5525.0000232

[73] "VN-100 IMU Datasheet," 2024. [Online]. Available: https://www.vectornav.com/products/detail/vn-100?gad_source=1&gclid=Cj0KCQjwir2xBhC_ARIsAMTXk85RiqJUR3xs_U4C8QLj8KT7RkNdTLQNkjUfxjEKMypEXBfapRvvuPQaAtz8EALw_wcB

[74] "IMU Specifications Explained · VectorNav," 2024. [Online]. Available: https://www.vectornav.com/resources/inertial-navigation-primer/specifications--and--error-budgets/specs-imuspecs

[75] "GS-3T-NANO GNSS Reciever Datasheet." [Online]. Available: https://satsearch.co/products/gnssmart-gs-3t-nano-gnss-receiver

[76] K. Bolshakov, "Digital Sun Sensor Design For Nanosatellite Applications," Master's thesis, York, Toron, Jan. 2020. [Online]. Available: https://yorkspace.library.yorku.ca/server/api/core/bitstreams/6353c2af-925d-4dbd-9916-38e99c67acf1/content

[77] "SLCD-61N8 Photodiode Datasheet." [Online]. Available: https://canada.newark.com/advanced-photonix/slcd-61n8/photodiode-planar-chip/dp/05M1251?CMP=KNC-GCA-GEN-DSA-KWL-PMAX&mckv=_dc|pcrid||plid||kword||match||slid||product||pgrid||ptaid||&s_kwcid=AL!8472!3!!!!x!!&gad_source=1&gclid=Cj0KCQjwir2xBhC_ARIsAMTXk840wKh44blbZkN7naVoOKYweoskKL-eUWx4EywKo5zyBEU_TA-aLw4aAikLEALw_wcB

[78] "BPW21R Photodiode Datasheet," Mar. [Online]. Available: https://octopart.com/bpw21r-vishay-39390634?gad_source=

1&gclid=Cj0KCQjwir2xBhC_ARIsAMTXk854mbZsuMZNOK_DtzdkgIAlBX-VzLeNbfycCh701LmptqE3cyV2O4IaAl43EALw_wcB

[79] J. C. Springmann, "Satellite Attitude Determination with Low-Cost Sensors," Doctoral Theis, University of Michigan, Ann Arbor, Michigan, 2013. [Online]. Available: https://deepblue.lib.umich.edu/bitstream/handle/2027.42/102312/jspringm_1.pdf?sequence=1

[80] G. Wahba, "A Least Squares Estimate of Spacecraft Attitude," *SIAM Review*, vol. 7, no. 3, pp. 409–409, Jul. 1965. [Online]. Available: https://doi.org/10.1137/1007077

[81] F. L. Markley and D. Mortari, "New Developments in Quaternion Estimation From Vector Observations," 2000. [Online]. Available: https://ntrs.nasa.gov/api/citations/20000034107/downloads/20000034107.pdf

[82] M. Shuster, "Three-Axis Attitude Determination from Vector Observations," *Journal of Guidance and Control*, vol. 4, no. 1, p. 9, Jan. 1981. [Online]. Available: https://malcolmdshuster.com/Pub_1981a_J_TRIAD-QUEST_scan.pdf

[83] F. L. Markley, "Multiplicative vs. Additive Filtering for Spacecraft Attitude Determination," in *6th International Conference on Control of Systems and Structures in Space*. Riomaggiore, Italy: NASA Goddard Space Flight Center, Dec. 2003. [Online]. Available: https://ntrs.nasa.gov/citations/20040037784

[84] Y. Yang, *Spacecraft Modeling, Attitude Determination, and Control Quaternion-based Approach*, 1st ed. Boca Raton, FL : CRC Press, 2019. | "A science publishers book.": CRC Press, Feb. 2019. [Online]. Available: https://www.taylorfrancis.com/books/9780429822148

[85] P. D. Groves, "Inertial Sensors," in *Principles of GNSS, Inertial, and Multi-sensor Integrated Navigation Systems*, 2nd ed. Boston, Mass: Artech House, 2013, pp. 137–161.

[86] Z. Wen, G. Yang, and Q. Cai, "An Improved Calibration Method for the IMU Biases Utilizing KF-Based AdaGrad Algorithm," *Sensors*, vol. 21, no. 15, p. 5055, Jul. 2021. [Online]. Available: https://www.mdpi.com/1424-8220/21/15/5055

[87] Z. Y.-C. Liu, S. Tarlow, M. Akbar, Q. Donnellan, and D. Senkow, "Improved Orbital Propagator Integrated with SGP4 and Machine Learning," in *Small Satellite Conference*, Logan, Utah, 2021. [Online]. Available: https://digitalcommons.usu.edu/cgi/viewcontent.cgi?article=5067&context=smallsat

[88] E. Vautour, "Development and Validation of Guidance, Navigation, and Control Strategies for CubeSat Earth Observation Missions," Master's thesis, Dalhousie University, Halifax, NS, Nov. 2022. [Online]. Available: https://dalspace.library.dal.ca//handle/10222/82068

[89] A. Mander and S. Bisnath, "GPS-based precise orbit determination of Low Earth Orbiters with limited resources," *GPS Solutions*, vol. 17, no. 4, pp. 587–594, Oct. 2013. [Online]. Available: http://link.springer.com/10.1007/s10291-012-0303-7

[90] R. Ottemark, "Autonomous Satellite Orbit Determination Based on Magnetometer and Sun Sensor Measurements," Master's thesis, Lulea University of Technology, Lulea, Sweden, 2015. [Online]. Available: https://ltu.diva-portal.org/smash/record.jsf?pid=diva2%3A1029683&dswid=-915

[91] E. M. Wesam, X. Zhang, Z. Lu, and W. Liao, "Kalman filter implementation for small satellites using constraint GPS data," *IOP Conference Series: Materials Science and Engineering*, vol. 211, p. 012015, Jun. 2017. [Online]. Available: https://iopscience.iop.org/article/10.1088/1757-899X/211/1/012015

[92] O. Montebruck and E. Gill, *Satellite Orbts: Models, Methods, and Applications*, 1st ed. Springer Berlin Heidelberg, Jun. 2000.

[93] B. Kuiack, "Spacecraft Formation Guidance and Control on J2-Perturbed Eccentric Orbits," Master of Applied Science, Carleton University, Ottawa, Ontario, 2018. [Online]. Available: https://repository.library.carleton.ca/concern/etds/cn69m482z

[94] J. H. Mathews and K. D. Fink, *Numerical methods using MATLAB*, 4th ed. Upper Saddle River, N.J: Pearson Prentice Hall, 2004.

[95] C. J. Voesenek, "Implementing a Fourth Order Runge-Kutta Method for Orbit Simulation," in *IAME 2022*, Busan, Korea, Jun. 2022, p. 3.

[96] T. Hao, S. Kawajiri, K. Tawara, and S. Mutunaga, "A Practical Rapid Attitude Maneuver Control System using Control Moment Gyros for Microsatellite TSUBAME," *Transactions of the Japan Society For Aeronautical and Space Sciences, Aerospace Technology Japan*, vol. 13, no. 0, pp. 37–43, 2015. [Online]. Available: https://www.jstage.jst.go.jp/article/tastj/13/0/13_TJSAS-D-15-00012/_article

[97] S. Durga Nair, P. S. Lal Priya, and A. Narayanan, "Quaternion Based Sliding Mode Attitude Controller for a Spacecraft with Control Moment Gyros," in *2018 15th International Workshop on Variable Structure Systems (VSS)*. Graz: IEEE, Jul. 2018, pp. 245–250. [Online]. Available: https://ieeexplore.ieee.org/document/8460457/

[98] S. Eshghi and R. Varatharajoo, "Singularity-free integral-augmented sliding mode control for combined energy and attitude control system," *Advances in Space Research*, vol. 59, no. 2, pp. 631–644, Jan. 2017. [Online]. Available: https://linkinghub.elsevier.com/retrieve/pii/S0273117716305671

[99] J. Liu and X. Wang, *Advanced Sliding Mode Control for Mechanical Systems*. Berlin, Heidelberg: Springer Berlin Heidelberg, 2011. [Online]. Available: http://link.springer.com/10.1007/978-3-642-20907-9

[100] C. Creaser and R. Bauer, "Logic-based gimbal compensator for the double-gimbal scissored-pair control moment gyroscope using magnetic torquers," *Advances in Space Research*, vol. 73, no. 1, pp. 254–270, Jan. 2024. [Online]. Available: https://linkinghub.elsevier.com/retrieve/pii/S0273117723008414

[101] M. Leomanni, "Comparison of control laws for magnetic detumbling," Università degli Studi di Perugia, Perugia, Italy, Technical Report, Oct. 2012.

[102] A. Colagrossi and M. Lavagna, "Fully magnetic attitude control subsystem for picosat platforms," *Advances in Space Research*, vol. 62, no. 12, pp. 3383–3397, Dec. 2018. [Online]. Available: https://linkinghub.elsevier.com/retrieve/pii/S0273117717307603

[103] A. Wailand and R. Bauer, "Investigation of Gain Tuning and Sensor Noise for CubeSat B-dot Detumbling and 3-axis PD Magnetic Attitude Control," in *Progress in Canadian Mechanical Engineering. Volume 3.* University of Prince Edward Island. Robertson Library, Sep. 2020. [Online]. Available: https://library.upei.ca/islandora/object/csme2020:31

[104] I. A. Courie, Y. I. Jenie, and R. E. Poetro, "Simulation of satellite attitude control using Single Gimbal Control Moment Gyro (SGCMG) system," *Journal of Physics: Conference Series*, vol. 1130, p. 012003, Nov. 2018. [Online]. Available: https://iopscience.iop.org/article/10.1088/1742-6596/1130/1/012003

[105] H. Kurokawa, "A Geometry Study of Single Gimbal Control Moment Gyros, (Singularity Problems and Steering Law)," Agency of Industrial Technology and Science, Japan, Technical Report 175, 1998.

[106] H. Kojima, "Calculation and fitting of boundaries between elliptic and hyperbolic singularities of pyramid-type control moment gyros," *Acta Astronautica*, vol. 104, no. 1, pp. 33–44, Nov. 2014. [Online]. Available: https://linkinghub.elsevier.com/retrieve/pii/S0094576514002562

[107] R. Saito, Y. Shoji, S. Satoh, and K. Yamada, "Agile rest-to-rest attitude maneuvering of spacecraft using pyramid-type SGCMG based on iteratively recalculated optimal trajectory," *Advances in Space Research*, vol. 70, no. 7, pp. 1988–2012, Oct. 2022. [Online]. Available: https://linkinghub.elsevier.com/retrieve/pii/S0273117722005270

[108] H. Kojima, R. Nakamura, and S. Keshtkar, "Model predictive steering control law for double gimbal scissored-pair control moment gyros," *Acta Astronautica*, vol. 183, pp. 273–285, Jun. 2021. [Online]. Available: https://linkinghub.elsevier.com/retrieve/pii/S0094576521001363

[109] Y. Bunryo, S. Satoh, Y. Shoji, and K. Yamada, "Feedback attitude control of spacecraft using two single gimbal control moment gyros," *Advances in Space Research*, vol. 68, no. 7, pp. 2713–2726, Oct. 2021. [Online]. Available: https://linkinghub.elsevier.com/retrieve/pii/S0273117721004075

[110] S. Kawajiri and S. Matunaga, "A low-complexity attitude control method for large-angle agile maneuvers of a spacecraft with control moment gyros," *Acta Astronautica*, vol. 139, pp. 486–493, Oct. 2017. [Online]. Available: https://linkinghub.elsevier.com/retrieve/pii/S009457651730351X

[111] B. Yost, S. Weston, J. Hines, and C. Burkhard, "An Overview of the Current State of the Art on Small Spacecraft Avionics Systems," in *AIAA SciTech Forum 2022*. San Diego, CA: American Institude of Aeronautics and Astronautics, Jan. 2022. [Online]. Available: https://ntrs.nasa.gov/api/citations/20210025472/downloads/AIAASciTech2022%20-%20Yost.pdf

[112] Y. Wu, F. Han, M. Zheng, M. He, Z. Chen, B. Hua, and F. Wang, "Attitude control for on-orbit servicing spacecraft using hybrid actuator," *Advances in Space Research*, vol. 61, no. 6, pp. 1600–1616, Mar. 2018. [Online]. Available: https://linkinghub.elsevier.com/retrieve/pii/S0273117718300073

[113] J.-F. Trégouët, D. Arzelier, D. Peaucelle, and L. Zaccarian, "Static input allocation for reaction wheels desaturation using magnetorquers," *IFAC Proceedings Volumes*, vol. 46, no. 19, pp. 559–564, 2013. [Online]. Available: https://linkinghub.elsevier.com/retrieve/pii/S1474667015363837

[114] K. Kimura, Y. Shoji, S. Satoh, and K. Yamada, "Attitude control experiment of a spinning spacecraft using only magnetic torquers," *Advances in Space Research*, vol. 71, no. 12, pp. 5386–5399, Jun. 2023. [Online]. Available: https://linkinghub.elsevier.com/retrieve/pii/S0273117723001370

[115] R. Opromolla, G. Fasano, G. Rufino, and M. Grassi, "A review of cooperative and uncooperative spacecraft pose determination techniques for close-proximity operations," *Progress in Aerospace Sciences*, vol. 93, pp. 53–72, Aug. 2017. [Online]. Available: https://linkinghub.elsevier.com/retrieve/pii/S0376042117300428

[116] S. Li and Y. She, "Recent advances in contact dynamics and post-capture control for combined spacecraft," *Progress in Aerospace Sciences*, vol. 120, p. 100678, Jan. 2021. [Online]. Available: https://linkinghub.elsevier.com/retrieve/pii/S0376042120300907

[117] R. Biesbroek, L. Innocenti, A. Wolahan, and S. M. Serrano, "e.Deorbit – ESA'S Active Debris Removal Mission," in *7th European Conference on Space Debris*, vol. 7. Darmstadt, Germany: ESA Space Debris Office, Apr. 2017. [Online]. Available: https://conference.sdo.esoc.esa.int/proceedings/sdc7/paper/1053/SDC7-paper1053.pdf

[118] R. Dudziak, S. Tuttle, and S. Barraclough, "Harpoon technology development for the active removal of space debris," *Advances in Space Research*, vol. 56, no. 3, pp. 509–527, Aug. 2015. [Online]. Available: https://linkinghub.elsevier.com/retrieve/pii/S0273117715002719

[119] J. L. Forshaw, G. S. Aglietti, T. Salmon, I. Retat, M. Roe, C. Burgess, T. Chabot, A. Pisseloup, A. Phipps, C. Bernal, F. Chaumette, A. Pollini, and W. H. Steyn, "Final payload test results for the RemoveDebris active debris removal mission," *Acta Astronautica*, vol. 138, pp. 326–342, Sep. 2017. [Online]. Available: https://linkinghub.elsevier.com/retrieve/pii/S0094576516310840

[120] Y. Zhao, F. Zhang, and P. Huang, "Capture dynamics and control of tethered space net robot for space debris capturing in unideal capture case," *Journal of the Franklin Institute*, vol. 357, no. 17, pp. 12 019–12 036, Nov. 2020. [Online]. Available: https://linkinghub.elsevier.com/retrieve/pii/S0016003220302805

[121] Y. Endo, H. Kojima, and P. M. Trivailo, "New formulation for evaluating status of space debris capture using tether-net," *Advances in Space Research*, vol. 70, no. 10, pp. 2976–3002, Nov. 2022. [Online]. Available: https://linkinghub.elsevier.com/retrieve/pii/S0273117722008651

[122] W. Huang, H. Zou, H. Liu, W. Yang, J. Gao, and Z. Liu, "Contact dynamic analysis of tether-net system for space debris capture using incremental potential formulation," *Advances in Space Research*, vol. 72, no. 6, pp. 2039–2050, Sep. 2023. [Online]. Available: https://linkinghub.elsevier.com/retrieve/pii/S0273117723004258

[123] C. Creaser and R. Bauer, "Two-stage estimator for the complete inertia tensor of uncooperative debris on CubeSat based Active Debris Removal missions," *Acta Astronautica*, vol. 219, pp. 481–496, Jun. 2024. [Online]. Available: https://linkinghub.elsevier.com/retrieve/pii/S0094576524001565

[124] X. Sun and R. Zhong, "Tether attachment point stabilization of noncooperative debris captured by a tethered space system," *Acta Astronautica*, vol. 177, pp. 784–797, Dec. 2020. [Online]. Available: https://linkinghub.elsevier.com/retrieve/pii/S0094576519314456

[125] B. Wang, Z. Meng, and P. Huang, "Attitude control of towed space debris using only tether," *Acta Astronautica*, vol. 138, pp. 152–167, Sep. 2017. [Online]. Available: https://linkinghub.elsevier.com/retrieve/pii/S0094576517300565

[126] C. Jia, Z. Meng, and P. Huang, "Attitude control for tethered towing debris under actuators and dynamics uncertainty," *Advances in Space Research*, vol. 64, no. 6, pp. 1286–1297, Sep. 2019. [Online]. Available: https://linkinghub.elsevier.com/retrieve/pii/S0273117719304600

[127] M. Shan and L. Shi, "Velocity-based detumbling strategy for a post-capture tethered net system," *Advances in Space Research*, vol. 70, no. 5, pp. 1336–1350, Sep. 2022. [Online]. Available: https://linkinghub.elsevier.com/retrieve/pii/S0273117722004811

[128] A. Nocerino, R. Opromolla, G. Fasano, and M. Grassi, "LIDAR-based multi-step approach for relative state and inertia parameters determination of an uncooperative target," *Acta Astronautica*, vol. 181, pp. 662–678, Apr. 2021. [Online]. Available: https://linkinghub.elsevier.com/retrieve/pii/S009457652100093X

[129] A. Nocerino, R. Opromolla, G. Fasano, M. Grassi, P. Fontdegloria Balaguer, S. John, H. Cho, and R. Bevilacqua, "Experimental validation of inertia parameters and attitude estimation of uncooperative space targets using solid state LIDAR," *Acta Astronautica*, vol. 210, pp. 428–436, Sep. 2023. [Online]. Available: https://linkinghub.elsevier.com/retrieve/pii/S0094576523000607

[130] Q. Meng, J. Liang, and O. Ma, "Identification of all the inertial parameters of a non-cooperative object in orbit," *Aerospace Science and Technology*, vol. 91, pp. 571–582, Aug. 2019. [Online]. Available: https://linkinghub.elsevier.com/retrieve/pii/S1270963818326166

[131] F. Zhang, I. Sharf, A. Misra, and P. Huang, "On-line estimation of inertia parameters of space debris for its tether-assisted removal," *Acta Astronautica*, vol. 107, pp. 150–162, Feb. 2015. [Online]. Available: https://linkinghub.elsevier.com/retrieve/pii/S0094576514004482

[132] D. Bourabah, L. Field, and E. M. Botta, "Estimation of uncooperative space debris inertial parameters after tether capture," *Acta Astronautica*, vol. 202, pp. 909–926, Jan. 2023. [Online]. Available: https://linkinghub.elsevier.com/retrieve/pii/S0094576522003927

[133] D. Bourabah, C. Gnam, and E. M. Botta, "Inertia tensor estimation of tethered debris through tether tracking," *Acta Astronautica*, vol. 212, pp. 643–653, Nov. 2023. [Online]. Available: https://linkinghub.elsevier.com/retrieve/pii/S0094576523004289

[134] S. Fan, F. Xing, X. Liu, X. Chen, and Z. You, "Quick-response attitude takeover control using multiple servicing spacecraft based on inertia properties identification," *Advances in Space Research*, vol. 70, no. 7, pp. 1890–1916, Oct. 2022. [Online]. Available: https://linkinghub.elsevier.com/retrieve/pii/S0273117722005348

[135] Y.-H. Wu, F. Han, M.-H. Zheng, F. Wang, B. Hua, Z.-M. Chen, and Y.-H. Cheng, "Attitude tracking control for a space moving target with high dynamic performance using hybrid actuator," *Aerospace Science*

and Technology, vol. 78, pp. 102–117, Jul. 2018. [Online]. Available: https://linkinghub.elsevier.com/retrieve/pii/S1270963817323957

[136] W. De Jongh, H. Jordaan, and C. Van Daalen, "Experiment for pose estimation of uncooperative space debris using stereo vision," *Acta Astronautica*, vol. 168, pp. 164–173, Mar. 2020. [Online]. Available: https://linkinghub.elsevier.com/retrieve/pii/S0094576519314390

[137] M. D. Lichter, "Shape, Motion, and Inertial Parameter Estimation of Space Objects using Teams of Cooperative Vision Sensors," Doctoral Theis, Massachusetts Institute of Technology, Cambridge, MA, Feb. 2005. [Online]. Available: https://dspace.mit.edu/handle/1721.1/30337

[138] J. R. Kopacz, R. Herschitz, and J. Roney, "Small satellites an overview and assessment," *Acta Astronautica*, vol. 170, pp. 93–105, May 2020. [Online]. Available: https://linkinghub.elsevier.com/retrieve/pii/S0094576520300540

[139] J. Fan and D. Zhou, "Nonlinear Attitude Control of Flexible Spacecraft with Scissored Pairs of Control Moment Gyros," in *2010 First International Conference on Pervasive Computing, Signal Processing and Applications*. Harbin, China: IEEE, Sep. 2010, pp. 719–722. [Online]. Available: http://ieeexplore.ieee.org/document/5635604/

[140] B. Goeree and B. Shucker, "Geometric Attitude Control of a Small Satellite for Ground Tracking Maneuvers," in *13th AIAA/USU Conference on Small Satellites*, Utah, 1999, p. 12. [Online]. Available: https://digitalcommons.usu.edu/smallsat/1999/all1999/58/

[141] G. Peng, G. Song, L. Xing, A. Gunawan, and P. Vansteenwegen, "An Exact Algorithm for Agile Earth Observation Satellite Scheduling with Time-Dependent Profits," *Computers & Operations Research*, vol. 120, p. 104946, Aug. 2020. [Online]. Available: https://linkinghub.elsevier.com/retrieve/pii/S0305054820300630

[142] Z. Yang, Y. Qin, J. Liu, N. Sun, D. Huo, H. Ji, Q. Cong, and Y. Li, "A Smooth Nadir-Pointing Attitude Guidance law for Satellites Constrained by the Deviation of Sun-Pointing," *Journal of Physics: Conference Series*, vol. 2361, no. 1, p. 012020, Oct. 2022. [Online]. Available: https://iopscience.iop.org/article/10.1088/1742-6596/2361/1/012020

[143] D. Cilden-Guler, H. Schaub, C. Hajiyev, and Z. Kaymaz, "Attitude Estimation with Albedo Interference on Sun Sensor Measurements," *Journal of Spacecraft and Rockets*, vol. 58, no. 1, pp. 148–163, Jan. 2021. [Online]. Available: https://arc.aiaa.org/doi/10.2514/1.A34814

[144] F. L. Markley, Y. Cheng, J. L. Crassidis, and Y. Oshman, "Averaging Quaternions," *Journal of Guidance, Control, and Dynamics*, vol. 30, no. 4, pp.

1193–1197, Jul. 2007. [Online]. Available: https://arc.aiaa.org/doi/10.2514/1.28949

[145] H. D. Curtis, *Orbital Mechanics for Engineering Students*, 4th ed. Cambridge, MA: Elsevier, 2020.

[146] "Reference Systems and Frames," Jan. 2024. [Online]. Available: https://gssc.esa.int/navipedia/index.php/Reference_Systems_and_Frames

[147] "Julian Date Converter." [Online]. Available: https://aa.usno.navy.mil/data/JulianDate

[148] "Calculate Earth-centered Earth-fixed (ECEF) position from geodetic latitude, longitude, and altitude above planetary ellipsoid - Simulink." [Online]. Available: https://www.mathworks.com/help/aeroblks/llatoecefposition.html?s_tid=doc_ta#mw_f5377f80-2092-4e2d-9428-3ad6e85f5b97

[149] "Reference frames and how they are used in inertial navigation · VectorNav." [Online]. Available: https://www.vectornav.com/resources/inertial-navigation-primer/math-fundamentals/math-refframes

[150] "Convert geodetic latitude and longitude to direction cosine matrix - Simulink." [Online]. Available: https://www.mathworks.com/help/aeroblks/directioncosinematrixeceftoned.html

[151] D. K. B. and S. Thomas, "Power rate exponential reaching law for enhanced performance of sliding mode control," *International Journal of Control, Automation and Systems*, vol. 15, no. 6, pp. 2636–2645, Dec. 2017. [Online]. Available: http://link.springer.com/10.1007/s12555-016-0736-9

[152] "MIT Space Systems Product Development Manual," 2003. [Online]. Available: https://ocw.mit.edu/courses/16-83x-space-systems-engineering-spring-2002-spring-2003/d326db0d57286cd4bd0cd24cae3c0c64_design_final_e.pdf

[153] J. M. Picone, A. E. Hedin, D. P. Drob, and A. C. Aikin, "NRLMSISE-00 empirical model of the atmosphere: Statistical comparisons and scientific issues," *Journal of Geophysical Research: Space Physics*, vol. 107, no. A12, Dec. 2002. [Online]. Available: https://agupubs.onlinelibrary.wiley.com/doi/10.1029/2002JA009430

[154] F. M. White, "Pressure Distribution in a Fluid," in *Fluid Mechanics*, 7th ed. New York, NY: McGraw Hill, 2011, p. 885.

[155] M. Voskuijl, "AE2104 Orbital Mechanics Slides.pdf," TU Delft, 2012. [Online]. Available: https://ocw.tudelft.nl/wp-content/uploads/AE2104-Orbital-Mechanics-Slides_10.pdf

Appendix A

Reference Frame Definitions

This appendix provides a summary of reference frames used primarily by the orbit propagator and space environment simulator. The reference frames derived in the appendix are typically applied to describe orbit geometry, spacecraft attitude, or are used to drive reference models used in the simulation.

A.1 Coordinate Frames

A.1.1 J2000 Earth-Centered Inertial Frame

The J2000 Earth-Centered Inertial (ECI) frame is used to represent a quasi-inertial reference system. For this reference frame defined by $\mathcal{F}_{ECI}$, the x-axis points towards the mean equinox at January 1st 2000 at 12:00 terrestrial time. The z-axis points towards celestial north and the y-axis completes the triad [145][146]. The mean equinox point is defined as the ascending node point where the orbital plane of the Earth around the Sun (more commonly known as the ecliptic) intersects with the celestial equator of Earth. The ECI frame is shown in Fig. A.1. $\mathcal{F}_{ECI}$ holds importance in the simulator developed in this thesis because all ephemeris data for other celestial bodies is expressed in this reference frame.

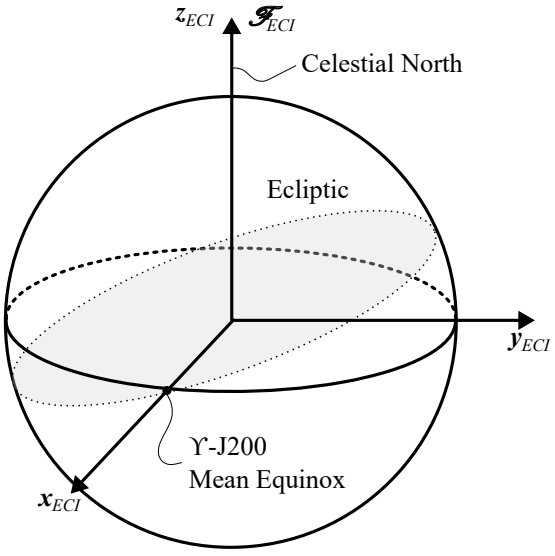

Figure A.1: J2000 Earth-Centered Inertial Frame With Mean Equinox Point

A.1.2 Earth-Centered Earth-Fixed Frame

The Earth-Centered Earth-Fixed (ECEF) frame defined by $\mathscr{F}_{ECEF}$ is fixed at the center of Earth and rotates with Earth as shown in Fig. A.2. The ECEF frame shares a common z-axis with $\mathscr{F}_{ECI}$ and is rotated about this axis through the Greenwich angle θ_G. The x-axis points towards the Greenwich prime meridian lying in the mean equatorial plane and the y-axis is directed 90° east of the x-axis [23][26]. The ECEF frame is shown rotated relative to the ECI frame in Fig. A.2.

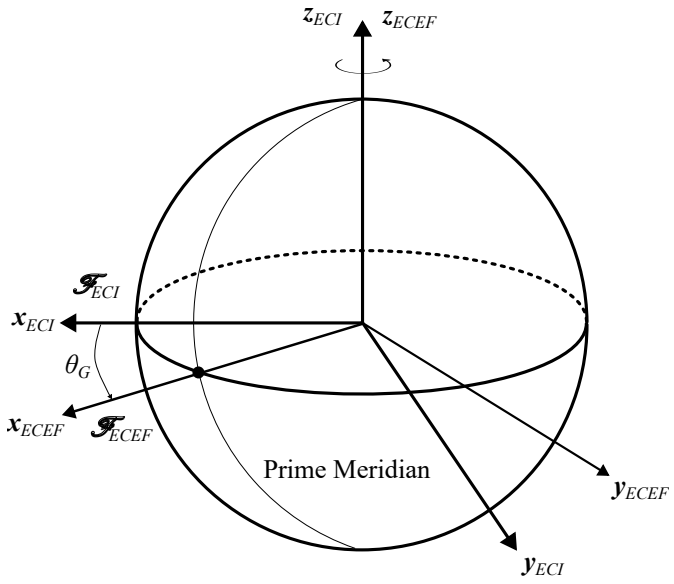

Figure A.2: ECEF Frame with Greenwich Prime Meridian Line

To realize the rotation from $\mathscr{F}_{ECI}$ towards $\mathscr{F}_{ECEF}$ it is critical to define the simulation start time. For the case of this thesis, a Two-Line Element (TLE) was obtained on Jan 11^{th} 2023 via the Celestrack.com database for the Low-Orbit Reconnaissance Imagery Satellite (LORIS) which provided the simulation epoch Universal Time (UT) and fractional day [15]Update Citation with proper page reference. The UT time of the simulation in decimal hours t_s for all simulation time t expressed in seconds is given as:

$$t_s = t_0 + \frac{t}{3600} \tag{A.1}$$

where t_0 is the UT time in decimal hours for the TLE epoch time. Following calculation of Eq. (A.1), the Julian Day must then be resolved. The Julian day is a continuous count of days elapsed since the beginning of the Julian period [147]. The Julian day number J_0 for the epoch start date at 0 UT is found in the following equation noting that Y, M, D represent year, month, and day respectively. The function

"fix" rounds the input number towards zero [145]:

$$J_0 = 367Y - \text{fix}\left(\frac{7\left(Y - \text{fix}\left(\frac{M+9}{12}\right)\right)}{4}\right) + \text{fix}\left(\frac{275M}{9}\right) + D + 1721013.5 \tag{A.2}$$

The Julian day at the current simulation UT time is then:

$$J_D = J_0 + \frac{t_s}{24} \tag{A.3}$$

With the J2000 convention being used for the inertial reference frame, the Julian centuries elapsed since the J2000 epoch is determined as [41]:

$$T_0 = \frac{J_D - 2451545}{36525} \tag{A.4}$$

The Julian centuries value enables the calculation of the Greenwich sidereal angle at 0 UT for the simulation epoch day θ_{G_0}. The θ_{G_0} term can then be updated for any simulation time to yield θ_G by applying the following two equations in sequence:

$$\theta_{G_0} = 100.4606184 + 36000.77004T_0 + 0.000387933T_0^2 - 2.583\text{E}10^{-8}T_0^3 \tag{A.5}$$

$$\theta_G = \theta_{G_0} + 360.98564724\frac{t_s}{24} \tag{A.6}$$

Finally, the DCM which expresses a vector from $\mathscr{F}_{ECI}$ to its equivalent representation in $\mathscr{F}_{ECI}$ is given as:

$$\boldsymbol{\mathcal{A}}_{ECI}^{ECEF} = \text{C3}(\theta_G) \tag{A.7}$$

A.1.3 Topocentric Reference Frame (East-North-Zenith)

The reference frame most applicable to target tracking applications is a Topocentric Reference Frame. In this work the East-North-Zenith (ENZ) frame defined by $\mathscr{F}_{ENZ}$ is centered at a target position on the surface of Earth as shown in Fig. A.3. A terrestrial target location at a given geodetic latitude ϕ_d and longitude λ_d is defined in the World Geodetic System of 1984 (WGS84) to account for the flattening of Earth. The z-axis of $\mathscr{F}_{ENZ}$ points in the direction of the geodetic zenith (normal and away from the surface of Earth), the x-axis points towards the local north of the target along the local line of latitude, and the y-axis completes the triad by pointing towards the local north direction from the target position [23]. The frame rotates with Earth which leads to the target position being time invariant when expressed in $\mathscr{F}_{ECEF}$. The ENZ frame is shown at an arbitrary target position with geodetic latitude and longitude expressed based on the position of the ECEF frame in Fig. A.3. Owing to the fact that the ENZ frame rotates with the ECEF frame, the transformation from ECEF to ENZ is also time-invariant and can be calculated as [23]:

$$\boldsymbol{\mathcal{A}}_{ECEF}^{ENZ} = \text{C1}\left(\frac{\pi}{2} - \phi_d\right)\text{C3}\left(\frac{\pi}{2} + \lambda_d\right) \tag{A.8}$$

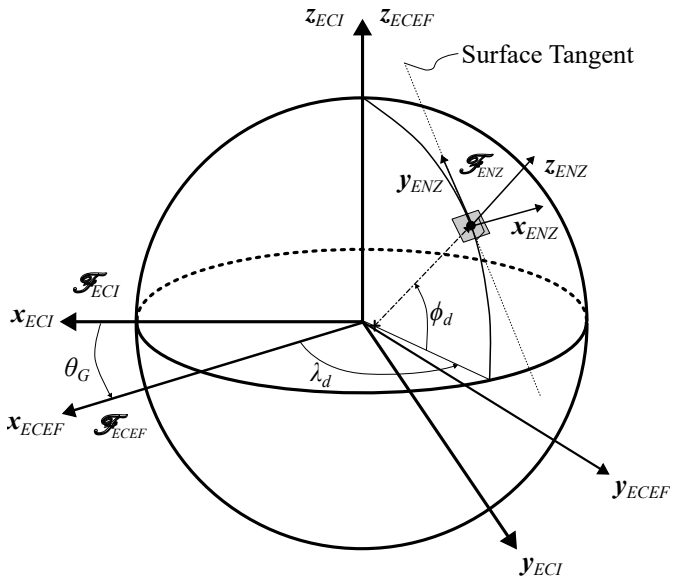

Figure A.3: ENZ Frame with Geodetic Latitude and Longitude Shown Relative to ECEF Frame Position

The time-invariant position of the target in $\mathcal{F}_{ECEF}$ accounting for the WGS84 realization can be obtained by first calculating the geocentric latitude at mean sea level ϕ_s and the radius at a surface point defined by r_s [148]:

$$\phi_s = \text{atan}((1-f)^2 \tan(\phi_d)) \tag{A.9}$$

$$r_s = \sqrt{\frac{R_e^2}{1 + (1/(1-f)^2 - 1)\sin^2(\phi_s)}} \tag{A.10}$$

The parameter R_e is the radius of Earth at the equator and is equal to 6378137 m. f is the WGS84 Earth flattening parameter which is equal to 1/298.257223563 [148]. Correspondingly, the $\mathcal{F}_{ECEF}$ target position can be calculated as:

$$\boldsymbol{r}_t = \begin{bmatrix} r_s \cos(\phi_s)\cos(\lambda_d) + h\cos(\phi_d)\cos(\lambda_d) \\ r_s \cos(\phi_s)\sin(\lambda_d) + h\cos(\phi_d)\sin(\lambda_d) \\ r_s \sin(\phi_s) + h\sin(\phi_d) \end{bmatrix} \tag{A.11}$$

A.1.4 Perifocal Frame

The Perifocal frame defined by $\mathcal{F}_P$ is a intermediate frame used to develop the Nadir Pointing frame. $\mathcal{F}_P$ is obtained by a 3-1-3 principal rotation sequence from $\mathcal{F}_{ECI}$ through the classical orbital elements consisting of the Right Angle of the Ascending Node (RAAN) Ω, inclination i and, the argument of perigee ω as demonstrated by Fig. A.4. The x-axis of $\mathcal{F}_P$ lies in the orbital plane and points in the direction of the perigee point. The y-axis lies in the orbital plane 90° from the x-axis while respecting

the dextral properties of reference frames defined in this work. Finally, the z-axis is directed normal to x and y.

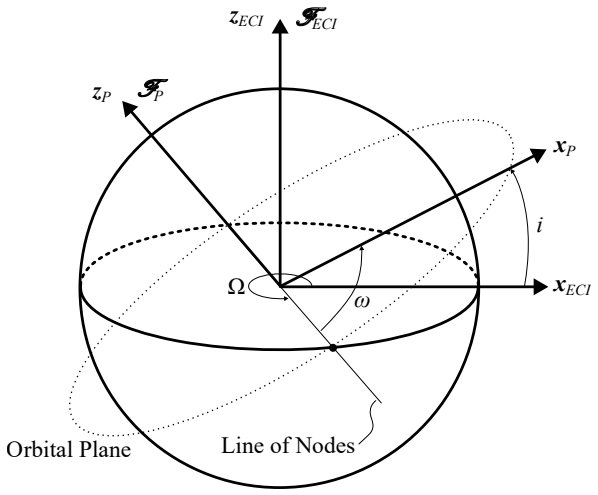

Figure A.4: Perifocal Frame in Relation to the ECI Frame (y-axes omitted)

The DCM used to transform a vector expressed in $\mathcal{F}_{ECI}$ to its representation in $\mathcal{F}_P$ is accomplished through the following sequence of rotations. First, a C3 principal rotation by Ω aligns the x-axis to the line of nodes. An intermediate C1 principal rotation about this new x-axis through i aligns the intermediate z-axis to be normal to the orbital plane. Finally, a C3 principal rotation about the z-axis through ω aligns the x-axis in its final position towards the perigee point. The subsequent DCM may be calculated as [26]:

$$\mathcal{A}_{ECI}^{P} = \mathrm{C3}(\omega)\mathrm{C1}(i)\mathrm{C3}(\Omega) \tag{A.12}$$

A.1.5 Nadir Pointing Frame

The Nadir Pointing frame defined by $\mathcal{F}_{NP}$ is centered at the current satellite position on its orbit as shown by Fig. A.5. The satellite position in $\mathcal{F}_{ECI}$ is represented by $\boldsymbol{r}_{ECI}$ which leads to the Nadir direction from the satellite position to be in the direction of $-\boldsymbol{r}_{ECI}$. Therefore, the z-axis of $\mathcal{F}_{NP}$ is directed along $-\boldsymbol{r}_{ECI}$, the x-axis is directed along the orbital velocity vector $\boldsymbol{v}_{ECI}$, and the y-axis completes the triad. Fig. A.5 displays the orientation of $\mathcal{F}_{NP}$ with respect to $\mathcal{F}_{ECI}$. Addressing Fig. A.5, the most convenient method for developing the Nadir Pointing frame is to perform a rotation sequence from the Perifocal frame. The DCM which performs this rotation can be formed by a 3-2-3 principal rotation sequence through the true anomaly angle ν, $-\frac{\pi}{2}$ and, $\frac{\pi}{2}$ respectively [26]:

$$\mathcal{A}_{P}^{NP} = \mathrm{C3}\left(\frac{\pi}{2}\right)\mathrm{C2}\left(-\frac{\pi}{2}\right)\mathrm{C3}(\nu) \tag{A.13}$$

The true anomaly angle can be taken from the TLE which drives the simulation.

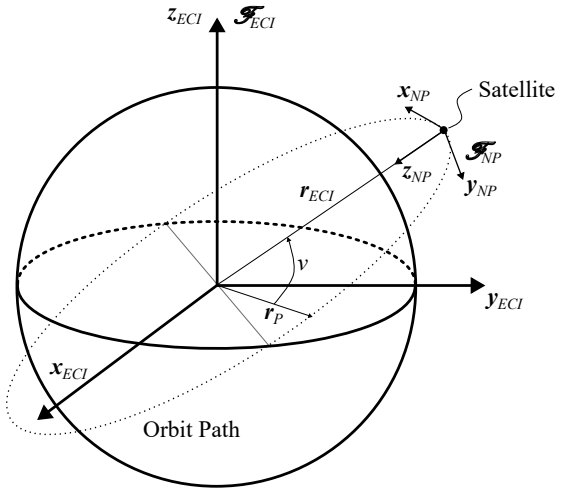

Figure A.5: Nadir Pointing Frame Defined for General Inclined Orbit

A.1.6 Body-Fixed Frame

The Body-Fixed frame defined by $\mathcal{F}_{BF}$ is fixed at the Center of Mass (COM) of the satellite as shown by Fig. A.6. In this work, it is assumed that the z-axis of $\mathcal{F}_{BF}$ is the observing basis vector for the satellite. That is, it is the axis which is desired to be pointed towards either the ground or at other targets of interest. The inertial properties of the satellite are also calculated correspondingly to the defined Body-Fixed frame. Fig. A.6 displays a general configuration of the spacecraft Body-Fixed frame. With respect to the attitude control formulations presented in this work, it

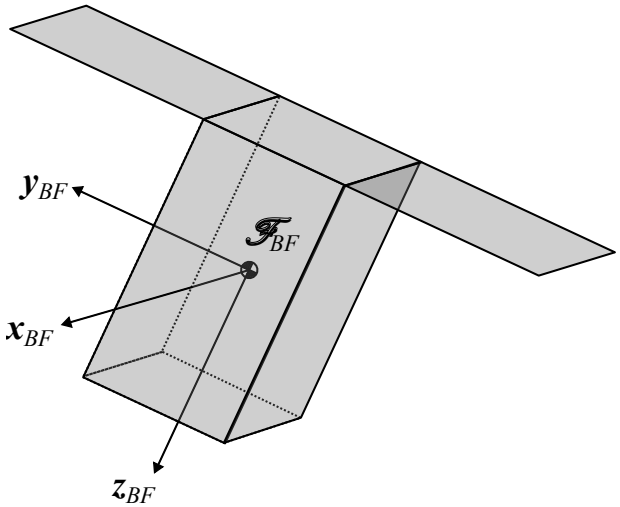

Figure A.6: Body Frame Fixed to Generalized Spacecraft Geometry

is typically desired to align $\mathcal{F}_{BF}$ with another coordinate frame which exhibits the

desired attitude with respect to $\mathscr{F}_{ECI}$.

A.1.7 In-Cross-Range Orbit Frame

The In-Cross-Range Orbit (ICR) frame $\mathscr{F}_{ICR}$ is defined for convenience in assessing pointing and mapping errors for the target tracking campaigns presented in this work. For the case of this work, $\mathscr{F}_{ICR}$ is not required for orbit propagation, but it is justifiably presented here as context for later error analyses. $\mathscr{F}_{ICR}$ is centered at the spacecraft COM and the z-axis basis vector points in the radial direction of the orbit along $\boldsymbol{r}_{ECI}$ as demonstrated by Fig. A.7. The x-axis basis vector points along the orbital velocity vector $\boldsymbol{v}_{ECI}$ and the y-axis points in the direction of the cross product between $\boldsymbol{r}_{ECI}$ and $\boldsymbol{v}_{ECI}$. The direction of motion of the spacecraft is considered the "In-Track" direction, and the final remaining direction along y is the "Cross-Track" direction [58]. The subject reference frame and track directions are shown in detail in Fig. A.7. The DCM which transforms a vector expressed in $\mathscr{F}_{ECI}$

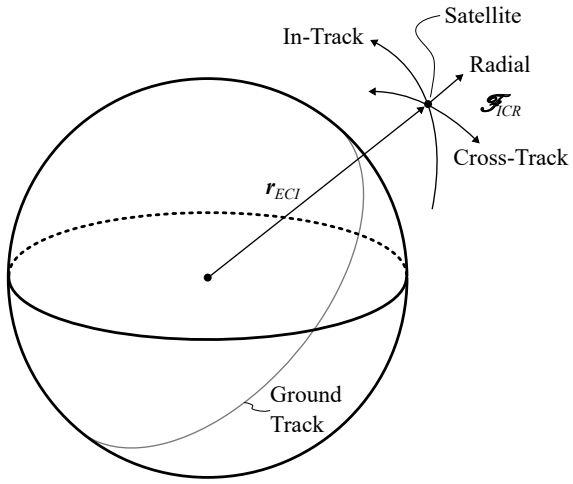

Figure A.7: In-Cross-Range Frame Shown for Inclined Orbit

to an equivalent representation in $\mathscr{F}_{ICR}$ can be developed from the bases vectors defined for each respective frame. Let $\boldsymbol{x}_{ECI}$, $\boldsymbol{y}_{ECI}$ and, $\boldsymbol{z}_{ECI}$ be equal to $[1,0,0]^T$, $[0,1,0]^T$, $[0,0,1]^T$ respectively when the bases vectors of $\mathscr{F}_{ECI}$ are defined in $\mathscr{F}_{ECI}$. Then, the following set of equations may be applied to compute the bases vectors of $\mathscr{F}_{ICR}$ expressed in $\mathscr{F}_{ECI}$:

$$\boldsymbol{z}_{ICR} = \frac{\boldsymbol{r}_{ECI}}{|\boldsymbol{r}_{ECI}|}, \quad \boldsymbol{x}_{ICR} = \frac{\boldsymbol{v}_{ECI}}{|\boldsymbol{v}_{ECI}|}, \quad \boldsymbol{y}_{ICR} = \boldsymbol{z}_{ICR}^{\times}\boldsymbol{x}_{ICR} \tag{A.14}$$

With both sets of bases vectors defined, the DCM for rotation from $\mathscr{F}_{ECI}$ to $\mathscr{F}_{ICR}$ can be obtained from:

$$\mathcal{A}_{ECI}^{ICR} = \begin{bmatrix} \boldsymbol{x}_{ICR}^T \boldsymbol{x}_{ECI} & \boldsymbol{x}_{ICR}^T \boldsymbol{y}_{ECI} & \boldsymbol{x}_{ICR}^T \boldsymbol{z}_{ECI} \\ \boldsymbol{y}_{ICR}^T \boldsymbol{x}_{ECI} & \boldsymbol{y}_{ICR}^T \boldsymbol{y}_{ECI} & \boldsymbol{y}_{ICR}^T \boldsymbol{z}_{ECI} \\ \boldsymbol{z}_{ICR}^T \boldsymbol{x}_{ECI} & \boldsymbol{z}_{ICR}^T \boldsymbol{y}_{ECI} & \boldsymbol{z}_{ICR}^T \boldsymbol{z}_{ECI} \end{bmatrix} \tag{A.15}$$

The resulting DCM is valid provided that, for each set of bases vectors, the vectors are orthonormal and dextral.

A.1.8 Local Horizon Frame

The Local Horizon (LH) frame defined by $\mathcal{F}_{LH}$ is used in this thesis to enable the use of gravity harmonics in the subject work. $\mathcal{F}_{LH}$ is centered at the spacecraft COM and moves with the spacecraft about its orbit as presented in Fig. A.8. $\mathcal{F}_{LH}$ can be defined by a set of spherical coordinates r, δ, λ which define the position of the spacecraft measured from $\mathcal{F}_{ECI}$. The parameter r is the radial distance to the satellite from the center of Earth, δ is the declination angle which is the angle between $\boldsymbol{r}_{ECI}$ and the equatorial plane, and λ is the celestial longitude, which is the angle (measured in the equatorial plane) from the $\mathcal{F}_{ECI}$ x-axis basis vector towards the projection of $\boldsymbol{r}_{ECI}$ in the equatorial plane. Each parameter can be visualized in Fig. A.8. Adopting the methods in [44], the Local Horizon frame can be obtained

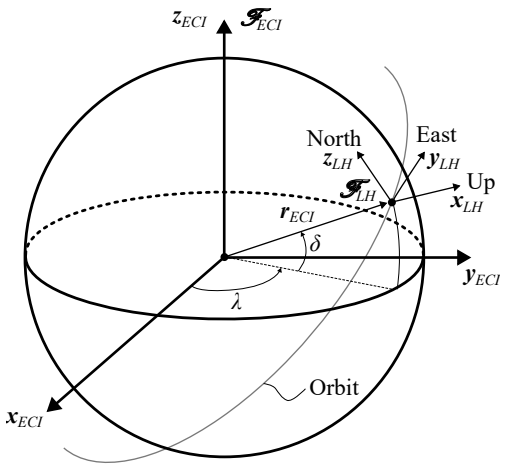

Figure A.8: Local Horizon Frame with Local Directions Labeled

following a 2-2-3 principal rotation from the ECI frame. Firstly, the declination angle δ and the celestial longitude λ can be found by using the position of the spacecraft r_{ECI} in:

$$\delta = \sin^{-1}\left(\frac{r_{ECI_3}}{|\boldsymbol{r}_{ECI}|}\right) \tag{A.16}$$

and:

$$\lambda = \sin^{-1}\left(\frac{r_{ECI_2}}{|\boldsymbol{r}_{ECI}|\cos(\delta)}\right) \tag{A.17}$$

It follows the DCM which transforms a vector from its expression in $\mathscr{F}_{ECI}$ to its expression in $\mathscr{F}_{LH}$ can be obtained by [44]:

$$\mathcal{A}_{ECI}^{LH} = \mathrm{C2}\left(\frac{-\pi}{2}\right)\mathrm{C2}\left(\frac{\pi}{2} - \delta\right)\mathrm{C3}(\lambda) \tag{A.18}$$

A.1.9 North-East-Down Frame

The North-East-Down Frame (NED) defined by $\mathscr{F}_{NED}$ is used in this thesis to provide coordinate transformations for geomagnetic field vectors derived from the International Geomagnetic Reference Field Generation 13 (IGRF-13). The NED frame cab be obtained through a sequential rotation from the ECEF frame as shown in Fig. A.9. As demonstrated by the geometry in Fig. A.9, the three basis vectors of $\mathscr{F}_{NED}$ are oriented such that the z-axis points along the flattened Earth surface normal vector, the x-axis points in the local north direction, and the y-axis completes the triad [149].

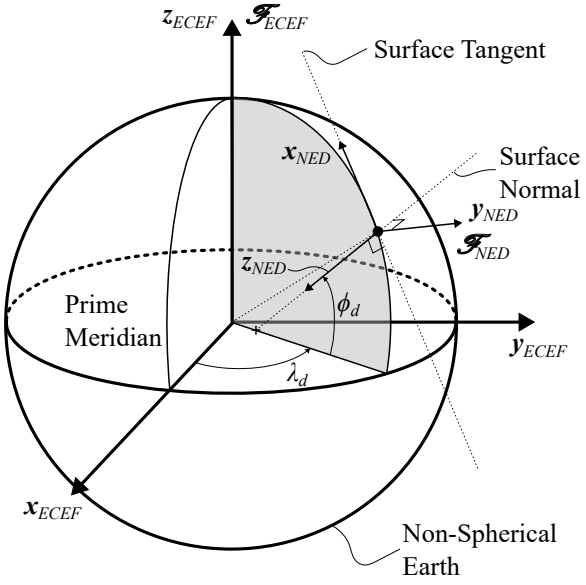

Figure A.9: NED Frame Show Relative to ECEF Frame For WGS84 Flattened Earth

Following Fig. A.9, a 3-2-2 principal rotation sequence can be applied to transform a vector expressed in $\mathscr{F}_{ECEF}$ to its equivalent expression in $\mathscr{F}_{NED}$ [150]. The DCM performing this transformation can be constructed using the following relationship:

$$\mathcal{A}_{ECEF}^{NED} = \mathrm{C2}(-90^\circ)\mathrm{C2}(-\phi_d)\mathrm{C3}(\lambda_d) \tag{A.19}$$

where the position of the spacecraft, expressed in geodetic latitude ϕ_d and longitude λ_d, was obtained in the simulator by feeding the spacecraft position vector expressed in $\mathscr{F}_{ECEF}$ to the MATLAB "ECEF Position to LLA" aerospace block.

Appendix B

Supplementary Simulator Data

GeomagneticData.txt

```
Format: IAGA-2002
Source of Data: GFZ, Helmholtz-Zentrum Postdam, Germany
Station Name: Kp index
IAGA CODE : Kp
Geodetic Latitude
Geodetic Longitude
Elevation          Reported : Kp, ap, Ap, Cp, C9 and related values
Data Interval Type     3-hours
Data Type              Definitive
# Converted to IAGA2002 format by the International Service of
#  Geomagnetic indices ISGI, https://isgi.unistra.fr.
# The values in the raw of 00:00:00.000 are the mean values
#  between 00:00UT and 03:00UT, etc.
# Kp: Planetary three-hour-range index
#     Expressed in a scale of thirds, it ranges from 0o to 9o
# ap: represents a Kp-value converted back to a linear scale in nT
#     It ranges from 0 to 400 nT
# Ap: arithmetic mean of the day's eight ap values, unit 1 nT
# Cp: Planetary daily character figure
#     It ranges from 0quiet to 2.5 disturbed in steps of 0.1
# C9: Conversion of the 0 to 2.5 range of Cp index to one digit
#     between 0 and 9
# BSRN: Bartels solar rotation number - a sequence of 27-day
#     intervals counted continuously from February 8, 1832
# NdB: Number of day within the Bartels 27-day cycle
#
# License: CC BY
#          https://creativecommons.org/licenses/by/4.0/
#
# For more information on Kp and related indices, please visit
#  GFZ "Indices of Global Geomagnetic Activity" service website:
#  https://www.gfz-potsdam.de/Kp-index/
DATE       TIME         DOY Kp  ap    Ap  Cp C9  BSRN  NdB

2023-01-07 00:00:00.000 007 1o   4     6 0.2  1  2583   17
2023-01-07 03:00:00.000 007 2+   9     6 0.2  1  2583   17
2023-01-07 06:00:00.000 007 1o   4     6 0.2  1  2583   17
2023-01-07 09:00:00.000 007 0+   2     6 0.2  1  2583   17
2023-01-07 12:00:00.000 007 0+   2     6 0.2  1  2583   17
2023-01-07 15:00:00.000 007 3-  12     6 0.2  1  2583   17
2023-01-07 18:00:00.000 007 2+   9     6 0.2  1  2583   17
2023-01-07 21:00:00.000 007 0+   2     6 0.2  1  2583   17
2023-01-08 00:00:00.000 008 2o   7     7 0.4  2  2583   18
```

```
2023-01-08 03:00:00.000 008 2+   9     7 0.4  2  2583   18
2023-01-08 06:00:00.000 008 2o   7     7 0.4  2  2583   18
2023-01-08 09:00:00.000 008 2-   6     7 0.4  2  2583   18
2023-01-08 12:00:00.000 008 3o  15     7 0.4  2  2583   18
2023-01-08 15:00:00.000 008 1+   5     7 0.4  2  2583   18
2023-01-08 18:00:00.000 008 1o   4     7 0.4  2  2583   18
2023-01-08 21:00:00.000 008 1-   3     7 0.4  2  2583   18
2023-01-09 00:00:00.000 009 2-   6     4 0.2  1  2583   19
2023-01-09 03:00:00.000 009 0+   2     4 0.2  1  2583   19
2023-01-09 06:00:00.000 009 0+   2     4 0.2  1  2583   19
2023-01-09 09:00:00.000 009 1o   4     4 0.2  1  2583   19
2023-01-09 12:00:00.000 009 1-   3     4 0.2  1  2583   19
2023-01-09 15:00:00.000 009 2-   6     4 0.2  1  2583   19
2023-01-09 18:00:00.000 009 2o   7     4 0.2  1  2583   19
2023-01-09 21:00:00.000 009 1+   5     4 0.2  1  2583   19
2023-01-10 00:00:00.000 010 1-   3     6 0.3  1  2583   20
2023-01-10 03:00:00.000 010 1-   3     6 0.3  1  2583   20
2023-01-10 06:00:00.000 010 1-   3     6 0.3  1  2583   20
2023-01-10 09:00:00.000 010 1-   3     6 0.3  1  2583   20
2023-01-10 12:00:00.000 010 2o   7     6 0.3  1  2583   20
2023-01-10 15:00:00.000 010 3o  15     6 0.3  1  2583   20
2023-01-10 18:00:00.000 010 2-   6     6 0.3  1  2583   20
2023-01-10 21:00:00.000 010 2o   7     6 0.3  1  2583   20
2023-01-11 00:00:00.000 011 2-   6     7 0.4  2  2583   21
2023-01-11 03:00:00.000 011 3-  12     7 0.4  2  2583   21
2023-01-11 06:00:00.000 011 2-   6     7 0.4  2  2583   21
2023-01-11 09:00:00.000 011 2-   6     7 0.4  2  2583   21
2023-01-11 12:00:00.000 011 1o   4     7 0.4  2  2583   21
2023-01-11 15:00:00.000 011 2o   7     7 0.4  2  2583   21
2023-01-11 18:00:00.000 011 2+   9     7 0.4  2  2583   21
2023-01-11 21:00:00.000 011 2+   9     7 0.4  2  2583   21
```

SunSensorData.txt

```
Sun-Sensor Vectors File.
Created by: Cameron Creaser
Date: 2024-05-30
-----------------------------------------------------------------------
Optical Plane Normal Vectors
-----------------------------------------------------------------------
Reference Coordinate System: F_BF
Data Format: [Row 1-6  - Fine Sensors  ]
             [Row 7-24 - Coarse Sensors]
-----------------------------------------------------------------------
    1.0000         0         0
   -1.0000         0         0
         0    1.0000         0
         0   -1.0000         0
         0         0    1.0000
         0         0   -1.0000
    0.4330   -0.2500   -0.8660
```

```
   -0.4330   -0.2500   -0.8660
    0.0000    0.5000   -0.8660
    0.4330    0.2500    0.8660
   -0.4330    0.2500    0.8660
    0.0000   -0.5000    0.8660
   -0.4330   -0.8660   -0.2500
    0.4330   -0.8660   -0.2500
    0.0000   -0.8660    0.5000
   -0.8660    0.4330   -0.2500
   -0.8660   -0.4330   -0.2500
   -0.8660         0    0.5000
    0.4330    0.8660   -0.2500
   -0.4330    0.8660   -0.2500
    0.0000    0.8660    0.5000
    0.8660   -0.4330   -0.2500
    0.8660    0.4330   -0.2500
    0.8660   -0.0000    0.5000
----------------------------------------------------------------------
Position Vectors
----------------------------------------------------------------------
Reference Coordinate System: Expressed from bottom dead center to SS
                             position. Reference frame aligned with
                             F_BF.
Data Format: [Row 1-6  - Fine Sensors  ]
             [Row 7-24 - Coarse Sensors]
----------------------------------------------------------------------
    0.0500         0   -0.0100
   -0.0500         0   -0.0100
         0    0.0500   -0.0100
         0   -0.0500   -0.0100
         0         0   -0.0200
         0         0         0
         0         0         0
         0         0         0
         0         0         0
         0         0   -0.0200
         0         0   -0.0200
         0         0   -0.0200
         0   -0.0500   -0.0100
         0   -0.0500   -0.0100
         0   -0.0500   -0.0100
   -0.0500         0   -0.0100
   -0.0500         0   -0.0100
   -0.0500         0   -0.0100
         0    0.0500   -0.0100
         0    0.0500   -0.0100
         0    0.0500   -0.0100
    0.0500         0   -0.0100
    0.0500         0   -0.0100
    0.0500         0   -0.0100
```

SolarFluxData.txt

```
Solar Weather Data File
Obtained: spaceweather.gc.ca
License: Reproduced for non-commerical applications
Monthly Average Flux:
YEAR        MONTH        Observed Flux        Adjusted Flux        Absolute Flux
2022        12           148.46               143.83               129.46
2023        01           182.47               176.63               158.97
2023        02           172.09               167.91               151.11
Daily Flux:
DATE                TIME        Observed        Adjusted        Absolute
2023-01-10        18:00:00        199.0        192.5        173.2
2023-01-10        20:00:00        193.0        186.6        168.0
2023-01-10        22:00:00        190.1        183.8        165.5
2023-01-11        18:00:00        196.7        190.2        171.2
2023-01-11        20:00:00        195.1        188.7        169.8
2023-01-11        22:00:00        200.8        194.2        174.8
```

Appendix C

Attitude Controller Lyapunov Stability Analysis

The proposed DGSPCMG-equipped ADCS employs a Sliding Model Controller for commanding attitude control torques. When exposed to a bounded disturbance, the stability of the controller can be confirmed through a Lyapunov test. The Lyapunov stability derivation is provided in this section for the focus sliding mode attitude controller.

C.1 Lyapunov Criteria

For the proposed controller to be Globally Asymptotically Stable (GAS) a Lyapunov function must be defined which satisfies a set of criteria:

1. A Lyapunov function $V(z)$ must be defined to be positive definite. $(V(z) > 0)$

2. The selected Lyapunov function shall satisfy $\dot{V}(z) < 0$, $\forall\, z \neq 0$

If the set of criteria is met the energy in the system is dissipated at all time t as $t \to \infty$ and $\dot{x} = f(x)$ converges to zero, thereby making it GAS.

C.1.1 Derivation

Following the work provided in [97] a Lyapunov function candidate may be defined as:

$$V = \frac{1}{2}\boldsymbol{\sigma}^T\boldsymbol{\sigma} \tag{C.1}$$

The Lyapunov function leads to solving the partial derivative with respect to time as:

$$\begin{aligned} \frac{\partial V}{\partial t} &= \frac{1}{2}(2\boldsymbol{\sigma}^T\dot{\boldsymbol{\sigma}}) \\ \frac{\partial V}{\partial t} &= \boldsymbol{\sigma}^T\dot{\boldsymbol{\sigma}} \end{aligned} \tag{C.2}$$

From the attitude controller definition in Section. 5.1 the sliding variable was expressed as:

$$\boldsymbol{\sigma} = \boldsymbol{\omega}_e + \boldsymbol{\lambda}\boldsymbol{q}_{e_{1:3}}\text{sign}(q_{e_4}) \tag{C.3}$$

For quaternion attitude parameterization it is possible for $\lim_{t\to\infty} q_{e_4} = 1$ and $\lim_{t\to\infty} q_{e_4} = -1$ to both represent attitude convergence and, therefore, the signum function must be introduced into the sliding variable σ so that the attitude converges along the shortest attitude trajectory [96]. The goal of the controller is to drive

the sliding variable through sliding mode to zero, in which case Eq. (**??**) can be rearranged as:

$$\boldsymbol{\omega}_e = -\boldsymbol{\lambda}\boldsymbol{q}_{e_{1:3}}\text{sign}(q_{e_4}) \tag{C.4}$$

The time derivative of the sliding variable can also be expressed as:

$$\dot{\boldsymbol{\sigma}} = \dot{\boldsymbol{\omega}}_e + \boldsymbol{\lambda}\dot{\boldsymbol{q}}_{e_{1:3}}\text{sign}(q_{e_4}) \tag{C.5}$$

In the general case for the satellite achieving attitude pointing for a simple rest-to-rest maneuver, the error in the body rates of the spacecraft $\boldsymbol{\omega}_e$ may be defined as $\boldsymbol{\omega}_e = \boldsymbol{\omega}$. This definition leads to a convenient expression for the rotational dynamics of the rigid-body satellite as:

$$\boldsymbol{J}\dot{\boldsymbol{\omega}} + \boldsymbol{\omega}^{\times}\boldsymbol{J}\boldsymbol{\omega} = \boldsymbol{u}_{cmg} + \boldsymbol{T}_d \tag{C.6}$$

Assuming the general case where the CMG produces exactly the commanded torque from the controller we may state $\boldsymbol{u} = \boldsymbol{u}_{cmg}$ so that the rotational dynamics may be rearranged as:

$$\dot{\boldsymbol{\omega}} = -\boldsymbol{J}^{-1}\boldsymbol{\omega}^{\times}\boldsymbol{J}\boldsymbol{\omega} + \boldsymbol{J}^{-1}\boldsymbol{u} + \boldsymbol{J}^{-1}\boldsymbol{T}_d \tag{C.7}$$

Defining the commanded torque from the controller $\boldsymbol{u}$ by the sum of the equivalent torque and the reaching law as $\boldsymbol{u} = \boldsymbol{u}_{eq} + \boldsymbol{u}_n$ as described by the following equation:

$$\boldsymbol{u} = \boldsymbol{J}((\boldsymbol{J}^{-1}\boldsymbol{\omega})^{\times}\boldsymbol{J}\boldsymbol{\omega} - \boldsymbol{\lambda}\text{sign}(q_{e_4})\dot{\boldsymbol{q}}_{e_{1:3}}) - k|\boldsymbol{\sigma}|^{\alpha}\text{sign}(\boldsymbol{\sigma}) \tag{C.8}$$

The commanded control signal of Eq. (C.8) can be substituted into Eq. (C.7) as:

$$\dot{\boldsymbol{\omega}} = -\boldsymbol{J}^{-1}\boldsymbol{\omega}^{\times}\boldsymbol{J}\boldsymbol{\omega} + \boldsymbol{J}^{-1}\left(\boldsymbol{J}((\boldsymbol{J}^{-1}\boldsymbol{\omega})^{\times}\boldsymbol{J}\boldsymbol{\omega} - \boldsymbol{\lambda}\text{sign}(q_{e_4})\dot{\boldsymbol{q}}_{e_{1:3}}) - k|\boldsymbol{\sigma}|^{\alpha}\text{sign}(\boldsymbol{\sigma})\right) + \boldsymbol{J}^{-1}\boldsymbol{T}_d \tag{C.9}$$

Knowing that $\boldsymbol{J}$ is a square matrix and $\boldsymbol{J}^{-1}\boldsymbol{J} = \boldsymbol{I}_{3\times 3}$ allows the above equation to be reduced to:

$$\dot{\boldsymbol{\omega}} = -\boldsymbol{\lambda}\text{sign}(q_{e_4})\dot{\boldsymbol{q}}_{e_{1:3}} - \boldsymbol{J}^{-1}k|\boldsymbol{\sigma}|^{\alpha}\text{sign}(\boldsymbol{\sigma}) + \boldsymbol{J}^{-1}\boldsymbol{T}_d \tag{C.10}$$

The analytical solution for rotational acceleration of the spacecraft subjected to the commanded torque signal from the attitude controller has, therefore, been solved. The result of Eq. (C.10) may be substituted into Eq. (C.2) as:

$$\begin{aligned}
\dot{V} &= \boldsymbol{\sigma}^T\dot{\boldsymbol{\sigma}} \\
\dot{V} &= \boldsymbol{\sigma}^T\left[\dot{\boldsymbol{\omega}} + \boldsymbol{\lambda}\dot{\boldsymbol{q}}_{e_{1:3}}\text{sign}(q_{e_4})\right] \\
\dot{V} &= \boldsymbol{\sigma}^T[\cancel{-\boldsymbol{\lambda}\text{sign}(q_{e_4})\dot{\boldsymbol{q}}_{e_{1:3}}} - \boldsymbol{J}^{-1}k|\boldsymbol{\sigma}|^{\alpha}\text{sign}(\boldsymbol{\sigma}) \\
&\qquad + \boldsymbol{J}^{-1}\boldsymbol{T}_d + \cancel{\boldsymbol{\lambda}\dot{\boldsymbol{q}}_{e_{1:3}}\text{sign}(q_{e_4})}] \\
\dot{V} &= \boldsymbol{\sigma}^T\left[-\boldsymbol{J}^{-1}k|\boldsymbol{\sigma}|^{\alpha}\text{sign}(\boldsymbol{\sigma}) + \boldsymbol{J}^{-1}\boldsymbol{T}_d\right]
\end{aligned} \tag{C.11}$$

The final result of Eq. (C.11) may be set equal to 0 to solve the minimum required k to ensure stability for case of the smallest principal moment of inertia exposed to the largest expected axial torque T_d. The Lyapunov equation is then considered in terms of worst-case axial scalar components as:

$$\begin{aligned} 0 &= \sigma\left[-\boldsymbol{J}_{3,3}^{-1}k|\sigma|^{\alpha}\text{sign}(\sigma) + \boldsymbol{J}_{3,3}^{-1}T_d\right] \\ 0 &= -\sigma\boldsymbol{J}_{3,3}^{-1}k|\sigma|^{\alpha}\text{sign}(\sigma) + \sigma\boldsymbol{J}_{3,3}^{-1}T_d \\ 0 &= \boldsymbol{J}_{3,3}^{-1}\left(-k|\sigma|^{\alpha+1} + \sigma T_d\right) \\ -\sigma T_d &= -k|\sigma|^{\alpha+1} \\ k &= \frac{T_d}{|\sigma|^{\alpha}} \end{aligned} \tag{C.12}$$

The result obtained in Eq. (C.12) corresponds directly to that obtained in [97], however, for the case that a bounded disturbance affects the system. Clearly from Eq. (C.12), the solution to k has a functional dependence on both α and σ. Because $\dot{\sigma}$ has been solved for its dependence on σ, α, and $\boldsymbol{J}$ in the final line of Eq. (C.11), $\dot{\sigma}$ may be computed for a range of σ to demonstrate expected performance during sliding mode [151]. It is shown in Fig. C.1 that $\alpha \approx 0$ leads to a larger $\dot{\sigma}$ when σ is small, however, faster reaching performance may be achieved with $\alpha \approx 1$ when σ is very large.

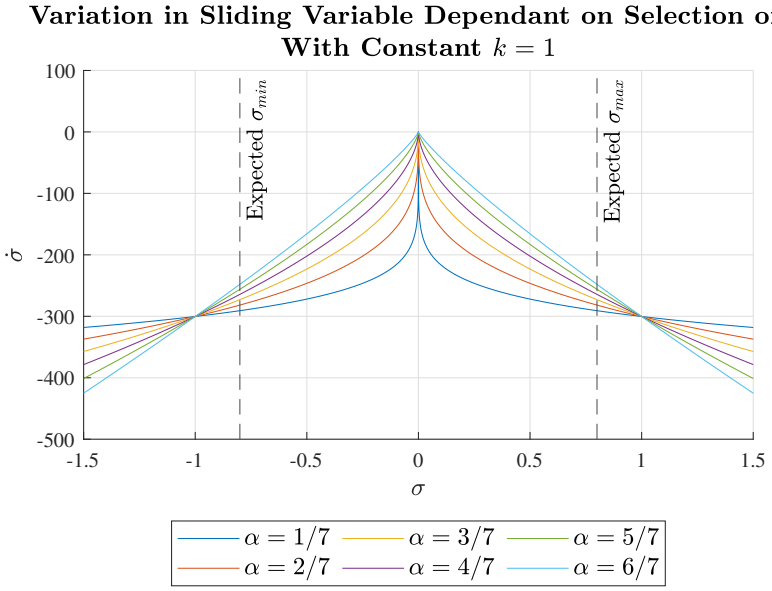

Figure C.1: Variation in $\dot{\sigma}$ Dependent on α and σ.

In this study, α was selected as $3/7$ to achieve balanced reaching law performance by considering the results in Fig. C.1. Based on the α selection, the minimum required k for asymptotic stability can be solved using the result of Eq. (C.12) for the range of σ as shown in Fig. C.2. The maximum expected axial disturbance torque

T_d required for the computation of k was found to be $1.12\text{E}-05$ N during a 150 orbit simulation by accounting for the sum of all environmental torques and the magnetic torquer gimbal compensation torque. As demonstrated by Fig. C.2, the solution to k is not defined for $\sigma = 0$. This result, however, is not problematic because the equivalent control law will dominate the control signal when σ is near 0 to ensure the system states stay on the sliding surface with $\sigma \approx 0$. Considering Fig. C.1, the rate of change of the sliding variable $\dot{\sigma}$ begins to reduce rapidly for most tested values of α when $\sigma \approx 0.01$. For a power rate reaching law, this observation would imply that the system states are near the desired values and the equivalent control signal will begin to dominate the control effort. Therefore, the minimum required k parameter was solved more conservatively at $\alpha = \frac{3}{7}$ and $\sigma = 0.002$ to yield 0.00016. To ensure a large margin of safety for stability, k was selected as 0.0025. Such a selection of k is magnitudes larger than that required for asymptotic stability, which implies that the controller will be robustly stable over the range of σ.

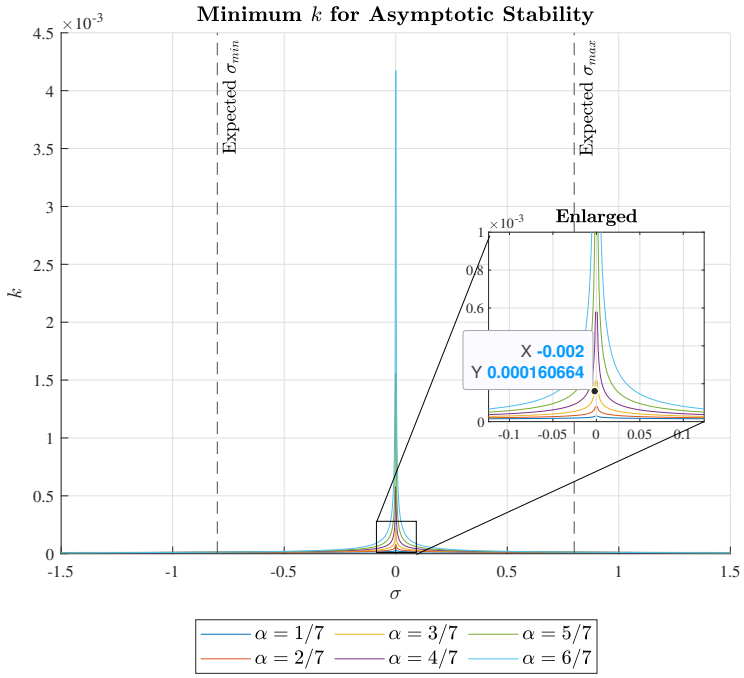

Figure C.2: Minimum Required k for Asymptotic Stability Dependent on α and σ.

The expected σ_{min} and σ_{max} points in both Fig. C.1 and Fig. C.2 were calculated using Eq. (C.3) for an expected worst-case attitude state error where the spacecraft had a yaw and roll error of π rad and a 2-norm body rate error of 0.6 rad/s.

Appendix D

DGSPCMG Flywheel Sizing

D.1 Total Angular Impulse Sizing Method

This thesis applied a total angular impulse sizing method to select an appropriate size for the DGSPCMG flywheels. Angular impulse describes the change in angular momentum over time. For a sum of torques $\boldsymbol{M}$ acting on a rigid body, the angular impulse can be computed in the following relationship:

$$\Delta \boldsymbol{H} = \int_0^t \boldsymbol{M} dt \tag{D.1}$$

The DGSPCMG was sized in this thesis to only require desaturation after approximately 70 orbits of continuous nadir pointing when subject to the orbital environment developed in Section. 3.4.2. To form the sum of all torques $\boldsymbol{M}$ acting on the spacecraft the rotational equation of motion and CMG momentum rate command should be considered. Both these equations are repeated here for convenience:

$$\boldsymbol{J}\dot{\boldsymbol{\omega}} + \boldsymbol{\omega}^{\times}\boldsymbol{J}\boldsymbol{\omega} = \boldsymbol{u}_{cmg} + \boldsymbol{T}_d \tag{D.2}$$

$$\boldsymbol{\tau} = -\boldsymbol{u}_{cmd} - \boldsymbol{\omega}^{\times}\boldsymbol{h} \tag{D.3}$$

Neglecting the commanded control torque $\boldsymbol{u}_{cmd}$, the torques which produce angular impulses to be absorbed by the CMG include the environmental torques $\boldsymbol{T}_d$, the spacecraft gyric torque $\boldsymbol{\omega} \times \boldsymbol{J}\boldsymbol{\omega}$, and the CMG gyric torque $\boldsymbol{\omega} \times \boldsymbol{h}$ leading to the expression of $\boldsymbol{M}$ as:

$$\boldsymbol{M} = \boldsymbol{T}_d - \boldsymbol{\omega} \times \boldsymbol{J}\boldsymbol{\omega} - \boldsymbol{\omega} \times \boldsymbol{h} \tag{D.4}$$

The maximum 2-norm angular impulse over 70 orbits may be obtained by running the simulator for a strictly nadir-pointing spacecraft and storing $|\Delta \boldsymbol{H}|$ from Eq. (D.1) over the course of the simulation. It was found for the simulation conditions used in this research that the maximum angular impulse was:

$$\Delta \boldsymbol{H} = \begin{bmatrix} 0.0010 \\ -0.0119 \\ -0.0124 \end{bmatrix} \text{ kgm}^2/\text{s} \tag{D.5}$$

where this $\Delta \boldsymbol{H}$ vector corresponds to a maximum 2-norm angular momentum magnitude of 0.0171 kgm^2/s. For a spacecraft starting with the desired attitude and the DGSPCMG configured so that the gimbal angles were set to $\boldsymbol{\delta} = [0.1, 0, 0]^T$ at the beginning of the simulation, then at the time of maximum angular impulse the case

of $\boldsymbol{h}_a = \Delta\boldsymbol{H}_{max}$ should be valid. $\boldsymbol{h}_a$ is the angular momentum absorbed by the CMG and can be calculated as the difference between the current CMG momentum $\boldsymbol{h} - t$ and the starting CMG momentum $\boldsymbol{h}_{t=0}$:

$$\boldsymbol{h}_a = \boldsymbol{h}_t - \boldsymbol{h}_{t=0} \tag{D.6}$$

To confirm that the $\boldsymbol{h}_a$ angular momentum vector does not correspond to a singular direction of the DGSPCMG, let $\boldsymbol{u}_H$ be the unit direction vector corresponding to $\Delta\boldsymbol{H}_{max}$. Because $\boldsymbol{\delta}_{t=0} = [0.1, 0, 0]^T$, $\boldsymbol{h}_a$ *should* be in the same direction as $\boldsymbol{h}_t$. If $\delta_{i_{t=0}}$ or $\delta_{o_{t=0}} \neq 0$, then the previous definition for $\boldsymbol{h}_a$ may not be true. Provided the definition holds, $\boldsymbol{u}_H$ may be solved as:

$$\boldsymbol{u}_H = \frac{\Delta\boldsymbol{H}_{max}}{|\Delta\boldsymbol{H}_{max}|} = \begin{bmatrix} 0.0587 \\ -0.6906 \\ -0.7208 \end{bmatrix} = \begin{bmatrix} \sin(\delta_i) \\ \cos(\delta_i)\sin(\delta_o) \\ \cos(\delta_i)\cos(\delta_o) \end{bmatrix} \tag{D.7}$$

The right side of Eq. (D.7) equates $\boldsymbol{u}_H$ to the general equation for the direction of the DGSPCMG momentum vector as a function of its gimbal angles $\boldsymbol{\delta}$. Using Eq. (D.7) to solve for the δ_i angle leads to:

$$\delta_i = \sin^{-1}(0.0587) \approx 0.0 \text{ rad} \tag{D.8}$$

Because δ_i only experiences a singularity at $\pm\frac{\pi}{2}$ and δ_o is free to rotate, the maximum angular impulse vector can be achieved by the DGSPCMG provided the following relationship does not lead to computing $|\delta_{sp}| = \frac{\pi}{2}$:

$$2H_w \sin(\delta_{sp}) = |\Delta\boldsymbol{H}_{max}| \tag{D.9}$$

The present flywheel sizing problem aims to select the flywheel momentum H_w such that when $\Delta\boldsymbol{H}_{max}$ is experienced by the CMG during a 70 orbit period, δ_{sp} is not required to be larger than the threshold for momentum management of $\epsilon_s = 0.4$ rad. Therefore, Eq. (D.9) may be solved for H_w as follows:

$$H_w = \frac{|\Delta\boldsymbol{H}_{max}|}{2\sin(\epsilon_s)} = 0.022\text{kgm}^2/\text{s} \tag{D.10}$$

The result of Eq. (D.10), for the simulation conditions used in this research, sizes the required stored angular momentum of the individual flywheels in the DGSPCMG to allow the DGSPCMG to operate for about 70 orbits without requiring momentum management from magnetic torquers. Some deviations from the 70 orbit duration should be expected because of possible variations in solar activity which could impact the rate of momentum loading into the CMG.

D.2 Preliminary Flywheel Design

Each flywheel must be designed to possess the required H_w angular momentum as calculated in the previous section. The angular momentum of a flywheel may be

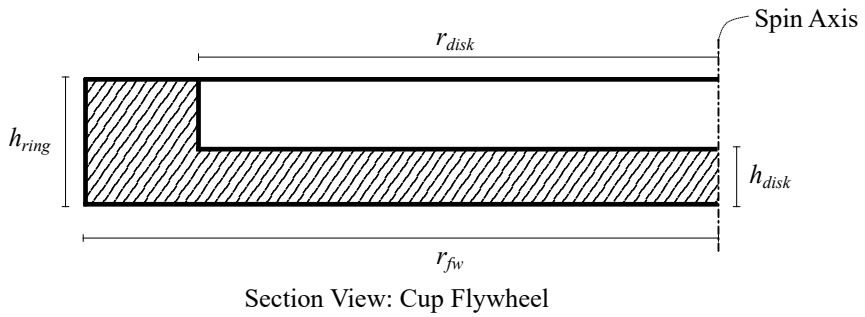

Figure D.1: Design Parameters for Cup Flywheel Design Used in DGSPCMG

calculated as:

$$H_w = I_{fw}\omega_{fw} \tag{D.11}$$

where I_{fw} is the inertia of the flywheel about its spin axis, and ω_{fw} is the angular rate of the spinning flywheel. To produce a more optimal flywheel design, a "cup flywheel" is generally desired so that the mass of the flywheel is pushed to the outer radius, increasing the flywheel inertia for a given mass. A schematic of a cup flywheel with the relevant design parameters is provided in Fig. D.1.

The MIT Space Systems Product Development Manual provides an equation for the calculation of a cup flywheel inertia as [152]:

$$I_{fw} = \frac{\rho\pi}{2}\left[h_{ring}\left(r_{fw}^4 - r_{disk}^4\right) + h_{disk}r_{disk}^4\right] \tag{D.12}$$

where ρ is the density of the flywheel material. In the present thesis the flywheel material was selected as brass for its relatively high density of 8750 kg/m^3. The remaining parameters outlined in Fig. D.1 were selected to ensure conformance with the CubeSat standard for a 2U satellite as $r_{fw} = 2$ cm, $h_{ring} = 3$ cm, $r_{disk} = 1.25$ cm, and $h_{disk} = 0.5$ cm. These parameters substituted in Eq. (D.12) yield a flywheel inertia of $I_{fw} = 2.0068\text{E} - 04$ kgm^2. Substituting the design value of I_{fw} and the required flywheel angular momentum H_w into Eq. (D.11) leads to solving the required flywheel angular velocity ω_{fw} as 109.63 rad/s. This flywheel speed can be converted to a rotational speed of 1046.9 rpm which is easily achievable with motors such as the MAXON Brushless DC EC14 Flat. Because this motor is rated to higher speeds, it may be desirable for future designs to reduce the size of the flywheel and increase the operational speed of the DC motor to achieve the same flywheel momentum.

Appendix E

Simulator Verification

In this section efforts made to validate high-fidelity effects developed for the simulator are addressed. Validation strategies used in this section are mostly summarized by simulator comparisons to analytical equations or external sources of data which provide a means of ensuring the simulator output is aligned with well established quantitative values.

E.1 Propagator & Environmental Validations

E.1.1 Validation of Perturbed Orbit Dynamics

The most significant result from the implementation of a zonal harmonic gravity model is nodal precession. Nodal precession describes an effect where the orbital plane of the satellite rotates around the rotational axis of Earth because of variations in gravity. The effect is easily observable by comparing the orbital path over 75 orbits from J3 propagation to a spherical Earth propagation in Fig. E.1.

The precession rate is most easily observable quantitatively by examining the change in the RAAN angle with respect to time. The rate of change of the RAAN

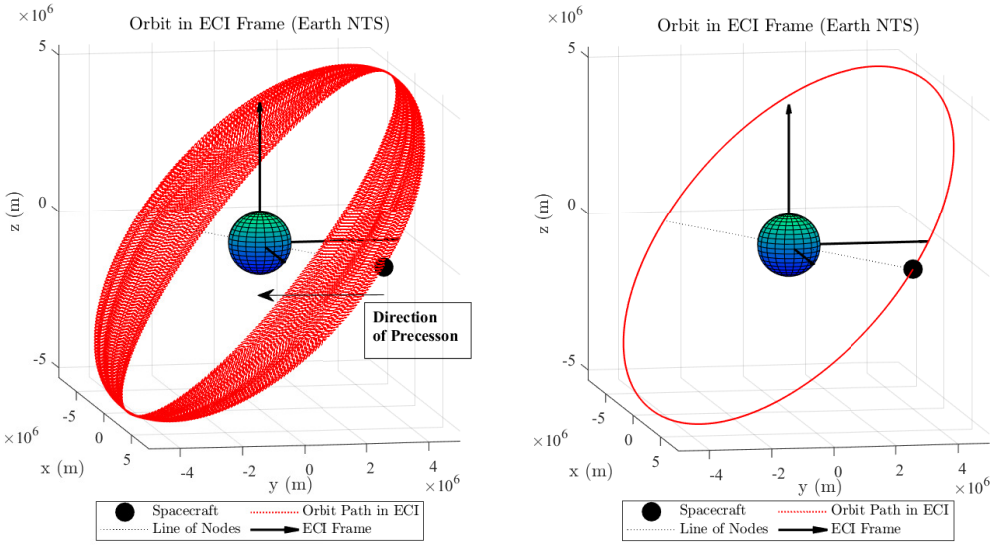

(a) (b)

Figure E.1: J3 Orbital Path (left) Compared to Spherical Earth Orbital Path (right)

angle $\dot{\Omega}$ from the simulator was compared to an approximate solution for J_2 precession in the following analytical equation:

$$\dot{\Omega} = -\frac{3}{2}\frac{R_e^2}{(a(1-e^2))^2} J_2 \omega \cos(i) \tag{E.1}$$

Eq. (E.1) produced a precession rate of $-4.98°$/day. By computing the slope of the line provided in Fig. E.2 a precession rate of $-4.99°$/day was produced by the simulator. It is clear that the simulator implementation agrees closely with the approximate analytical solution. As an additional degree of verification, the simulation data was compared to the RAAN precession of the ISS which orbits very similarly to the satellite orbit discussed in this thesis. For RAAN angles of 320.47 and 324.99 degrees obtained with epoch times of April 4, 2024 1:18pm and April 3, 2024 3:24pm respectively, the RAAN angle precession of the ISS was $-4.95°$/day. With good conformance between analytical and real world data, the implementation of the harmonic gravity model was considered valid.

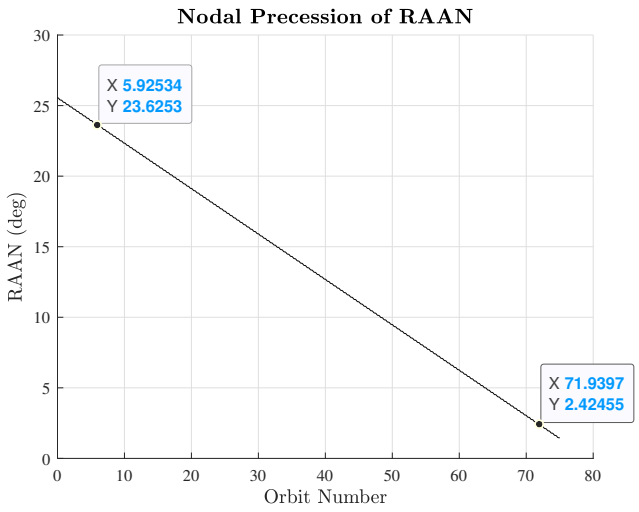

Figure E.2: Precession of RAAN Angle Over 75 Orbit Simulation

E.1.2 Validation of Rotational Equations of Motion

The rotational dynamics of the subject CubeSat are modeled after a rigid-body generalized CubeSat. The implementation of the rotational equations of motion can subsequently be validated by comparing the torque-free motion of the axisymmetric body to the analytical result provided in Section. 3.3.1. That is, the path traced by the body angular velocity vector should roughly trace a circle in ω-space provided an initial condition where the rate of rotation about each axis is equal. In addition, the simulation output data should demonstrate that a spin about the minor principal inertial axis is a stable spin. These torque-free rotational motion characteristics are demonstrated in Fig. E.3a and Fig. E.3b.

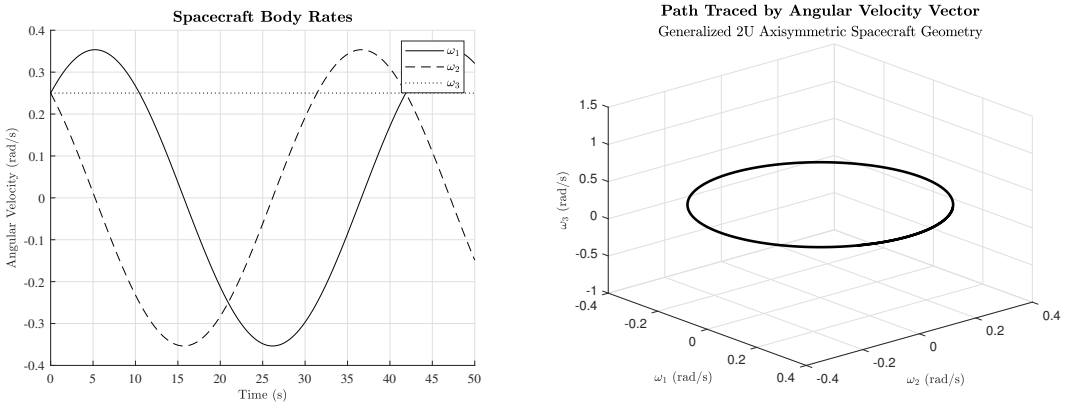

(a) (b)

Figure E.3: Demonstration of Torque-Free Axisymmetric Body Rotational Motion from Simulator Output

In Fig. E.3a it is shown that the spin about the minor principal axis ω_3 is stable because it was constant for all time. The plot in Fig. E.3b clearly reflects the expected result from Section. 3.3.1 by observing the circular trace of the angular momentum vector in ω-space. The simulator, was therefore, considered to be validated in regards to rotational motion of a rigid-body spacecraft.

E.1.3 Validation of High Fidelity Aerodynamic Model

NRLMSISE-00 Validation

The reader is directed to [153] for the original citable work addressing the development of NRLMSISE-00 which is discussed in this section. Validating the implementation of a MATLAB-based NRLMSISE-00 can be conveniently achieved by comparing it to the NASA Community Coordinated Modeling Center (CCMC) Instant Run system for NRLMSISE-00 by providing the NASA instance with the same inputs for solar and geomagnetic activity as the MATLAB Model.

By simulating the MATLAB model a solution for atmospheric density is obtained based on varying altitude, latitude and longitude, however, the CCMC model can only output a solution with respect to longitude at constant latitude and altitude. On account of this limitation, it cannot be expected for the output data from each instance of the model to agree perfectly when an inclined eccentric orbit is analyzed. To compensate for the CCMC limitation, the models were both run for an equatorial orbit with no eccentricity. In this scenario, the only variation in the independent variables is longitude. To visualize this scenario, the MATLAB model was plotted globally at a 414km altitude (apogee altitude for the simulated TLE) in Fig. E.4. The orbit line is superimposed in the figure to emphasize that there is no change in latitude in the equatorial orbit.

By obtaining data along the equatorial orbit line, the MATLAB model can be

compared to the CCMC model to ensure agreement when the input parameters are matching. This comparison is shown in Fig. E.5.

As shown in Fig. E.5, the models agree closely. The peak density can be observed to show good agreement between both models. In general, both models follow the same profile and reach the same peak values. At the minimum observed density, occurring around 325 degrees of travel in longitude, the CCMC model predicts a slightly lower density than MATLAB. One explanation for this difference could be attributed to the MATLAB model using the exact TLE epoch time, where the CCMC model can only take epoch times in steps of 15 minutes, leading to a roughly

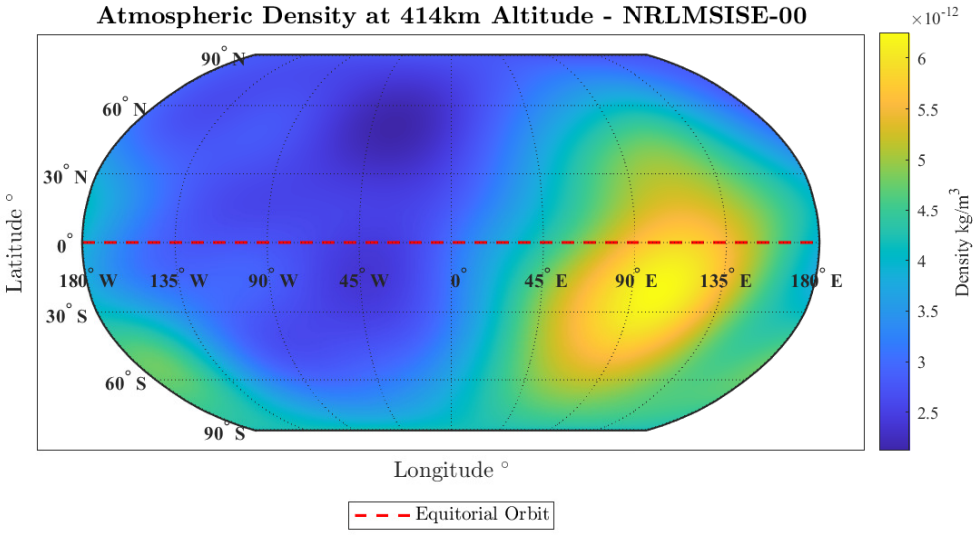

Figure E.4: Global Contour Plot of Atmospheric Density (MATLAB)

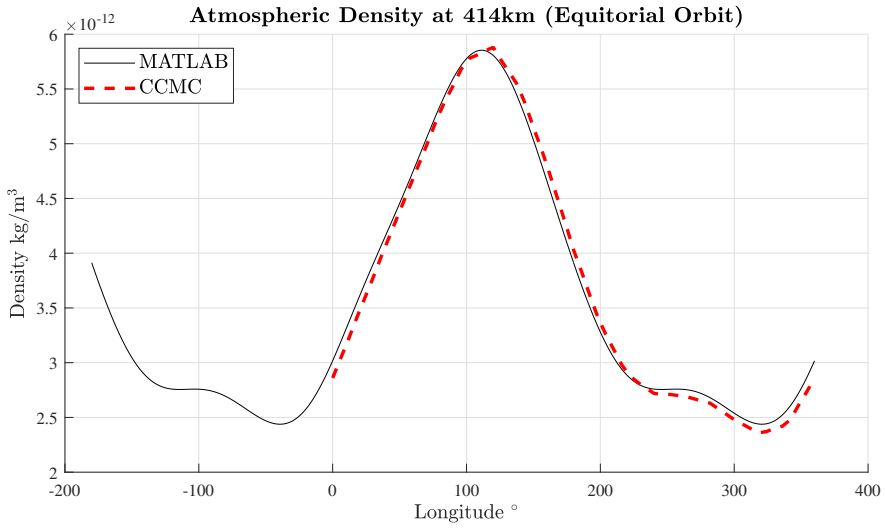

Figure E.5: MATLAB Simulation vs CCMC Data (Equatorial Orbit)

6 minute difference between the MATLAB data set and the CCMC data set. Despite the minor differences, the MATLAB model can be considered validated by the CCMC model. Moreover, the accuracy improvement achieved by implementing the NRLMSISE-00 model over a constant density model would justify its use even in the case the MATLAB NRLMSISE-00 has subtle inaccuracies.

Another consideration which could be made related to the atmospheric density models is where the peak density occurs. In the case of the CCMC model, the longitude axis begins at 0 degrees. In the MATLAB convention, longitude ranges from -180 degrees (west) to 180 degrees (east). While not explicitly stated by each model, the assumption that the models share an identical prime meridian (0 degrees longitude) would indicate that both models reasonably agree in terms of density distribution. Fig. E.4 and Fig. E.6 can be compared noting that the shared prime meridian is at 0 degrees longitude. It is clear that both models share a region of peak density which occurs in the southern hemisphere around 100° longitude.

Verification of Projected Area Calculation

To verify the proposed dynamic projected area model, the projected area may be computed at various satellite attitudes relative to the flow direction and compared to the projected area computed by SolidWorks for the same satellite attitude and geometry. In Fig. E.7 projected areas are compared for the case that only 1 or 2 faces are exposed to the flow by incrementally rotating the satellite about its Z+ axis in the flow. In Fig. E.8 the case that 3 faces are exposed to the flow is compared.

As shown in the Fig. E.7 and Fig. E.8 the proposed dynamic calculation method agrees very closely with the SolidWorks solutions. The method is accurate for any case that 1 to 3 faces are exposed to the flow in an arbitrary orientation. As a result

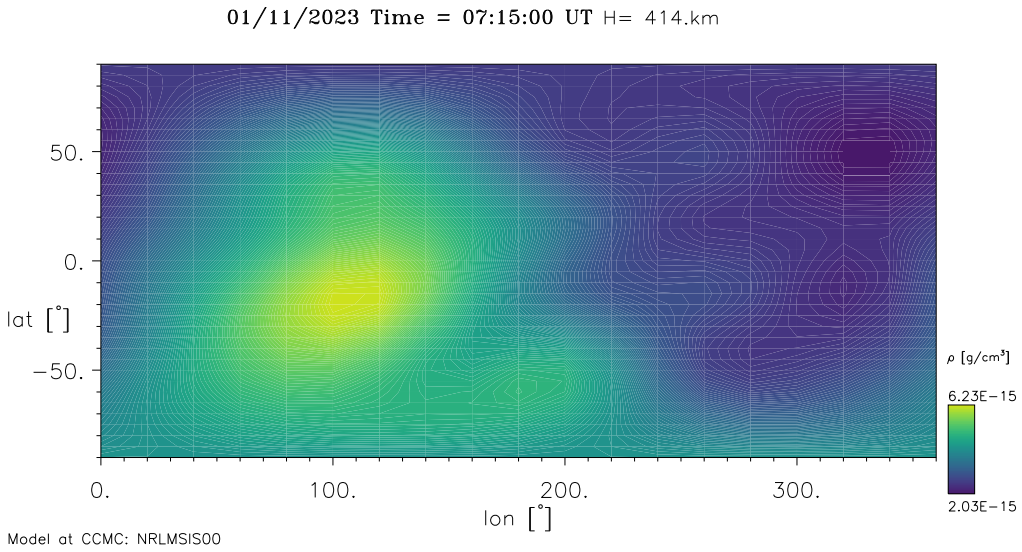

Figure E.6: Global Contour Plot of Atmospheric Density From CCMC Instant Run Service (Obtained and Used with Permission from ccmc.gsfc.nasa.gov)

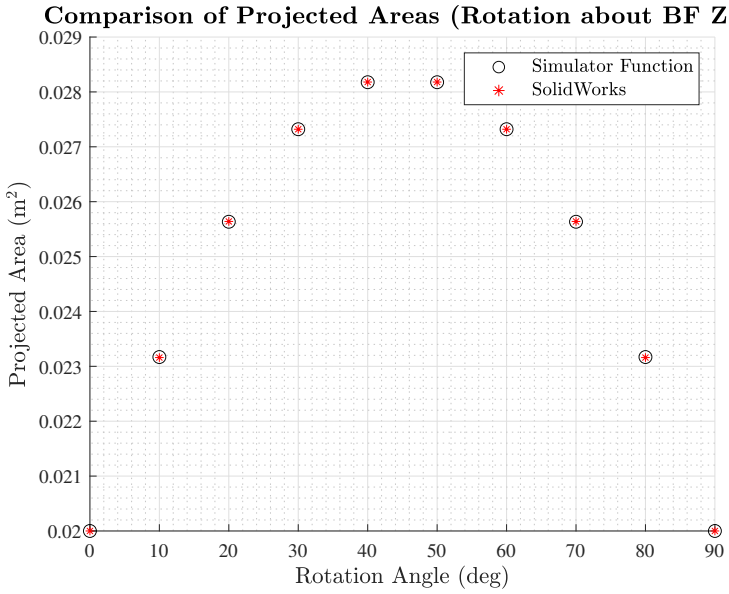

Figure E.7: Projected Areas (Rotation about Z-axis in Flow)

of the agreement between both methods, the dynamic projected area calculation was considered validated.

Verification of Dynamic Center of Pressure

The verification of the dynamic center of pressure is a less trivial task than that considered for the dynamic area calculation. It was discussed in [57] that the flow regime in LEO is far from continuous, and is largely characterized by particles randomly impacting and smoothly sliding off the orbiting body. Like [57], the present work only considers normal pressures exerted at the centroid of the external faces of the body. In addition, only the pressures exerted on the faces in the flow are considered, and pressures exerted on the faces out of the flow are neglected. The result of this pressure treatment leads to a model which is bias towards a worst-case model. Including atmospheric pressures on the out of flow faces would have the effect of moving the COP closer to the COM – thereby reducing the aerodynamic torque.

In this thesis, the continuum assumption from [57] was adopted so that the dynamic center of pressure could be validated with analytical equations provided from [154]. While the present model is a dynamic example, the assumptions in place make the calculation of $\boldsymbol{s}_{cp}$ functionally similar to a hydrostatic example. Therefore, the force exerted on one external face from a uniform pressure field is:

$$F = \int p \, dA = pA \tag{E.2}$$

where p is the pressure and A is the area of the face. Additionally, by drawing on the theory presented in [154] the center of pressure offset (in the y axial direction) from

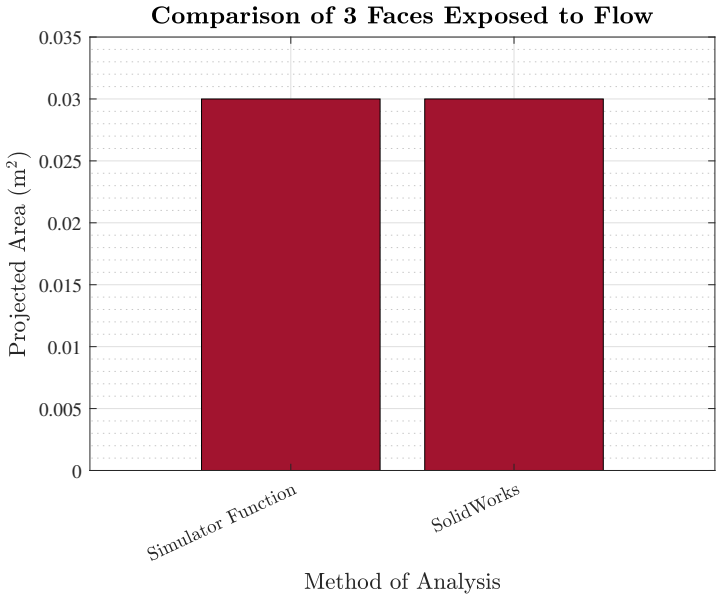

Figure E.8: 3 Faces Exposed to Flow Projected Area

the centroid may be calculated as:

$$Fy_{cp} = \int yp \, dA = 0 \tag{E.3}$$

Clearly the hydrostatic theory supports the alignment of the COP and the geometric centroid of the face when a uniform pressure is applied to the face. While the theory agrees with the proposed model, an additional verification is provided in Fig. E.9 - Fig. E.10. As shown in the subject figures, when the satellite acquires a

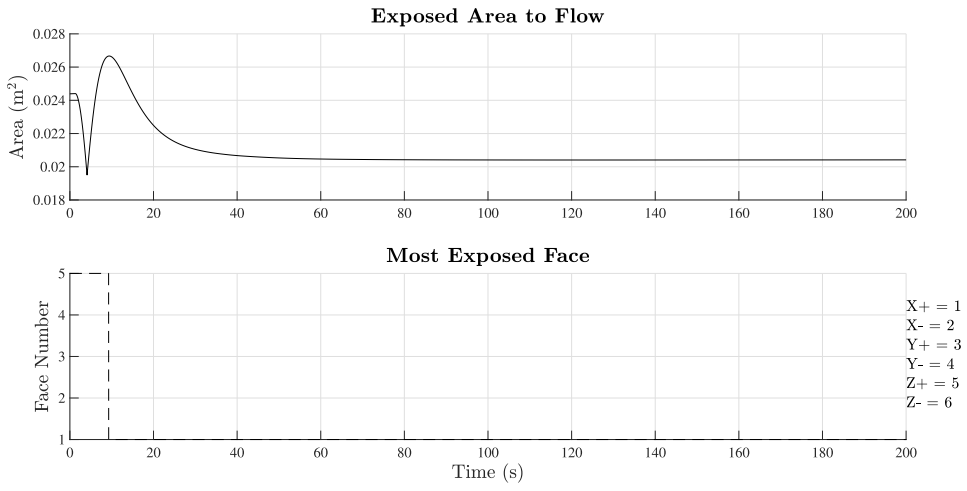

Figure E.9: Projected Area in Flow for A Spacecraft Reorientation to Nadir Pointing

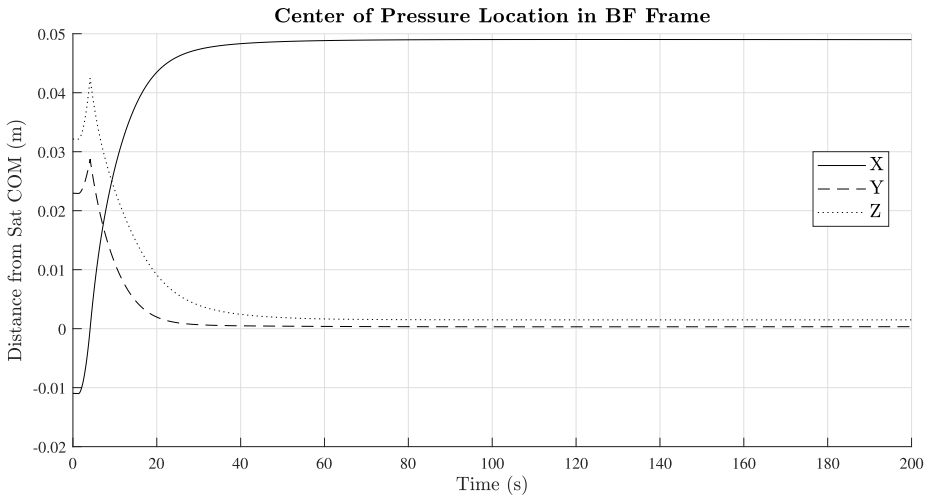

Figure E.10: Dynamic COP Position for A Spacecraft Reorientation to Nadir Pointing

nadir pointing attitude and aligns the $\mathscr{F}_{BF}$ x-axis with the flow direction, the x face becomes the most exposed to the flow. Correspondingly, the exposed area to flow becomes roughly the area of the x face, and the COP aligns with the centroid of the x face. Based on the provided analysis and theory, the center of pressure calculation was considered validated within the scope of the thesis.

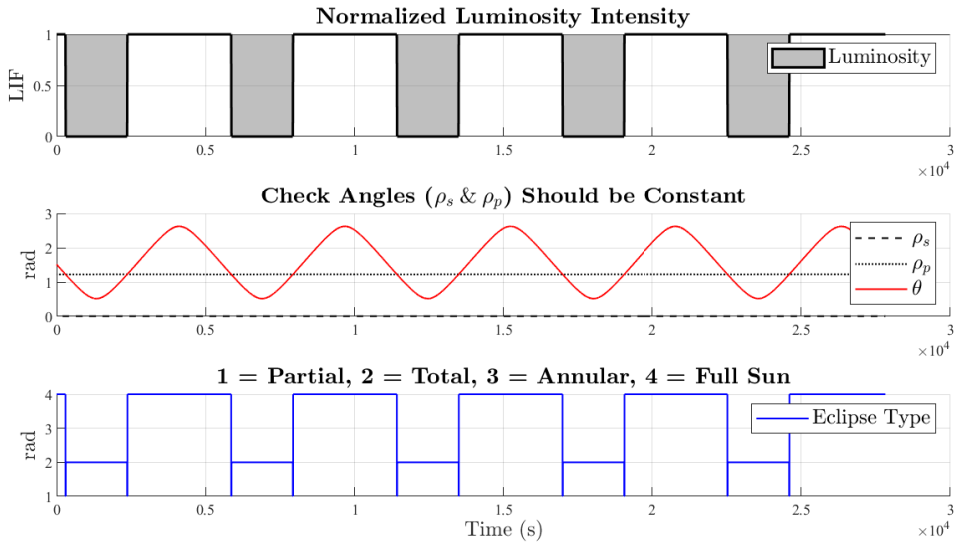

Figure E.11: Key Eclipse Model Parameters Over 5 Simulated Orbits

E.1.4 Validation of Eclipse Model

Physical and mathematical validation efforts were employed to validate the eclipse model. One such physical validation factor was ensuring that the duration of the eclipse derived from the model was reasonably close to the real world eclipse duration. According to [155], the average percent of time spent in eclipse per orbit for a satellite with an orbital altitude around 400 km is approximately 37.5%. Over the course of 5 orbits, the average eclipse duration for the simulated satellite was 37.4% which agrees closely with the real world physical data. From a mathematical standpoint, the identified angles ρ_s and ρ_p representing the angular radii of the Sun and Earth, respectively, must remain roughly constant for all time to be considered valid. While ρ_s and ρ_p are dependent on the variable Earth to Sun distance S, short-term variations in this distance are sufficiently small that the angles are effectively constant in the short-term. It is shown in Fig. E.11 that these angles were calculated to be constant by the simulator which further validates the output of the eclipse model.

E.1.5 Validation of Ephemeris Data

To ensure that the ephemeris data employed in the simulator was valid, the MATLAB-produced ephemeris data was compared with data derived from the NASA JPL Horizons System running DE432t. At the TLE epoch time, the simulation outputs a lunar position vector expressed in $\mathscr{F}_{ECI}$ of $[-3.7165\text{E}05, 1.2805\text{E}05, 8.9679\text{E}04]$ km. The JPL Horizons System yields a lunar position vector from the center of Earth equal to $[-3.7163\text{E}05, 1.2809\text{E}05, 8.9700\text{E}04]$ km. The percent difference between the MATLAB ephemeris data compared to the JPL data was $0.0054, 0.0312, 0.0234\%$, respectively, for all three components. Through this analysis it is clear that the MATLAB model closely matches the JPL system. The lunar ephemeris model may, therefore, be considered to be verified.

Solar ephemeris data was also utilized in the simulations and was, therefore, validated following an identical process to what was undertaken for Lunar ephemeris validation. At the TLE epoch time, the simulation outputs a solar position vector in $\mathscr{F}_{ECI}$ of $[5.1434\text{E}07, -1.2646\text{E}08, -5.4821\text{E}07]$ km. The JPL Horizons System yields a solar position vector of $[5.1433\text{E}07, -1.2647\text{E}08, -5.4821\text{E}07]$ km. The percent difference between the MATLAB ephemeris data compared to the JPL data was $0.0030, 0.0004, 0.0004\%$, respectively. Through this analysis it is clear again that the MATLAB model closely matches the JPL system. The solar ephemeris data, therefore, may be considered to be validated.